Transition Metal-doped Calcium Oxide as Model Catalyst for the Oxygen Activation in the Oxidative Coupling of Methane (OCM) Reaction

vorgelegt von

M.Sc.

Lukas Thum

ORCID: 0000-0001-7622-2302

von der Fakultät II – Mathematik und Naturwissenschaften

der Technischen Universität Berlin

zur Erlangung des akademischen Grades

Doktor der Ingenieurwissenschaften

- Dr.-Ing. –

genehmigte Dissertation

Promotionsausschuss:

Vorsitzender:	Prof. Dr. Thomas Friedrich
Gutachter:	Prof. Dr. Reinhard Schomäcker
Gutachter:	Prof. Dr. Robert Schlögl
Gutachter:	P.D. Dr. Evgenii Kondratenko

Tag der wissenschaftlichen Aussprache: 17. November 2020

Berlin 2020

Danksagung

Ich danke Herrn Professor Schomäcker für die Zeit, die ich in seinem Arbeitskreis verbringen durfte, um dort meine Doktorarbeit anzufertigen. Besonders danke ich Ihn für den Freiraum, der mir während meiner Forschung gewährt wurde, sowie für seine Unterstützung und Geduld.

Mein Dank gilt auch Herrn Professor Schlögl. Ohne den Zugriff auf die Ressourcen des FHIs wäre die Arbeit nicht durchführbar gewesen. Die Diskussionen in den Doktorandentagen waren sehr hilfreich, um über die eigene Arbeit zu reflektieren und neue Inspirationen zu finden.

Mein besonderer Dank gilt Annette Trunschke, die mich in ihren Arbeitskreis aufgenommen hat und sich immer Zeit nahm für Diskussionen über aktuelle Ergebnisse. Hiermit möchte ich mich auch beim stets hilfsbereiten Kollegium des FHIs bedanken, besonders aber bei Jasmin, Maike, Andrey, Yuanqing und Frank.

Ich möchte mich auch herzlich bei Prof. Risse, Prof. Dinse aber insbesondere bei Wiebke Riedel von der FU bedanken für deren Unterstützungen bei meiner Forschung. Das Gleiche gilt für die Kollegen vom BasCat. Dafür danke ich herzlichst Guam, Michael, Ralph Krähnert und Frank Rosowski.

Meinen Studenten Ludger, Maik, Natasa und Ben gilt mein größter Dank für deren wertvollen Beitrag zu meiner Arbeit. Auch wenn die Arbeit oft frustrierend war, hoffe ich sie konnten die Zeit mit mir so schätzen wie ich mit ihnen.

Für die freundliche und entspannte Arbeitsatmosphäre in der TC08 Gruppe würde ich gerne meinen Kollegen danken, besonders aber bei Max, Natasa und Georg für die emotionale Unterstützung, sowie Gabi für den meist unkomplizierten technischen Support. Hiermit möchte ich natürlich auch dem Team der Werkstätten danken, ohne die ein kontinuierliches Arbeiten nahezu unmöglich wäre. Vielen Dank deshalb insbesondere an Axel, Carsten, Erik und Rolf.

Meine Eltern Marianne und Uwe haben mir mein Studium, sowie die anschließende Promotion erst ermöglicht und mich dabei stets unterstützt, ohne jeglichen Druck aufzubauen. Dafür gilt Ihnen mein größter Dank.

Auch meinen Freunden gilt ein großer Dank für deren emotionalen Unterstützung, sowie willkommenen Ablenkungen von der oft frustrierenden Arbeit. Dafür möchte ich Carlo, Anton, Wenjamin und Heiko, sowie meinen Bruder Aron danken.

Zusammenfassung

Um alternative Ausgangsstoffe für die chemische Industrie zu finden, wurde in den 1980er Jahren die oxidative Kupplung der Methanreaktion (OCM) entwickelt, die die Herstellung von Ethylen aus Methan ermöglicht. Obwohl dies in den letzten 40 Jahren Gegenstand vieler Untersuchungen war, ist der bisherige Erfolg begrenzt und eine Ausbeute von 30% wurde bisher noch nicht übertroffen. Ein Hauptproblem der Reaktion ist die Aktivierung von Methan. Bei einer Dissoziationsenergie von 423 kJ/mol werden hochreaktive Reaktanden oder hohe Reaktionstemperaturen benötigt. Die Kontrolle der Aktivierung des Oxidationsmittels ist somit wichtig, um eine Überoxidation der gewünschten Produkte zu vermeiden und eine hohe Selektivität zu erreichen. Da bereits viele Materialien ohne signifikanten Durchbruch als Katalysator für das OCM gescreent wurden, ist weitere Grundlagenforschung erforderlich, um die begrenzenden Faktoren dieser Reaktion zu verstehen. Es wurde festgestellt, dass Calciumoxid interessante Wechselwirkungen mit Sauerstoff zeigt, wenn es mit Übergangsmetallen dotiert ist, wodurch die Sauerstoffdissoziationsbarriere stark verringert werden kann, was diese Materialien zu interessanten Materialien für die Untersuchung von Oxidationskatalysatoren machen.

In dieser Arbeit wurden mit Übergangsmetallen dotierte Calciumoxidmaterialien (0,1 Atom-% Mn, Ni, Cr, Co und Zn) synthetisiert, charakterisiert und für die OCM-Reaktion getestet. Zunächst wurden dotierte Carbonatvorläufer durch ein Co-Präzipitationsverfahren hergestellt. Die Syntheseparameter wurden optimiert, um Materialien mit einer reinen Calcit Phase zu erhalten, welche durch XRD verifiziert wurde. EPR-Messungen an den Mn-dotierten CaO-Materialien zeigen eine erfolgreiche Substitution von Ca^{2+} durch Mn^{2+} im CaO-Gitter. Die Materialien wurden auf ihre Leistung in der OCM-Reaktion getestet, wobei Verbesserung der Selektivität und der Aktivität für Mn-, Ni- und Zn-dotierte Proben beobachtet werden konnte, bei Co- und Cr-dotiertem CaO war die Selektivität stark verringert. Die optimale Dotierungskonzentration wurde im Bereich von 0,05 bis 0,10 Atom-% gefunden, wo die stärkste Abnahme der scheinbaren Aktivierungsenergie sowie die maximale Zunahme der Selektivität gefunden wurde. Die Gesamtverbesserung des Katalysators war jedoch nur gering.

In-situ-Raman-, IR- und TG-Experimente zeigten die Bildung von Carbonaten während der Reaktion. Hydroxidspezies oder Sauerstoffspezies wurden nicht gefunden. Um die Sauerstoffaktivierungsfähigkeiten der Materialien zu untersuchen, wurden SSTIKA-Experimente durchgeführt und eine gepulste Isotopen-Scrambling-Technik entwickelt, implementiert und numerisch simuliert. Obwohl nicht viel Erkenntnis über die Rolle des Übergangsmetalls erlangt wurde, konnte die Kontamination der Oberfläche durch Wasser und Kohlendioxid als limitierender Faktor für das OCM auf basischen Oxiden identifiziert werden. Aufgrund der Blockierung der aktiven Stellen durch Bei- und Nebenprodukte der OCM-Reaktion sind hohe Temperaturen erforderlich, um die Katalysatoroberfläche zu regenerieren.

Abstract

To find alternative feedstocks for the chemical industry, the oxidative coupling of methane (OCM) reaction was developed in the 1980s, allowing the production of ethylene from methane. Though, being the topic of many investigations in the last 40 years, the success so far is limited and a yield of 30% has yet to be surpassed. One major issue of the reaction is the activation of methane. With a dissociation energy of 423 kJ/mol, highly reactive materials or high reaction temperatures are needed. Controlling the activation of the oxidant is essential to avoid an overoxidation of the desired products and achieve high selectivity. Since many materials have been screened as a suitable catalyst for the OCM without a breakthrough, basic research is necessary to understand the limiting factors of this reaction. In physical experiments, calcium oxide was found to show interesting interactions with oxygen when doped with transition metals, strongly reducing the oxygen dissociation barrier, making these materials an interesting target to study oxidation catalysts.

In this work, first-row transition metal-doped calcium oxide materials (0.1 atom% Mn, Ni, Cr, Co, and Zn) were synthesized, characterized, and tested for the OCM reaction. First, doped carbonate precursors were prepared by a co-precipitation method. The synthesis parameters were optimized to yield materials with a pure calcite phase, which was verified by XRD. EPR measurements on the Mn-doped CaO materials indicate a successful substitution of Ca^{2+} with Mn^{2+} in the CaO lattice. The materials were tested for their performance in the OCM reaction, where a beneficial towards selectivity and activity effect could be observed for Mn-, Ni-, and Zn-doped samples, where the selectivity of Co- and Cr-doped CaO was strongly reduced. The optimum doping concentration could be identified in the range of 0.05-0.10 atom%, showing the strongest decrease in the apparent activation energy, as well as the maximum increase in selectivity. The overall improvement of the catalyst was though was only minor.

In situ Raman, IR, and TG experiments revealed the formation of carbonates during the reaction. Hydroxide species, or oxygen species were not found. To investigate the oxygen activation capabilities of the materials, SSTIKA experiments were performed and a pulsed isotopic scrambling technique was developed and implemented and numerically simulated. Though giving not much insight on the role of the dopant, the contamination of the surface by water and carbon dioxide could be identified as the limiting factor for the OCM on basic oxides. Due to the blocking of the active sites of the by- and side-products of the OCM reaction, high temperatures are needed to regenerate the catalyst surface.

Erklärung zur Dissertation

Ich erkläre hiermit, dass ich bislang an keiner anderen Hochschule oder Fakultät eine Promotionsabsicht beantragt habe.

Die vorliegende Dissertation wurde bereits teilweise in Form von wissenschaftlichen Publikationen veröffentlicht. Es handelt sich dabei vor allem um große Teile der folgenden Veröffentlichung:

L. Thum, M. Rudolph, R. Schomäcker, Y. Wang, A. Tarasov, A. Trunschke, and R. Schlögl, "Oxygen Activation in Oxidative Coupling of Methane on Calcium Oxide", *J. Phys. Chem. C*, **2019**, 123, 13, 8018-8026.

Eigenanteil (Erstauthor): Die Arbeit und die damit verbundenen Messungen, Synthesen, Methodenentwicklung, Probenvorbereitungen und Auswertungen wurden weitestgehend von mir persönlich oder in meinem Beisein durchgeführt. Ausgenommen davon ist nur die Durchführung der ex situ TG, ex situ XRD, ICP-OES sowie die BET Messung, welche zusammen nur einen geringfügigen Anteil der Arbeit darstellen.

Weitere Teile der Arbeit werden voraussichtlich in einem anderen Manuskript veröffentlicht:

L. Thum, W. Riedel, Natasa Milojevic, A. Trunschke, Klaus-Peter Dinse, Thomas Risse, R. Schomäcker, and R. Schlögl, "Transition Metal Doped Calcium Oxide as Model Catalyst for the OCM Reaction".

Eigenanteil (Erstauthor): Die Arbeit und die damit verbundenen Messungen, Synthesen, Methodenentwicklung, Probenvorbereitungen und Auswertungen wurden weitestgehend von mir persönlich oder unter meinen Anweisungen durchgeführt. Dr. Riedel und Prof. Dinse haben die EPR Messungen durchgeführt und ausgewertet, die Ergebnisse wurden gemeinsam diskutiert.

Auf folgende Arbeiten wird Bezug genommen, aber maximal in geringem Umfang direkt in der Arbeit verwendet:

H. R. Godini, M. Khadivi, M. Azadi, O. Görke, S. M. Jazayeri, L. Thum, R. Schomäcker, G. Wozny, and J.-U. Repke, "Multi-Scale Analysis of Integrated C1 (CH4 and CO2) Utilization Catalytic Processes: Impacts of Catalysts Characteristics up to Industrial-Scale Process Flowsheeting, Part I: Experimental Analysis of Catalytic Low-Pressure CO2 to Methanol Conversion", *Catalysts*, **2020**, 10, 5, 505.

Eigenanteil (Co-Author): Konzeptionierung und Modifikation eines Reaktors für die Methanolsynthese. Umsetzung der Kopplung eines OCM Reaktors mit einer nachgeschalteten Methanolsynthese. Unterstützung bei der Durchführung der katalytischen Messungen, sowie deren Interpretation und Diskussion.

W. Riedel, L. Thum, J. Möser, V. Fleischer, U. Simon, K. Siemensmeyer, A. Schnegg, R. Schomäcker, T. Risse, and K.-P. Dinse, "Magnetic Properties of Reduced and Reoxidized Mn–Na2WO4/SiO2: A Catalyst for Oxidative Coupling of Methane (OCM)", *J. Phys. Chem. C*, **2018**, 122, 39, 22605-22614.

Eigenanteil (Co-Author): Entwicklung eines Verfahrens zur Messung und Präparation der Proben unter Ausschluss von Luft. Präparation aller vermessenen Proben. Unterstützung bei der Auswahl geeigneter Parameter für die Probenvorbehandlung. Unterstützung bei der Interpretation der Ergebnisse.

V. Fleischer, U. Simon, S. Parishan, M. Gracia Colmenares, O. Görke, A. Gurlo, W. Riedel, L. Thum, J. Schmidt, T. Risse, K.-P. Dinse, and R. Schomäcker, "Investigation of the role of the Na2WO4/Mn/SiO2 catalyst composition in the oxidative coupling of methane by chemical looping experiments", *Journal of Catalysis*, **2018**, 360, 102-117.

Eigenanteil (Co-Author): Entwicklung eines Verfahrens zur Messung und Präparation der EPR-Proben unter Ausschluss von Luft. Präparation von Vergleichsproben für die EPR Messungen. Unterstützung bei der Auswahl geeigneter Parameter für die Probenvorbehandlung. Unterstützung bei der Interpretation der Ergebnisse.

P. Schwach, N. Hamilton, M. Eichelbaum, L. Thum, T. Lunkenbein, R. Schlögl, and A. Trunschke, "Structure sensitivity of the oxidative activation of methane over MgO model catalysts: II. Nature of active sites and reaction mechanism", *Journal of Catalysis*, **2015**, 329, 574-587.

Eigenanteil (Co-Author): Hydrothermale Synthese von Referenzproben für die HR-TEM. Unterstützung bei der HR-TEM Messung für die Erstellung für die Arbeit relevanter Aufnahmen.

Table of Contents

1. Introduction

1.1. Motivation

With increasing economical and ecological challenges the demand for resource- and energy-efficient technologies becomes more and more eminent. Especially in the chemical industry fossil raw materials, such as crude oil are in high demand. Due to political instabilities, as well as a limited global abundance, the supply and price of crude oil cannot be endlessly sustained in its current rate of consumption. In 2017 the global refining capacity reached 98.7 million barrels per day and is predicted to even further increase.[1] Though most of the oil is used as gasoline or fuel, many chemical products e.g. polymers rely on precursors obtained from refined crude oil. To ensure the supply chain, existing routes have to be optimized to prevent losses and new routes have to be developed using different feedstocks.

One of the most important petrochemical compounds is ethylene with a production of 120 Mt/a in 2008 and annual growth of 5% now exceeding 200 Mt/a.[2] With the exponential growth of ethylene demand a stable and sustainable feedstock is needed. Currently, ethylene is obtained by steam cracking of higher hydrocarbons, especially naphtha, and from natural gas, e.g. dehydrogenation of ethane. Alternative routes such as the methanol to olefin (MTO) process can up to now not compare to the conventional process since methanol has to be synthesized first via synthesis gas, which is obtained by reforming of natural gas (see section 1.2.1.). This process though, as well as ethanol dehydration becomes more relevant with increasing crude oil prices and ethanol being synthesized by renewable resources (e.g. corn and sugar cane).[3] Half of the produced ethylene is consumed for the production of polyethylene, allowing no substitution of the ethylene via an alternative synthesis route of the product.[2]

A direct synthesis route for ethylene is the oxidative coupling of methane (OCM) proposed by Bhasin and Keller in the 1980s.[4] At temperatures above 700°C in an oxygen-containing atmosphere, methane is partially oxidized resulting in the formation of higher alkanes and alkenes, such as ethane and ethylene. A general problem of this process is the low selectivity. At these high temperatures, finding a suitable catalyst activating the stable C-H bond of methane with a dissociation barrier of 440 kJ/mol, while not over-oxidizing the products proved to be quite challenging. Though known nature being quite efficient at activating methane even at room temperature,[5] over the past years in research many materials were tested and an apparent yield barrier of 25% has yet to be overcome.[6] Nevertheless, siluria technologies already commercialized a process (Gemini) based on the OCM process to produce ethylene from methane, claiming improved catalyst performance at significantly lowered reaction temperatures.[7,8]

Though still much research is needed to improve the OCM performance, the utilization of methane as a feedstock for the chemical industry is highly desirable. As

the main component of natural gas and product of biological fermentation processes its abundance is quite secure.[9,10] Most of the methane is consumed as fuel in industry and residential applications.[11] Due to methane being odorless and not producing any particles such as coke while burning, it offers itself as an energy source. Its energy density of 55.7 MJ/kg compared to that of gasoline 46.4 MJ/kg and residue-free burning capabilities, make methane the superior fuel. A major issue of methane though is the liquefaction. With a critical point of -82°C liquid storing is quite unpractical and uneconomic. Alternatively, methane stored at high pressures consumes lots of energy for compression and requires thick and heavy pressure vessels for storage which adds to the transport cost, making it not profitable. Porous storage medias such as metal-organic frameworks (MOFs) are being developed and improved to allow storage of methane at moderate pressures enabling the transportation of methane and use in e.g. vehicles. Currently, the production costs of those materials are too high for industrial applications.[12,13]

With methane not suitable unfit for long distance transport (with exception of costly pipelines) large quantities of methane are produced in regions (e.g. oil platforms), where it cannot be economically shipped, resulting in the flaring of methane. Roughly 4% of the annually produced methane is flared (150 billion cubic meters[14,15] vs. 3800 billion cubic meters[11,16]). Given the ongoing discussions on humanity's contribution to climate change or global warming, CO_2 emission through flaring have to be avoided. Calculating the annual produced CO_2 from the 150bn m³ flared methane results in a value of 300 Mt/a, which contributes to almost 1% of the total annual CO_2 production (33400 Mt/a).[16] Since the greenhouse effect of methane is significantly higher for methane than for carbon dioxide[17] and methane being lighter than air, up to now no suitable alternative to the flaring is economically feasible. An on-site chemical conversion or storage and shipping of the methane is therefore highly desirable.

1.2. Chemical uses of Methane

1.2.1. Hydrogen and Synthesis Gas

With hydrogen becoming more and more relevant in the field of renewable energy sources for numerous applications and alternative routes, such as electrochemical or photocatalytic methods still being not mature for large scale industrial application, steam reforming (SR), especially of methane, is still the main source for hydrogen production. In a first step, methane reacts with water to form synthesis gas (equation (1)) in a second step more hydrogen can be obtained by a consecutive water gas shift reaction (WGS, equation (2)).[18]

$$CH_4 + H_2O \rightarrow CO + 3H_2 \quad (1)$$

$$CO + H_2O \rightarrow H_2 + CO_2 \quad (2)$$

With the reaction being quite endothermic (ΔH_R = 206 kJ/mol), parts of the methane are burned with oxygen or air to generate the necessary energy allowing an autothermal reforming (ATR) process. As catalyst materials, supported noble metals have been proven to be effective, with Rh being the most promising one. As a non-noble alternative, Ni was found to be active towards the SR as well as the WGS.[19] The reaction temperatures being at least 800°C and in a highly reductive feed, coking and sintering are main issues in this process, also catalyst poisoning by impurities in the feedstock have been reported to affect the catalytic performance.[18,20] Though this process is highly efficient, the formation of CO_2 as a byproduct in this process is undesired for climate-neutral hydrogen production.

Next to hydrogen, synthesis gas itself is a very important feedstock for the chemical industry, for example for the methanol production, being one of the top ten most used petrochemicals. Its main uses are the production of methyl tert-butyl ether (MTBA), acetic acid, methyl methacrylate (MMA)and dimethyl terephthalate (DMT), as well as solvent or gasoline extender.[21] With oil prices being unstable due to the political issues and the overall abundance, also the methanol to olefin (MTO) process is getting more attention.[22] A more direct route to higher alkanes is the gas-to-liquid process using the Fischer-Tropsch reaction (FT), also needing synthesis gas as feedstock. In this case, also in case of the hydroformylation, a higher CO/H_2 ratio is needed as what is produced in the SR process.[23,24] To yield higher CO amounts, the dry reforming of methane (DRM) can be performed (equation (3)).

$$CH_4 + CO_2 \rightarrow 2CO + 2H_2 \quad (3)$$

The DRM is in general coupled with the SR to yield the required ratio of CO/H_2 for the following processes.[18–20] A major problem of the mostly Ni-based catalyst for the DRM is the coking, while in case of the SR reaction the high amount of water in the

reactor prevents the coke formation, in case of the DRM reaction it poses a major problem for the lifetime of the catalysts and therefore requires frequent regeneration cycles. Nevertheless, catalyst optimization could significantly increase the catalyst performance and lifetime.[25–27]

1.2.2. Oxygenation of Methane

Another proposed route to directly utilize methane as a feedstock is the oxygenation of methane, and is considered since the beginning of the 20th century, [28] but has yet to reach acceptable yields.[29] Several industrial very relevant products such as methanol, formaldehyde, or even ethanol could be available by the selective oxidation of methane.[30–33] With methanol and formaldehyde being consecutive products of synthesis gas, the energy-intensive reforming step of methane could thus be circumvented.

A system for high yield methanol production from methane at mediocre temperatures (below 200°C) has been proposed before.[33,34] Methane is activated using sulfuric acid as oxidant forming methyl bisulfate (equation (4)), which is less likely to over-oxidize than methane.[35] On reaction with water, methanol is formed (equation (5)). As catalyst $HgSO_4$ is used.[33,34]

$$CH_4 + 2H_2SO_4 \rightarrow CH_3OSO_3H + 2H_2O + SO_2 \quad (4)$$

$$CH_3OSO_3H + H_2O \rightarrow CH_3OH + H_2SO_4 \quad (5)$$

The formed SO_2 can be re-oxidized and hydrated to recover the sulfuric acid. Even though the methanol yield was found to be quite high (> 40%),[8] an industrial application might be quite challenging due to the corrosive and toxic nature of the reaction media. Also, the upscaling of the reaction rate is limited by the amount of dissolvable mercury sulfate in the reaction mixture.[34] A similar approach was proposed with hydrogen peroxide as oxidant and trifluoroacetic anhydride, protecting the methanol as methyl trifluoroacetate, preventing an over-oxidation.[36]

A more easy reaction pathway to realize is the direct oxidation of methane in the gas phase over heterogeneous catalysts using O_2 or N_2O as oxidants. Similar to the OCM many materials, primarily supported transition metals, were screened for their suitability as oxygenation catalyst. The reaction temperatures are in general lower than the OCM temperatures (around 400°C up to 700°C) and the yields (below 5%) are as expected, which can be partially attributed to the low reaction rates, but also towards the poor selectivities.[30,31] The general problem of the high dissociation energy of the C-H bond in the methane molecule with 440 kJ/mol, compared to the usually significantly lower barriers in the reaction products significantly impedes the design of selective catalysts. Assuming similar rates for the methane oxidation and

methanol oxidation and disregarding all sorts of side reactions, a yield of 40% cannot be surpassed, where in reality it is even lower.[29]

To circumvent the low selectivities due to over-oxidation of the products, a chemical looping type of reaction was proposed using zeolite supported copper or iron materials. In this reaction, the reaction intermediate is protected from the exposure of oxygen preventing the over-oxidation. In a first step, the material is oxidized creating an active oxygen species on the catalyst (equation (6)). The next step is the reaction of the material with methane to form a methoxide intermediate (equation (7)). Afterward, the methanol is obtained by hydrolysis of the material (equation (8)), with those steps being carried out at temperatures below 300°C.

$$2MOH + \frac{1}{2}O_2 \rightarrow 2MO + H_2O \quad (6)$$

$$2MO + CH_4 \rightarrow MOCH_3 + MOH \quad (7)$$

$$MOCH_3 + H_2O \rightarrow CH_3OH + MOH \quad (8)$$

This procedure sounds promising for ensuring a high selectivity, which was reported to be up to 100%,[29] but there are several issues with the scalability to be overcome.

1. Since the reaction procedure is a cycle of at least 3 steps, not counting additional purging steps, the space-time yield for a reactor is very limited, with the catalyst, most of the time being in a regeneration step.
2. The methanol product is highly diluted, resulting in a costly purification.
3. The amount of methanol formed by cycle is directly linked to the number of metal centers on the catalyst surface. In the best possible case, each metal atom is isolated and active on its own allowing a maximum turnover frequency of 1 per metal atom per cycle.

These issues prevent an economic scaling of this kind of process so far. [32]

Another approach is a photocatalytic functionalization of methane. In absence of oxygen, methane is oxidized in water to methanol, ethanol, and ethane, forming hydrogen as a byproduct. In this case, the formation of hydroxyl radicals is proposed as the driving force of the reaction. However, the energy efficiency of photocatalytic processes is usually really bad. In this case about 2 TJ/mol of light energy.[37] Also, a scaling of photoreactors is quite a problem, scaling only with a square, where other reactors scale cubic.

1.2.3. Methane Dehydroaromatization

To circumvent the general issue of the over-oxidation in the oxidative upgrading of methane (e.g. oxygenation, OCM) a non-oxidative approach can be performed in the form of the methane dehydroaromatization (MDA). On Brønsted acids such as

zeolites, methane can be activated at high temperatures to form ethylene or acetylene, followed by aromatization of the latter forming benzene.[38–40] The zeolite performance can be enhanced by the incorporation of transition metals, with Mo showing the most promising results so far.[41,42] A major challenge in this process is the formation of coke. With the reaction being conducted at temperatures around 800°C the formation of aromatics consecutively and almost inevitably leads to the formation of coke, blocking the channels of the zeolites and thus deactivating the catalyst and clogging the reactor (equation (9)).[43]

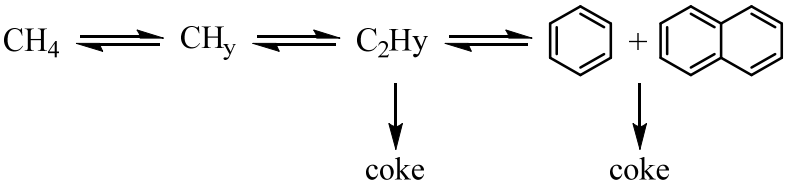

(9)

By site isolation and channel size optimization, the catalysts are optimized to minimize the amount of coking. [39,41,42]

Different catalytic systems proposed for this kind of reaction are single-site iron catalyst on silica. The absence of acidic sites significantly reduces coke formation, leading to a more stable catalytic performance. The reaction is performed at temperatures exceeding 1000°C and is mainly controlled by the thermodynamic equilibrium. By adding or removing H_2 from the reactor using membranes, the conversion can be enhanced and the product spectrum manipulated, achieving yields up to 30% at a selectivity of 99%.[44] Though sounding quite promising for methane upgrading, but due to the high reaction temperatures, finding suitable inert reactor materials will pose a major issue in the industrial realization of this process.

1.3. Oxidative Coupling of Methane

1.3.1. General Reaction

The oxidative coupling of methane (OCM) reaction has been a target of many studies since its first description in the '80s [4,45] and therefore also been subject of multiple extensive reviews over the years.[9,39,46–50] The general idea is to couple two methane molecules to produce the industrial more desired ethane/ethylene. Due to the high C-H bond strength of methane and its high symmetry, high reaction temperatures are necessary (500-900°C). The best option for this would be a thermal dehydrogenative coupling of, which is unfortunately thermodynamically unfavorable:

$$2\ CH_4 \rightarrow C_2H_6 + H_2 \qquad \Delta G°(1000K) = 71\ kJ/mol. \qquad (10)$$

To overcome the thermodynamic limitations, an oxidant has to be used:

$$2\ CH_4 + \frac{1}{2}O_2 \rightarrow C_2H_6 + H_2O \qquad \Delta G°(1000K) = -160\ kJ/mol. \qquad (11)$$

The formation of water as a byproduct of the reaction acts as the driving force of the reaction resulting in an exergonic process.[50]

The OCM process now has two major problems to be considered:

1. the use of oxidants facilitates the over-oxidation of methane to carbon dioxide and carbon monoxide,
2. the decreasing C-H bond strength of the higher alkanes.

Of all alkanes, methane has the strongest C-H bond with 440 kJ/mol, gradually decreasing with the chain length of the alkanes: 420 kJ/mol for ethane and 410 kJ/mol for propane (terminal C-H bond).[51] Designing now a catalyst to activate the C-H bond of methane, while being inactive towards the activation of the more reactive ethane can hardly be achieved, leading to unavoidable consecutive reactions of the product.[52] Even in the absence of oxygen, the reactivity of the reaction products would pose a major problem. The dehydrogenation will not stop at ethane or ethylene and will ultimately lead to the formation of coke (compare to section 1.2.3. "Methane Dehydroaromatization"). In the presence of oxygen though, the thermodynamically favored deep oxidation pathways pose a major problem and have to be suppressed:[53]

$$CH_4 + 2O_2 \rightarrow CO_2 + 2H_2O \qquad \Delta G°(1000K) = -800\ kJ/mol. \qquad (12)$$

Since thermodynamically the deep oxidation is much more favored compared to the coupling of methane, good catalysts are necessary to kinetically control the reaction, facilitating the formation of the desired higher alkanes.

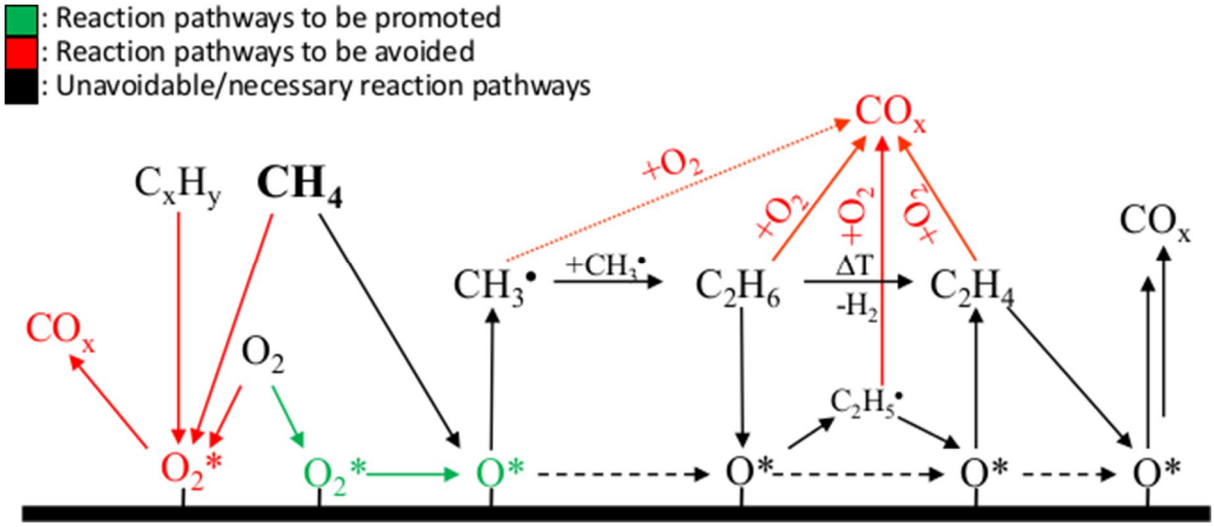

Scheme 1: Simplified reaction network of consecutive steps of methane oxidation on a catalyst surface.[a]

In Scheme 1 a reduced reaction network of the OCM on a catalyst is depicted.[52,54,55] It has to be noted, that this scheme is very simplified. Due to the high temperatures and radical mechanism of this reaction,[56] next to the reaction on the catalyst surface, numerous gas-phase reaction steps are thinkable and also proven to take place.[57–60] It is widely accepted, that for the activation of methane surface oxygen species is needed, however, the nature of this oxygen species directs the selectivity of the primary reaction (compare green vs. red surface pathway). Where one oxygen species, leads to the formation of methyl radicals, which can homogeneously couple in the gas-phase to yield ethane, other oxygen species can lead to the total combustion of the methane.[49] The formed ethane can then be dehydrogenated towards ethylene, either oxidatively, or, given the high reaction temperatures, thermally.[55] Next to the catalyzed methane combustion reaction, also gas-phase reactions can significantly contribute to a reduced selectivity. Given the biradical nature of oxygen and the radical reaction intermediates, homogeneous gas-phase reactions can hardly be avoided.[57,58] To reduce the impact of this reaction pathway, either an excess of methane can be used, to reduce the collision-probability with oxygen, or oxygen can be eliminated from the gas-phase by applying a chemical looping concept.[61] Both suggestions, however, still require a highly selective catalyst. Therefore, the key to OCM is still the direction of the nature of the surface oxygen species. The last pathway towards the total oxidation towards carbon monoxide and carbon dioxide can hardly be avoided. As stated before, the activation of methane is significantly more difficult compared to that of ethane and a catalyst activating the C-H bond of methane will also be able to activate that of ethane and ethylene. In TAP

[a] Adapted from Fleischer, V., et al., *J. Catal.* **2016**, *341*, 91–103, Beck, B, et al., Engineering. *Catal. Today* **2014**, *228*, 212–218, and Parishan, S, et al., Catalyst. *Catal. Letters* **2018**, *148* (6), 1659–1675.[52,54,55]

studies on $NaMnWO_x@SiO_2$ and MgO catalysts this pathway could be confirmed, showing, that the oxygen species responsible for selective methane activation, will also lead to consecutive combustion of the products. Due to these circumstances, the maximum yield of the reaction is intrinsically limited even on a perfect catalyst. To avoid the combustion of the product, the overall conversion has to be limited.[52]

1.3.2. Catalysts for the OCM Reaction

The selective activation of C-H bonds for the functionalization of hydrocarbons by oxidation reactions is a major challenge in catalysis. Although a large number of materials show high activity for these reactions, most of them also catalyze undesired side-reactions that finally produce deep oxidation products, namely CO_2 and water. A variety of metal oxides, either single or mixed oxides, represent the toolbox of the research field of oxidation catalysis. They are applied as catalysts as bulk materials or deposited as nanoparticles or monolayers at the surface of more or less inert support materials.[62–64] For the activity of the catalysts often a high specific surface is generated by high dispersion of the material. For a high selectivity, a very complex property profile is essential, which is governed mainly by the electronic properties of the oxide material. In a first step, all oxides may be distinguished as reducible or irreducible under the reaction conditions. Reducible oxides provide lattice oxygen (O^{2-}) from their surface or subsurface for oxygen inserting reactions or oxidative dehydrogenation reactions of hydrocarbons. This oxygen is considered as nucleophilic oxygen and can be observed to be very selective for the hydrocarbon oxidation reaction. Since the O^{2-} ion needs to be extracted from the lattice to form a vacancy, such reactions are only possible with rather reactive substrates like olefins or reactive hydrocarbons. The oxygen vacancies need to be replenished with gas-phase oxygen with a high reaction rate for avoiding the presence of further oxygen species in higher concentrations, which might cause unselective side reactions. This relation of the elementary steps of the reaction mechanism, that is assembled in the Mars-van-Krevelen mechanism, results in an overall reaction rate that is often independent of the oxygen partial pressure in the gaseous reaction mixture.[65] Irreducible oxides provide adsorption sites for oxygen molecules and control their activity by electronic interactions. This occurs in particular at non-ideal surfaces, offering defects steps and edged as adsorption sites.[66,67] On the contrary ideal single crystals are almost inactive.[68–70] In this situation, different oxidation states of the oxygen molecule are possible, dependent on the number and energy of available electrons. The resulting oxygen species are considered as electrophilic and highly active for C-H activation. This is especially true for the peroxo- and superoxo-species.[46] This difference in the selectivity behavior of reducible vs. irreducible oxides was nicely demonstrated by J. Haber and M. Witko.[71] Due to the high activity, such oxidation catalysts are also suitable for less reactive substrates like methane. For this reason, almost every metal oxide has been tested as a catalyst for the oxidative coupling of methane, one of the most promising but also most challenging reactions for a future methane utilization strategy.[6] Many irreducible oxides show activity for the

oxidative coupling of methane, but with rather low selectivity. The main reason for this observation is seen in the presence of different oxygen species with very different reactivity profiles.

1.3.3. High Valence Doped Alkaline Earth Oxides

Theoretically, wide-bandgap insulators are hardly able to activate oxygen[69] but in reality, it works due to natural abundance of impurities. In a thorough review by Voskresenskaya et al., the impact of different types of impurities and defect structures in alkaline earth oxides on the OCM performance is discussed.[46] Where in case of alkaline doped alkaline earth oxides many comprehensive studies have been conducted, showing the benefits of anion vacancy formation by the addition of Li or Na,[6,45,47,57,72–77] only a few studies targeted the effect of transition metal doping.[6,78,79] Here the O_2^- binding energy depends on the oxidation state of the dopant, the lower it is, the stronger is the binding energy. The effects depend on the nature of the transition metals, e.g. Mo^{2+}/Mo^{3+} dopants show electron donor abilities, acting as a Lewis base in the near-surface region, whereas Cr^{3+} in MgO is charge compensated by the formation of Mg^{2+} vacancies. Mo is an especially good donor that can provide several electrons to surface adsorbates due to the high energy state of 4d and 6s levels. The $Cr^{2+} \rightarrow Cr^{3+}$ transition occurs spontaneously in MgO due to a lattice misfit serving as an intrinsic electron trap.[68]

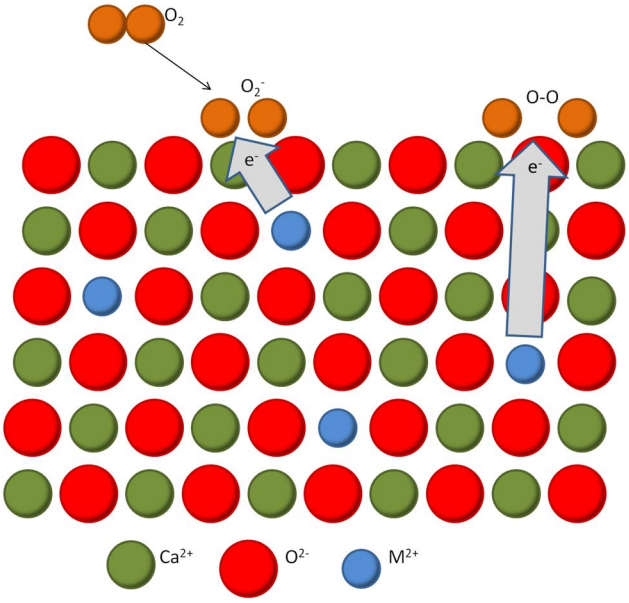

Scheme 2: Oxygen activation on irreducible oxides via electron tunneling from subsurface high valence dopants.[b]

[b] Adapted from Freund, H.-J. Oxygen Activation on Oxide Surfaces: A Perspective at the Atomic Level. Catal. Today 2014, 238, 2–9.

From observations in STM experiments, exposing Mo doped CaO films to oxygen, Freund et al. proposed a mechanism involving subsurface high valence dopants (up to 1 nm depth) donating electrons to oxygen adsorbates via tunneling causing a partial reduction of the adsorbed oxygen (Scheme 2).[80] Theoretical calculations revealed a significant increase in the oxygen binding energy over a Ca-Ca bridge position on an undoped site, compared to a site with a Mo^{3+} atom in the third subsurface layer (87 kJ/mol vs 13 kJ/mol), additionally the apparent activation barrier for the dissociation of the superoxo species is lowered from 110 kJ/mol on a pristine surface to 66 kJ/mol on a doped surface.[81] Since the activation of oxygen is the most important step in the OCM reaction, tuning the oxygen activation by transition metal doping might be a useful step in developing new catalysts. In case of MgO, though still far from being competitive, Fe doping resulted in a significant improvement of the catalytic performance in the OCM reaction, proving the significance of studies targeting high valence doped irreducible oxides.[78] Showing superior catalytical performance compared to MgO, CaO might be an interesting material to study the impact on high valence dopants on the OCM. BaO and SrO already exhibiting a significantly reduced bandgap compared to MgO and CaO (5.0 eV and 5.7 eV vs. 8.7 eV and 7.5 eV), as well as a known high abundance of intrinsic defects and the ability to form stable peroxides, are not suitable to create such systems.[46,82,83]

1.4. Aim of this Thesis

Although there is experimental evidence for the beneficial impact of doping of alkaline earth metal oxides (AEMO) by alkaline metal oxides (AMO) or rare-earth metal oxides (REMO) on the oxidative coupling of methane, the interpretation of such complex experimental results is very difficult. For this reason, model system studies were done, investigating the properties of the dopants inside their matrices, the interaction of oxygen with the surfaces, and the electronic properties of the doped materials with theoretical and spectroscopic techniques. The electronic properties of oxide surfaces may be investigated by photoluminescence studies that allow the monitoring of high energy defect sites.[84,85] The quenching of the luminescence signal by adsorbed oxygen is a sensitive probe for the interaction of the catalysts with the oxygen.[86,87] Deeper insight into the doping effects is obtained from theoretical studies that allow a prediction of the key descriptors of the oxidation reactions. The study by the Nørskov group demonstrates the influence of doping of AEMOs with traces of transition metal ions on the binding energy of hydrogen atoms and methyl groups as such descriptors. The derived volcano plot shows a strong impact and the room for improvement for the activity of the investigated catalysts by transition metal doping. Although this study was only focused on the activity it also suggests changes in the selectivity caused by doping.[70] Another interesting contribution to the understanding of doping effects was published by Freund and co-workers. They showed by STM studies how doping facilitates the dissociative adsorption of oxygen already at ambient conditions.[68]

To demonstrate the relevance of the model studies for real catalysts and to inspire our catalyst development a series of transition metal doped CaO samples was prepared with different dopant metals and concentrations. Due to the choice of CaO for the model studies, it was also chosen here, although pristine CaO is known to be a poor OCM catalyst. This starting position offers the chance for good visibility of positive doping effects. To link these experiments to the model studies the essential research questions of this study were:

How are the dopants dispersed with the CaO matrix? / Where are the dopants located?

Do the dopants change the surface or bulk properties of CaO?

Do dopants contribute additional active sites at the surface, performing as reducible oxide sites?

What is the impact on the catalyst selectivity?

What is the impact of the dopant on the oxygen activation?

2. Background

2.1. Synthesis Methods

In general, catalysts can be divided into two groups: bulk materials and supported catalysts. The bulk materials are usually more easily synthesized and characterized compared to multiphase systems but are often not industrially applicable. Since the catalytic performance of a material is a function of the surface of the catalyst, usually the high surface area is materials are desired as a highly active catalyst. Not all materials though can be synthesized with high surface areas. Thermodynamically low surface energies are favored, meaning the formation of flat highly coordinated surface sites (terrace sites) is favored compared to the formation of kinks, corners, steps, and other surface defects. Due to this, though there are quite stable high surface area materials available (usual ceramics such as alumina, silica, or boron nitride) materials such as alkaline earth oxides tend to sinter at high temperatures, especially in the presence of reactive gases, such as water or carbon dioxide, resulting in reduced surface area materials.[88–90] At temperatures close to the Tammann temperature of the material, due to the enhanced diffusion of the atoms in the lattice, creating a high surface area material is almost impossible. Another issue next to sintering can be the agglomeration of particles causing a huge loss in active area and may also ultimately lead to clogging of the reactor. Another downside of bulk materials, especially in industrial applications, is the cost. Often utilization of rare materials such as precious metals in electrocatalysis, lanthanides, or even costly synthesis routes of the active component, bulk catalysts are often economically not feasible. Since only the surface takes part in the reaction most of the material in the bulk will be inactive and only contribute to the cost, rather than the value chain. Disregarding the industrial side in basic research, bulk catalysts are often the materials of choice to analyze interactions of the material with the reactants. By adding multiple phases to a material, the system might often be too complex to assign observed effects to specific surface formations. Using supported catalysts, multiple effects can contribute to the performance of the material besides the contributions of the sole components. Supported metal particles, for example, can induce strong metal-support interactions (SMSI) which changes the properties of the supported component.[91,92] Even in case of the rather simple magnesium oxide, analyzing the surface and creating correlations between the catalytic performance and the material properties requires an extensive effort.[66,67,93,94]

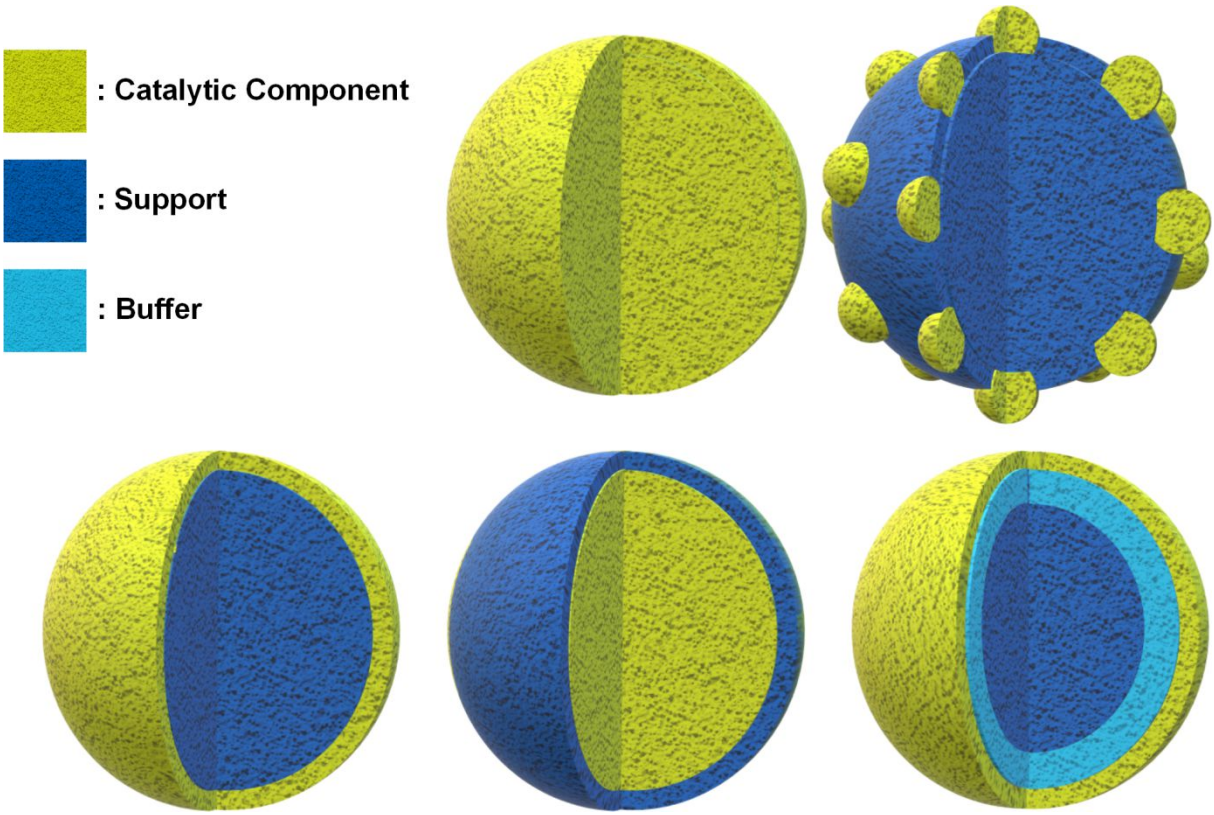

Scheme 3: Scheme of differently configured catalyst materials: from top left to bottom right: bulk, supported particles, core-shell, inverse core-shell, and buffered core-shell catalyst.

In Scheme 3 a selection of different catalyst configurations is depicted, showing the differences of the bulk catalyst compared to supported catalysts. Depending on the configuration, the support can take serve different roles in the material. By dispersing nanoparticles on the surface of an inert high surface area support, the surface area of the active component can be greatly increased by reducing the needed amount of necessary material. With strong enough adhesion to the support and a distance between the particles, sintering in form of Ostwald ripening can be prevented allowing the use of nanoparticles in heterogeneous catalysis. This also allows the use of porous supporting materials such as SBA-15, which might be beneficial for the reaction by creating confined reaction spaces. Using a core-shell type configuration thin layers of the active component can be dispersed on stable high surface area support, greatly reducing the required amount of catalytic material compared to the bulk material. By covering the whole supporting material participation of the supporting material in catalysis can be prevented. In this case, buffer layers might be needed to prevent epitaxial growth. An inverse core-shell catalyst requires a porous shell so that the reactants can diffuse to the catalytically active material. Reasons for using this type of material can be to take advantage of the surrounding porous system, or the inability to stabilize the inner particles on support. By covering the active component with several nanometers of porous inert materials, the agglomeration and Ostwald ripening of the catalyst can be prevented.

The chemical toolbox to synthesize such materials is very rich reaching from very simple methods such as physical mixing of multiple components to very sophisticated and experimentally complex methods such as atomic layer deposition (ALD). Finding an appropriate synthesis route for the desired material can be quite challenging. For supported catalysts, the most common methods used are impregnation/deposition methods such as the wetness impregnation or the incipient wetness impregnation. A good overview of this topic can be found in *Advances in Catalysis*.[95] For the synthesis of core-shell structures, a variety of methods are available, including solvochemical routes as well as gas-phase routes.[96,97] For the synthesis, a huge library of methods is available and would far exceed the scope of this work to discuss those in detail. In chapter 2 of the *Handbook of Heterogeneous Catalysis* a variety of methods are discussed in detail.[98]

The most common methods to synthesize bulk catalysts are, mainly due to their simplicity, and solid-state reactions. To create a multicomponent oxide material in a first step, all the reactants have to be carefully mixed. After successful mixing, the catalyst is heated or calcined at high temperature, decomposing precursor materials and allowing diffusion of the atoms to yield a homogeneous solid solution or mixed metal oxide. To achieve a good dispersion of the components, several techniques are available. The easiest one the physical mixing using an e.g. a ball mill. In this case, however, it depends strongly on the particle sizes and quantity ratios of the components, whether a good mixing is possible. In the case of doping, since one component is usually much less in quantity than the other, a good mixing might be difficult, leading to a heterogeneous distribution of the dopant in the host lattice. Other methods are e.g. gelation methods; all components are dissolved or dispersed in a solvent, which is then slowly evaporated (e.g. heating, spray drying, freeze-drying, etc.). In this case, dependent on the nucleation rare of the single components a phase separation can take place. The most common method for achieving a well-mixed material/material-precursor is the co-precipitation method.[99] Here, precursors solutions are prepared which are then precipitated by the addition of a precipitation agent. On reaching the supersaturation, spontaneous nucleation, e.g. induced by the stirrer, can take place causing the formation of nuclei, which then can grow. The growing and nucleation rate of the particles depends on many variables, such as temperature, degree of oversaturation, pH-value, solvent, etc., making this method quite complex. In the case of the co-precipitation, subsequent precipitation of the single components also has to be excluded, for example by continuously dosing precursor solution and precipitation agent to keep the concentrations in the reaction vessel constant. Since the nucleation process depends on many parameters, an automated precipitation setup is favored, controlling pH, stirring rate, and temperature at all times. Another critical step affecting the product is the aging time and drying after the precipitation affecting crystallization processes of formed metastable phases.[100] In the case of the precipitation of calcium carbonate, the temperature and aging time has a significant influence on the formed phase. The precipitation of calcium carbonate follows Ostwald's rule, first forming a metastable amorphous phase, which is then slowly converted to more stable vaterite, which then

can, dependent on the temperature, further be converted to its thermodynamically favored phase, which is at temperatures below 65°C calcite. At temperatures above 70°C or at high pressures the aragonite phase can be formed.[101]

2.2. General Characterization Methods for Heterogeneous Catalysts

The characterization of catalyst materials is indispensable for investigating the influences of material properties on the reaction behavior. Though a lot of standard analytical techniques for catalyst materials are in principle very easy in their experimental execution, the interpretation in regard to the history of the catalyst prior, as well as the characterization conditions can often be quite challenging. The most characterization methods are usually conducted at temperatures and pressures far from the reaction conditions. While interpreting the obtained data of such methods, one has always to remember, that the information obtained from such methods are limited in their meaningfulness towards the catalyst under reaction conditions. Though there are nowadays several options for in situ analyses, not all needed methods can be conducted at elevated temperatures or pressures. Also, the setups for in situ analyses usually require special geometric designs, e.g. for beam guidance, which might not be comparable to an ideal catalytical reactor. The reactor geometrics alone might be a hindrance, especially for high-temperature catalysis, where a narrow residence time distribution and dead volume minimization within the test cell is necessary to prevent consecutive gas-phase reactions or even coking. Nevertheless, ex-situ analyses are usually the starting point of all catalyst optimization studies and the linking of material properties with the catalytic performance a first step for getting insight into how the catalyst works and what is important for the catalyst design.

2.2.1. Surface Size Determination

An important parameter for the interpretation of catalytic results and the catalytic performance of different materials is the surface area. The number of active sites, especially in the case of bulk catalyst, should be proportional to the surface area of the active component on the material's surface. Therefore, the surface area is needed to normalize measured reaction rates. One generally accepted method for the surface size determination is the BET measurement.[102]

For this determination, an adsorption isotherm with a nonreactive gas is recorded. In most commercial devices, liquid nitrogen is used for the cooling of the sample, and nitrogen gas at sub saturation pressures is used for recording the isotherm. Using a multilayer adsorption model, the amount of adsorbed gas molecules on the surface of a material can be calculated:

$$\frac{p}{\nu(p_0 - p)} = \frac{1}{\nu_m c} + \frac{c-1}{\nu_m c} \cdot \frac{p}{p_0}, \tag{13}$$

with p the equilibrium pressure, p_0 the saturation pressure, ν the amount of adsorbed gas, ν_m the amount of gas needed for monolayer adsorption, and c the BET constant. By suitable linearization, the amount of adsorbed gas for the formation of a monolayer ν_m can now be calculated. With ν_m, using the cross-section of the adsorbent of the probe molecule, the surface area can be determined.[102]

Using this method, the surface areas of similar materials can be compared and normalization to the surface area is possible. Comparing chemically different materials might be quite challenging because the cross-section for the probe molecule might be different and not known for all investigated materials. Another limitation of this method is microporous samples. The here applied model for multilayer adsorption does not account for such structures, complicating the interpretation of the isotherms and requiring an extension of the BET-analysis.[103,104]

2.2.2. Structural Analysis

After synthesis of material, analyzing its bulk crystal structure is the first step for confirmation of a successful synthesis. For this purpose, the X-ray diffraction (XRD) can be applied. Diffracting monochromatic X-rays (usually the copper K_α radiation generated from an X-ray tube) at a crystal lattice will results in a distinct diffraction pattern, dependent on the lattice parameters of the crystals inside the sample. The condition for constructive can, in the most simple case, be expressed by Bragg's law:

$$n\lambda = 2d \cdot sin(\Theta), \tag{14}$$

which can be derived from Scheme 4, with $n\lambda$ being a multiple of the applied X-ray wavelength, Θ the incident angle and d the lattice constant.[105]

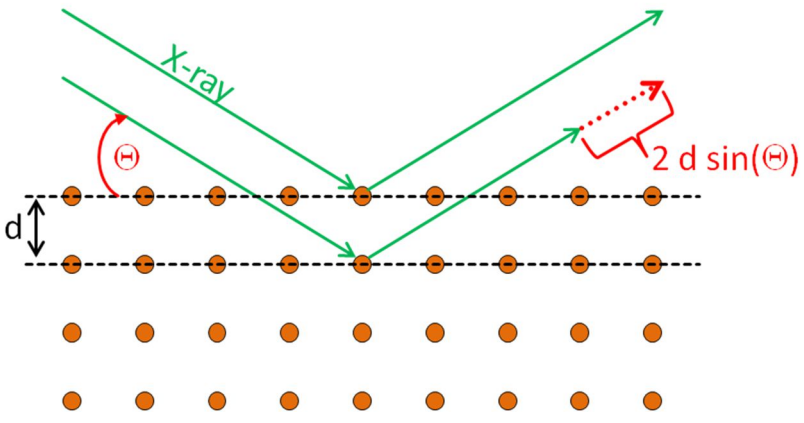

Scheme 4: Principle of constructive interference (Bragg's law)

The angle for constructive interference is dependent on the lattice constant and the geometric order of atoms in the structure and therefore highly specific, enabling the identification of crystal structures from an XRD pattern. In Figure 1 simulated powder patterns of CaO, MnO, and $CaCO_3$ (calcite) are depicted. With MnO and CaO exhibiting the same rock salt crystal structure, the pattern is identical but shifted due to the different lattice parameters. The XRD powder pattern of calcite though, exhibiting a trigonal much less symmetric crystal structure compared to the rock salt structure, shows much more reflexes and more complex patterns.

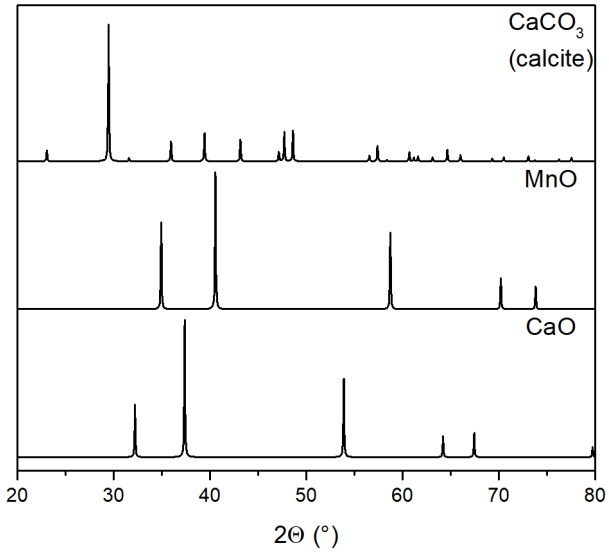

Figure 1: Simulated XRD powder patterns (Mercury 3.5.1) of CaO, MnO, and $CaCO_3$ (calcite).

Since MnO and CaO exhibit a similar crystal structure, the formation of a solid solution or substitution of Ca^{2+} by Mn^{2+} is possible. In this case, the XRD pattern of the host material will be shifted according to Vegard's Law:

$$\alpha_m = f \cdot \alpha_{MnO} + (1 - f) \cdot \alpha_{CaO} \,, \tag{15}$$

with f the fraction of substitution, α_m the lattice constant of the resulting material, α_{MnO} the lattice constant of MnO and α_{CaO} the lattice constant of CaO respectively.[106] Using XRD, the formation of a solid solution can thus be proven. Another information derived from the XRD pattern can be the mean crystallite size. With increasing crystallite size, the reflexes in the powder pattern become more distinct and vice versa with decreasing size broader. The size is often estimated by the Scherrer equation discovered in the early 20th century,[107] but the meaningfulness is debatable. Including an elusive shape factor and underestimating the presence of smaller particles, due to being a volumetric weighted method, the resulting particle size can

only be used for pointing the way. With nowadays more advanced techniques available, a more profound peak profile analysis is possible, considering strain broadening, anisotropic broadening, stacking faults, etc. but is a science of its own and not part of this work.

Another interesting aspect of XRD is its suitability for in situ studies. Since the measurement is unaffected by the gas phase and the effects of temperature on the crystal lattice can be considered by the use of the thermal expansion coefficient, XRD analysis can be used to observe major changes of the sample during a reaction. For example in case of the oxidative coupling of methane over $NaMnWO_x@SiO_2$ catalysts, phase changes of the catalyst at reaction temperatures can be observed indicating a melting or amorphic restructuring, proving, that the catalyst structure and its properties at room temperature, give only little insight on the properties of the "real" catalyst under reaction temperatures.[108]

With XRD being volume sensitive, a more surface sensitive structural characterization can be realized by low-energy electron diffraction (LEED), which works analogously to XRD. With a lower depth of penetration, this method can be used to analyze surface symmetries but requires high vacuum setups and an electron source and is therefore usually coupled to other methods, such as electron microscopes.

2.2.3. Infrared Spectroscopy (IR)

Infrared spectroscopy is a very versatile analysis technique, applicable e.g. in quantitative and qualitative gas-phase analyses, material characterization, as well as surface characterization using probe molecules. For the IR spectroscopy to be applicable, the target material has to go change in the dipole moment during excitation of the bond vibrations using infrared radiation, making these techniques especially suitable for probing functional groups, such as -OH, C=O, or carbonate groups. For analyzing surfaces of e.g. catalyst materials, IR active probe molecules can be adsorbed on the material surface. The amount of adsorbed species can be determined by the Lambert-Beer law, allowing quantification of certain surface sites:

$$A = \epsilon \frac{n}{S_A}, \tag{16}$$

with A the total absorbance, ε the extinction coefficient, n the amount of adsorbed probe molecules, and S_A the surface area of the probed surface. Using different probe molecules, e.g. pyridine, carbon dioxide, hydrogen, carbon monoxide, etc. surface sites with certain properties can be probed. With reaction gases e.g. the adsorption sites during the reaction can be probed, identifying e.g. competitive adsorption or poisoning of active surface sites. Pyridine adsorption can be used for quantifying the number of acidic surface sites, or CO_2 for probing the basic sites.[49] The CO adsorption on oxidic materials has been studied thoroughly and has been

comprehensively reviewed by Hadjiivanov und Vayssilov in 2002.[109] One of its applications is the probing of undercoordinated surface sites e.g. in alkaline earth oxides.[110,111] By correlating the number of specific surface sites with the catalytic performance of the material performance-property relationships can be derived. In the case of MgO as a catalyst for the OCM reaction, monoatomic step sites could be identified as possible active sites.[67]

With IR being a contact-free characterization method and requiring no vacuum or certain temperatures, it can also be used for in situ studies. The main limiting factor for in situ IR is the reaction medium, not hiding relevant features during the measurement, as well as the intensity of the black body radiation at really high temperatures. In previous studies in situ IR spectroscopy could be used to get insight into the active oxygen species on OCM catalyst. In studies on SrF_2/Nd_2O_3 superoxide species, showing broadband at 1128 cm^{-1}, could be identified to interact with CH_4.[112] Also in studies on $SrO\text{-}La_2O_3/CaO$ catalysts lattice oxygen was identified as active species for methane activation, regenerated by gas phase oxygen. Also, carbonate species formed during the reactions were observed to be regenerated in the presence of oxygen.[113]

2.2.4. Raman Spectroscopy

Contrary to infrared spectroscopy, Raman active vibrational modes have to undergo a change in polarizability making Raman spectroscopy complementary towards IR spectroscopy. Due to the very complex and often intense IR spectra of materials below 1000 cm^{-1}, this area is often regarded as the fingerprint region, usually used for identification and less suitable for investigations.[49] In contrast to that Raman spectroscopy can be successfully applied and analyzed in this region, allowing the observation of metal-oxygen bond vibrations.[114] A comprehensive theoretical background to Raman spectroscopy can e.g. be found in the *Handbook of Vibrational Spectroscopy*.[115,116] Another advance of this method compared to IR is the usage of UV-Vis lasers, shifting the method to higher excitation energies allows a wider temperature range of application in regards to the black body radiation during high temperature in situ experiments. By observing the metal-oxygen interactions in metal oxides, Raman spectroscopy is usually also less disturbed by the reaction medium, allowing good observation during in situ experiments. In the case of OCM studies, in situ Raman could prove the formation of peroxide species on Ba/MgO catalysts at 800°C, explained by the formation of segregated BaO_2 layers on the catalyst.[82] For CaO, intensities for Raman spectra of the bulk material as well as the surface are reported to be very weak, depending on the setup even elusive,[117,118] allowing easy observation of changes during in situ experiments.

2.2.5. Photoluminescence Spectroscopy (PL)

The relaxation processes after a photoinduced electron excitation can be very complex. In the case of materials with a necessary wide and defined band gaps, these processes can be radiative or non-radiative. Figure 2 shows doped calcium oxides samples irradiated by UV-light. At first glance, the emission of blue light from the samples becomes evident caused by radiative relaxation processes.

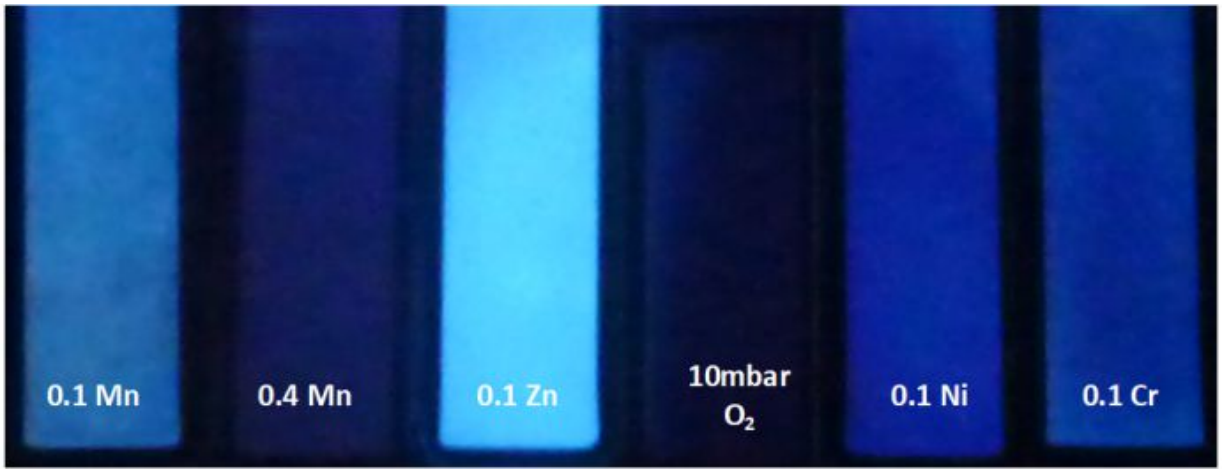

Figure 2: Doped CaO samples at room temperature under a laboratory UV light (255 nm).

In photoluminescence spectroscopy, the emitted light of the sample is analyzed as a function of the excitation energy. By analyzing the excitation and emission spectra, the electronic properties of the target analyte can be probed. In the case of solid materials, this technique is usually applied to probe the bulk properties of semiconducting materials. Not forming a bandgap, conductors usually show no photoluminescence, the relaxation steps after photoexcitation are due to the missing band gap energetically too small to emit visible radiation. In the case of insulating materials such as MgO and CaO, forming wide band gaps with (8.7 eV and 7.5 eV),[46] bulk photoexcitation can only be achieved in the far UV range. With modification of the insulating materials by doping or the creation of bulk defects centers, bulk photoluminescence can be created.[84,87,119] Another source for photoluminescence in insulating solids are the undercoordinated surface sites showing significantly reduced optical transition energies, where the smaller the coordination number, the smaller the needed excitation energy, reducing the needed excitation energy in case of CaO to 5.4 eV at terrace sites, 4.4 eV at kink sites down to 3.5 eV at corner sites respectively.[120] Analyzing the photoluminescence spectra of such materials, allows qualification of the surface site composition of the studied sample.[85,94,121] To discriminate between surface and bulk derived PL, molecular oxygen can be used to quench the surface derived PL,[86,87] which is exploited to created oxygen-sensitive detectors.[122]

2.2.6. Electron Paramagnetic Resonance (EPR)

As the name implies, electron paramagnetic resonance allows the probing of paramagnetic centers. For a sample to be eligible for EPR spectroscopy, unpaired electrons are therefore required, which can be found e.g. in radicals or also often in transition metals. In the case of transition metals, whether there are unpaired electrons depends on its oxidation state as well as its geometrical and chemical environment, making this method suitable for investigating the chemical environment of metal centers in a host matrix. To be able to excite and thus probe the spin transition in the analyte, first the energy levels have to be separated. For this purpose, a strong external magnetic field B_0 is applied, causing splitting of the different m_S states according to the Zeeman effect:

$$E = m_S g_e \mu_B B_0, \tag{17}$$

with m_S the spin quantum number, g the g-factor of the free electron, and μ_B the Bohr magneton. As an energy source for the excitation, a standing microwave is used in a resonance chamber, while the external magnetic field is altered to achieve a resonance of the spin transition with the microwave. Another aspect contributing to the EPR spectrum is the hyperfine coupling. If the sample contains atoms with a nuclear spin $I \neq 0$ coupling of the nuclear and electron spins occurs, causing a further splitting of the spectra with I. This can e.g. be exploited to analyze the nature of the paramagnetic center or also reveal interactions with diamagnetic atoms in the vicinity possessing an $I \neq 0$, making EPR a complex but powerful tool to analyze electronic interactions in a material. For example, this method could be successfully applied to observe the formation of the paramagnetic superoxide O_2^- species on CaO, while co-adsorbing oxygen and hydrocarbons at 77K.[123] Another application is the observation of metal impurities in diamagnetic host lattices. With EPR being highly sensitive, even small quantities of impurities can be easily detected. Biasi et al. published several papers on the behavior of different paramagnetic atoms in CaO (Fe^{3+}, Mn^{2+}, Cu^{2+}, Gd^{3+}) by analyzing primarily the line width and deriving a model for their interactions. Next to the dipolar broadening of the spectra,[124] with increasing dopant concentration the exchange interactions of two neighboured centers become more evident. By synthesizing series of doped CaO, the range of exchange interactions could be quantified to 0.59 nm for Mn^{2+} up to 0.83 nm for Gd^{3+}.[125–129]

2.2.7. Thermal Methods

2.2.7.1. Thermogravimetry and Differential Scanning Calorimetry

One of the most basic methods used in material/catalyst characterization is thermogravimetric analysis (TG), which is also often coupled with the differential scanning calorimetry (DSC).

In general, this method is very simple: in a thermally well-controlled oven, a sample is placed in a crucible, which is coupled to a balance. Upon applying a heating rate and steady gas flow, the thermal stability of a material can be investigated. When reaching the decomposition temperature material loss in the form of gases can be observed and analyzed when coupled with a mass spectrometer. Using an additional DSC unit, next to the mass loss, the heat of reaction becomes measurable, allowing additionally the observation of phase transitions, which do not exhibit a mass loss. This method is especially interesting for the development of activation strategies for catalysts and stability tests.[130–133]

This method is also suitable for in situ investigations of catalysts. By conducting catalytic experiments in a thermobalance, the observation of e.g. the coke formation on the sample,[134] formations of surface intermediates,[135] or measuring the heat of reaction. In case of the OCM reaction over $NaMnWO_x@SiO_2$, the heat of reaction of oxygen with the reduced catalyst could be determined at 185 and 350 kJ/mol, indicating multiple oxygen species present on the catalyst.[136]

2.2.7.2. Temperature Programmed Reduction/Oxidation

The temperature-programmed reduction/oxidation (TPR/TPO) is often used to analyze the reducibility of metal catalysts. While the TPR is often used to characterize catalyst materials, TPO measurements are less common. In a TPR experiment, an appropriate amount of pre-oxidized sample is loaded in a plug-flow reactor and heated in a reducing (most common H_2,[26,78,137–142] but also other gases are suitable e.g. CH_4, or CO[139,143]) feed gas. The effluent gas is analyzed with a time-resolved detector, such as a mass spectrometer (MS) or a thermal conductivity detector (TCD). By careful parameter studies, Monti and Baiker derived criteria to find suitable reaction parameters to yield good TPR results.[138] The parameters can be found in the experimental section (3.8, page 29). The integral consumption of the reduction gas can be used to quantify the number of reducible species in the material and the peak reduction temperature(s) can be interpreted in terms of reducibility of the material. While in general, TPR experiments can be performed in every residence time optimzied tube reactor, TPO experiments can be quite challenging, requiring more sophisticated setups. Oxides are often quite stable at room temperature, reduced metals however tend to readily reoxidize, requirering ovens that can be operated over a wide range of temperatures even down to liquid nitrogen temperatures.

The doping of oxide materials often leads to strongly altered catalytical behavior. Using TPR, the metal-oxygen bond strength can be probed. In the case of alkali doped Co_3O_4, the presence of alkaline metals was found to significantly weaken the Co-O bond causing a significantly lowered reduction temperature for the Co^{3+}, Co^{2+} transition.[137] In the case of transition metal-doped MgO, H_2-TPR could be applied to verify the stability of the catalyst, as well as the dissolution of the dopant into the host lattice. "Weakly" bonded oxygen at Fe atoms at the material surface was found to be

removed by TPR/TPO cycles and converted to strongly bound oxygen, only reducing at very high temperatures, indicating the incorporation of Fe in the MgO host lattice.[78] A similar effect was observed for Ni^{2+} dissolved in MgO, reducing at 750°C,[140] which is highly elevated compared to what usually can be found for supported Ni catalysts (< 600°C).[26,141,142] Studying TPR profiles for supported metal materials, also different trends can be observed depending on the nature of the support. For example Ni on Al_2O_3, strong metal-support interaction can be found, resulting in a stabilization the Ni-O bond leading to higher reduction temperatures, where on other supports, such as SiO_2, or TiO_2, the reduction temperature can be even lowered.[142]

While often used for more complex materials, such as supported or doped materials, the interpretation of TPR measurements is often not straightforward and requires deep insights into the reduction behaviors of the single components in the material. In the case of manganese oxide, for example, depending on the starting material the TPR profiles can appear very different, even the surface area appears to affect the reduction. A hausmannite Mn_3O_4, for example, can exhibit depending on the surface area a single event type TPR profile, or a multi-step profile over a large temperature range, wherein the case of the large surface area Mn_3O_4 the removal of oxygen is easier.[139] Since the TPR/O techniques are indirect characterization methods, for data interpretation usually a spectroscopic method has to be applied as well to confirm the findings. Nevertheless, it is a powerful tool, which can also be coupled with the catalytic testing providing post-reaction analysis of the sample while avoiding contamination due to sample transfers.

2.2.7.3. Temperature Programmed Desorption

Temperature programmed desorption (TPD) techniques are also a very potent tool for catalyst characterization. On a clean catalyst surface, at sufficiently low temperatures, a probe molecule is adsorbed and applying programmed heating rate, gradually desorbed. From the desorption temperatures, the heat of adsorption can be derived, for example for the reactants of the investigated reaction.

For example for the NO oxidation the TPD profiles of N_2, O_2, and NO were studied on cobalt catalysts, binding N_2 only weakly, if at all, while NO quite significant and oxygen strongly.[137] Information like this can be quite useful in debottlenecking the reaction rate of the investigated reaction. If either one of the reactants binds too strongly compared to the other one, in the case of competitive adsorption on the catalyst surface, the stronger adsorbed reactant might block the other one, thus lowering the reaction rate. The same is true if the product adsorbs too strongly.

Next to analyzing the heat of adsorption of the reactants, probing the acidic and basic surface sites is commonly performed by TPD. For this, either a basic probe molecule, e.g. NH_3, or an acidic probe molecule such as CO_2 is adsorbed at low temperatures on a pre-cleaned surface and the desorbed. Integral and position of the desorption

peaks can be used to compare a series of catalysts in terms of acidity and basicity.[82,144–148]

2.2.8. Isotopic Labeling Experiments

One very powerful tool to investigate the interaction of molecules with the catalyst or other reactants is the tracing of isotopically labeled atoms. By labeling e.g. oxygen atoms of target molecules in oxidation reactions over oxide catalysts, the participation of lattice oxygen can be revealed, which can hint to the surface mechanism of the reaction. One generally applied technique for this purpose is e.g. the steady state isotopic transient kinetic analysis (SSITKA). Usually performed in a plug flow reactor, a constant gas flow is applied containing solely one type of isotope of the investigated target atom. The feed can be a reaction mixture in steady state or, if only the interactions of the target molecule with the catalyst is of interest, a diluted feed containing the probe molecule. After reaching a steady state the supply of the probe molecule is switched to an isotopically labeled supply and the transients of the isotope in the reaction products are analyzed. The distribution of the isotopes in the reaction products can give clues on the mechanism of the reaction and the delay of release the interaction of the labeled atom with the catalyst material. In the case of V_2O_5/Nb_2O_5 catalyzed acrolein synthesis, SSITKA experiments with ^{16}O and ^{18}O revealed a Mars-van-Krevelen type kinetic, proving the source of oxygen is the lattice oxygen from the catalyst, which is replenished by the gas phase.[114] In the case of doped MgO, Aika et. al suggested by analyzing SSITKA experiments combined with TPD studies the formation of O^- species on the catalyst surface to be a key factor towards the activation of methane in the OCM reaction.[75] A detailed analysis of the transients is often difficult due to the variety of possible catalyst-adsorbate interactions. Especially at high temperatures oxygen diffusion in the bulk material can overshadow contributions from the catalyst surface. One for the current work more relevant technique applied before is the temporal analysis of product (TAP) experiment. Under highly controlled reaction conditions, the interactions of gas molecules with the catalyst surface is studied using a mass spectrometer operating in a millisecond regime. Operating under a high vacuum, the criteria of the Knudsen diffusion regime can be met, allowing a profound analysis of the responses of the catalytic system to pulses of reactive gases.[149] As the name of the technique implies it is usually used to study reaction products by dosing all reagents to the material. In case of the OCM reaction by pulsing methane and oxygen over a MgO and $NaMnWO_x@SiO_2$ and changing the time delay of these pulses, the presence of weak and strongly bound oxygen species could be identified, where the strongly bound species, more so in case of the redox-active $NaMnWO_x@SiO_2$ catalyst, appear to be more selective towards the OCM reaction, whereas the weakly bound oxygen on the catalyst surface more unselective.[52] In cases of Na doped CaO, Kondratenko et al. used labeled oxygen pulses in the TAP reactor to investigate the adsorbant-catalyst interaction. Their study suggests that the addition of Na increases the ratio of dissociated oxygen to molecular adsorbed oxygen resulting in beneficial catalyst

properties for the OCM reaction.[150] Next to SSITKA and TAP other techniques can be applied to analyze the oxygen-catalyst interactions. A more detailed comparison of a few labeling techniques is presented in a later chapter (see 4.6, page 70ff).

3. Experimental

3.1. Material Synthesis

Calcium carbonate was prepared as a calcium oxide precursor for the measurements by the following co-precipitation procedure. A 10.7 wt% calcium nitrate solution $Ca(NO_3)_2x4H_2O$, Fisher Scientific analytical reagent grade, dissolved with the appropriate amount of millipore water) and an 8.03 wt% ammonium carbonate solution $(NH_4)_2CO_3$, Roth, p.a., dissolved in the appropriate amount of millipore water) were simultaneously added in one hour to an 0.74 wt% ammonium carbonate solution at 25-30°C under constant stirring using an automated LabMax® reactor (Mettler Toledo). The product was aged in the solution from 1 h to 72 h, filtered, washed multiple times with millipore water and dried 65 - 80°C for 24 h. Transition metal-doped calcium carbonates ($M_xCa_{1-x}CO_3$, with 0.05% - 3.2%) were prepared by co-precipitation as oxide precursors in a similar manner as described before. In this case, a mixed metal nitrate solution containing 10.7 wt% calcium nitrate ($Ca(NO_3)_2x4H_2O$, Fisher Scientific analytical reagent grade) and the appropriate amount of transition metal nitrate (Cr^{3+}, Mn^{2+}, Ni^{2+}, Co^{3+}, Zn^{2+}, Acros Organics) was used. For catalytic measurements the resulting powder was pressed at 200 bar, crushed, and sieved to yield a sieve fraction of 200-300 µm.

3.2. Elemental Analysis by ICP-OES

ICP-OES measurements were carried out using a Varian ICP-OES 715 ES. For sample preparation 50-500 mg calcium carbonate (depending on the metal concentration) were dissolved with 3 ml 69% HNO_3 (ROTIPURAN® Supra ROTH) and diluted to a total volume of 15 ml with water (VWR, ultrapure, HPLC grade), to achieve a similar metal concentration in every sample. For calibration, a dilution series of an ICP standard from Sigma-Aldrich was prepared containing 33 elements of the main and first transition metal group elements (Periodic table mix 1 for ICP, TraceCERT®).

3.3. Nitrogen Adsorption (BET)

Surface area determination of the sealed sample minimizing air contact was carried out using an Autosorb® iQ by Quantachrome® Instruments, performing an 11-point BET surface area analysis. The sample was activated in a 4 mm inner diameter quartz tube reactor with flowing air (40 ml/min) at 900°C for 6 h applying a heating rate of 5 °C/min. After activation, the feed gas was switched to helium at 900°C and cooled down to room temperature. The sample was sealed inside the reactor using a methane-oxygen torch, transferred into a glove box, and afterward filled into the measuring cell. For the carbonates and samples where air contact could not be avoided, the samples were used as prepared and degassed at 300°C before the BET measurement.

3.4. X-Ray Diffraction (XRD)

XRD analysis was performed using an STOE STADI P transmission diffractometer equipped with a Cu anode, primary Ge(111) monochromator, and a Dectris MYTHEN 1K position-sensitive microstrip solid-state detector. The samples were crushed before analysis using an agate mortar.

3.5. Ex-Situ Thermogravimetric Analysis (TG)

Using an STA 449 Jupiter thermoanalyser (Netsch) equipped with the pulse box for PulseTA, 10 mg of the carbonate samples were decomposed under a constant flow synthetic air (20.5% O_2 in N_2) applying a heating rate of 2 °C/min up to 1000 °C, the decomposition gases were analyzed using a quadrupole mass spectrometer.

3.6. Photoluminescence Spectroscopy (PL)

Photoluminescence spectra were recorded using a Varian LS-55 Fluorescence Spectrometer. Calcium carbonate/oxide samples were placed in a quartz cuvette attached to a vacuum pump and gas supply line. For the activation the samples were heated under dynamic vacuum to 900 °C for 6 hours applying a rate of 5 °C/min, reaching a vacuum of less than $5*10^{-6}$ mbar. For quenching experiments, oxygen was introduced to the sample. For some experiments, the samples were sealed in the cuvette using a torch.

3.7. Electron Paramagnetic Resonance (EPR)

The oxide samples for EPR measurements were all prepared similarly as the PL samples to avoid air contact. SupraSil 2.9 mm EPR tubes were attached to a quartz flange and connected to a vacuum line. 0.5 – 1.0 cm of the catalyst was loaded in the tubes, degassed and heated under dynamic vacuum (< $5*10^{-6}$ mbar) to 900 °C for 6 h, applying a heating rate of 5 °C/min. After cooling down, the samples were sealed under vacuum with a torch. The carbonate samples were measured as prepared without any activation process.

Two samples comparing the pre and post-reaction condition of the catalyst were prepared in a reactor setup suitable for the OCM reaction, equipped with 4 MFCs (Bronkhorst), providing methane, nitrogen, oxygen, and helium, a GC and a folding oven. Reactors were prepared to consist in the middle of a 2.9 mm outer diameter EPR tube attached to 6 mm outer diameter quartz tubes to fit in the catalytical setups (a picture of the reactor can be found in the appendix Figure S 7, page cc). The carbonate sample was diluted with 0.4 mm quartz spheres and fixed in the reactor with quartz wool. The silicon carbide diluent used in the catalytical tests was found to disturb the EPR measurements. The amount of catalyst was chosen to yield a bed

length of roughly 1 cm. Both samples were activated at 900 °C for 6 hours in synthetic air (20% O_2 in N_2) and cooled to 750°C. For the pre-reaction sample, the feed was switched to helium, cooled down to room temperature, and both ends of the 2.9 mm tube were sealed with a torch. For the post-reaction sample, the feed was switched to an OCM feed of 4:4:1 (CH_4:N_2:O_2) and kept on stream for 12 h. The feed was again switched to helium, the sample was cooled down and sealed, to avoid contact to air.

The setups used for EPR spectroscopy are well described here.[151] CW EPR measurements were conducted at 9.8 GHz and 34 GHz microwave (mw) frequencies. For room-temperature cw EPR spectra at X-band frequencies (9.8 GHz), a Bruker B-ER420spectrometer upgraded with a Bruker ECS 041XG microwave bridge and a lock-in amplifier (Bruker ER023M) was employed using a Bruker SHQor a Bruker TE102 resonator for samples sealed in quartz tubes of 2.9 mm outer diameter, respectively. For cw Q-band (34 GHz) EPR measurements at room temperature, a Bruker B-ER420 spectrometer upgraded with a Bruker ER051 QG microwave bridge and a lock-in amplifier (Bruker ER023M) using an ER051QT resonator was employed. Transient nutation (TN) measurements at 34 GHz were conducted applying a PEANUT (Phase-inverted Echo-Amplitude detected Nutation) pulse mw sequence15 with a π/2 pulse length of 32 ns, a delay time τ of 200 ns, and a high turning angle (HTAx) pulse of 2048 ns. Phase-inversion time within the HTAx pulse was incremented by 2 ns starting with an initial inversion after 32 ns.

3.8. Temperature-Programmed Reduction (TPR)

For the TPR experiments, up to 1 g of carbonate precursor material (sieve fraction 200-300 µm) was loaded in a 4 mm i.D. quartz tube reactor and fixed with quartz wool. The material was calcined at 900 °C for 6 h in synthetic air (flow rate 20 ml/min, 5 °C/min) to yield the corresponding amount of calcium oxide catalyst. After cooling to 50°C, the feed was changed to 5% H_2 in Ar (Air Liquide), which was further purified with an SGT Triple Filter (F0301). After achieving a stable baseline, the catalyst was heated with (if not noted otherwise) a heating rate of 12 °C/min up to 900°C. The effluent gas was dried using a mole sieve 4 Å bed before entering a TCD (Messkonzept FTC 200). To ensure a good reproducibility, a LabVIEW program was deployed for controlling the setup. The time was corrected (Δt) using tracer experiments yielding a setup specific function of:

$$\Delta t = \frac{13.65\ ml}{\dot{V}}, \tag{18}$$

with $\dot{V}$ being the total volume flow.

The catalyst mass was chosen according to the criteria established by Monti and Baiker:

$$K = \frac{S_0}{\dot{V} \cdot c_0}, \tag{19}$$

with S_0 the total amount of reducible species, c0 the H_2 concentration, and K a characteristic number. The TPR parameters were chosen to yield 55s < K < 140s.[138] In the case of the low doped samples this was not possible, for either causing overloading of the reactor when increasing the catalyst mass or a too low gas flow, resulting in significant back mixing and thus distortion of the TPR profile.

3.9. Steady State Catalytic Tests

For the steady state catalytic test 50 mg of carbonate, the precursor was diluted in 750 mg of silicon carbide and fixed with quartz wool in a 4 mm inner diameter quartz tube reactor resulting in a bed length of 40 mm. The catalysts were tested in automated reactor units testing 6 to 8 catalysts in parallel. The analysis of the reaction products was achieved using a GC equipped with a TCD and FID. Before the catalytic testing, the catalysts were activated in the reactor at 800°C in synthetic air (N_2: O_2, 4:1, 40 ml/min) for 6 hours. Applying a fixed feed composition (3:3:1 N_2:CH_4: O_2, if not indicated otherwise) the flows were varied between 37.5 ml/min up to 200 ml/min and the temperatures between 650°C and 800°C. The methane conversion X_{CH4} was calculated using equation (20) and the selectivity S_i using equation (21), with x_i the molar fraction of compound i, ν the stoichiometric factor, and p the index for the reaction products (C_2H_6, C_2H_4, CO, and CO_2).

$$X_{CH_4} = 1 - \frac{x_{CH_4}}{x_{CH_4} + \sum \frac{1}{\nu_p} x_p} \tag{20}$$

$$S_i = \frac{\frac{1}{\nu_i} x_i}{\sum \frac{1}{\nu_p} x_p} \tag{21}$$

3.10. Temperature Programmed Catalytic Tests

The catalytic tests in constant as well as pulsed feed were carried out in an 8 mm inner diameter quartz tube reactor equipped with an internal thermocouple positioned inside an inner quartz tube of 2 mm outer diameter (for setup see section 3.17, page 35, Scheme 6). For the tests, 100 mg calcium carbonate (200-300 µm) were diluted in 1400 mg of silicon carbide (300-400 µm). Before the catalytic tests, the carbonate was decomposed at 850°C for 6 h in synthetic air (30 ml/min). In constant feed mode a gas composition of 6:1:3, He:O_2:CH_4 was mixed using Bronkhorst mass flow controllers. In the pulsed mode the feed was set to 9:1, He:O_2 and conducted through a pneumatic 6-port diaphragm valve by Valco VICI equipped with a 1 ml sample loop. Methane was pulsed every 10 min (every 20°C) applying this loop. The total gas flow

was fixed at 30 ml/min for each experiment. The products were quantitatively analyzed using a GAM 200 mass spectrometer. The conversion in case of constant feed mode was calculated by:

$$X_{CH_4}(T) = 1 - \frac{c_{CH_4}(T)}{c_{CH_4}(Baseline)} \quad (22)$$

with c_{CH4}(Baseline) the initial methane concentration determined by an initial baseline before and after the experiment. In pulsed mode the time-resolved methane peaks were integrated and compared to mean integral of pulses performed at 50°C:

$$X_{CH_4}(T) = 1 - \frac{\int c_{CH_4}(T)}{\int c_{CH_4}(50°C)} \quad (23)$$

3.11. In-Situ Thermogravimetric Analysis (TG)

The in situ thermogravimetric experiments were carried out using a DynTHERM magnetic suspension balance (Rubotherm) described in 3.16 (page 34).[134] For the experiments 500 mg of calcium carbonate (200-300 µm) were placed in the ceramic crucible and decomposed by heating in argon (500 ml/min) with 5 °C/min up to 900°C. After complete conversion to calcium oxide (mass loss expected from M_{CaCO3} = 100.1 g/mol to M_{CaO} = 56.1 g/mol), temperature and feed were varied. For OCM conditions a feed composition of (3:1:3, Ar:O_2:CH_4) was applied. For buoyancy correction, a blank experiment was performed. It has to be noted, that under the investigated temperatures for OCM (>700°C) the conversion of oxygen was always 100% due to metal parts inside the balance (e.g. thermocouples: stainless steel shell, suspension: Pt/Ir alloy) and the catalytic activity of the material could therefore not be tested.

3.12. In Situ Infra-Red Spectroscopy (IR)

In situ IR measurements were carried out using a Varian 670 FTIR spectrometer equipped with an MCT detector. The spectra were recorded at a resolution of 2 cm^{-1} accumulating 128 scans. Self-supporting wafers of $CaCO_3$ were produced and activated in the cell before the reaction in helium at 780°C. The oxidative coupling of methane was investigated at atmospheric pressures with a feed composition of 3:3:1 of CH_4:Ar:O_2 between 600 and 800°C. For background correction, the gas phase was recorded separately before the experiment. The products were analyzed using an online µGC (Varian Mirco GC 490) equipped with 10 m Pora Plot Q and 1 m COX column modules and with TCD detectors.

3.13. Raman Spectroscopy

Raman spectroscopy was carried out using a TriVista TR557 spectrometer (S&I Spectroscopy & Imaging GmbH) equipped with a confocal Raman microscope. Different laser sources were used, the power was chosen to reduce beam damage influences. The resolution is dictated by the laser wavelength and grating used, in this case, 600 grooves/mm, which yield a resolution of approximately 1 cm^{-1}. For in situ studies a Linkam CCR-1000 reactor stage was used coupled with a µGC (Agilent). Prior exposure to the feed, 10 mg of carbonate material (200-300 µm) were placed inside the in situ cell and activated in synthetic air (10 ml/min) at 900°C. A feed of 3:1:3 of He:O_2:CH_4 (10 ml/min) was used and the temperatures were varied between 700°C and 800°C. It has to be noted that due to heated metal parts inside the cell (e.g. thermocouples, heating system), the oxygen conversion above 700°C was almost 100%. For ex-situ experiments, the same samples were used as the sealed samples from the photoluminescence experiments (3.6, page 28).

3.14. Pulsed Isotopic Exchange Experiments

The setup for the pulsed isotopic exchange experiments can be found in section 3.17 (page 35, Scheme 6). It was used without further modifications.

For the tests, 50 mg of the carbonate precursor material (200-300 µm) was diluted in 730 mg silicon carbide and fixed with quartz wool in a 4 mm inner diameter tube, which results in a total bed length of 50 mm. Before the tests, the carbonate was activated to yield the oxide catalyst. The activation was performed at 900°C in synthetic air (20% O_2 in He).

The pulse mode isotopic scrambling experiments were carried out at a constant feed of 30 ml/min synthetic air (20% O_2 in He). In experiments containing carbon dioxide or water, equal parts of He were replaced by the oxygen. Usually, 20% CO_2 were used, provided by an additional MFC, and 4% H_2O added via a saturator. After equilibrating the reactor at the desired temperature, the isotope mixture (20% $^{36}O_2$ in 80% N_2) was introduced via the diaphragm valve. For the experiments, a sample loop of 1 ml was used. It was evacuated and purged with the test gas several times before filling the sample loop with 500 µl of the labeled gas. The gases were analyzed using the quadrupole mass spectrometer (MS). Due to a lack of suitable reference gases, a calibration of the observed species was not possible and only the relative data was used. With the different isotope containing gases behaving very similar, physically and chemically, the response factors were used for the same gases containing different isotopes, such as $^{32}O_2$,$^{34}O_2$ and $^{36}O_2$, or $^{18}H_2O$ and $^{20}H_2O$, or $^{44}CO_2$, $^{46}CO_2$ and $^{48}CO_2$. Under this assumption, the calculation of the ^{18}O-distribution ($x_{i,\,F}$) from the recorded signal intensities (I) for the component (i), with F being the number of substituted oxygen atoms (e.g. 1 for $^{34}O_2$ and 2 for $^{36}O_2$) can be performed as followed:

$$x_{i,F} = \frac{F\int I(m_{i,F})}{\sum_{j=1} j\int I(m_{i,j})}, \quad (24)$$

with $m_{i,F}$ being the m/z value for the corresponding component (e.g. 36 for $^{36}O_2$). The whole pulse is integrated and analyzed in this case.

To get the total conversion of the oxygen isotope entering the reactor, the nitrogen pulse can be used as an internal standard. Using a reference experiment at 50°C with no visible conversion the calculation can be performed as followed:

$$X(^{36}O_2) = 1 - \left(\frac{\int I(m_{Std})}{\int I(m_{O_2,2})}\right)_{50°C} \cdot \left(\frac{\int I(m_{O_2,2})}{\int I(m_{Std})}\right)_T, \quad (25)$$

with m_{Std}, being the m/z value of the used internal Standard (either 28 for the positive pulse of N_2, or 4 for the negative peak of He).

The overall mole fractions for the components in the gas mixture can now also be calculated:

$$x_F(CO_2) = \left(1 - \left(\frac{\int I(m_{Std})}{\sum_{j=1} j\int I(m_{O_2,j})}\right)_{50°C} \cdot \left(\frac{\sum_{j=1} j\int I(m_{O_2,j})}{\int I(m_{Std})}\right)_T\right) \cdot x_{CO2,F} \quad (26)$$

To investigate the influence of impurities in the feed gas on the isotopic exchange, an additional dryer was installed before the reactor. For this purpose, a stainless steel tube with 1/2" inner diameter was filled with 10 g of $CaCO_3$ and activated at 900°C for 24 h.

3.15. Steady State Isotopic Transient Kinetic Analysis

The SSITKA experiments were performed in the setup for dynamic experiments (section 3.17, page 35, Scheme 6). The lines towards the switching valve were adjusted to allow switching of the continuous gases instead of pulsing the content of the sample loop. For this purpose, additional MFCs were introduced. The catalyst loading and pretreatment were performed analogous to the pulsed isotopic exchange experiments (see section 3.14, page 32). For the tests the reactor was heated to the desired temperature (700 to 800 °C), a volume flow of 20 ml/min synthetic air was applied (20% O_2 in N_2). After obtaining a stable baseline of the mass spectrometer signal, the switching valve was used to change the gas feed to a labeled air, by mixing 16 ml/min He with 4 ml/min 18,18-oxygen (Westfalen AG). For the calculation

of the composition, the same assumptions were made as in pulsed experiments (see section 3.14, page 32), that the response factors for all oxygen isotopes in the mass spectrometer are identical.

3.16. Setup Magnetic Suspension Balance

In Scheme 5 the DynTHERM magnetic suspension balance (Rubotherm) used for in situ thermogravimetric experiments is depicted:

1) being the balance unit,
2) the purge gas inlet,
3) the coupling unit for the magnets,
4) a cooling jacket to protect the magnets,
5) the gas inlet for reactive gases,
6) the sample holder in the furnace unit and
7) the outlet.

The inlet flows are mixed and controlled by Brooks MFCs, outlet gases are analyzed with a GAM 200 mass spectrometer by IPI Instruments. The sample holder is made of corundum ceramics the suspension parts made out of heat resistant Pt/Ir alloy. For optimal operation, a minimum pressure of 0.5 bar is applied.

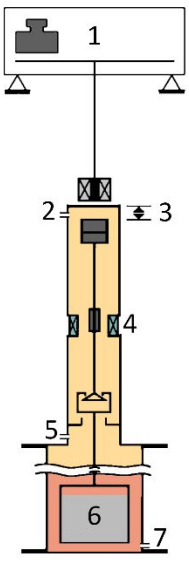

Scheme 5 Scheme oft the magnetic suspension balance used for in situ thermogravimetric experiments.

3.17. Setup for Dynamic Experiments

For dynamic experiments a flexible setup was used, allowing the exchange of MFCs for different capacities, the addition of extra MFCs for experiments requiring more gases, and also the adaption of the tubing if necessary.

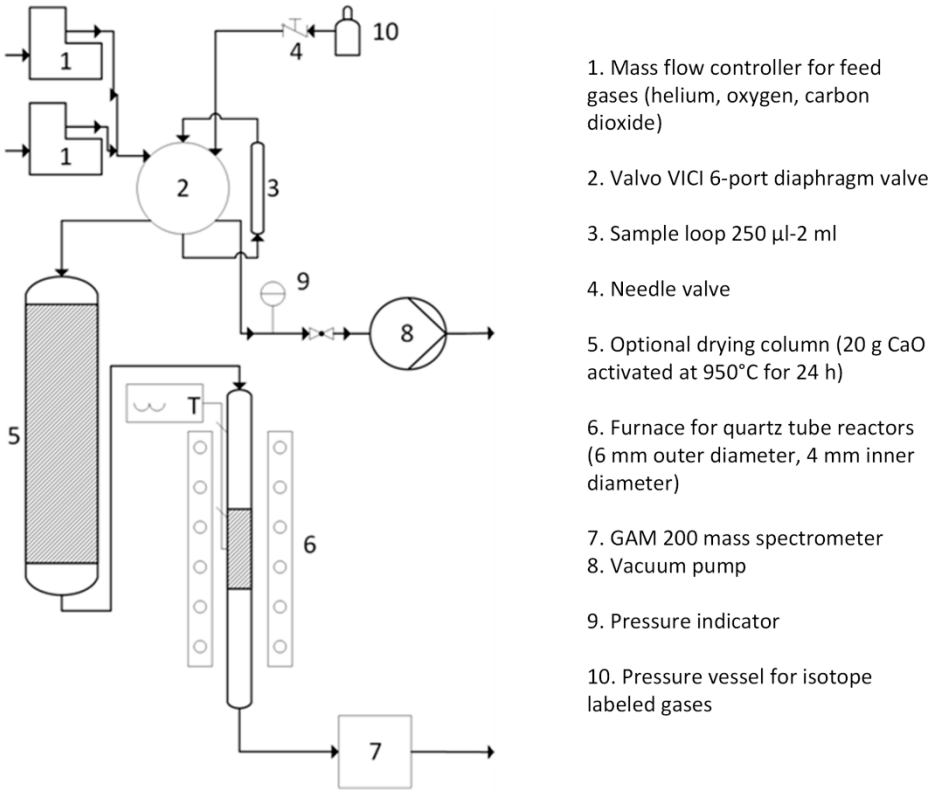

Scheme 6: Scheme of reactor used for dynamic experiments.

In Scheme 6 a flow diagram of the setup is depicted as it is used for pulsed experiments. The mass flow controllers (Bronkhorst El-Flow, 1) are used to mix the gases to yield the for the experiment necessary reaction mixture, a diaphragm valve (Valco Vici, 2) is used for pulsing the content in sample loop (3) to the feed gas. For filling the sample loop, either MFCs can be used or as here depicted, the gases were extracted directly from the pressure vessel (10), the loop can be purged with a vacuum pump (8). The loop is filled manually to the desired pressure indicated by the pressure indicator (9), with needle valve (4) the rate of the pressurization can be controlled. An additional dryer (5) can be equipped in line for further purging of the gases. In the furnace (Reetz, 6) the furnace, the reactor temperature can be controlled in a range between 50°C and 1000°C. The exiting gases can be analyzed with an online mass spectrometer (GAM 200 IPI Instruments, 7). The MFCs and are digitally controlled using a computer.

4. Results and Discussion

4.1. Synthesis of phase doped Calcium Carbonate Precursor Materials

For the synthesis of doped calcium oxide materials, carbonates were chosen as suitable precursors due to their better resistance towards moisture and carbon dioxide in the atmosphere compared to calcium oxides which rapidly reacts to form hydroxides and carbonates. Nitrate precursors were used as metal sources and ammonium carbonate as a precipitating agent to avoid alkaline impurities in the materials, which can highly affect the catalytic performance.[47,72,152,153] The precipitation temperature of 25 °C was applied to exclude the formation of an aragonite phase during the synthesis, which is favored to be formed at 29 °C.[154]

For a first rough screening for the suitability different dopants on the catalysis, Cr^{3+}, Mn^{2+}, Co^{3+}, $Ni^{2+,}$ and Zn^{2+} nitrates were co-precipitated to yield $M_xCa_{(1-x)}CO_3$ with x being 0.1% applying an aging time of 1h. The synthesis was repeated for the Mn and Ni-doped samples while optimizing the doping concentration and phase purity of the carbonate precursors.

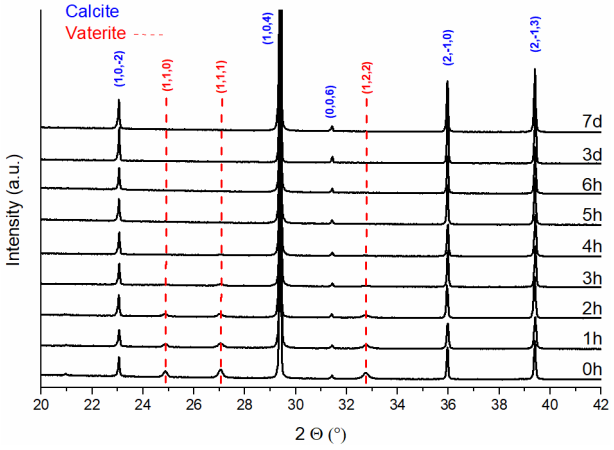

Figure 3: XRD patterns precipitated and dried $CaCO_3$ with different aging times.

To obtain phase pure precursor materials, the aging time after precipitation has been varied from 1 hour up to 7 days. XRD analysis of the precipitates (Figure 3) reveals two carbonates being formed during synthesis: vaterite and calcite. Aragonite, being thermodynamically favored at elevated pressures or temperatures, as well as a complete amorphous phase was not found. The drying temperature of 65 °C ensured the prevention of aragonite being formed during the drying process. Upon aging, the metastable vaterite is subsequently converted to the thermodynamically favored calcite structure.[101] After 4 hours no phase next to calcite could be observed. The initial formation of vaterite can be explained by the presence of ammonia in the

solution, which is known to promote the formation of vaterite instead of calcite.[154] To ensure a complete phase transition towards calcite an aging time of 24 hours was chosen for the doped samples to ensure a complete phase transition.

Table 1: Synthesis data of precipitated carbonates.

Dopant	**Ni**		**Mn**			
xi target (mol%)	xi* (mol%)	BET (m²/g)	xi* (mol%)	BET (m²/g)	α** (Å)	γ** (Å)
ref	0	1.7	0	1.7	-	-
0.05	0.02	0.42	0.02	1.2	4.992	17.071
0.10	0.04	0.47	0.04	1.1	4.991	17.067
0.20	0.08	0.22	0.08	-	4.990	17.045
0.40	0.16	0.28	0.17	0.79	4.991	17.067
0.80	0.29	0.62	0.36	0.79	4.989	17.060
1.60	0.38	-	0.69	1.3	4.987	17.005
3.20	-	-	1.41	-	4.990	17.067

*determined by ICP- OES, **determined by the fit of XRD data

In Table 1, the concentrations determined by ICP-OES and surface areas of the precipitates are presented. All precipitates exhibit a very small surface area below 1 m²/g and vary with no clear trend. It is also noteworthy, that a lot of doping metal is lost during synthesis and not incorporated into the host lattice. In the case of manganese doped calcium carbonate, roughly half of the transition metal is lost during synthesis, wherein the case of nickel the loss increases with increased doping. Since nickel is known for forming stable amine complexes,[155] the loss is likely a result of the choice of precipitating agent. The high concentration of ammonia and the low concentrations of transition metals in solution results in incomplete precipitation of the transition metal. For simplicity reasons, the doped catalysts are from here on referred to using their target concentrations rather than the real measured ones.

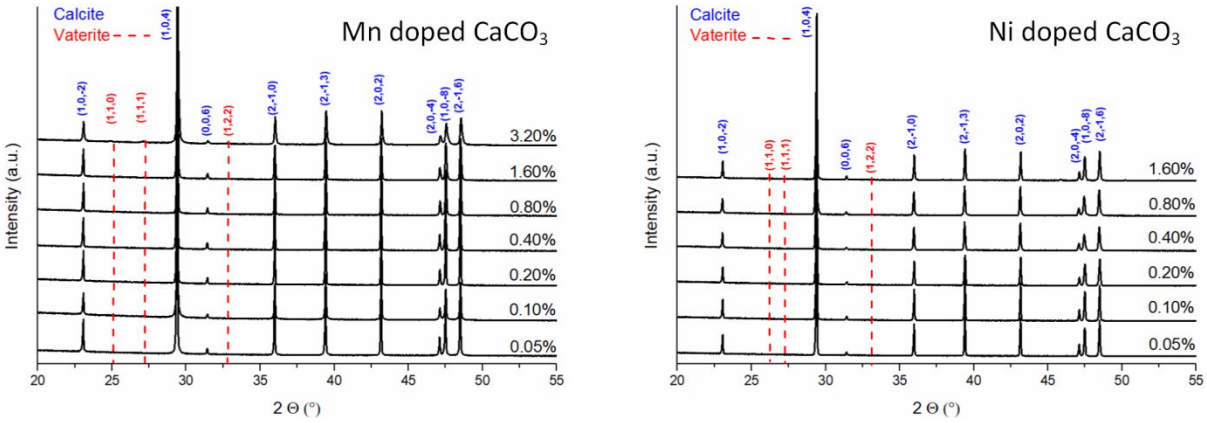

Figure 4: XRD pattern precipitated and dried Mn (left) and Ni (right) doped $CaCO_3$ aged for 1 day.

Inspecting the XRD patterns of the resulting materials no additional signals indicating segregation of the doping during carbonate synthesis were observed. Fitting the XRD data of the manganese series, a slight lattice contraction can be observed hinting an insertion of transition metals into the calcite lattice, though the total change of the lattice constants (α and γ) is less than 0.1% (Table 1). In the case of the highest nickel doped carbonate, hints of vaterite can be found even after aging for 24 hours (Figure 4).

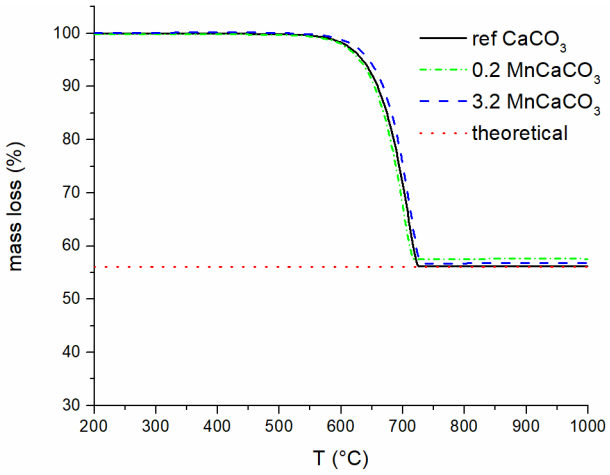

Figure 5: Decomposition of manganese doped $CaCO_3$ under synthetic air in a thermogravimetric balance at 1 °C/min up to 1000 °C.

To investigate the influence of the doping on the decomposition exemplary manganese doped samples were decomposed under synthetic air using thermogravimetric analysis (Figure 5). The theoretical value was determined to assume a molar mass of 100.1 g/mol for the carbonates and 56.1 g/mol for calcium oxide. For all three samples, the decomposition starts around 550 °C and is completed at 730 °C, which is in good agreement with the literature (start 540°C).[154]

No major impact of the doping on the carbonate decomposition can be observed. To inspect a phase separation of the doping metal during decomposition of the carbonate, the highest doped sample (3.2 $MnCaCO_3$) was decomposed in a transfer holder allowing a glove box handling of the material. XRD analysis did not reveal additional signals, also a lattice contraction could be determined to imply an incorporation of the doping metal into the calcium oxide lattice (Figure 6).

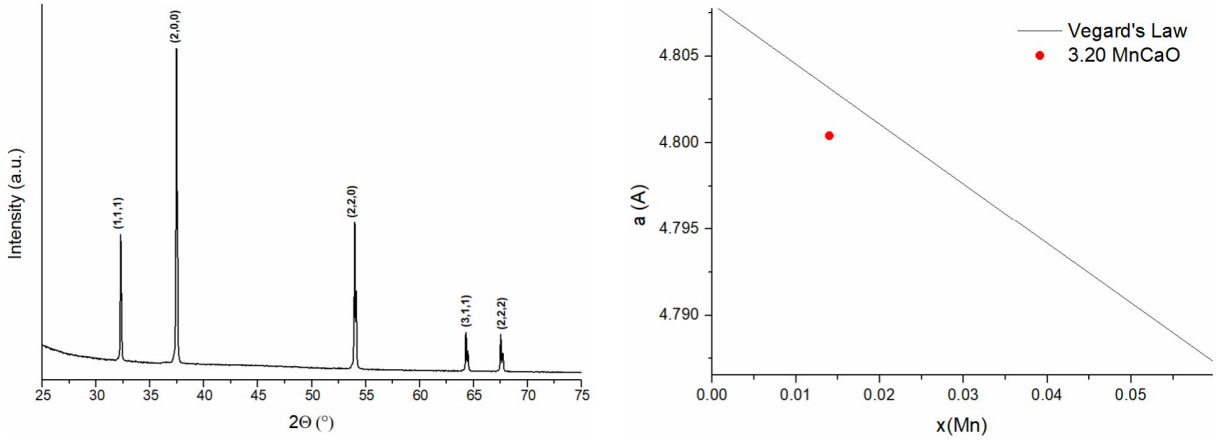

Figure 6: XRD pattern of Mn-doped CaO (left, 3.20 $MnCaCO_3$ decomposed for 6 hours at 900 °C applying a heating rate of 5 °C/min), lattice parameter A compared to Vegard's Law assuming solid solution of CaO and MnO.

4.2. Characterization of doped Calcium Oxide

4.2.1. Photoluminescence Spectroscopy on doped and undoped CaO

To analyze the impact of the dopant on the electronic structure of the catalyst surface photoluminescence spectroscopy was conducted, which has been proven to be a useful tool in the surface characterization of alkaline earth oxides.[67,85,121,156] Due to the large bandgap of CaO, irradiation with UV light (>200 nm) cannot induce bulk photoluminescence and all measured signals can be exclusively attributed to under-coordinated surface ions.[85,157] To exclude influences from adsorbates, hydroxyl, or carbonate groups all samples were measured under vacuum ($p < 5*10^{-6}$ mbar) and were before the experiments activated at 900 °C for 6 hours.

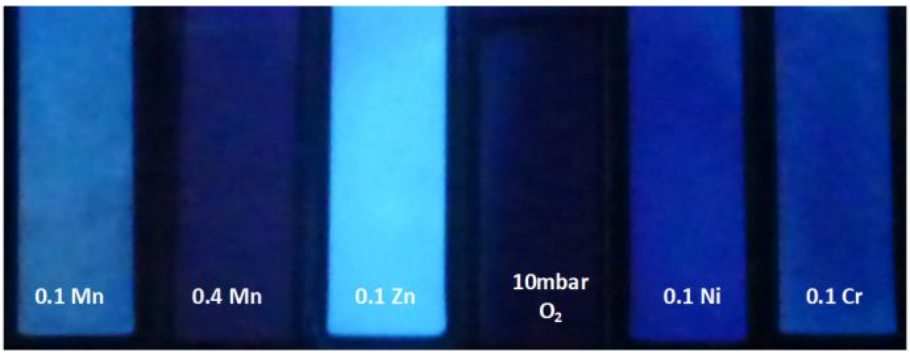

Figure 7: Photograph of doped CaO samples sealed under vacuum (p < 5*10-6 mbar) under a laboratory UV lamp (255 nm, 4th sample CaO in 10 mbar O_2 atmosphere). The samples were obtained by activating the corresponding carbonate precursors at 900 °C under vacuum for 6 h.

It has to be mentioned, that the overall intensity for different samples in the photoluminescence measurements differed strongly and the samples could not be measured at the same spectrometer settings. A quantitative analysis of the received spectra is therefore limited. In general, it was observed that pure samples not containing any dopants exhibited broad, intense excitation spectra compared to doped samples (see Figure 7). It also has to be mentioned that the sample containing Zn was not stable and metallic Zn evaporated during preparation.

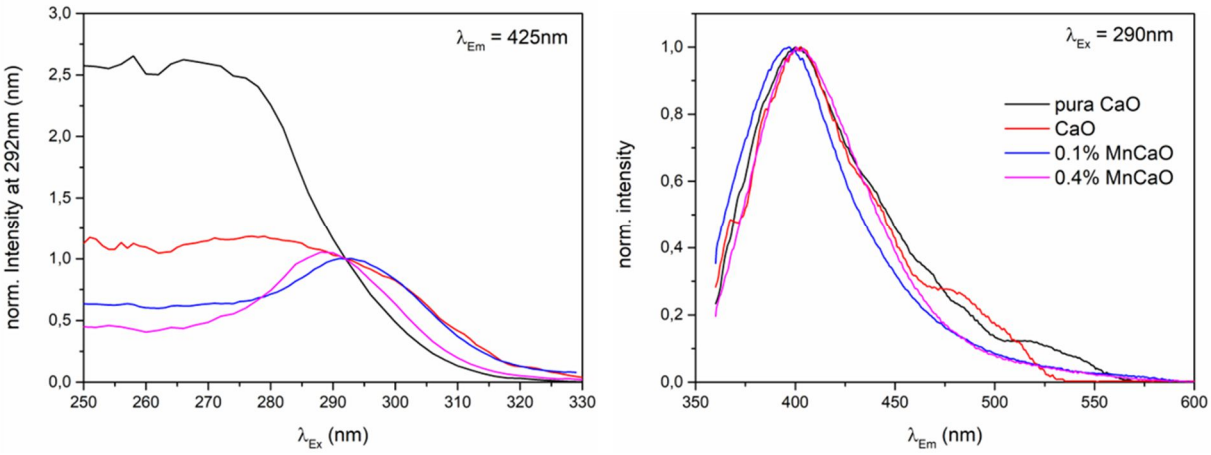

Figure 8: Normalized excitation and emission spectra at λ_{Em}= 425nm and λ_{Ex}= 290nm of CaO and Mn-doped CaO samples under vacuum. The samples were obtained by activating the corresponding carbonate precursors at 900 °C under vacuum for 6 h. Pura CaO as reference (puratronic Sigma Aldrich, purity >99.998% trace metal analysis)

Comparing the excitation spectra of pure and doped CaO (Figure 8, Figure 9), shows a significant change in the shape of excitation spectra, where the emission spectra appear to be almost unaffected, indicating the same surface defects being responsible for the emission for all samples. In general, a maximum of emission can be found at $\lambda_{Em} = 410$ nm for all samples which is unaffected by the applied

excitation energy and in accordance with results reported for CaO nanocrystals.[85] The excitation spectra, however, are strongly affected by the doping where the undoped samples (Pura and ref CaO) exhibit broad intense spectra with no clear maximum, the doped samples exhibit a clear maximum around λ_{Ex} = 290 nm (Figure 8) which can be attributed to surface edge sites (lit. O_{4C}^{2-} 4.4 eV, 280 nm).[120] The deviation from the literature values might be explained by particle size dependence of the excitation energy.[94] The broader spectrum of the can be explained by the contribution of luminescence from the plane sites (lit. O_{5C}^{2-} 5.3-5.5 eV, 225-235 nm),[85,120] as well better isolation of the luminescent sites in the doped oxides due to their reduced abundance. Luminescence derived from corner sites was not observed in no sample. Adding too much transition metals to CaO resulted in a complete loss of signals (Figure S 1).

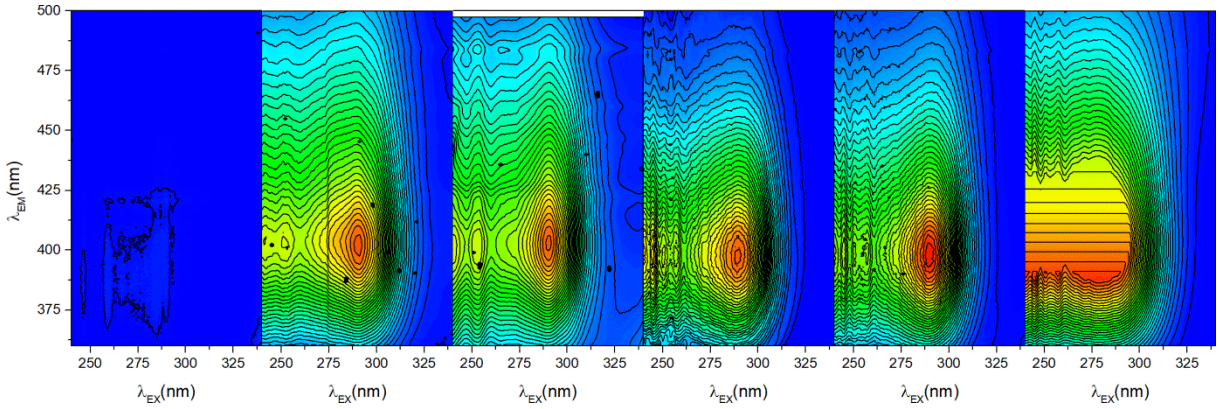

Figure 9: 2D photoluminescence spectra of sealed CaO samples. From left to right: pure CaO with 10 mbar O_2, 0.1 atom% Mn-doped CaO under vacuum, 0.4 atom% Mn-doped CaO under vacuum, 0.1 atom% Cr doped CaO under vacuum, 0.1 atom% Ni doped CaO under vacuum, 0.1 atom% Zn doped CaO under vacuum. The samples were obtained by activating the corresponding carbonate precursors at 900 °C under vacuum for 6 h.

Upon oxygen exposure, the photoluminescence could be completely quenched (see Figure 7, 4th sample), proving the recorded photoluminescence still being exclusively related to surface sites and no bulk phosphor was created by the dopant.[86] Figure 10 shows exemplary the full 2D photoluminescence spectra recorded at excitation wavelengths between 250 nm and 340 nm and emission wavelengths between 360 nm and 600 nm of the 0.4 MnCaO sample recorded before and after addition of oxygen to the sample. In vacuum one prominent signal can be observed at λ_{Em} = 400 nm and λ_{Ex} = 290 nm (Figure 10, left). Upon adding 1 mbar oxygen to the sample the signal is completely quenched (Figure 10, right).

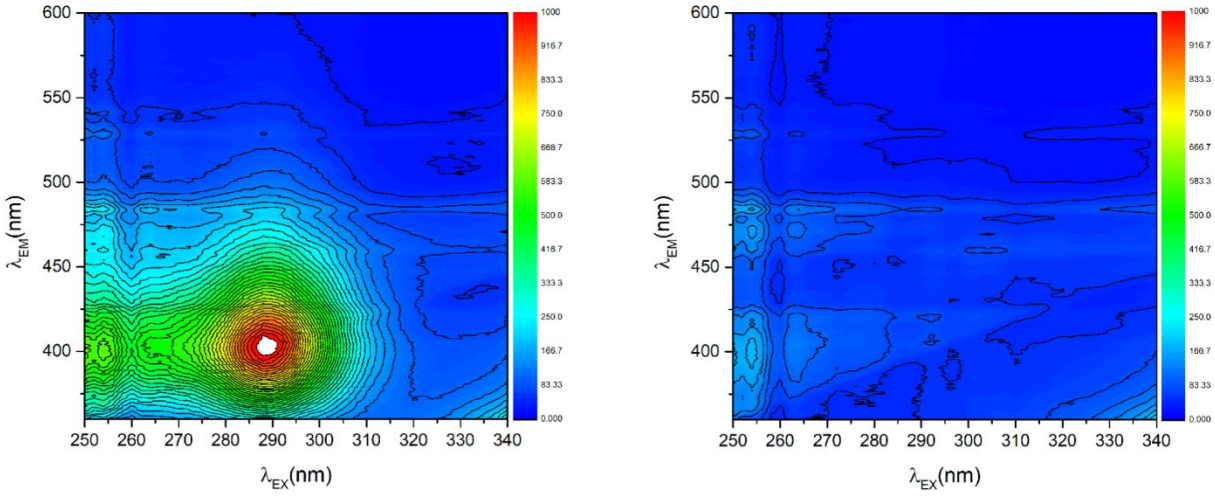

Figure 10: 2D Photoluminescence spectra of Mn-doped CaO (0.4 MnCaO) under vacuum (p < 5*10-6 mbar, left) and exposed to 1 mbar O_2 (right). The samples were obtained by activating the corresponding carbonate precursors at 900 °C under vacuum for 6 h.

Reapplying vacuum resulted in regeneration of the signal, proving the reversibility of the process, though not the complete signal was retrieved (see Figure S 4). Comparing the signals before the addition of O_2 and after reapplying vacuum (Figure 11) shows no difference in the shape of the obtained spectra, indicating no difference in the nature of the reversible and irreversible quenched sites.

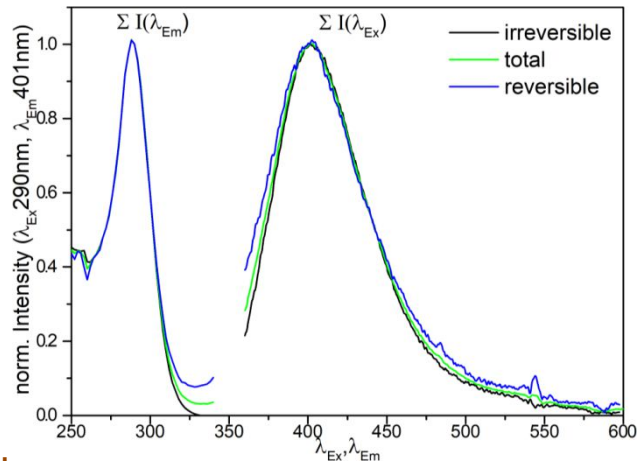

Figure 11: Normalized loss of photoluminescence (difference spectra of 0.4 MnCaO on exposure to oxygen (total) and after reapplying vacuum (reversible). The samples were obtained by activating the corresponding carbonate precursors at 900 °C under vacuum for 6 h.

4.2.2. Electron Paramagnetic Resonance Spectroscopy on Mn doped CaO

A method to analyze diluted transition centers in a host matrix can be EPR spectroscopy, which is highly sensitive towards paramagnetic centers. In Figure 12

the electron spin echoes are shown of Mn-doped CaO and undoped $CaCO_3$ in pulsed EPR experiments. Compared to the doped sample, the signal of the undoped carbonate sample is negligible, though one has to note, that not all manganese species are EPR active. Mn^{2+} with d^5- and Mn^{4+} and d^3-configuration respectively always being paramagnetic and therefore presumably EPR active, for Mn^{3+} with a d^4-configuration spin pairing is possible, which can lead to the formation of EPR inactive species. The presence of Mn^{7+} can be excluded for those being either liquid (as oxide) or soluble and therefore removed, if even existed, in the synthesis during the washing process. With respect to the ICP analysis and comparing cw-EPR experiments of the doped to the undoped carbonate (see Figure S 5, page bb), with all doped samples showing significant Mn^{2+} signals, the amount of Mn in the undoped sample and its influence on the EPR spectra can be neglected.

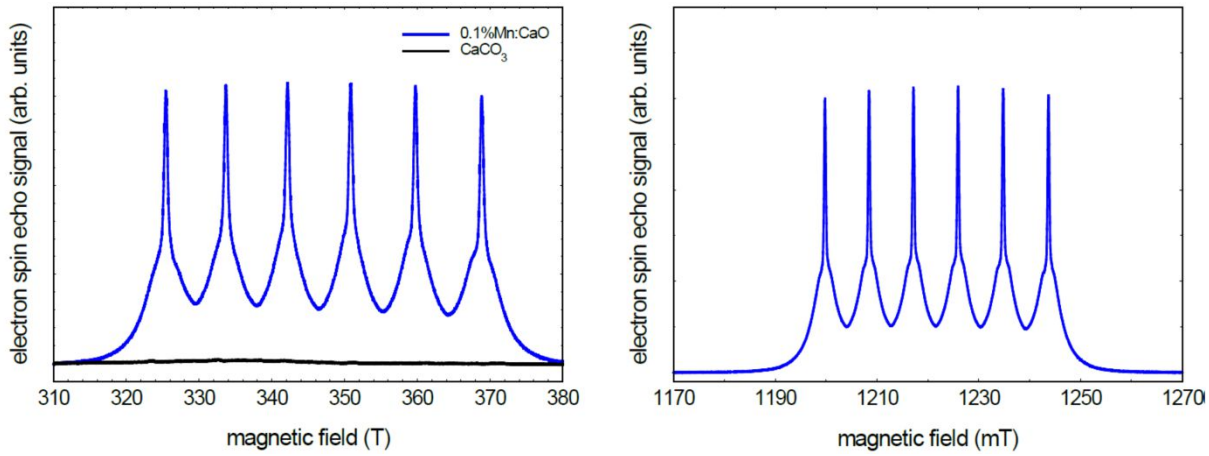

Figure 12: Electron spin echo of 0.1% Mn-doped CaO and undoped $CaCO_3$ recorded at 9 GHz (left) and Mn-doped CaO recorded at 34GHz (right). The CaO sample was activated under a dynamic vacuum at 900°C and sealed in the EPR tube.

Looking at the spin-echo spectra (Figure 12), CaO samples containing 0.1% Mn give rise to 6 intense EPR signals originating from the hyperfine splitting of the I = 5/2 system, consisting of narrow lines with a “pedestal” powder pattern arising from the orientation-dependent transitions in the S = 5/2 spin state of Mn^{2+}. The $|\pm 1/2, m_I\rangle \leftrightarrow |\pm 1/2, m_I\rangle$ transitions result in sharp narrow lines, due to the almost isotropic hyperfine matrix, whereas the orientation dependent $|\pm 1/2, m_I\rangle \leftrightarrow |\pm 3/2, m_I\rangle$ and $|\pm 3/2, m_I\rangle \leftrightarrow |\pm 5/2, m_I\rangle$ transitions contribute to the line broadening.[158] Comparing the measurements at different microwave frequencies, a slight improvement of the spectra can be observed. The peaks and pedestals appear more distinct using the higher frequency. Presumably, at the lower field strength, the high field approximation is not given, resulting in the rise of the forbidden transitions $|\pm 1/2, m_I\rangle \leftrightarrow |\pm 1/2, m_I \pm 1\rangle$ adding to the pedestals. A similar observation can be made using cw-EPR (Figure 13).

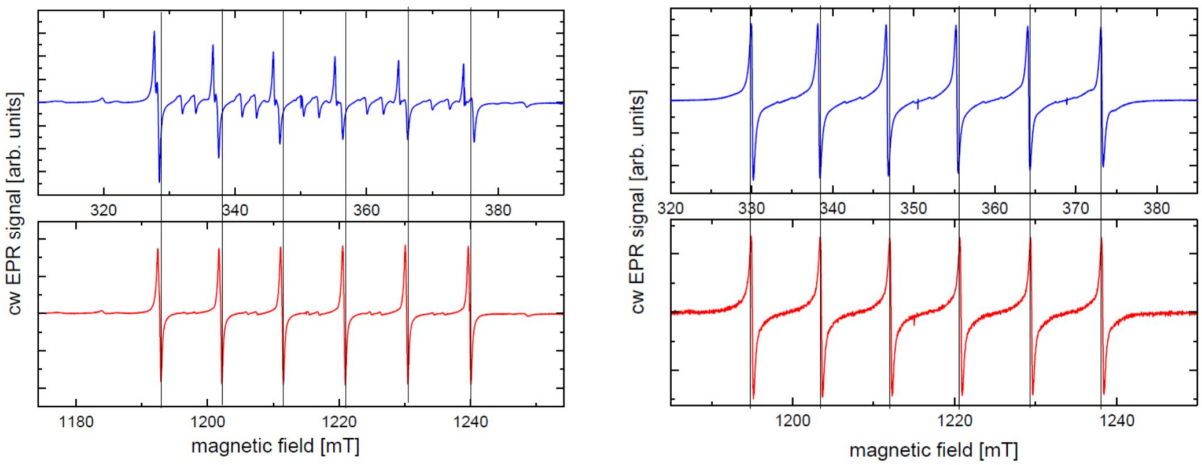

Figure 13: EPR measurement of 0.1% Mn-doped $CaCO_3$ as prepared(left) and 0.1% Mn-doped CaO activated at 900°C under dynamic vacuum and sealed in the EPR tube (right) recorded at 9.8 GHz (top, blue) and 34 GHz (bottom, red).

Applying a low field strength gives rise to 5 doublets located between the 6 peaks of the Mn hyperfine structure. With increasing field strength these transitions are suppressed resulting in cleaner spectra. Due to the different symmetries of the host lattices, the spectra for Mn in CaO and $CaCO_3$ are expected to be slightly different. Comparing the carbonate spectra to the literature, they are in good agreement with those of Mn^{2+} replacing a Ca^{2+} atom in calcium carbonates, such as dolomite or calcite, indicating already a good substitution of Ca in the precursor material.[159] To analyze the nature of the manganese ion in the oxide the sextet can be analyzed by the following expression for resonant fields:[160]

$$H_m = H_0 - A_0 \cdot m_I - \left(\frac{A_0^2}{8H_0}\right) \cdot (35 - 4 \cdot m_I^2), \tag{27}$$

with:

$$H_0 = \frac{h_P \nu}{g\beta_e}, \tag{28}$$

and A_0 the splitting parameter, n the frequency of the microwave radiation, h_P the Planck constant and g the g-factor. Fitting the equation to the peak positions of the spectra recorded for manganese doped calcium oxides, yield a g value of 2.002 and a splitting constant A of -86.3 G, suggesting Mn^{2+} in an octahedral symmetry (Figure S 6, page bb).

Using a nutation-frequency correlated EPR (phase-inverted echo-amplitude detected nutation PEANUT) technique at 34 GHz (Figure 14) each of the 6 signals for the I = 5/2 transitions can be separated in 5 regions, allowing an assignment of the

before discussed m_S transitions. The narrow line widths of the $|\pm 1/2, m_I\rangle \leftrightarrow |\pm 1/2, m_I \pm 1\rangle$ in all of the measured powder pattern proves a high symmetry of the Mn^{2+} center indicating substitution of Ca^{2+} centers at the site of octahedral symmetry.

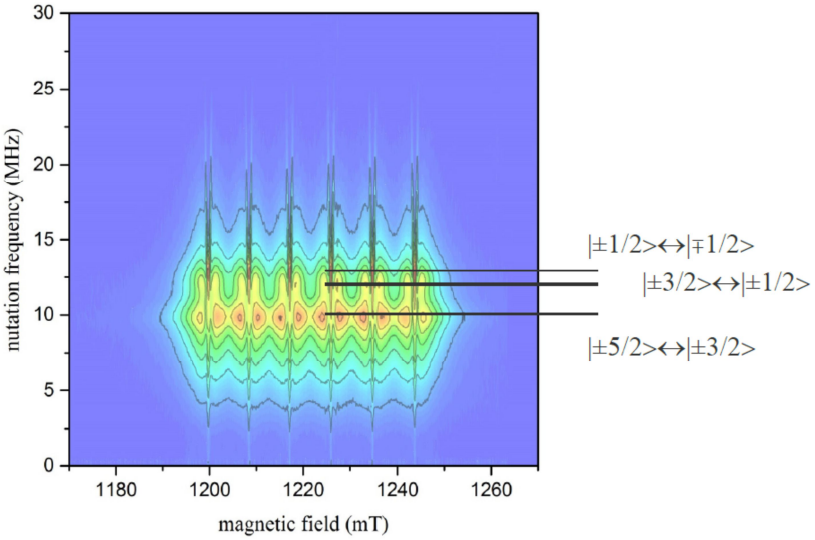

Figure 14: Intensity plot of 2D PEANUT spectrum of 0.1% Mn-doped CaO prepared by decomposition of $CaCO_3$ under dynamic vacuum at 900°C and sealed in the EPR tube.

With increasing manganese loading, the g value and splitting constant remain the same, though the peak width broadens significantly (Figure 15). The line broadening is explained by dipolar coupling, which can be assumed to be linear with the concentration at low doping amounts.[124] Next to the dipolar coupling, which dominates the line shape, an exchange interaction of the metal centers has to be considered, which is a function of the occupancy of metal centers in the coordination spheres, where the range of interaction appears to be dependent on the nature of the metal center. In case of Mn^{2+} centers in a CaO host matrix, the range of interaction was determined to be 0.59 nm including 42 cationic sites in the 4th coordination sphere.[125–129,161]

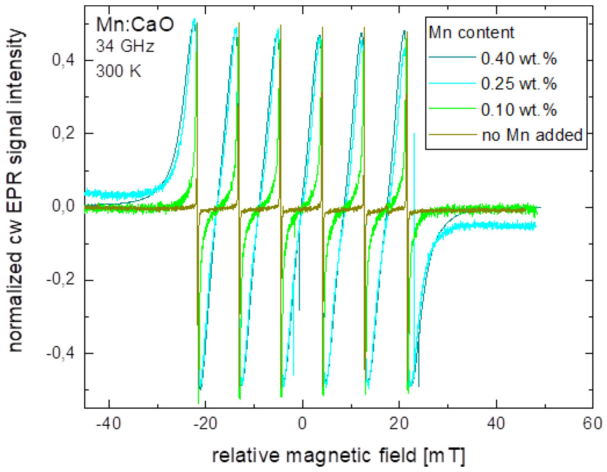

Figure 15: 34GHz EPR spectra of different Mn-doped CaO samples prepared by decomposition of the carbonate precursors under dynamic vacuum at 900°C and afterward sealed in an EPR tube.

Inspecting the EPR spectra of two 0.1% Mn-doped CaO samples, one activated at 900°C for 6 h, then cooled down and sealed, and one sealed at room temperature after being on OCM feed (750°C 4:4:1 of CH_4:N_2:O_2) for 12 h (Figure 16) no significant changes can be observed indicative for the formation of new Mn species, such as clustered species/segregated species.

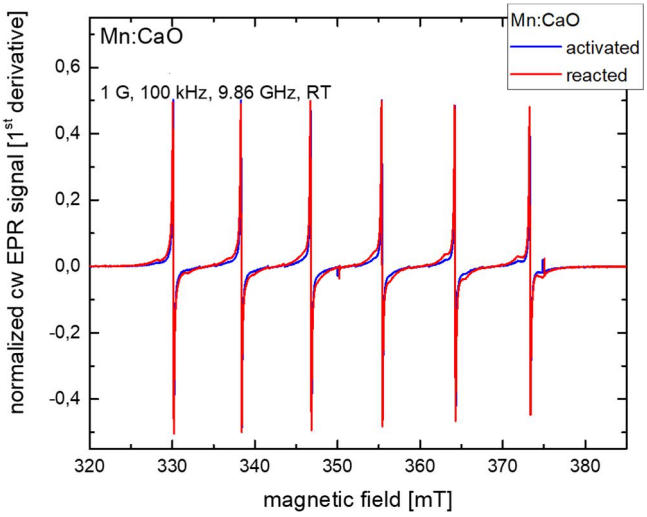

Figure 16: EPR spectra of 0.1%Mn-doped sample after activation (900°C for 6h in synthetic air) and after reaction (750°C 4:4:1 of CH_4:N_2:O_2 for 12h).

4.2.3. Temperature-Programmed Reduction of doped CaO

The temperature-programmed reduction technique is a useful tool to get insight into the transition metal dopant is incorporated into the CaO host matrix. For the experiments, the carbonate precursors were activated inside the reactor in synthetic air, to ensure complete oxidation of the catalyst. Afterward, the catalyst is heated in a

reducing feed. The onset and peak of reduction are dependent on the nature of the reducible metal.

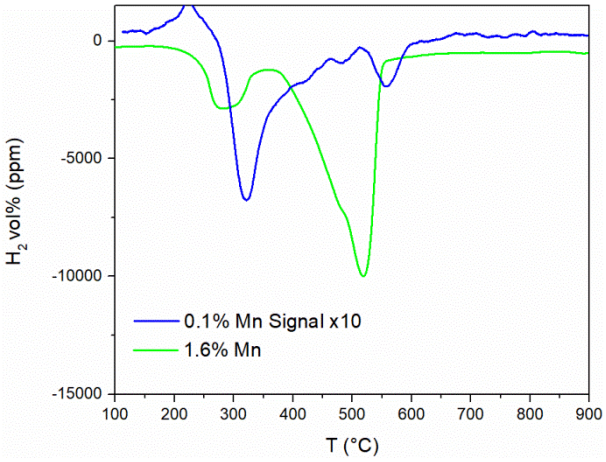

Figure 17: TPR of Mn-doped CaO activated in synthetic air at 900°C for 6 h and afterward heated in 5% H2 in Ar (12 °C/min). Blue: 0.1%, Mn 1.0 g carbonate precursor, 20 ml/min gas flow, green: 1.6%, Ni 0.5 g carbonate precursor, 20 ml/min gas flow. Integral areas are attributable to the total Ni content of the sample.

Figure 17 shows a TPR profile of a low and high Mn-doped calcium oxide catalyst. The low and high Mn-doped CaO show reducibility which, by quantification of the consumed hydrogen can be attributed to an oxidation change of -2 referred to the Mn atoms, though due to the very small amount of Mn in the reactor, the signal for the 0.1% doped sample is quite poor and leaves quite some room for errors in the integration. In the sample doped with low amounts of Mn the majority of reducible sites reduce at quite low temperatures, around 300°C and only a very minor fraction appears to bond oxygen strongly. This changes with the amount of loading, where the material binds oxygen even at higher temperatures and the major part of reduction takes place at temperatures above 500°C, which is higher compared to pure MnO_2, which reduces in all its configurations (α, β, γ) at lower temperatures, indicating an incorporation into the material rather a segregation of the manganese oxide. The two-step reduction of the manganese oxides can be explained by a consecutive reduction, though it is not observed for all manganese oxides:[139]

$$2\,MnO_2 + H_2 \rightarrow Mn_2O_3 + H_2O \quad (29)$$

$$3\,Mn_2O_3 + H_2 \rightarrow 2\,Mn_3O_4 + H_2O \quad (30)$$

$$Mn_3O_4 + H_2 \rightarrow 3\,MnO + H_2O \quad (31)$$

In the case of Ni-doped CaO (see Figure S 8, page dd) the differences in the reduction traces are not so major for the lower and higher doped sample. Both

maximum reduction peaks can be found around 600°C with an onset of about 400°C, indicating not so major changes in the nature of the metal sites compared to that of the manganese doped samples. In the case of Ni-doped CaO, only an increase of a shoulder at lower temperatures to the peak can be observed with increased metal loading. The high temperature of reduction might also be an indication of the successful incorporation of nickel into the CaO host lattice. For support, even with strong support interaction, or pristine nickel oxide, the reduction requires much less energy (<500°C) compared to the 600°C measured in this case.[142] The high reduction temperature for ionic isolated nickel species could be observed before for Ni in a magnesium oxide host lattice.[140]

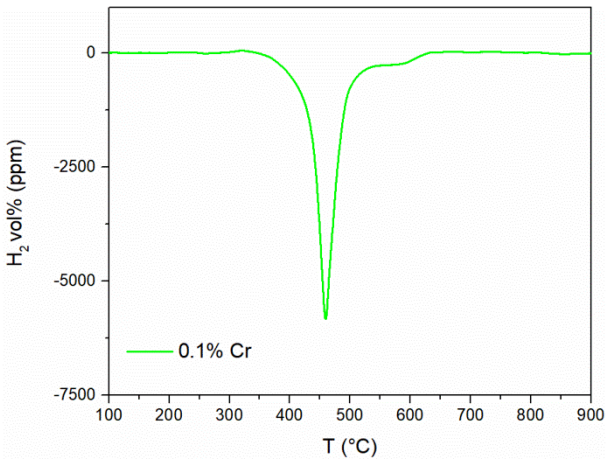

Figure 18: TPR of 0.1% Cr doped CaO activated in synthetic air at 900°C for 6 h and afterward heated in 5% H_2 in Ar (12 °C/min, 1 g carbonate precursor, 15 ml/min gas flow)

In Figure 18 the TPR for the Cr-doped CaO sample is presented. A narrow single event reduction is observed with an onset at about 350°C and a maximum at 450°C. Comparing the total integral of the hydrogen consumption with the Cr loading of the material shows complete reducibility of the transition metals assuming a Cr^{6+} to Cr^{3+} transition:

$$CrO_3 + 3H_2 \rightarrow Cr_2O_3 \quad (32)$$

Comparing the obtained profile to literature data, an agglomeration of bigger chromium particles on the surface can be excluded, supported chromium oxides reduce at significantly lower temperatures. More Isolated chromium sites, however, for example on alumina, show an increased less defined reduction temperature.[162,163] Also doping of chromium oxide with calcium is known to stabilize the high oxidation state by formation of calcium chromate, significantly increasing the reduction temperature up to 700°C.[164] In this case, despite the high Ca/Cr ratio, the TPR profile

is not comparable of that of supported $CaCrO_4$, indicating a different way of the incorporation Cr in the CaO host matrix.

4.3. Steady State Catalytic Tests

In a first screening different first-row transition metals were tested as suitable dopants for calcium oxide as OCM catalyst. The testing conditions were chosen to avoid a full conversion of oxygen over a wide parameter range of temperatures and flow rates. Due to the oxygen-rich feed (3:3:1 of CH_4:N_2:O_2), the overall C_2 selectivities are pretty low. According to the mechanism proposed by Lunsford et al. methyl radicals are released from the catalyst surface and upon the combination of two radicals, ethane is formed.[45] Therefore, a high oxygen concentration of oxygen in the gas phase promotes the collision of the methyl radicals with the oxygen di-radical resulting in deep oxidation results. Nevertheless, a full oxygen conversion would result in a loss in information and strongly decreases the comparability of the obtained results. Before varying temperature and total gas flow, the catalyst was held for 150 hours on stream to reach a stable catalytic performance (Figure 19). Alkaline earth oxides are known to sinter at high temperatures altering the surface area resulting in inconstant reaction results during the sintering.[165,166] The sintering is enhanced by the presence of water and carbon dioxide, by- and side products of the OCM reaction.[88]

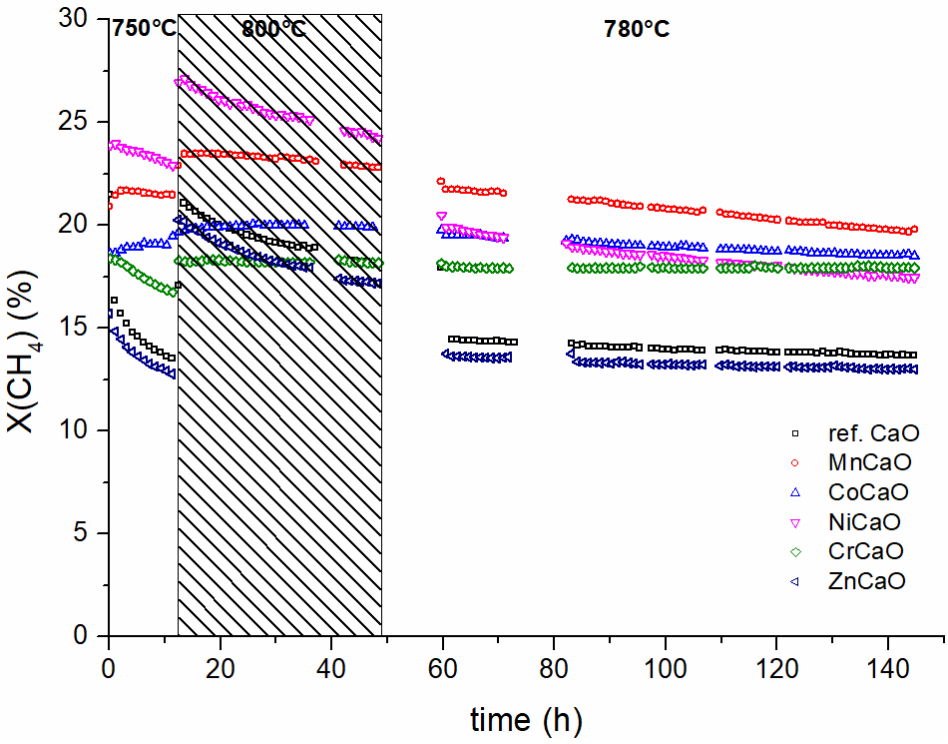

Figure 19: OCM time on stream experiments (50 mg cat, 750 mg SiC, 50 ml/min, 3:3:1 of CH_4:N_2:O_2) for metal-doped CaO (<0.1mol%).

In Table 2 the results of the catalytic testing with different doping metals are summarized. The doping of calcium oxide has a significant influence on catalytic performance, dependent on the used transition metal. Except for Zn, all other used transition metals appear to decrease the apparent activation energy significantly and enhance the reaction rates, allowing higher overall conversions to be reached. The strongest effect on the activation energy is observed in the manganese doped catalyst, reducing the activation energy from 131 kJ/mol to 108 kJ/mol, followed by Cr, Ni, and Co. In terms of selectivity, the influence of the dopants appears to be erratic. Where especially Ni, as well as Mn and Zn, increase the overall C_{2+} selectivity, Co and Cr doping lead to a decrease in selectivity with Cr almost completely preventing any C_2 products to be formed.

Table 2: Results of OCM tests using transition metal-doped CaO catalysts (50 mg cat, 750 mg SiC, 50 ml/min, 3:3:1 of CH_4:N_2:O_2). ** determination by ICP-OES.

			700°C			750°C			800°C		
Catalyst	x_i (mol%)**	E_A (kJ/mol)	X(CH_4) (%)	S(C_{2+}) (%)	S(CO_x) (%)	X(CH_4) (%)	S(C_{2+}) (%)	S(CO_x) (%)	X(CH_4) (%)	S(C_{2+}) (%)	S(CO_x) (%)
CaO	-	131	3.7	3.8	96.2	8.6	9.0	91.0	17.4	16.5	83.1
CaO:Mn	0.029	102	7.9	5.0	95.0	14.4	12.4	87.4	21.7	19.7	79.7
CaO:Co	0.074	123	7.6	2.8	97.2	14.3	6.1	93.9	19.7	9.6	90.2
CaO:Ni	0.062	117	5.7	5.5	94.5	12.1	13.6	86.2	21.5	24.4	74.7
CaO:Cr	0.067	108	6.6	0.4	99.6	14.0	0.5	99.5	18.0	0.7	99.3
CaO:Zn	0.063	127	4.1	5.8	94.2	8.8	11.4	88.6	16.7	20.2	79.3

A contact time variation employing flow variation is presented in Figure 20, showing the significantly altered catalytic behavior of the doped catalyst at similar conversions. The different offsets and slopes in the presented plots prove, that new catalytic active centers are formed at the catalyst surface.

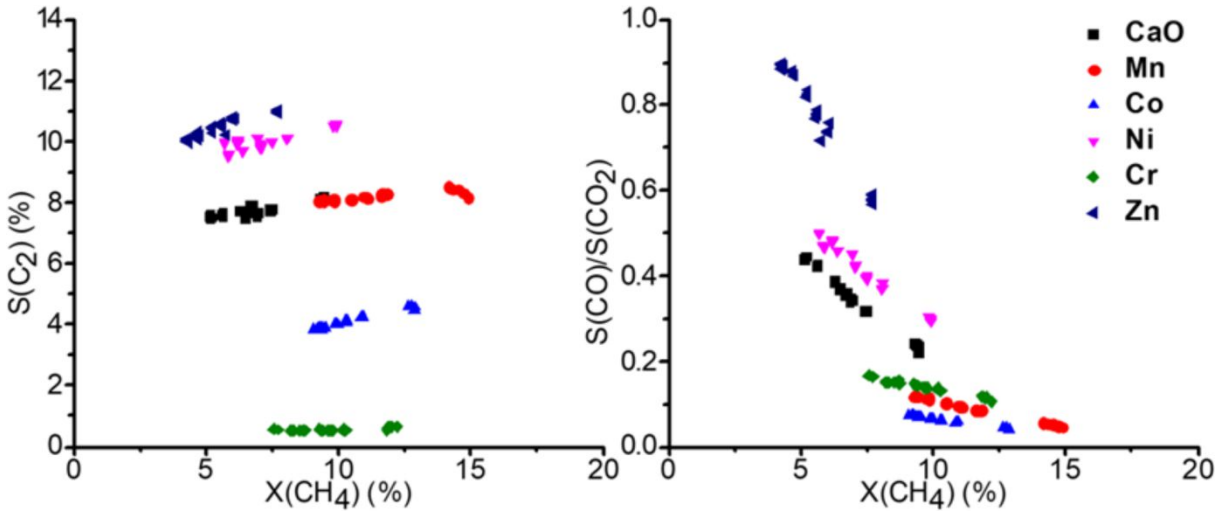

Figure 20: Contact time variation at 750°C by adjusting the total gas flow rate (from 37.5 ml/min up to 150 ml/min, 50 mg carbonate precursor, 750 mg SiC, 3:3:1 of CH_4:N_2:O_2).

The effect of flow variation on the C_{2+} selectivity is almost negligible. At most, a small increase can be observed with increasing conversion, which is mainly due to the increased formation of ethylene (Figure S 10, page ff). The small effect of the conversion on the C_2 selectivity implies the deep oxidation being a parallel reaction of methane, rather than consecutive oxidation of the C_2 products. With the increasing conversion, the CO to CO_2 ratio drops, indicating CO_2 being a consecutive product of CO. It has to be considered though, that the contact time variations were conducted varying the volume flows of the gases, rather than changing the catalyst mass. Therefore, other effects might alter the obtained results. Due to the increased volume flow, the thickness of the diffusion film around the heterogeneous catalysts will decrease and the reaction rate is expected to rise. Recently it was also suggested, that the diffusion barrier might influence the reaction selectivity.[55] Another issue that has to be considered is the total increase conversion, which, due to the exothermic nature of the reaction, will also increase the temperature in the reactor when the flow is increased and the conversion does not decrease by the same factor. Those two effects combined explain why even by changing the contact time by a factor of 4 only results in a decrease of the conversion by a factor of 2. Considering the effect of temperature, the highest temperature would be expected at the lowest conversion (4 times the flow, about half conversion resulting in double the amount of heat produced). Looking at the temperature dependence of the reaction (Figure S 9, page ee) the C_2 selectivity is expected to be increased and CO and CO_2 selectivity decreased with increasing temperature. This would mean that the measurements overestimate the C_2 selectivity at low conversion, which would indicate that the observed slight increase might, in reality, be more pronounced. The effect of the diffusion film on the selectivity suggests a jump in selectivity upon meeting certain flow conditions,[55] which was not observed, instead, steady curves are observed for all products (Figure S 9, page ee). Therefore, an alteration of the obtained results by such an effect can also be excluded. For a better understanding of the impact of the

dopant on the catalytic performance, the synthesis for the doped precursors was optimized (see above) and a series of Mn and Ni-doped catalysts were synthesized and tested in OCM with dopant concentrations between 0.01 and 1% loading. Since the results for Mn doping and Ni doping yielded similar trends, the results for the Ni doping series are reported in the appendix (Figure S 12, page hh and Figure S 13, page ii).

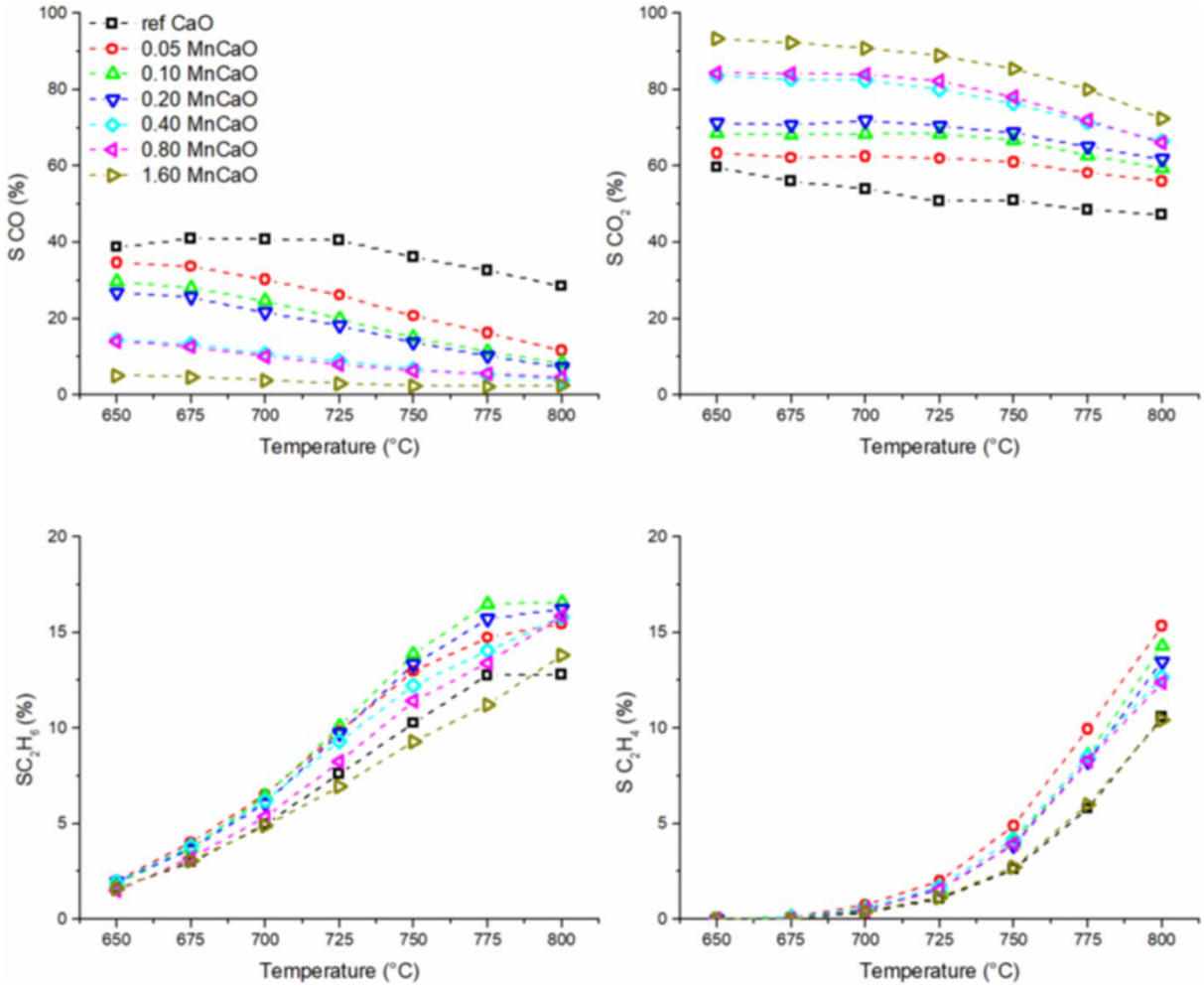

Figure 21: Temperature dependence of OCM products using Mn-doped CaO catalysts (50 mg carbonate precursor, 750 mg SiC, 50 ml/min 3:3:1 of CH_4:N_2:O_2).

Before the testing, the catalysts were kept on stream for 3 days at 780 and 800°C to accelerate the sintering of the catalyst and ensure a stable performance at lower temperatures. In Figure 21 the temperature dependence of the OCM products is presented. The selectivity trend for all the samples is following the findings made with the differently doped CaO catalysts. A clear trend for the Mn-doped samples can be found for the CO and CO_2 selectivity. While pure CaO produces significant amounts of CO, the selectivity towards CO decreases with the Mn loading and the CO_2 selectivity rises accordingly. The trend for the ethane and ethylene selectivity is not as clear as for the deep oxidation products. In terms of combined ethane and

ethylene yield (Figure 22) maximum productivity can be found for lower and medium doped catalysts, whereas higher doping (1.6 atom%) results in a reduced yield. The improvement by adding Mn as a dopant is quite significant, increasing the yield by 75% (at 800°C), though one has to add, that the overall yield is still rather low, which might be due to the reaction conditions which were chosen for better comparability and not for best performance.

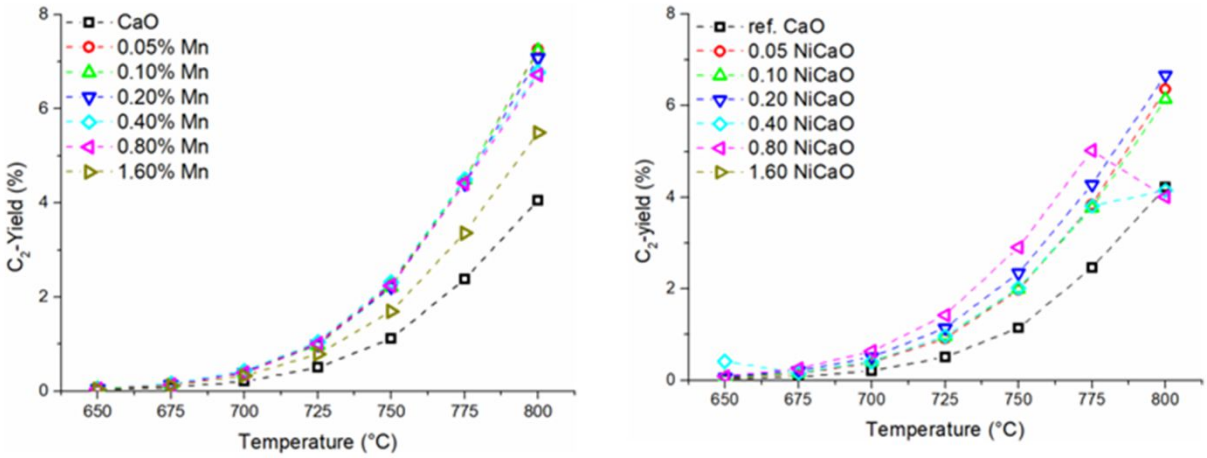

Figure 22: Temperature dependence of combined ethane and ethylene yield of manganese doped CaO catalysts (50 mg carbonate precursor, 750 mg SiC, 50 ml/min 3:3:1 of CH_4:N_2:O_2).

The results of the flow variations for the series of manganese doped catalysts can be found in Figure 23, showing the product selectivities (left column) and the yields (right column) dependent on the manganese content. The biggest difference can be seen between the undoped sample and the least doped sample. A major increase of the activity is observed by adding small amounts of Mn to the CaO sample. Upon further increasing, though always doubling the amount, the change in activity is not as major as the initial one, from 0.18% the reaction rate seems to level out. A mass transfer problem causing the overall conversion to be limited can be excluded. At the high GHSVs, meaning high Reynolds numbers, the conversion does not exceed 10%. At the lowest GHSV, the conversion can reach over 15%. In case of mass transfer issues, the conversion at lower flow rates should be more affected compared to the higher flow rates, meaning even in case of mass transfer limitations in the reactor, at high velocities the conversion of 15% should still be achievable. Another trend that can be observed is the constant increase of carbon dioxide formation and the decline of the carbon monoxide formation, which can be in the first instance be explained by the enhanced reaction rate, favoring the formation of consecutive reaction products. To avoid a misinterpretation of the data due to differences in the conversion level, which could be attributed to several reasons, e.g. bad packing of the reactor, balancing errors, or flow rate issues. The selectivities have to be compared at similar conversions to avoid a misinterpretation.

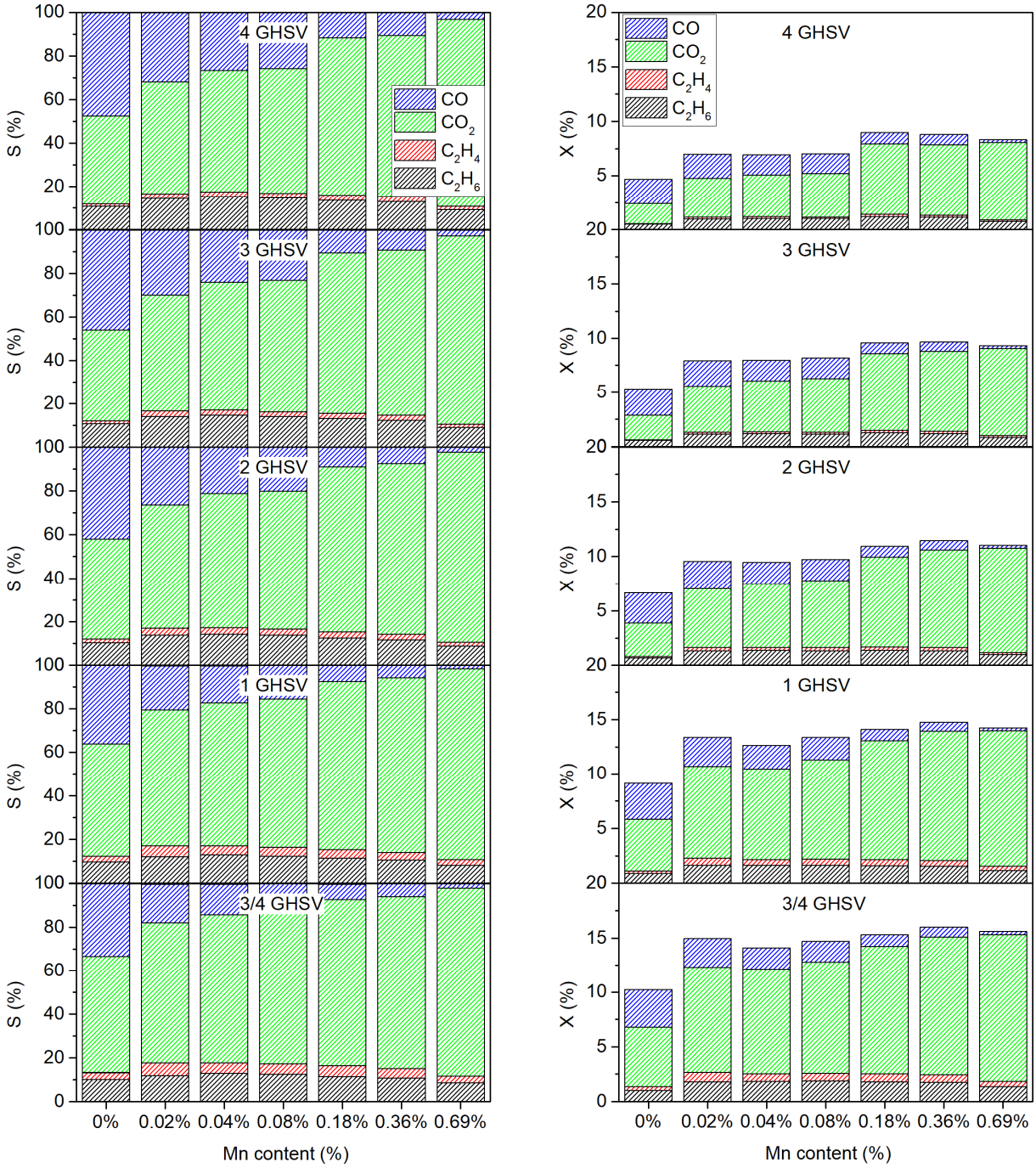

Figure 23: Contact time variation at 750°C by adjusting the total gas flow rate (from 37.5 ml/min up to 150 ml/min, 50 mg carbonate precursor, 750 mg SiC, 3:3:1 of CH_4:N_2:O_2). Left: normalized product distribution, right; product yields.

In Figure 24 the doped catalysts are compared at similar oxygen and methane conversions at 750 °C. The catalytic data was again obtained by variation of the volume flow and has to be interpreted under the same restrictions as mentioned before for the metal series data. To achieve similar conversions the contact time between different data points might differ by a factor of 5 (CaO vs. 0.69% doped MnCaO). Again, it becomes quite evident that adding Mn promotes the deep

oxidation to CO_2 and strongly reduces the CO selectivity, almost reducing the selectivity to 0 at the highest investigated doping concentration. For the ethane and ethylene selectivity, a maximum can be found for lower doping concentrations (0.05-0.1 atom%), while with higher doping concentrations, the selectivity declines again. Interestingly again, the trend for the deep oxidation products is completely different compared to the trend for ethane and ethylene.

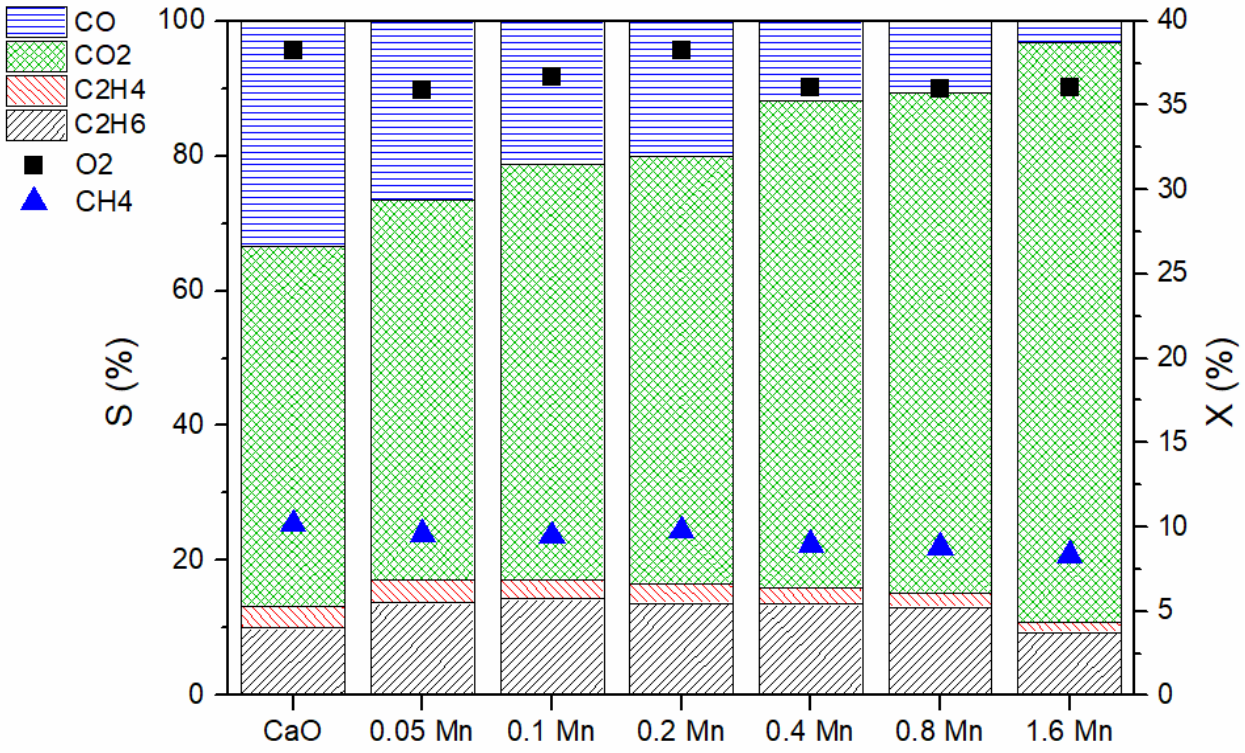

Figure 24: Comparison of catalytic performance of Mn-doped CaO catalysts at 750°C at similar O_2 conversions (50 mg carbonate precursor, 750 mg SiC, GHSV can be different by a factor of 5).

Figure 25 shows the apparent activation energies for oxygen and methane consumption rate are plotted vs. the metal loading concentration obtained by ICP-OES analysis (Arrhenius plots can be viewed in Figure S 14). The shape of the trends for both activation energies are pretty similar, but appear to have an offset of about 15 kJ/mol, which makes sense, looking at the selectivity trends (Figure 21). With increasing temperature, the selectivity towards ethane and ethylene increases, where the selectivity to CO and CO_2 decreases. Due to deep oxidation consuming more oxygen and less methane compared to coupling and dehydrogenation (equations (33)-(36)), the slopes for the individual consumption rates are expected to be different and therefore results in an offset of the activation energy.

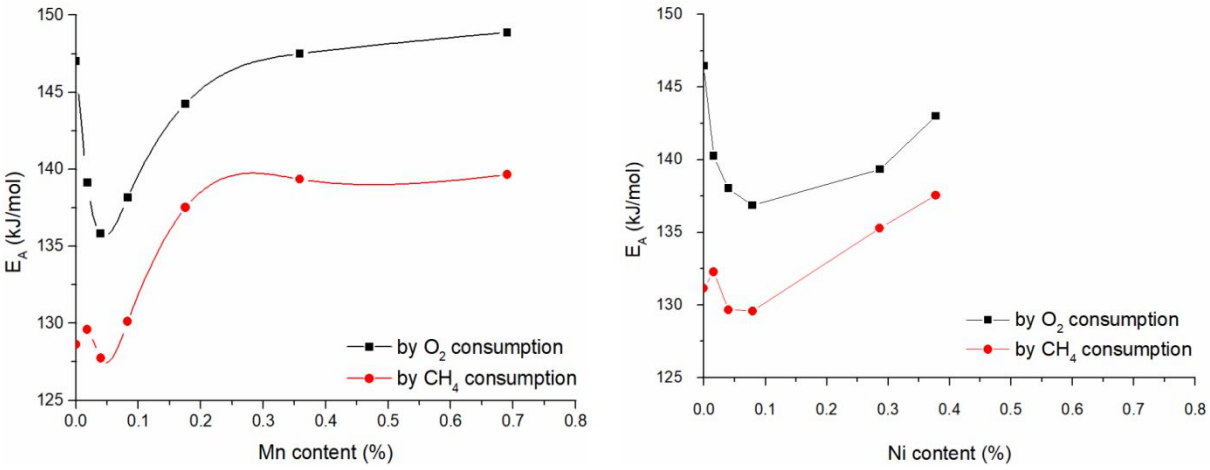

Figure 25: Calculated apparent activation energy of methane and oxygen consumption vs metal content of doped CaO catalysts (50 mg carbonate precursor, 750 mg SiC, 50 ml/min 3:3:1 of CH_4:N_2:O_2, in the temperature range between 650 °C and 800 °C), lines to guide the eye.

$$CH_4 + \frac{3}{2}O_2 \rightarrow CO + 2H_2O \quad (33)$$

$$CH_4 + 2O_2 \rightarrow CO_2 + 2H_2O \quad (34)$$

$$2CH_4 + \frac{1}{2}O_2 \rightarrow C_2H_6 + H_2O \quad (35)$$

$$2CH_4 + O_2 \rightarrow C_2H_4 + 2H_2O \quad (36)$$

It also has to be noted, that the activation energy is higher compared to what was found before during metal screening (Table 2, page 50). This can be explained by the altered synthesis method. Allowing a longer aging time of the carbonates (24h vs. 1h) resulted in very low surface area precursors (Table 1). It was found before, that the surface structure of alkaline earth oxides can have a strong impact on the catalytic performance.[67] Nevertheless, even with increased activation energy, the trend for the apparent activation energies is quite interesting. With small amounts of dopant, the activation barrier can be lowered to a certain extent, exceeding a concentration of 0.1 atom%, the apparent activation energy for the OCM reaction rises again and levels out at similar activation energy as for pure CaO (in case of oxygen consumption rate). It also has to be noted, that the offset between oxygen and methane activation barrier on pure CaO is higher compared to that of doped CaO.

4.4. Temperature-Programmed Catalytic Tests

The Temperature-programmed oxidative coupling of methane on CaO is presented in Figure 26 (left). With the initial activity observed at roughly 600°C, the onset temperature is slightly higher compared to the findings for oxygen scrambling activity. Upon heating, the conversion rises as expected and an increasing product formation

is observed. The increased CO_2 release between 700°C and 750°C hardly affects the formation of the other products (such as CO, C_2H_6, or C_2H_4) or the conversion of methane, meaning CO_2 formed at lower temperatures and fixed in form of carbonates on the catalyst surface is being released at the higher temperatures to a large extent by decomposition of carbonates, but it does not (or hardly) affect the activity of the catalyst by site blocking. Increasing the temperature above 750°C, the formation of carbon dioxide and carbon oxide increases less in favor of the formation of C_2 products, mainly C_2H_4. An explanation for this behavior can be the decreased abundance of oxygen in the gas phase due to the high conversion, reducing the over-oxidation of the formed C_2-hydrocarbons.

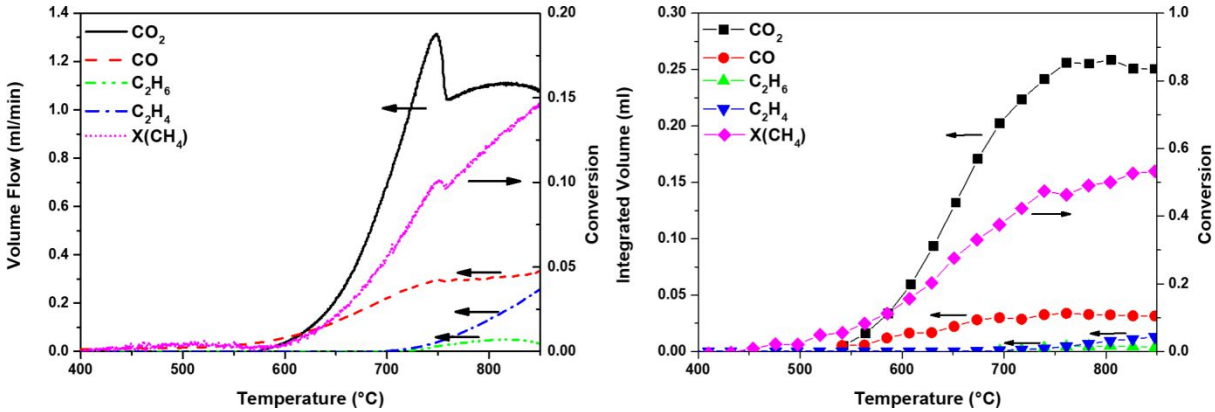

Figure 26: Temperature programmed reaction over 55 mg CaO (24254) in 1400 mg SiC with 30 ml/min gas feed and a heating rate of 5 °C/min under continuous operation (left) with 6:3:1, He:CH_4:O_2 and pulsed operation (right) with 9:1, He:O_2 and 1 ml CH_4 pulse every 10 minutes.

Experimenting with a pulsed mode by introducing methane to a feed consisting of oxygen and helium, major differences can be found in the reactivity (Figure 26, right). One difference is the reduced onset temperature of the reaction, slightly above 500°C. Another difference is the omission of the CO_2 release compared to the continuous flow experiment. Due to the higher ratio of oxygen to methane, higher overall conversions were obtained. The reduced C_2-product formation can also be explained by the higher abundance of oxygen in the gas phase. Assuming the widely accepted mechanism involving methyl radicals being released to the gas phase and combining to ethane,[45] the collision of the radicals with oxygen becomes more likely in an oxygen-rich atmosphere, favoring the unselective gas-phase reactions leading to CO and CO_2.[59]

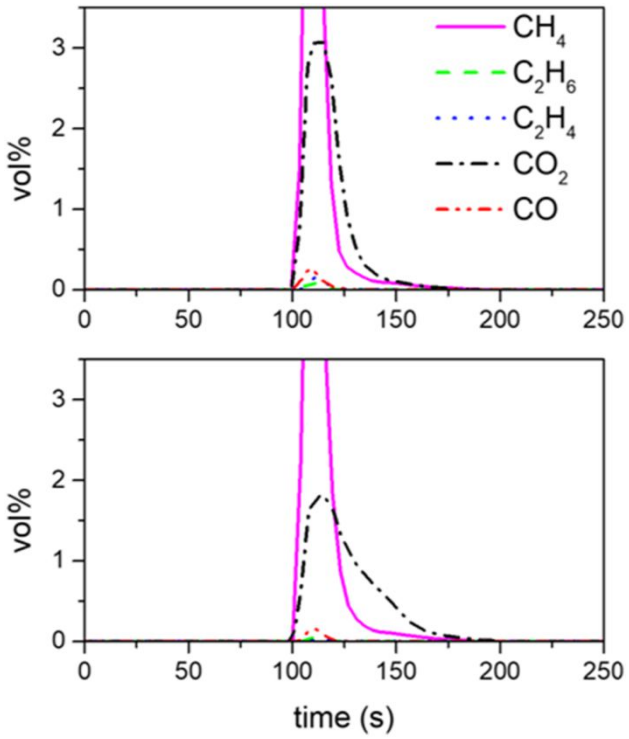

Figure 27: Time-resolved pulses of 1 ml methane added to 30 ml/min 9:1, He:O_2, at 700°C (bottom) and 760°C (top) over 55 mg CaO (24254) in 1400 mg SiC.

Having a closer look at the time-resolved pulses (Figure 27), the carbon dioxide release is strongly delayed compared to the other gases, indicated by a pronounced tailing of the corresponding peak. At low temperatures (700°C), the tailing of the peak is quite significant, proving that under steady state conditions an accumulation of CO_2 on the catalyst has to be assumed. But even at temperatures above 750°C, the release of CO_2 is slightly delayed compared to the methane peak, indicating a strong CO_2-surface interaction and a possible formation of surface carbonate species.

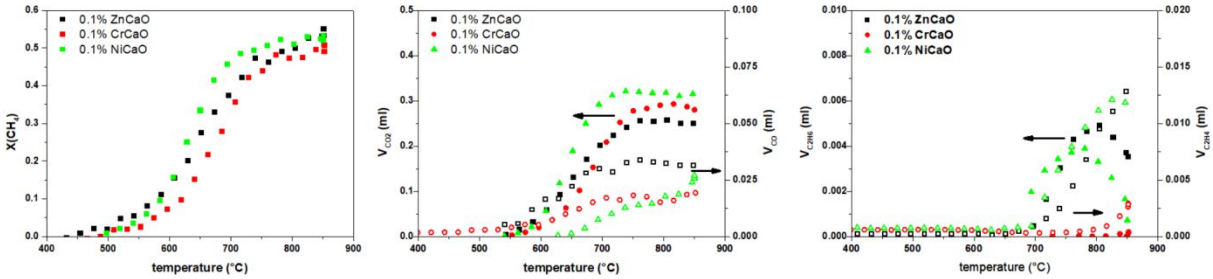

Figure 28: Temperature programmed reaction over transition metal-doped 55 mg CaO (24254) in 1400 mg SiC with 30 ml/min gas feed and a heating rate of 5 °C/min under pulsed operation with 9:1, He:O_2 and 1 ml CH_4 pulse every 10 minutes, left: methane conversion, middle: CO_2 (filled, left axis) and CO (hollow, right axis) production, right C_2H_6 (filled, left axis) and C_2H_4 (hollow, right axis).

Comparing the doped CaO catalyst with the pulsed temperature-programmed method (Figure 28) slight differences can be observed. The onset of the reaction is hardly changed with the doping also the activity can be found in a similar range, indicating the active sites to be chemically quite similar and activated/deactivated by the same mechanisms. The selectivities, however, are quite different. The overall trends observed are similar towards those of CaO (Figure 26). The selectivity towards hydrocarbons is rather low, due to the before discussed high oxygen concentration, and the formation of the consecutive products CO_2 and C_2H_4 are significantly enhanced. The Ni doped sample shows a slightly enhanced activity compared to the Zn doped one and following that a slightly enhanced selectivity towards the consecutive products as well, nevertheless, they behave very similarly. The only sample with a considerable selectivity is the Cr-doped one, showing almost no selectivity towards hydrocarbons, only at temperatures exceeding 800°C a small fraction of ethylene can be observed.

4.5. In situ Analysis

4.5.1. In Situ Thermogravimetric Analysis on CaO

To investigate the influences of adsorbates, carbonate, or hydroxide formation, in-situ thermogravimetric measurements were conducted. Using a very sensitive balance and a high amount of catalyst, small changes in the mass can be observed enabling the quantification of adsorbed surface species. [134] In Figure 29 the MS traces of the OCM reaction products and educts are shown in a thermogravimetric experiment in the temperature range between 700°C and 800°C. For the blank experiment, only the empty ceramic crucible was used in the thermobalance, for the test with catalyst, 500 mg of CaO was loaded in the crucible and activated in argon at 800°C for one hour, before switching to OCM conditions (3:3:1 of Ar:CH_4:O_2).

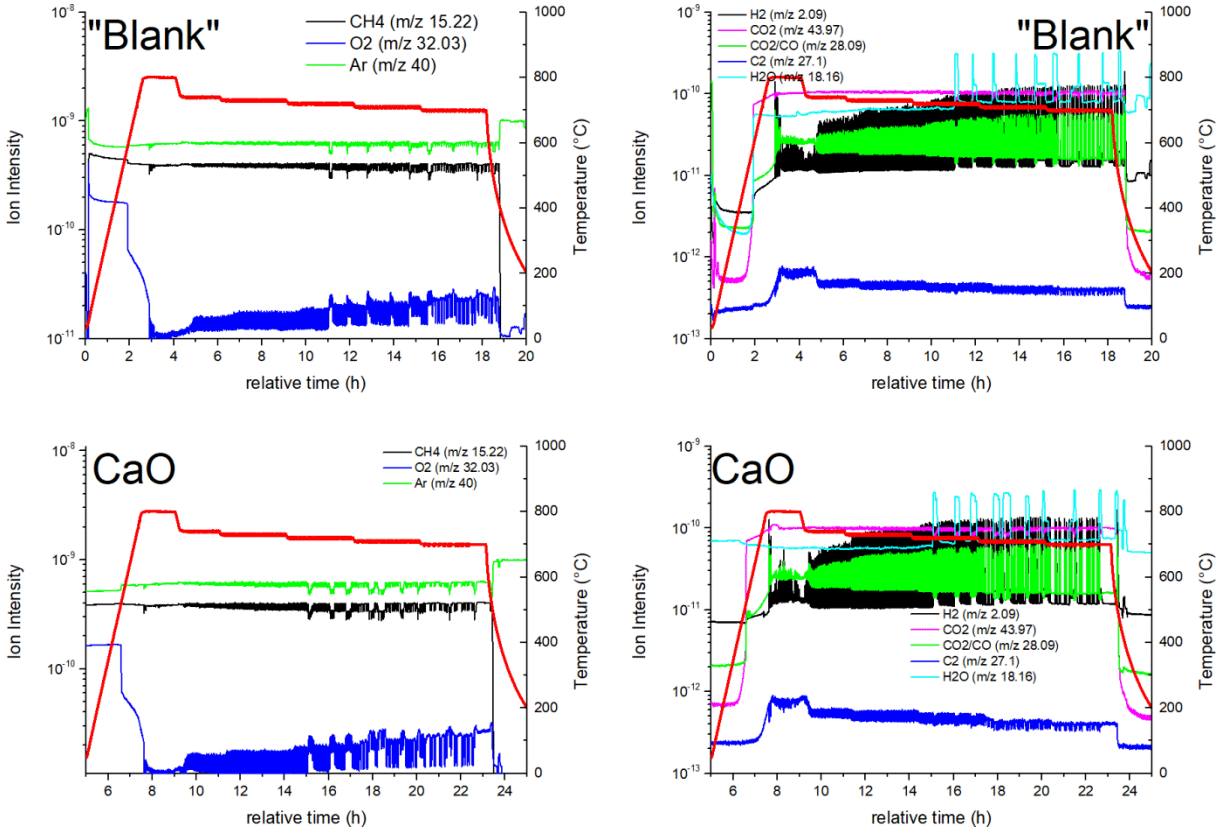

Figure 29: Educt (left) and product (right) MS traces during thermogravimetric experiments at temperatures between 700 and 800 °C without (top) and with catalyst (bottom, 500 mg $CaCO_3$ (24254) activated in the balance at 900°C in OCM feed, 500 ml/min 3:3:1 of Ar:CH_4:O_2).

Comparing these two results, no major differences can be observed. Apparently, the setup itself is active towards methane oxidation and dominates the overall activity of the reactor. Whether it is filled with a catalyst or not does not make any difference. In all experiments above 700°C, the oxygen conversion reached almost 100% and the selectivity towards C_2-products was negligible. One can note, that the ripples are caused by condensed water forming droplets, blocking the line towards the

spectrometer. Another observation that can be made is the oscillating behavior of the hydrogen, oxygen, and carbon monoxide signal. This might be an indication for hotspots forming on metal surfaces inside the balance, such as the suspension or the thermocouples. Since the catalyst can therefore not be investigated under "real" reaction conditions, these experiments particularly provide information regarding the interaction of by- and side-products of the OCM reaction with the catalyst material, such as H_2O, CO_2, and CO.

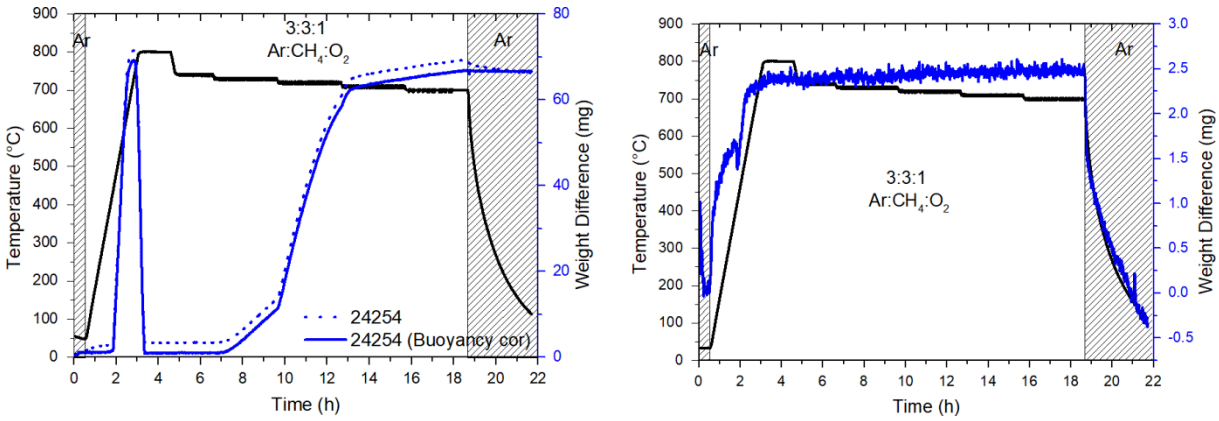

Figure 30: Absolute mass change of 500 mg $CaCO_3$ (24254) activated in the balance at 900°C in Ar and afterward exposed to OCM feed (500 ml/min 3:3:1 of Ar:CH_4:O_2) at temperatures between 800°C and 700°C (left) and blank experiment (right).

The mass changes of CaO at temperatures between 700°C and 800°C in the presence of methane combustion gases are presented in Figure 30. After activation in argon, cooling back to room temperature and taring the balance, the catalyst is heated up in the OCM feed and the mass change recorded. The mass of the catalyst increases abruptly during initial heating when the onset temperature of the OCM reaction is reached but decreases again during holding at a reaction temperature of 800°C. Afterward, the reaction temperature was stepwise decreased. Reducing the temperature from 750°C to 740°C, an increase in the catalyst mass can be observed, which is enhanced by further reducing the temperature to 730°C. The buoyancy was corrected using the blank measurement (Figure 30, right). Due to the heat in the measurement chamber and the change of the gas phase, the density of the gas mixture changes, affecting the measured weight. Changing the temperature from 800°C to 750°C, no significant change in mass was observed, which could hint at the presence of surface carbonates or hydroxides. At best, a mass gain of 25 µg can be observed, which is very likely caused by an error in the buoyancy correction. Comparing this to the catalyst surface (determined to be 17.3 m²/g), 25 µg corresponds to roughly 3% of a monolayer covered with carbon dioxide. Extensive surface carbonate formation under the generation of chains, which are known to be formed on CaO at lower temperatures,[167] is, therefore, unlikely to occur in the temperature range 800°C - 750°C.

In Figure 31 the experiment is repeated, this time holding the temperature at 750°C for 10 h. At this temperature, over the whole course of the reaction, no changes in mass are observed. While in the previous experiment the mass gradually increased due to the absorption of product gases, the catalyst remains stable.

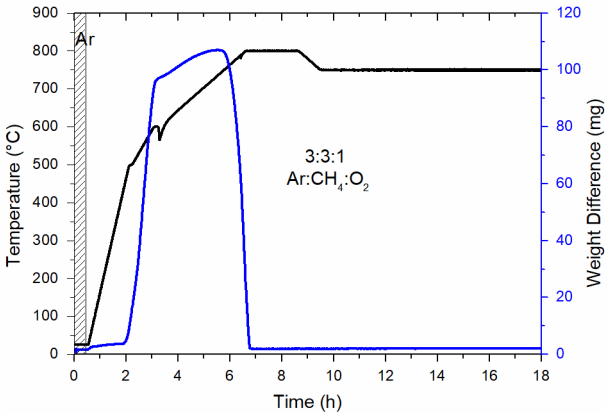

Figure 31: Absolute mass change of 500 mg $CaCO_3$ (24254) activated in the balance at 900°C in Ar, cooled down and afterward heated in OCM feed (500 ml/min 3:3:1 of Ar:CH_4:O_2) to 800°C and 750°C.

Having now a closer look at the processes at 740 °C (Figure 32, left), after activating $CaCO_3$ at 800°C in argon yielding CaO, the temperature was set to 740°C and the feed composition was changed to an OCM feed (3:3:1 of CH_4:Ar:O_2). The mass of the material increases quite rapidly for the first 6 hours. After that, the rate of mass increase slows down significantly reaching a final mass after 32 h of 90% of the initial $CaCO_3$ mass. The abrupt change in the CO_2 absorption rate can be attributed to mass transport problems. In the initial stage, the surface is free of adsorbates and can be easily saturated. Upon reaction with calcium oxide, a carbonate surface layer is formed. For the reaction with deeper parts of the catalyst, solid diffusion will limit the rate of further absorption. XRD analysis reveals the formation of a calcite phase next to the CaO phase, no hydroxide species can be detected (Figure 32, right). Whereas at room temperature the direct formation of calcite from calcium oxide is known to proceed very slowly and is usually formed successively from calcium hydroxide:

$$CaO + CO_2 \rightarrow CaCO_3 \text{ (very slow)} \quad (37)$$

$$CaO + H_2O \rightarrow Ca(OH)_2 \text{ (fast)} \quad (38)$$

$$Ca(OH)_2 + CO_2 \rightarrow CaCO_3 + H_2O \text{ (slow)} \quad (39)$$

direct conversion from CaO to $CaCO_3$ is known to readily take place at temperatures above 600°C and is even accelerated by the presence of water, which can be exploited in carbon capturing units (CCU).[168]

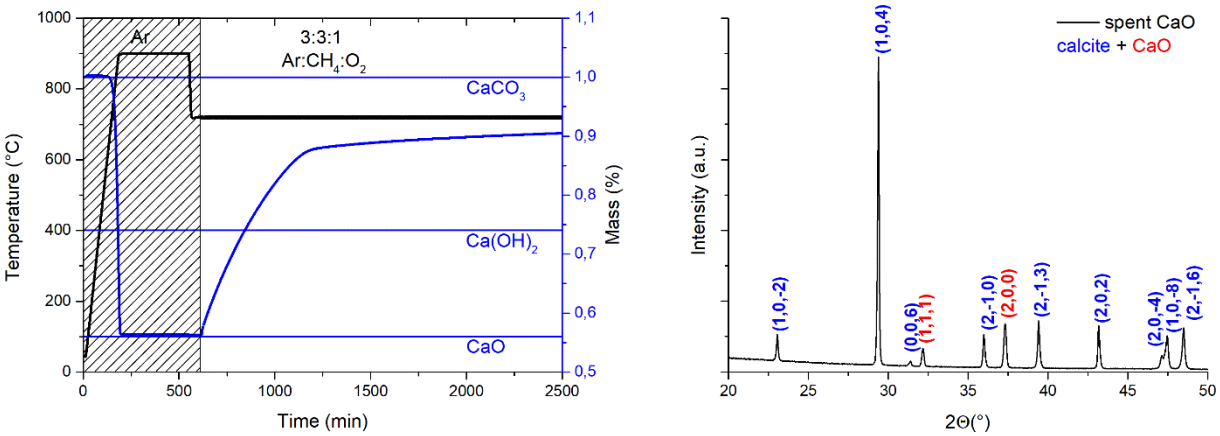

Figure 32: Relative mass change of 500 mg $CaCO_3$ (24254) activated in the balance at 900°C in Ar and afterward exposed to OCM feed (500 ml/min 3:3:1 of $Ar:CH_4:O_2$) at 740°C (left). Horizontal blue lines represent corresponding masses of equal amounts of CaO, $Ca(OH)_2$ and $CaCO_3$, XRD pattern of the catalyst after the experiment (right).

Since real OCM conditions could not be applied, the transferability of those results towards the reaction is limited. Nevertheless, due to the full conversion and bad selectivity, as well as the slight overpressure in the reactor, the CO_2 and water partial pressures in these experiments are likely to exceed the actual partial pressures in OCM experiments. Finding no indication for bulk formation of hydroxides and carbonates at temperatures above 750°C, the formation of those during the reaction can also be excluded. At high conversions, bad selectivities, and temperatures below 750°C though, the formation of especially carbonates cannot be neglected.

4.5.2. Raman Spectroscopy

For the in-situ Raman experiments, calcium carbonate materials were activated in the in-situ cell at 900°C in 10 ml/min synthetic air. After reaching the reaction temperature, the gas feed was changed from synthetic air to an OCM feed (3:3:1 of $Ar:CH_4:O_2$) and Raman spectra were recorded. The laser source of 532 nm was chosen to be least likely to produce beam damage and its applicability at high temperatures. Due to Planck's law, the sample irradiates visible light, rendering laser sources with higher wavelength useless. UV lasers are not favorable due to the fluorescence of the sample. A small feature can be observed around 600 cm^{-1}, which was identified as a spectrometer artifact.

In Figure 33 (top left) the Raman spectra of CaO at 800°C is shown in air and OCM atmosphere. Very small signals around 600 and 300 cm^{-1} can be observed, which

can be attributed to residual hydroxide species.[117] Next to that, nothing can be observed. Due to its isotropic crystal lattice, CaO itself shows often no Raman spectrum. Also, no indication of surface oxygen species consumed by the presence of methane can be observed. In Raman studies on MgO-supported BaO materials, a peroxide species was found to be in equilibrium with a barium carbonate phase covering the magnesium oxide surface,[82] which is in agreement with the well-known formation of stable peroxides for BaO and SrO in contrast to CaO and MgO.[169]

Reducing the temperature below 750°C, calcite formation can be observed (peaks at 136, 250, 708, 1078, and 1738 cm^{-1}), which is reversible upon heating to higher temperatures (Figure 33, top right). Reheating the sample to 750°C, the calcite phase can be decomposed subsequently in a time frame of more than 30 mins (Figure 33, bottom left). After cooling the sample back to room temperature in OCM feed, the observed peaks shift slightly and get more narrow, which can be explained by thermal lattice expansion (Figure 33, bottom right).[170,171]

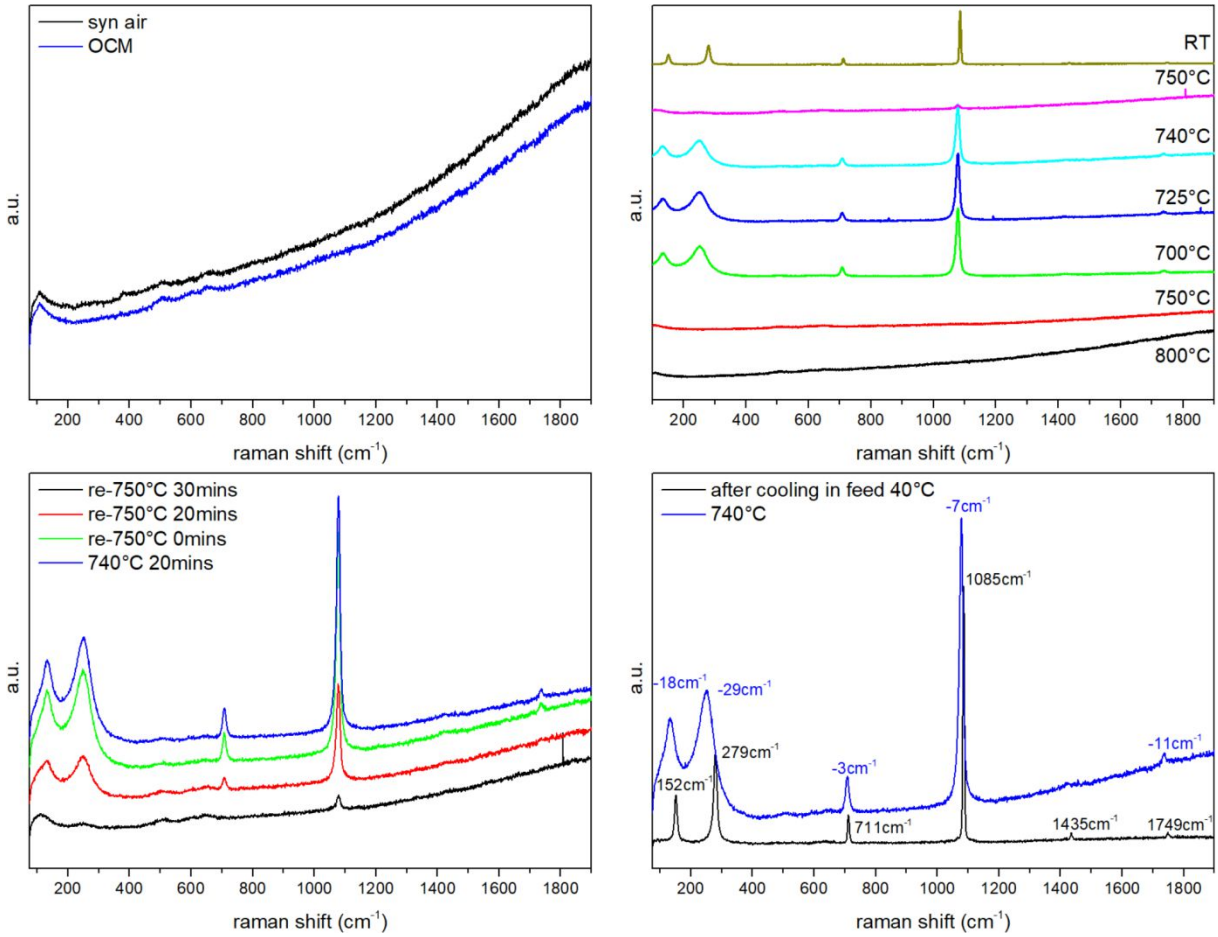

Figure 33: Raman spectra of CaO catalyst (25763) obtained with a 532 nm laser under OCM feed (10 ml/min, 3:3:1, He:CH_4:O_2) at temperatures from 700°C to 800°C. Top left: activated CaO at 800°C switching from synthetic air to OCM feed, top right: CaO in OCM feed changing, temperature between 800 and RT starting at the bottom (black) to the top, bottom left: time series of CaO in OCM feed heating from 740°C to 750°C, bottom right: comparison of spectra obtained at 40°C and 740°C.

In Figure 34 the ex-situ Raman spectra of CaO and low Mn-doped CaO activated at 900°C under vacuum and sealed in a quartz cuvette are compared. Next to the identified spectrometer artifact at 600cm^{-1}, no particular additional signals are observed in the case of the CaO sample. Using the UV laser (266 nm), a distinct signal at 390 cm^{-1} can be seen, which can again be attributed to residual hydroxide species, but no signals indicating a separate manganese oxide phase can be observed. At higher Mn concentrations additional Raman signals are observed, which can be neither attributed to hydroxide, nor carbonate species (185 cm^{-1}, 337 cm^{-1}, 481 cm^{-1}, 577 cm^{-1}, Figure S 15, page jj), but also not to any Mn_xO_y species or $CaMnO_3$.[172–175]

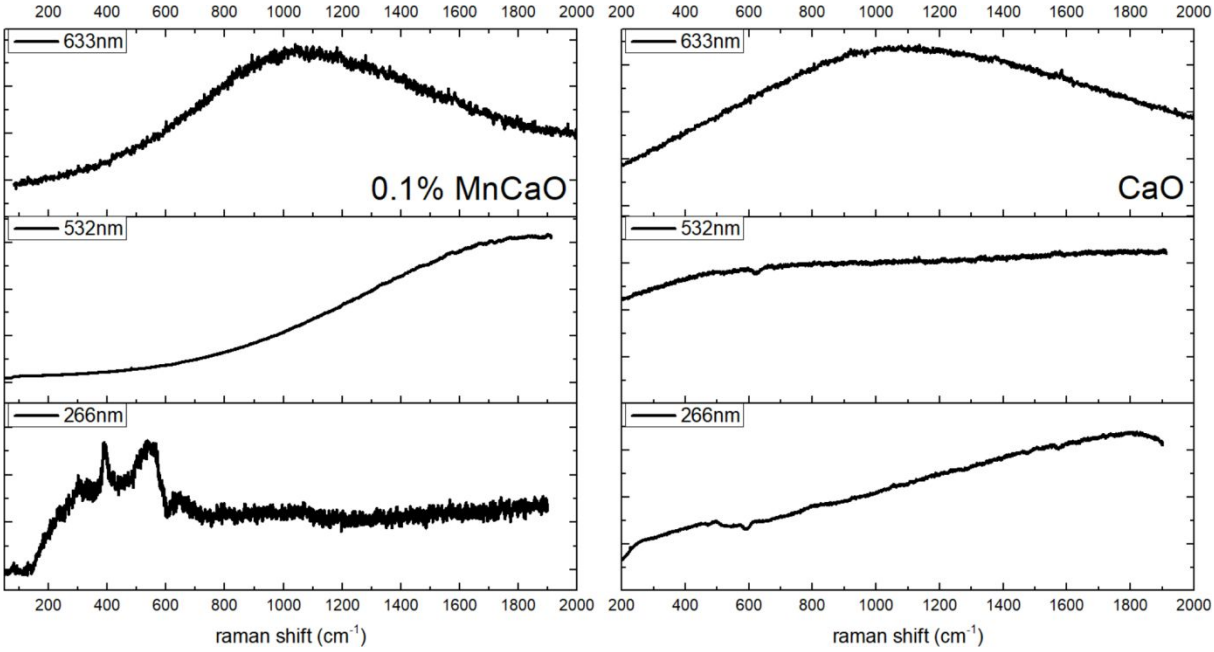

Figure 34: Raman spectra using different laser excitation sources (633 nm, 532 nm, and 266 nm) of vacuum-sealed CaO samples derived from carbonate precursors at 900°C in vacuum. The feature at 600 cm^{-1} can be attributed to a spectrometer artifact.

Because the high temperatures during the in-situ experiments might result in the desorption of oxygen species on the catalyst surface, Raman spectra were also recorded at room temperature for a CaO sample sealed with 10 mbar oxygen in a quartz cuvette (Figure 35). Also, in this case, no indication for an active oxygen species on the surface can be observed.

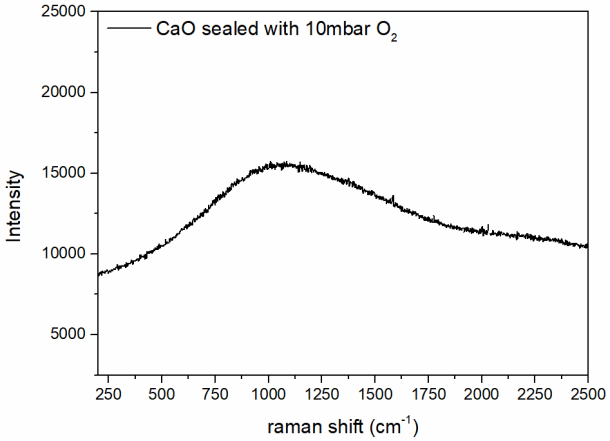

Figure 35: Raman spectra of sealed CaO sample in 10 mbar O_2 atmosphere using a 633 nm laser source. The sample was activated under vacuum at 900 °C for 6h and exposed to 10 mbar oxygen before sealing the sample in the cuvette.

4.5.3. In Situ Infra-Red Spectroscopy

The IR spectra were recorded in transmission mode. For this purpose, the catalyst was pressed to a very thin wafer and placed in a gold sample holder attached to a quartz guiding staff. Due to the requirements for the sample and measuring mode, that reactor volume of the in situ cell was quite large. Especially the spectroscopic glasses and its seals had to be protected from the heat, adding a lot of dead volume to the reactor due to their distance towards the sample, also limiting the maximum temperature of this apparatus to 780°C. All these factors contribute to a rather large residence time and a bad residence time distribution of the setup. With the OCM reaction taking place at a rather high temperature, gas-phase reactions, as well as interactions with the thermocouple and the sample holder can therefore hardly be neglected. Since the beam path is quite long compared to that through the sample, gas-phase contributions to the IR spectra are quite significant.

Figure 36 (left) shows the gas phase IR spectra of the reaction feed (3:3:1 of $Ar:CH_4:O_2$) at 630°C to 780°C without a catalyst. As expected, due to the above-mentioned reasons, a significant gas phase spectra can be recorded consisting mainly of the hydrocarbon vibrations, mainly from CH_4, and the CO_2 vibration, indicating also a very high conversion even in the absence of the catalyst (also confirmed by the µ-GC). interestingly, even though present in the gas phase, signals to correspond to the CO vibrations (2200-2100 cm^{-1}) cannot be found.

In Figure 36 (right) the IR spectrum of $CaCO_3$ activated in helium at 780°C is presented. Contrary to previous experiments (Raman, EPR, XRD, TG) signals between 800-1100 cm^{-1} can be observed, which can be attributed to the out-of-plane deformation and symmetric stretching mode of carbonates, though it is not clear which carbonate species is formed.[176,177] A reason for this might be the low activation temperature (in the other experiments at least 800°C). At this temperature deeply embedded bulk carbonates are not easily being removed. Another reason might be the gas atmosphere. Judging from the signals in the IR spectrum, still, a lot of

contaminants can be observed. Due to the discussed dead volumes in the setup, complete flushing of the setup is hardly achieved. Also due to the high temperatures, the seals for the glasses were damaged, causing leaking of hydrocarbons out as well as air into the measuring chamber.

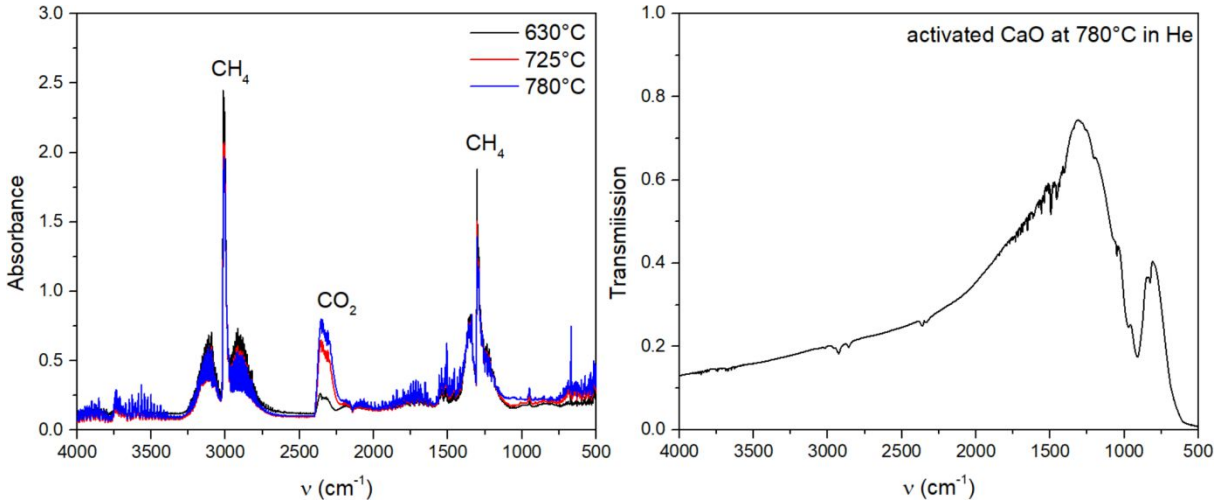

Figure 36: Gas-phase IR spectra at reaction temperatures and OCM reaction atmosphere (3:3:1 of CH_4:Ar:O_2) (left, absorbance) and "activated" CaO (from $CaCO_3$ waver) in helium flow on the right (transmission).

After activating the catalyst in the cell, OCM feed gas was introduced. In Figure 37, the IR spectra of the catalyst are presented after exposure to the reaction gas. For a better representation, the spectrum of activated CaO (Figure 36, right) was used as a background signal. Upon exposure, the rise of a feature between 800 and 1100 cm-1 can be observed, which can be attributed again to carbonates.[176] Other than that, only a slight increase in the quantity of carbon dioxide in the atmosphere can be observed.

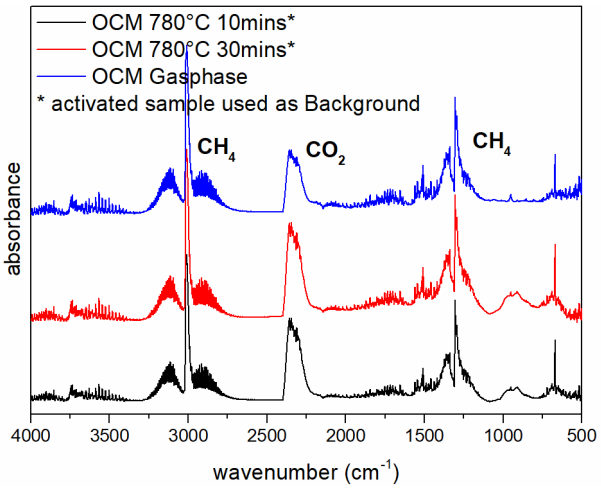

Figure 37: Gas-phase transmission FTIR spectra at reaction temperatures and OCM reaction atmosphere (3:3:1 of CH_4:Ar:O_2) without catalyst (blue) and with CaO after 10 min of exposure (black) and 30 min of exposure (red).

No species, which could be attributed to oxygen or surface hydroxides could be identified. Comparing the reaction products during the catalyzed and "blank" reaction (Figure 38), the conversion is only slightly enhanced by the presence of the catalyst. Especially at high temperatures, the conversion, as well as product selectivities the catalyst only has a minor effect on the outcome of the reaction. But this is, due to the small exposed catalyst surface (in total 4 cm²) in comparison to the big reactor, not unexpected. Since the activity of the reactor itself is already high, and the gas flow is not forced over the catalyst surface, only minor changes are expected. The IR spectra were also recorded at lower temperatures but give only negligible additional information. At best at lower temperatures, next to the carbonate groups at 800-1100 cm^{-1}, the asymmetric stretching mode of carbonates at 1400-1500 cm^{-1} can be observed as well (Figure S 16). But due to the high-temperature difference, a good comparison is hardly possible. Due to Planck's law, at high temperatures a significant amount of radiation is emitted by the sample itself. Using a common background signal is therefore impossible, rendering the observation of small changes impossible.

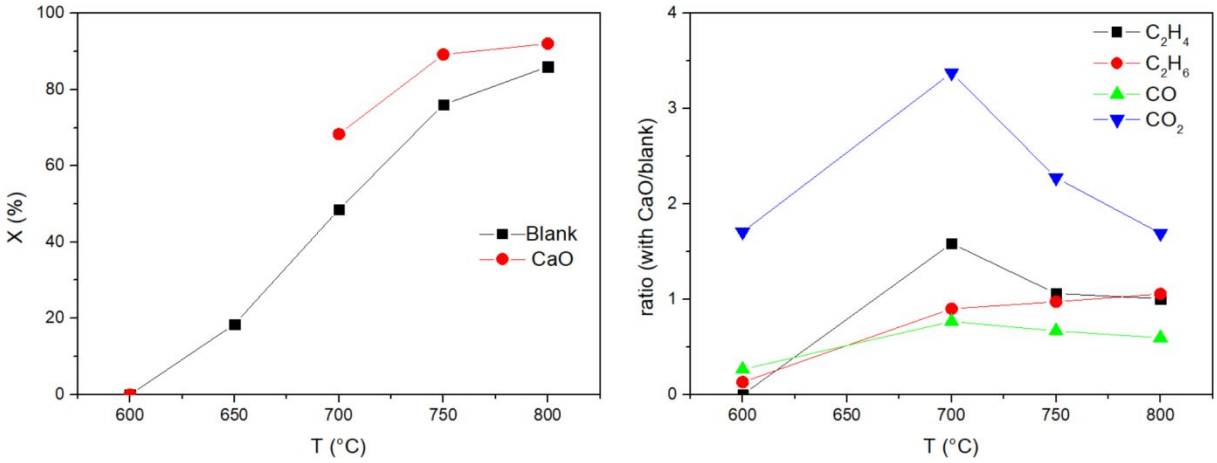

Figure 38: Conversion of oxygen (left) during in situ IR experiments and the ratio of products with/without catalyst during in situ IR experiments (right). The carbonate was pressed to a 1x2 cm wafer and activated in the cell at 780 °C in air, for OCM measurements, the feed was switched to a ratio 3:3:1 of CH_4:Ar:O_2.

4.6. Oxygen Activation

To understand the activation of oxygen over oxide materials, isotopic exchange experiments have been proven to be powerful tools. Several different techniques can be applied, such as SSITKA (steady state isotope transient kinetic analysis, Figure 39A), temperature-programmed isotopic exchange techniques (Figure 39B, and C) as well as TAP (temporal analysis of products, Figure 39D) experiments.

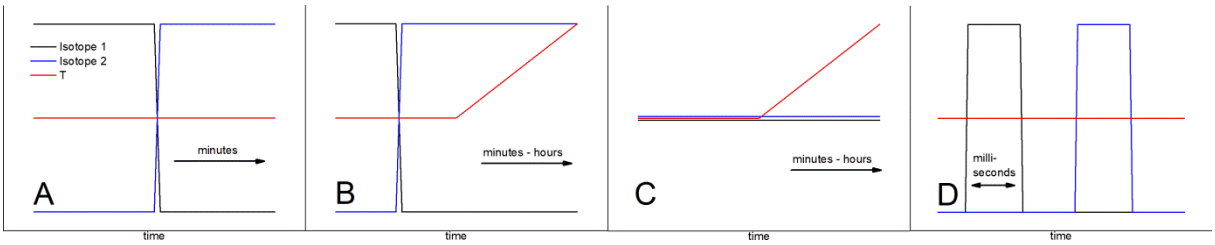

Figure 39: Scheme of different isotope exchange experiments: SSITKA A, temperature-programmed isotopic exchange B and scrambling C and TAP D.

In Figure 39 the procedures of these experiments are depicted. In general, all experiments start the same. First, the oxide will be activated, usually in a 16-oxygen containing atmosphere, resulting in ^{16}O saturated oxide material at the start. In a second step, an oxygen isotope containing gas will be fed to the oxide material at a set temperature (A and D) or during a temperature ramp (B and C) and the isotope distribution in the outlet is analyzed using a mass spectrometer. The isotope experiments are usually conducted with 18-oxygen containing gases which are considerably cheaper than 17-oxygen, though sometimes the use of 17-oxygen can be useful too. Due to its nuclear spin of 5/2 ^{17}O facilitates the use of NMR and depending on the material also EPR techniques for further investigations.

Several steps of oxygen activation have to be considered in these experiments, which can run in significantly different time scales:

1. The adsorption of oxygen,
2. The surface activation/dissociation of oxygen,
3. The exchange of surface oxygen with the bulk,
4. The bulk diffusion of lattice oxygen,

with the 4th step being significantly slower compared to the 1st and 2nd. Depending on the objective of the investigation suitable experimental conditions and setups have to be chosen, with none of the above-mentioned experiments yielding reliable information for all those steps. Also, the nature of the material has to be considered when choosing a suitable technique.

Figure 39A shows the scheme of a classic SSITKA experiment. At a fixed temperature after equilibrating with the first isotope (here ^{16}O) using a fast switching

valve the feed is switched to an isotope-labeled mixture (here ^{18}O). The mass traces of all oxygen-containing components are being analyzed at the reactor outlet. After the experiment the catalyst material needs to be regenerated with the first isotope, the reaction conditions (e.g. temperature) can be changed and the experiment repeated. A major advantage of this technique is, that it can be applied directly under reaction conditions, allowing not only the investigation of the isotope exchange with the catalyst material but also the isotope distribution in different reaction products. The ^{16}O gets replaced from the gas phase in the reactor, leaving the catalyst material the only source of ^{16}O. The time-dependent 16/18-oxygen distribution in the reaction products now can give insights, on whether the oxygen is provided by the bulk material or directly from activated gas phase oxygen. Depending on the temperature and nature of the analyzed material, this experiment can take quite long. With increasing temperature using an oxide material, the bulk diffusion of oxygen will have a major impact on the experiment. In the case of bulk oxide catalysts (e.g. alkaline earth or lanthanides), the material contains a huge quantity of oxygen atoms compared to the gas phase. Achieving a full isotope exchange of all oxygen atoms in the bulk and with that, a steady state is therefore hardly to be achieved after switching. Also, the regeneration with ^{16}O afterward might be challenging depending on the bulk diffusion rate. Since perfect switching is not possible, during the experiments both isotopes are present in the gas phase for some time allowing gas-phase reactions as well as catalyzed isotopic scrambling. This part of the experiment can be used to analyze the activation behavior of the labeled component on the tested material. Due to the duration of the experiments, the isotope consumption can be quite significant and therefore costly. Another issue of SSITKA experiments is a full qualitative analysis. Even though a qualitative analysis already gives good insights into the mechanism of the activation, sometimes a full qualitative analysis is needed. For this purpose, profound knowledge of the mixing behavior of the reactor is necessary to convolute the component traces afterward making this task quite challenging. This technique has been applied much time for multiple types of materials to provide a deep understanding of the activation process.[178,179]

Figure 39B shows a temperature-programmed isotope exchange (TPIE) experiment after saturating the material with 16-oxygen, starting at a low temperature, where no catalyst-oxygen exchange interactions are expected, the feed gets switched to the isotope containing feed and heated up. This experiment is very simple and can be used to find the temperature onset of the surface-gas phase oxygen interaction and when bulk diffusion becomes significant. The obtained data, however, cannot be easily interpreted. Upon the start of the exchange of oxygen atoms with the gas phase, the isotope saturation inside the material changes continuously as does the temperature. The resulting component traces, therefore, are dependent on the temperature ramp as well as isotope saturation, resulting in a complicated analysis. Another drawback is the large consumption of isotopes needed for a run. Simultaneously feeding other reactants one can again investigate the origin of the oxygen in the products, whether they come from the gas phase or the bulk. However

only to the point where only a few atoms on the catalyst surface are exchanged with the isotope ones.[180]

In Figure 39C a similar experiment is depicted. Here, the difference compared to the experiment described before is the co-feeding of both isotopes. In contrast to the methods described before, this offers the opportunity to investigate the isotope scrambling activity of the material. If the investigated material, for example, is “non-reducible” and does not exchange oxygen atoms easily with the gas phase (or is not an oxide) it might still be active to catalytically activate oxygen atoms allowing a scrambling on the surface. To observe this effect, both isotopes need to be present in the gas phase at the same time. While heating, the onset of this activity as well as activation energy might be found, the experiment can only be carried out until the material itself starts to exchange oxygen atoms with the gas phase. Since the isotope saturation inside the material is different from the gas phase isotopic composition, the results will be distorted. Again, even though this experiment can give insight into the oxygen activation over a large temperature range, due to its duration, it might be costly.

Figure 39D shows a scheme of a TAP (temporal analysis of products) experiment. Compared to the other experiments this experiment is conducted under vacuum conditions and requires a special setup. The low pressure allows the measurement in the Knudsen diffusion regime allowing a good description of the gas-material interaction during the reaction. After activation, by pulsing oxygen over the tested material, a time-shifted isotope pulse can be fed through the catalyst bed. By using a very sensitive fast measuring mass spectrometer the pulses can be analyzed in the microsecond regime. By analyzing the peak form of the pulse, information about the oxygen-material interaction and exchange can be obtained. Varying carefully the time of the pulses, also the adsorption of the components and their interaction with each other can be investigated.[150] Even though this method potentially offers a lot of insight, due to the low-pressure conditions, the meaningfulness of the obtained results on the real catalysis has to be considered. Due to the low pressure, materials can auto-reduce resulting in a different oxidation state of the material compared to that under catalytic conditions. The impact of a pre-reduced surface compared to an oxidized one has been investigated before and shows major differences even on “non-reducible” oxides.[181]

4.6.1. Pulsed Isotopic Oxygen Scrambling (PIOS)

One main target of this work is the investigation of the oxygen activation on the calcium oxide surface under OCM relevant conditions. The reduction of oxygen on a catalyst surface has been proposed to progress consecutively:[46]

$$O_2(g) \rightleftharpoons O_2(s) \overset{e^-}{\rightleftharpoons} O_2^-(s) \overset{e^-}{\rightleftharpoons} O_2^{2-}(s) \rightleftharpoons 2\,O^-(s) \overset{2e^-}{\rightleftharpoons} 2\,O^{2-}(s). \quad (40)$$

The adsorption step, as well as reduction to the superoxide, are elusive for indirect methods. The cleavage of the O_2^{2-} though should be detecting the oxygen scrambling by using labeled oxygen molecules:

$$^{16,16}O_2 + {}^{18,18}O_2 \rightleftharpoons 2\,{}^{16,18}O_2. \quad (41)$$

Since the oxygen reduction is reversible, if an oxygen molecule on the catalyst surface reduces and cleaves in close vicinity with a labeled oxygen molecule, the isotopes in the molecules can be scrambled. If the reduction goes even further towards O^{2-} also the reaction with lattice or surface oxygen should be observable. Since CaO is a "non-reducible" oxide the interaction of isotopic exchange of gas-phase oxygen with that of the catalyst can be assumed to play a minor role. Therefore, a method is required, where the observation of the oxygen scrambling is easily detected.

For this reason, a pulsed isotopic scrambling experiment was performed in this study. At a set temperature with a constant feed of synthetic air (20% $^{32}O_2$ in He), a pulse of 250 µl labeled air (20% $^{36}O_2$ in N_2) was added to the gas mixture (see Scheme 7) and passed over the catalyst. The isotope distribution in the gas feed is then analyzed using a mass spectrometer.

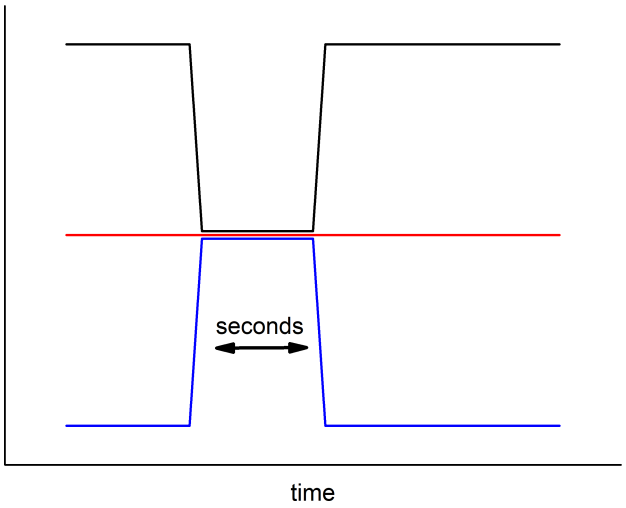

Scheme 7: Schematic representation of a pulsed isotopic scrambling experiment.

There are a few benefits but also drawbacks to this method compared to the methods mentioned before. One obvious advantage is the low amount of isotope gases needed for this kind of experiment compared to the experiments depicted in Scheme 7 A-C. Another one is the constant presence of the more abundant ^{16}O in the gas phase. While in case of the SSITKA and temperature-programmed isotopic exchange experiments, after switching, the gas phase consists purely of the labeled isotope meaning from the point of lattice or surface oxygen interaction with the gas phase,

those two are being depleted of ^{16}O and enriched with ^{18}O constantly changing the isotope distribution inside the material. Due to the omnipresence of ^{16}O in the pulsed experiment and the pulse time being only a few seconds, the material surface gets constantly regenerated with ^{16}O and ^{18}O enrichment at the surface between two pulses can be neglected, reducing the regeneration time and experiment duration drastically. But this can also be a major drawback of this experiment. Due to the pulsing of the isotope gas, the gas phase isotopic composition changes constantly during the whole experiment, which makes a quantitative evaluation hardly possible. In comparison to the TAP reactors, where the experimental conditions are very well controlled, the here described experiment has a major advantage, that it runs at atmospheric pressures. Since the oxygen pressure has an effect on the catalyst surface and reactivity,[181] applying an oxygen pressure relevant to the reaction conditions is crucial.

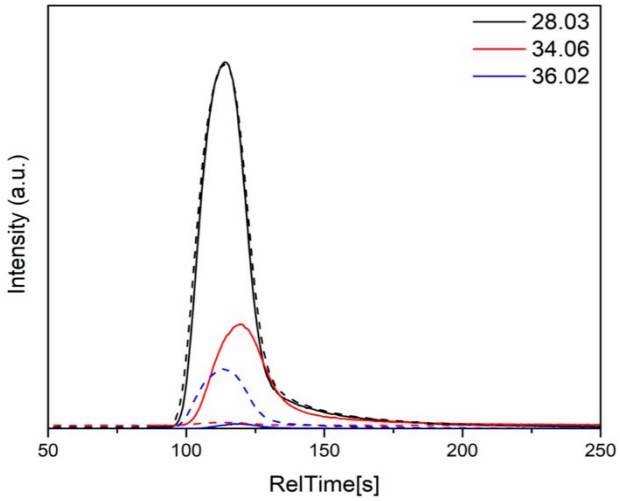

Figure 40: Exemplary pulsed isotopic scrambling experiment with (line) and without (dashed) reaction over CaO, with mass 28 representing the N_2 trace, 34, the $^{16,18}O_2$, and 36 the $^{18,18}O_2$.

In Figure 40 the recorded mass spectrometer data for the pulsed isotopic scrambling experiment is shown with and without reaction. In the case without any reaction, only the simultaneous nitrogen and $^{36}O_2$ pulse are visible, wherein the case of the reacted the formation of the scrambled oxygen ($^{34}O_2$) becomes visible. A minor time shift between the scrambled oxygen and the nitrogen can be observed, indicating a weak interaction of the oxygen with the catalyst surface, whereas the nitrogen peak appears to be unaffected, thus not interfering with the catalyst surface.

Comparing the experiment with a redox-active OCM catalyst such as a silicon oxide supported sodium-tungsten-manganese mixed metal oxide (NaMnWOx@SiO_2), major differences in the resulting isotope traces become evident. Since the peaks for the NaMnWOx@SiO_2 catalyst are very distorted and delayed, a graphical comparison of those would be challenging, therefore the $^{34}O_2$ responses were integrated and are presented in Figure 41.

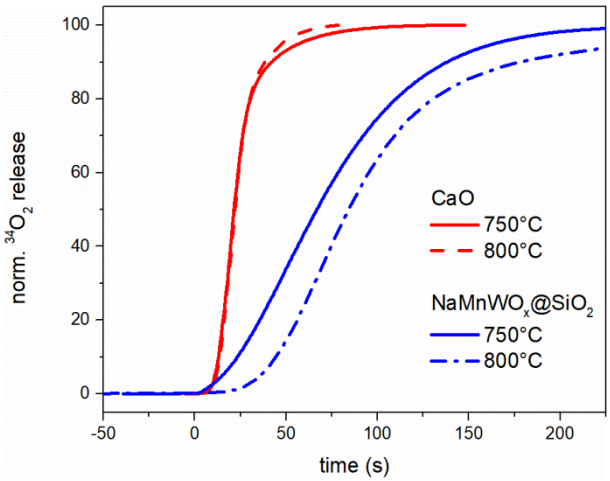

Figure 41: Integrated $^{34}O_2$ releases after pulsing 250 µl of $^{36}O_2$ over a CaO (red) and a NaMnWO$_x$@SiO$_2$ to a $^{32}O_2$ containing synthetic air flow of 20 ml/min at 750°C and 800°C.

At first glance, major differences become visible. The response to the isotope pulse on the calcium oxide catalyst is the almost spontaneous release of the scrambled oxygen, whereas, in the case of the NaMnWO$_x$@SiO$_2$, the release is strongly delayed. Even though the pulse width is well below 50 s, 18-oxygen is being released from the catalyst for several minutes, which can only be explained by the catalyst material exchanging oxygen atoms with the gas phase and storing the isotope in its lattice. This requires the catalyst to be able to completely reduce the oxygen towards O^{2-} and a good bulk diffusion rate of oxygen even at "low" temperatures. Only small amounts of the scrambled oxygen molecules are released over time indicating, that the emission of the oxygen molecules from the surface might not be the same place on the catalyst where they are absorbed. The mechanism for this type of oxygen will most likely involve oxygen vacancy formation:

$$2\ {}^{16}O^{2-}(s) \rightleftharpoons {}^{16,16}O_2(g) + 2V_O'' \quad (42)$$

$$^{18,18}O_2(g) + 2V_O'' \rightleftharpoons 2\ {}^{18}O^{2-}(s) \quad (43)$$

$$^{18}O^{2-}(s) + {}^{16}O^{2-}(s) \rightleftharpoons {}^{16,18}O_2(g) + 2V_O'' \quad (44)$$

In Figure 42 the time course of a labeled oxygen pulse over a NaMnWO$_x$@SiO$_2$ catalyst is depicted. For better visualization, a baseline was subtracted from the $^{32}O_2$ trace. At t = 0 s the labeled oxygen (blue line) reaches the catalyst material and is completely consumed. Instead, unlabeled oxygen (black trace) is being released from the catalyst surface, substantiating the statement made in eq. (42) and (43), that the absorption rate of oxygen on this material is fast in comparison to the rate of activation of oxygen on the surface. As a consequence, the chance for a gas-phase oxygen molecule adsorbing on the catalyst surface meeting another adsorbed oxygen is low and therefore no immediate scrambling takes place.

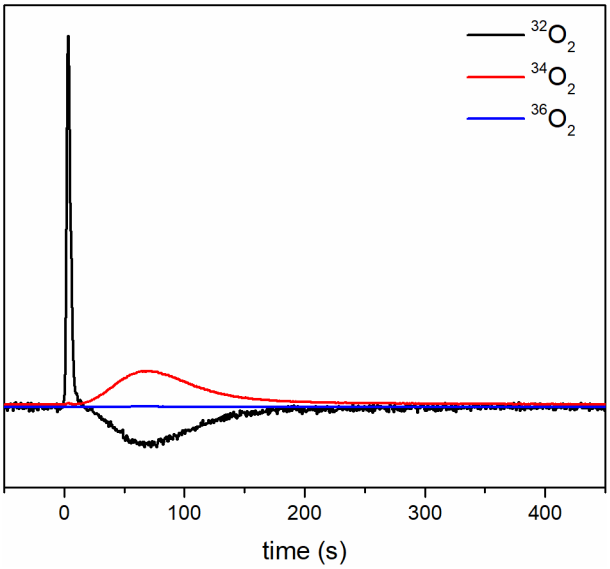

Figure 42: Baseline corrected MS traces of a pulse of 250 µl 18-labeled O_2 at t = 0 s passed over a $NaMnWO_x@SiO_2$ catalyst at 800°C in 20 ml/min synthetic airflow.

With increasing temperature (from 750°C to 800°C) the peak shape of the oxygen response becomes even more delayed for the $NaMnWO_x@SiO_2$ catalyst. Since the bulk diffusion rate can be expressed with an Arrhenius approach, a higher diffusion rate of the oxygen into the bulk can be assumed, allowing the isotopes to reach deeper inside the catalyst. In the case of $NaMnWO_x@SiO_2$, the aggregate state of the active phase has also to be considered. At temperatures above 775°C (depending on synthesis) the material is known to become amorphous or even liquid.[182] Considering a liquid or at least a highly dynamic surface, a strongly delayed oxygen release also becomes very plausible. In the case of bulk diffusion, the catalyst material can be considered as a dead volume which poses as a sink for the isotope. The dead volume is not directly flushed by the gas phase, and therefore the release during the residence time of the isotopes inside the reactor becomes retarded. The isotope enrichment will be highest near the surface, decreasing with the depth of the catalyst. In the case of a highly dynamic surface/material, the catalyst can be considered as a mixed storage vessel for the isotope oxygen atoms with no gradient of the isotopes. Since the overall isotope concentration on the surface is then highly diluted, the regeneration will be constantly slow as well. In contrast to that, the residence time of the oxygen in the case of CaO is hardly affected by the temperature between 750°C and 800°C. At best, the retardation of the oxygen becomes slightly weaker which can also be an effect of the reactor itself to the temperature. Due to the increased temperature, the space-time velocity inside the catalyst bed is slightly enhanced, resulting in a narrower pulse. Also, the rate of gas diffusion at dead volumes around the catalyst particles is increased resulting in a more ideal behavior of the catalyst bed. Considering all that, it becomes evident that in contrast to the $NaMnWO_x@SiO_2$ catalyst, which allows lattice oxygen to directly interact with the gas phase oxygen, indicating an active O^{2-} species near the surface,

CaO does not have active surface oxygen species. The reactivity of oxygen on the calcium oxide surface appears to derive solely from adsorbed oxygen species:

$$O_2(g) \rightleftharpoons O_2(ads), \quad (45)$$

$$^{16,16}O_2(ads) + {}^{18,18}O_2(ads) \rightleftharpoons {}^{16,18}O_2(ads), \quad (46)$$

though the degree of reduction of the oxygen species on the surface remains elusive.

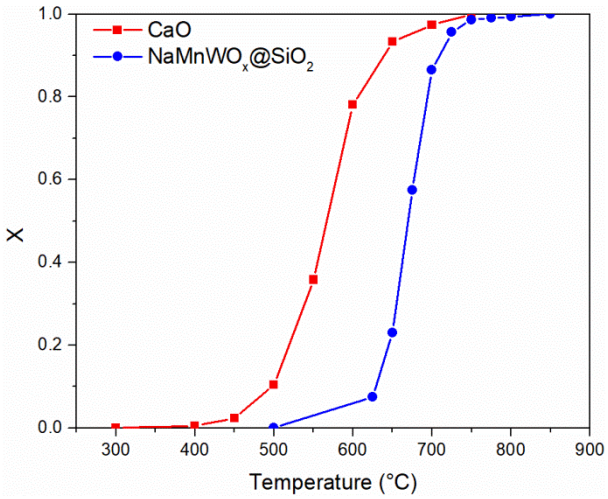

Figure 43: Temperature-dependent oxygen scrambling activity measured by pulsing 250 ml of $^{36}O_2$ to a 20 ml/min feed of $^{32}O_2$ containing synthetic air feed over CaO and NaMnWO$_x$@SiO$_2$.

Calculating now the conversion of isotopic scrambling/exchange measured at different temperatures, differences between those two materials become visible (Figure 43). The CaO catalyst onset of oxygen scrambling is much lower in comparison to that of the NaMnWO$_x$@SiO$_2$ catalyst and the slope is less steep. Since it was mentioned before, that the activation of oxygen on CaO is more likely a catalytic surface reaction and the activation on NaMnWO$_x$@SiO$_2$ a matter of vacancy formation, a larger activation barrier for the NaMnWO$_x$@SiO$_2$ catalyst is therefore also very plausible. What is also interesting, is the low activity of the NaMnWO$_x$@SiO$_2$ catalyst far below 700°C. These catalysts show almost no activity for the OCM reaction at these temperatures. Nevertheless, a significant oxygen exchange can be observed indicating this not being the only descriptor for OCM activity. Another step in the reaction cycle might be rate determining and not the activation of oxygen.

The here proposed PIOS method can be easily used to differentiate between those activation mechanisms of oxygen. It has to be mentioned though, that in the case of NaMnWO$_x$@SiO$_2$, an SSITKA experiment could be more easily evaluated for the rates of bulk diffusion. Nevertheless, in the case of the "non-reducible" CaO, the desired information, regarding the oxygen activation on the surface was obtained.

Since the temperatures in these experiments are quite high, and a large amount of diluent (silicon carbide) was used for the catalyst, gas-phase reactions have to be excluded, therefore the activity of SiC itself was tested (Figure 44).

4.6.2. Oxygen PIOS on Calcium Oxide Catalysts

Using the described PIOS technique a deeper investigation of the oxygen activation on CaO can be performed. In the presented experiments, CaO was activated in the reactor at 900°C in synthetic air before starting oxygen exchange. In Figure 44 (black symbols) the ^{18}O distribution after oxygen scrambling on the activated calcium oxide at different temperatures in flowing oxygen is presented. Showing no activity at temperatures below 400°C, the catalyst becomes quite active at temperatures above 500°C. On magnesium oxides, a similar behavior was observed before.[75] It was concluded that the removal of surface OH by the release of H_2 triggered the onset of the reactivity with molecular oxygen. Since the calcium oxide was dehydroxylated by activation before the oxygen exchange experiments at 900°C, coverage with OH is not likely, however, OH groups might be re-formed due to reaction of CaO with traces of water in the feed. To get rid of any possibly remaining impurities in the gas supply, a column of 20 g CaO was introduced in front of the actual reactor in a subsequent experiment to trap all traces of impurities in the oxygen feed (for example H_2O and/or CO_2) as far as possible (blue data points in Figure 1). Now that impurities were removed, the onset of the oxygen exchange activity decreases down to a temperature of 50°C, suggesting that even very little amounts of surface hydroxide or carbonate can quench the oxygen exchange activity of calcium oxide completely. The apparent activation energy of 80 kJ/mol determined from this experiment is lower than the calculated dissociation barrier for oxygen on pristine flat CaO surfaces with 110 kJ/mol,[81] but comparable to what was found for the double oxygen exchange on a pre-oxidized CaO surface with 74 kJ/mol before.[181]

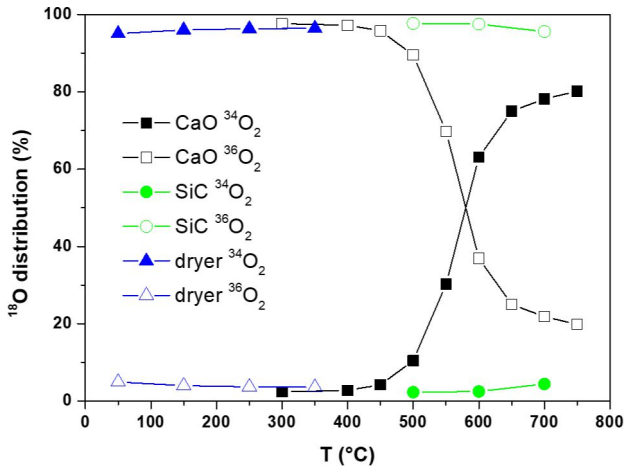

Figure 44: ^{18}O distribution in O_2 after dosing a pulse of 500 µl of labeled synthetic air (80% N_2 and 20% $^{36}O_2$) into 30 ml/min unlabeled synthetic air (80% He and 20% $^{32}O_2$) at temperatures between 50°C and 800°C over 27.7 mg CaO (25763) diluted in 730 mg SiC (black symbols), with the additional upstream introduction of a 20 g CaO sacrificial column (blue symbols) and over 750 mg SiC without the column (green symbols).

The ability of alkaline earth oxides such as MgO to activate oxygen and even exchanging a fraction of a surface monolayer with the gas phase is well known.[74,183,184] Since the pristine flat calcium oxide surface should not be able to activate oxygen in absence of a reducing agent or dopant,[81] the capability of irreducible oxides to activate oxygen is often attributed to the presence of trace amounts of dopants, such as transition metals or alkali metals.[46] In the case of alkali metal dopants, the oxygen exchange could be correlated down to 0.001 at% Na impurities in the used CaO catalyst. However, such low concentrations can hardly be avoided in catalyst synthesis. Here, a Na content of < 0.005 at% was determined, which was the detection limit of the applied analysis method.[150] According to proposed mechanisms, the oxygen exchange involves O^- species at the surface, forming an ozonide O_3^- species with gas phase oxygen as an intermediate.[183,184] O^- species at the catalyst surface were assumed to be formed by the splitting of O_2^{2-} acting as surface terminations on step sites.[185] Those sites have also been related to the presence of Na ions in the vicinity creating a hole structure identified by EPR.[186] In the case of low Na-doped CaO, the presence of sodium influenced the ratio of k_{ads}/k_{dis} reducing the coverage of the catalyst surface with molecular oxygen.[150] A value of 89 kJ/mol was found for the adsorption enthalpy, but for the dissociation, a barrier of 249 kJ/mol was determined.[150]

To investigate the influence of by- and side-products occurring in OCM feeds on the oxygen activation, water and carbon dioxide were co-fed (Figure 7). By the addition of carbon dioxide and thus stabilizing calcium carbonate, it becomes evident that the carbonate is not able to interact with gaseous oxygen in a manner of dissociating oxygen in order to induce a scrambling of the oxygen isotopes. Scrambling is only observed at temperatures at which the carbonate becomes thermodynamically unstable and decomposes (dashed line in Figure 2, left). Similar behavior was observed earlier for rare earth oxide catalysts in OCM investigated by TPIE.[180] Carbonates were found to shift the onset of the isotopic oxygen exchange with the catalyst lattice to higher temperatures. It has to be noted, that in this case primarily the impact of bulk properties such as oxygen diffusion was investigated. At temperatures above carbonate decomposition, oxygen exchange is observed and the ^{18}O is found in oxygen as well as in carbon dioxide. Due to the higher abundance of ^{16}O sources (20% in the synthetic air plus the ^{16}O in the 20% carbon dioxide), the overall conversion of $^{36}O_2$, assuming a statistical distribution, is expected to be higher in these experiments compared to oxygen exchange experiments in absence of CO_2. It is known that the scrambling of oxygen with carbon dioxide does not take place in the gas phase, even not at high temperatures.[187] A mechanism for the oxygen exchange between $C^{18}O_2$ and CaO on well-ordered $Ca^{16}O$ films was recently reported.[188] The exchange occurs even on defect-free CaO (001) planes due to rotation and other motions of the adsorbed carbonate. Monodentate isolated carbonate species are easily able to exchange oxygen atoms with the calcium oxide lattice, especially on monoatomic steps and corner sites, where the intrinsic barrier

for oxygen scrambling is reduced to 80 kJ/mol and 27 kJ/mol, respectively.[188] Finding an almost statistical distribution of the ^{18}O among the oxygen as well the carbon dioxide in the present experiment, it can be assumed that the scrambling of oxygen and carbon dioxide takes place at similar surface sites, which in both cases can be step sites on the catalyst surface. The activation energy, in this case, was determined to be much higher compared to the theoretical value with 150 kJ/mol, indicating that not the scrambling, but the CO_2 release from the surface might be rate determining.

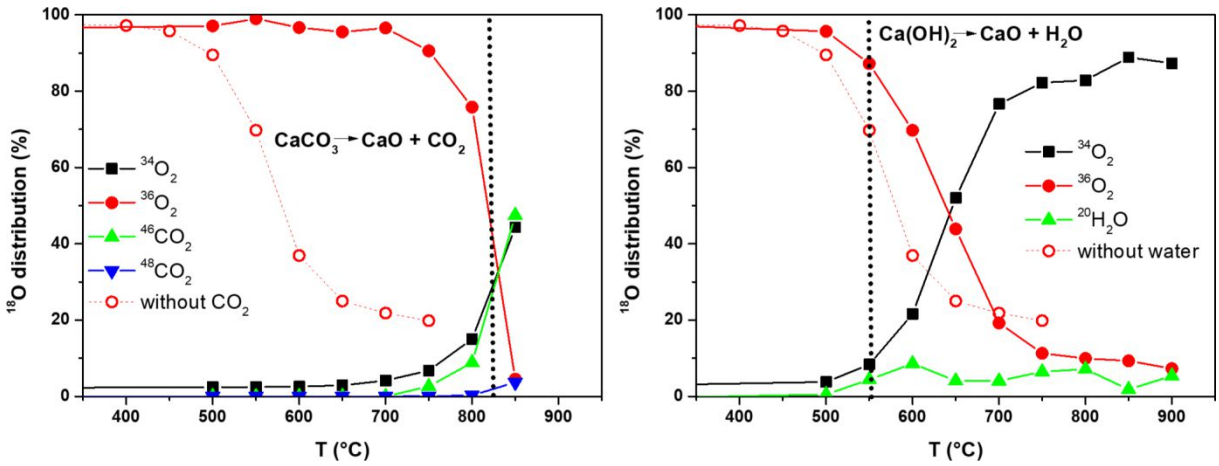

Figure 45: ^{18}O distribution in outlet pulses after dosing a pulse of 500 µl of labeled synthetic air (80% N_2 and 20% $^{36}O_2$) over 27.7 mg CaO (25763) diluted in 730 mg SiC between 50°C and 800°C in a carbon dioxide containing feed (60% He, 20% O_2, 20% CO_2, left) and with the addition of water (78% He, 18% O_2 and 4% H_2O, right). Hollow symbols represent experiments without the addition of CO_2 or H_2O.

The addition of water induces a similar behavior and shifts the oxygen scrambling also to higher temperatures, which proves that OH compensated sites and hydroxides are not or less able to dissociate oxygen (Figure 2, right). An isotope exchange with the water is also observed, but to a lower extent compared to CO_2. The activation energy, in this case, was found to be slightly elevated compared to the pure oxygen experiments with about 110 kJ/mol. The results also indicate that water interacts with the active sites even above the hydroxide decomposition temperature. In summary, oxygen activation was studied applying oxygen scrambling experiments on calcium oxide. It becomes apparent that by- and side-products of the OCM reaction, such as CO_2 and water, act as poisons for the sites active towards oxygen activation on calcium oxide catalysts.

Repeating the oxygen activation experiment with the Ni and Mn-doped CaO catalysts, showing improved catalytic activity towards in the OCM reaction, no significant differences can be observed (Figure 46). In the best case, a minor increase in activity for the Ni-doped sample at 500°C can be observed. It appears that the before stated limitations for "pure" CaO, which appears to mainly derive from the presence of impurities blocking the active sites, remain the same for the doped

samples. This also suggests, that the site for activation of oxygen remains mostly unchanged on the CaO surface and not on surface metal atoms or clusters which might have been elusive for the used spectroscopic methods. However also the depth of reduction of the oxygen molecules cannot be probed with this technique.

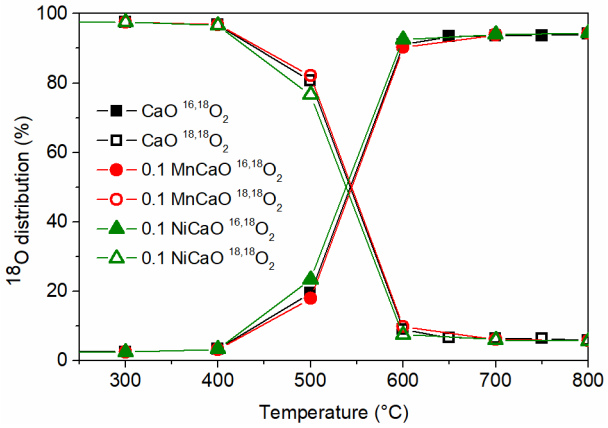

Figure 46: ^{18}O distribution in outlet pulses after dosing a pulse of 500 µl of labeled synthetic air (80% N_2 and 20% $^{36}O_2$) over 27.7 mg undoped (black), Mn (red) and Ni-doped (green) CaO diluted in 730 mg SiC between 50°C and 800°C.

Even though the reaction profiles might look very similar, the most abundant oxygen species on the surface cannot be identified, which might change on the doped and undoped samples. Another aspect that might have been altered is the oxygen conductivity of the material by doping. Since the transition metals have a significantly lower ion radius compared to that of Ca, the doped materials crystal structure might be more favorable for oxygen mobility in the lattice. To analyze this, a profound analysis of the peak shape would be necessary, which also requires a profound knowledge of the reactor mixing behavior. As stated before, SSITKA experiments might, in this case, be the better choice for achieving better insights.

4.6.3. SSITKA Experiments

4.6.3.1. Results of the SSITKA Experiments

For the SSITKA experiments, the setup for dynamic experiments (refer to 3.17 page 33) was used. The carbonate precursors were diluted in SiC (50 mg in 720 mg SiC) and activated before the experiments inside the reactor at 900°C in synthetic air. After setting the reaction temperature and equilibrating for at least 15 minutes, the gas feed was switched from synthetic air (20% O_2 in N_2) containing the natural abundant 16-oxygen isotope to a feed of 20% 18,18-oxygen (also referred to as $^{36}O_2$) in helium, mixed by suitable MFCs. The reaction courses were recorded using a mass spectrometer. After about 5 minutes of the experiment, the feed was switched back to the 16-oxygen containing synthetic air and the temperature was set to 900°C

for the regeneration of the 16-oxygen saturated catalyst. The response factors of the mass spectrometer for all species were assumed to be the same, allowing a balancing and normalization.

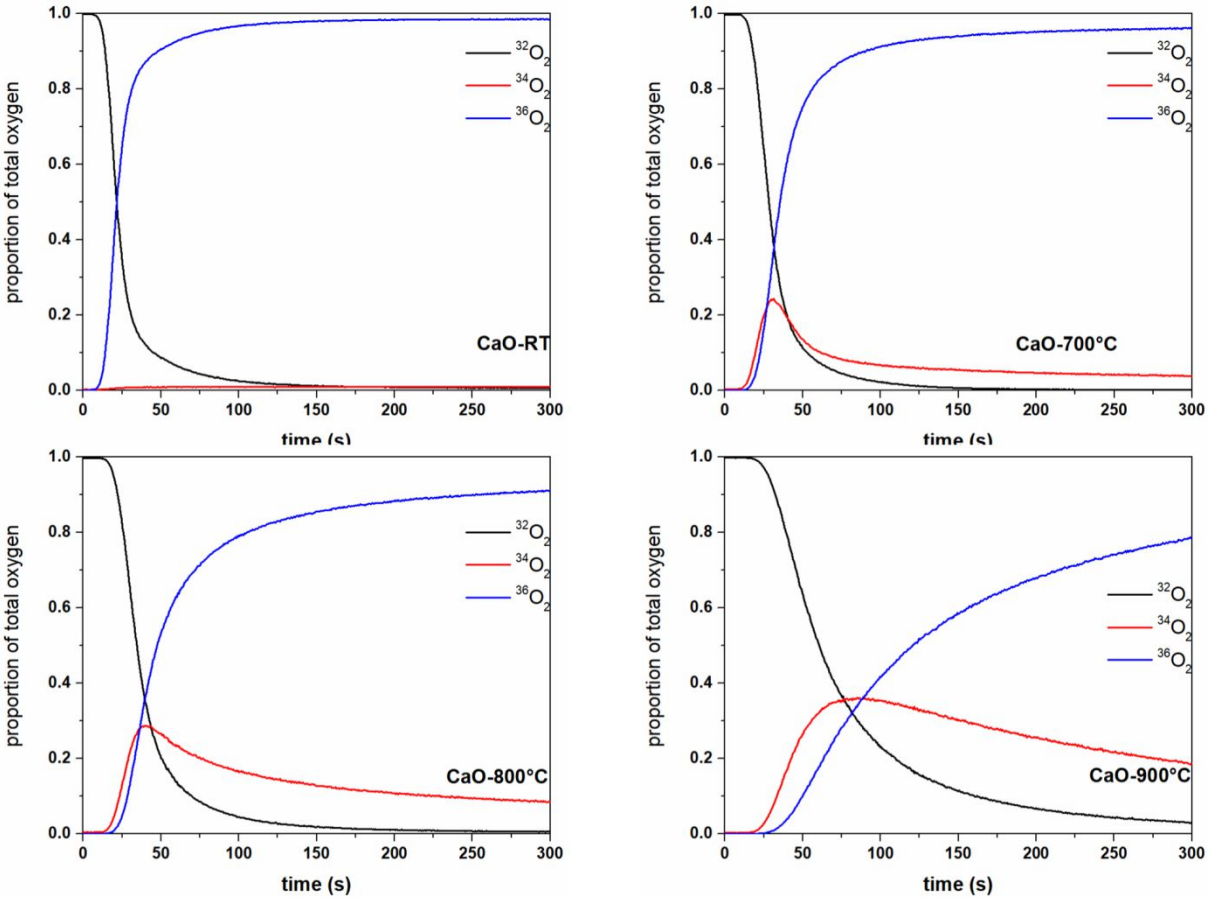

Figure 47: Normalized oxygen courses during SSITKA experiments on CaO at different temperatures (28 mg CaO in 720 mg SiC, 20 ml/min gas flow).

In Figure 47 the courses of the three oxygen species over the reaction course are depicted. Due to switching the $^{32}O_2$ (black curve) is displaced from the reactor and replaced by the $^{36}O_2$ (blue curve). At room temperature, no formation of the scrambled $^{34}O_2$ (red curve) can be observed. Going to higher temperatures, a delay of the displacement of 16-oxygen from the reactor can be observed. At 700°C, a distinct peak of $^{34}O_2$ formation can be observed at the start of the experiment, due to the scrambling of the gas phase oxygen at the catalyst surface, followed by a long tailing. With increasing temperature, the displacement of the 16-oxygen from the reactor gets more and more delayed and the tailing of the $^{34}O_2$ signal is strongly enhanced. The delayed displacement of the 16-oxygen with the temperature indicates a temperature dependent storage capacity of the catalyst material inside the reactor, which was up to now elusive with the before applied pulse method and is sometimes disregarded in transient kinetic studies in TAP reactors and on "non-reducible" oxides such as MgO, CaO and La_2O_3,[150,189] though especially at

temperatures relevant for the OCM reaction it cannot be neglected.[181] Due to the complementarity of the different oxygen traces, for comparison, only the $^{34}O_2$ traces of the SSITKA experiments are discussed.

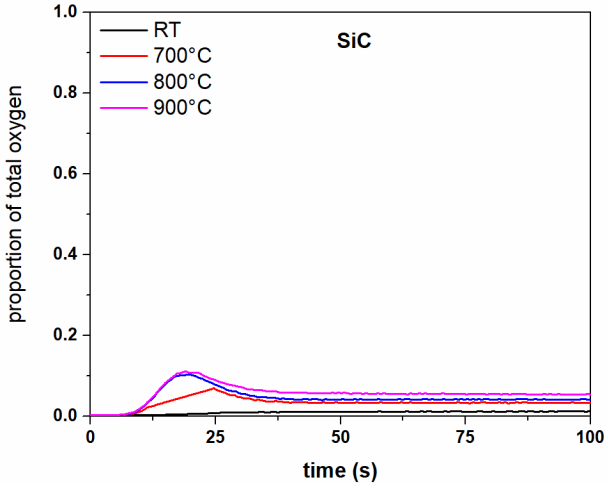

Figure 48: Normalized $^{34}O_2$ courses during SSITKA experiments on SiC at different temperatures (720 mg SiC, 20 ml gas flow).

Since the experiments were conducted at OCM relevant temperatures (700°C to 900°C), the contribution of the diluent (SiC) to the activation of oxygen has to be considered as well. Also, the reactor, consisting of quartz glass, can pose as an almost infinite reservoir of 16-oxygen. In Figure 48 "blank" SSITKA experiments over silicon carbide are depicted. Due to a corruption of the dataset during the measurement, the trace recorded at 700°C (red line) is missing data points between 10 and 25 seconds. A comparison of these datasets to the ones measured with a catalyst (Figure 47) shows a quite significant contribution to the effect, which is interestingly not strongly temperature e dependent. As stated before, the quartz tube acts as a larger oxygen reservoir, and also silicon carbide is known to oxidize at elevated temperatures,[190] making it also a possible oxygen source in the reactor, which can be an explanation for the altered offset after the switching of the feed gas. The increase of the offset with temperature is also an indication for a diffusion-limited source of 16-oxygen, hinting more towards the quartz tube since deep oxidation of silicon carbide at 900°C is less likely.[190,191] Why the initial scrambling of the oxygen appears to be temperature independent cannot be easily explained. Nevertheless, even though not being insignificant, the reactivity of the catalyst is high enough, to be easily differentiated from the reactor activity.

Comparing now the SSITKA experiments of pure CaO with those on the 0.1% Mn-doped CaO (Figure 49) no significant differences can be observed. The shapes of the $^{34}O_2$ traces are almost identical, only a small deviation of the overall magnitude can be observed at higher temperatures, indicating at best minor effects of the doping on the oxygen activation and diffusion in the material.

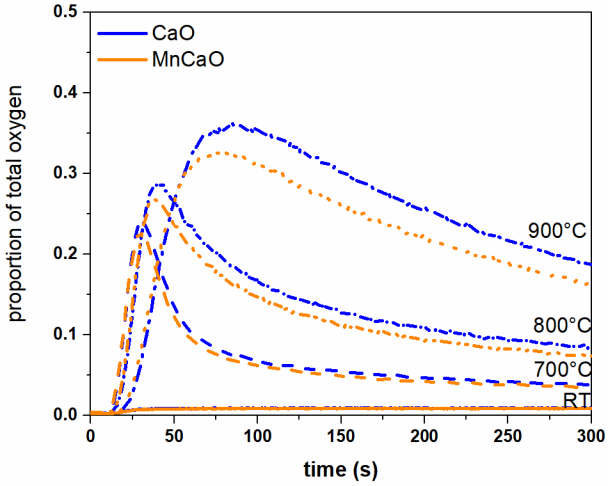

Figure 49: Comparison of $^{16,18}O_2$ releases during SSTIKA experiments on CaO (blue) and 0.1% Mn-doped CaO (orange) at different temperatures, by switching the gas feed from a 16-oxygen containing synthetic air to an 18-oxygen labeled air.

Figure 50 depicts the amount of absorbed oxygen by the catalyst material. The dashed line shows the integral amount of 18-oxygen entering the reactor, subtracting the amount of 18-oxygen leaving the reactor in form of $^{34}O_2$ or $^{36}O_2$ and the amount absorbed by the reactor (Figure 48) will give the total amount 18-oxygen which is taken up by the catalyst material.

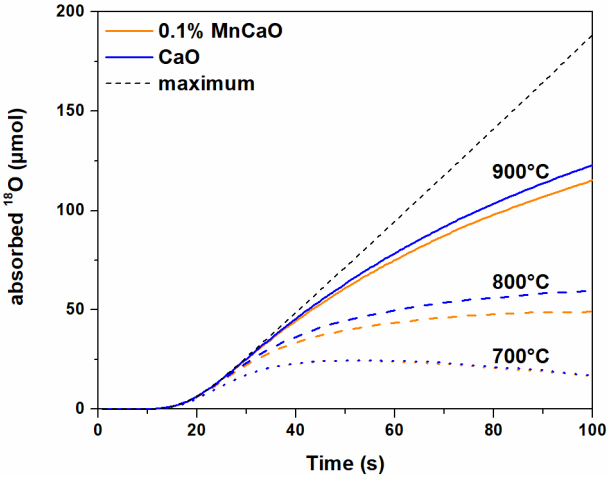

Figure 50: Comparison of 18-oxygen uptake of CaO (blue) and 0.1% Mn-doped CaO (orange) at different temperatures during SSITKA experiments, by switching the gas feed from a 16-oxygen containing synthetic air to an 18-oxygen labeled air.

Since the differences of the oxygen traces were very similar, to begin with, the amount of absorbed oxygen is similar as well, with the amount absorbed by the doped material being slightly less. At the beginning of the experiment, all the 18-

oxygen entering the reactor is absorbed by the material and the rate of absorption is, therefore, being limited by the gas supply rather than the reaction rate. with the ongoing experiment, the uptakes level out at lower temperatures, indicating a limited reservoir of oxygen in both catalysts, which increases with temperature. (At 700°C the curve appears to drop which is due to the corrupted data of the blank experiment. The baseline from 800°C was used instead of that of 700°C and therefore a slightly higher uptake by the reactor was used resulting in decay, due to changes in the setup and gas supply, a reproduction of the data for 700°C under the exact same conditions was not possible.) At 900°C, a leveling was not observed over the time of the experiment, though still being far from exchanging the whole oxygen in the catalyst material (500µmol) bulk oxygen has to be involved to store this much oxygen.

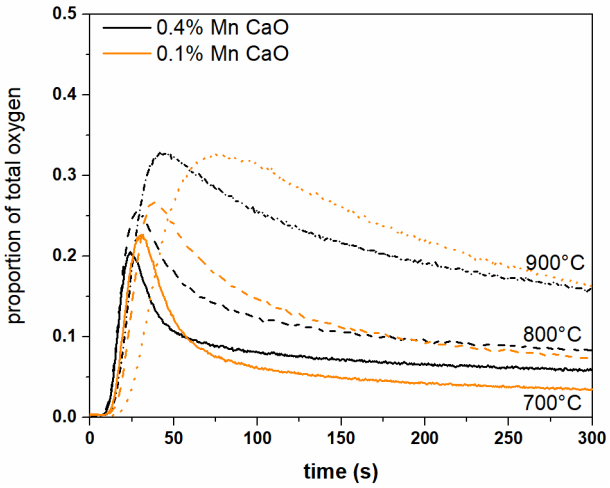

Figure 51: Comparison of $^{16,18}O_2$ releases during SSTIKA experiments on 0.1% (orange) and 0.4% (black) Mn-doped CaO at different temperatures, by switching the gas feed from a 16-oxygen containing synthetic air to an 18-oxygen labeled air.

Comparing now two manganese doped calcium oxide catalysts with different loading (Figure 51) differences in the shape of the $^{34}O_2$ can be determined. In both cases at the start of the reaction, the reaction rate is both again limited by the supply of 18-oxygen to the reactor, therefore a conclusion comparing the rate of oxygen activation on the surface of both is hardly possible. In the later course of the reaction, the baseline of the scrambled oxygen species is slightly enhanced in the case of the higher doped oxide, compared to the lower doped one, which might be an indication for a better bulk conductivity of the oxygen by diffusion. The $^{34}O_2$ traces of the doped samples also appear to be slightly shifted, where the higher doped preserves a peak like a shape with a strong tailing even at higher temperatures, the lower doped sample traces appear to be stretched in comparison. To analyze these curves a suitable model and a fit of the model parameters to the data are necessary.

4.6.3.2. Quantitative SSITKA of the Catalyst-Oxygen Interaction

To quantitatively analyze the response courses of SSITKA experiments, the response function of the setup on the gas switching itself has to be known and subtracted from the results. Therefore, at first experiments were run without any oxygen to analyze the residence time distribution of the reactor and the influence of the temperature on the obtained courses. In Figure 52 the courses of the inert gases are shown during an SSITKA experiment. Though a strong change can be observed comparing the curves at room temperature and those at a higher temperature, the influence of the temperature on the curve above 700°C can be neglected.

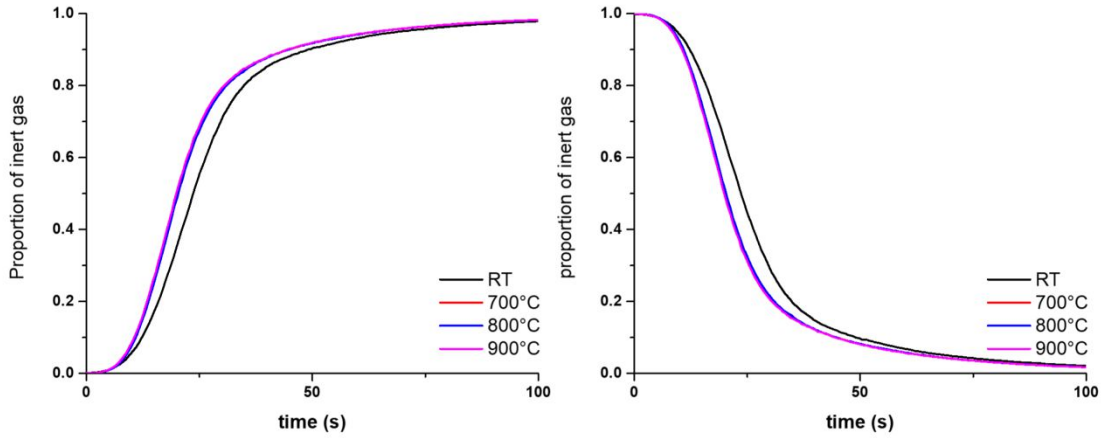

Figure 52: Courses of inert gases during SSITKA experiments at elevated temperatures.

Assuming an ideal gas behavior (pV = nRT) and constant pressure and reactor volume, the increase of temperature from room temperature to 700°C results in a reduction of molecules in the reactor by a factor of >3, which by then reduces the residence time accordingly at these temperatures, explaining the longer time for replacing the inter gases at room temperature compared to higher temperatures. At higher temperatures, though the factor from 700 to 900°C is still at around 1.2, has almost no visible effect on the course, indicating that the heated reactor (due to its small volume and almost ideal displacement behavior) now has almost no influence on the residence time distribution and other parts of the setup dominate the shape of the inert gas exchange. Since the tubing of the setup has a very small diameter (<1 mm i.D.) next to the reactor only the mass spectrometer has a significant volume which can cause the observed dispersion of the signal. With a significant bigger tubing 1/4" compared to 1/16" and a manifold inlet, poorly mixed volumes are highly likely. Another aspect to be considered is the dispersion of the gases in the vacuum chamber.

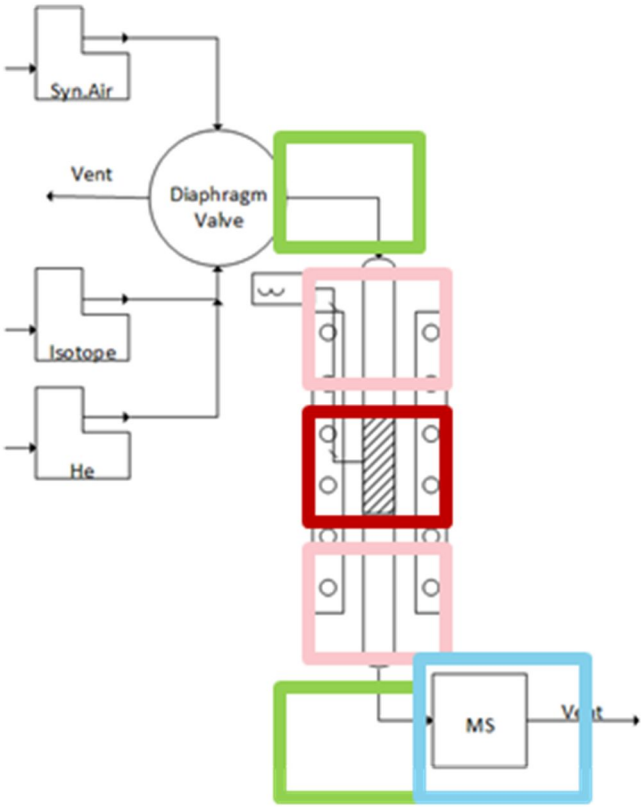

Scheme 8: Segmented reactor model, tubing (green), quartz reactor (pink), catalyst bed (red), and mass spectrometer (blue).

To find a suitable model that fits the experimental residence time distribution, the reactor was segmented in 6 parts (Scheme 8 and Scheme 9). For applicability reasons, the tubing (tubing in Ti, and tubing out To), the quartz reactor (before catalyst bed ci and after catalyst bed co) and catalyst bed (cat) were each treated as cascades of ideally mixed CSTRs, with the balance for each tank:

$$\frac{dp_{i,N}}{dt} = \frac{p_{i,N-1} - p_{i,N}}{\tau_N}, \tag{47}$$

with τ_N being the residence time or the individual tank using:

$$\tau_N = \frac{\tau}{N} \tag{48}$$

and:

$$\tau = \frac{V}{\dot{V}}, \tag{49}$$

with V the volume of the individual part and $\dot{V}$ the volumetric flow rate and N the number of CSTRs in the cascade. The volume (V) was estimated for each part from the inner diameter (ID) of the parts and its length (L). The number of ideally mixed

CSTRs (N_i) was chosen for each part to be 10. For the MS part, a parallel circuit was implemented containing a poorly flushed part simulated by a "big" volume CSTR, which could represent a dead volume (V_{dead}) either in the manifold inlet or in the vacuum chamber and an ideally flushed (V_{cas}) part simulated again as a cascade of small CSTRs. The length and inner diameter were unknown, therefore those parameters had to be fitted. Since the MS was fitted as a circuit of two in parallel flushed systems, the ratio (split) in which those parts are flown through has to be fitted as well, with:

$$split = \frac{\dot{V}_{cas}}{\dot{V}_{cas}} \tag{50}$$

and

$$\dot{V} = \dot{V}_{Dead} + \dot{V}_{cas} \, , \tag{51}$$

giving:

$$\dot{V}_{cas} = \frac{\dot{V}}{1 + \frac{1}{split}} \tag{52}$$

and:

$$\dot{V}_{Dead} = \dot{V} - \dot{V}_{cas} \, . \tag{53}$$

Due to the abundance of suitable calibration gases, especially for the isotopes, the mass spectrometer could not be calibrated. Therefore, the calibration factors had to be fitted as well as a factor f_i:

$$I_{i,out} = f_i \cdot p_{i,out} \, , \tag{54}$$

with I the intensity of the mass spectrometer signal.

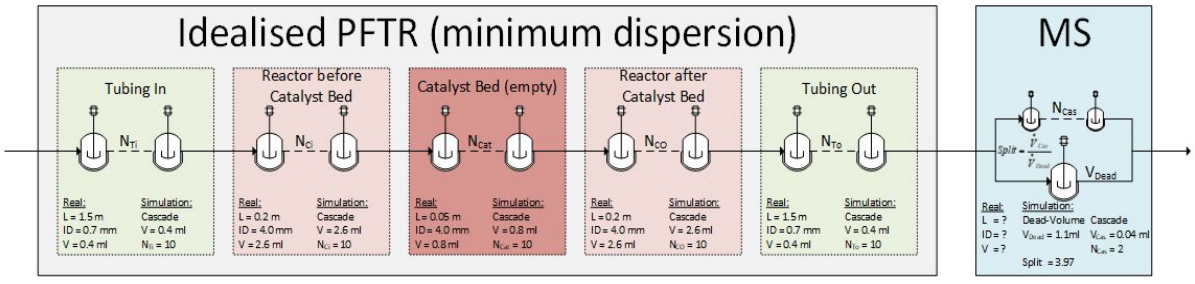

Scheme 9: Cascade model for modeling the residence time behavior of the SSITKA setup.

The numerical simulation was performed using the Berkeley Madonna software using the Auto-stepsize method. In Figure 53 the results of the simulation with optimized parameters can be compared to the data obtained from the blank experiment.

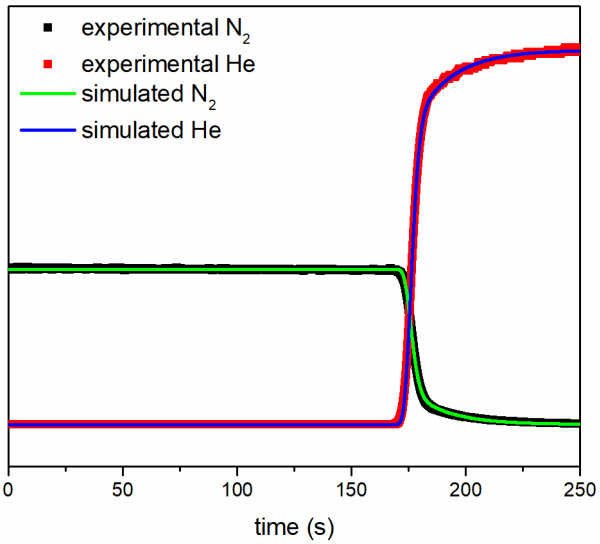

Figure 53: Comparison of simulated and experimental data from switching gas feeds in a reactor filled with 750 mg SiC, with V_{cas} = 0.04 ml, N_{cas} = 2, V_{Dead} = 1.10 ml, split = 3.96, $f_{He} = 7.41*10^{-8}$ and $f_{N2} = 1.79*10^{-7}$.

Using the described model, the experimental data can be fitted quite well, though one has to admit a lot of free parameters were used, which makes it likely to find a suitable parameter sets fitting the experimental data. Therefore, it is necessary to verify the plausibility of the fitted parameters. The results for the fitted parameters hint to a rather large dead volume in the MS part of the setup with 1.1 ml compared to the volume which is perfectly displaced with just 0.04 ml. The high split of 3.96 also supports the idea of a dead volume in the MS part. A poorly displaced volume even of just 1 ml which is flushed by a volumetric volume flow of only 5 ml/min will delay the presence of the displaced gas quite significantly and is the main reason for the here observed tailing of the signal. Though it is not easily possible to verify those parameters, they are physically plausible and in their magnitude also reasonable.

For quantitative analysis, the signals have to be normalized, starting for nitrogen at 100% going to zero at 250 s and vice versa for the He signal. The residence time distribution of the inert gases (N_2 and He) was then compared to those of oxygen. Since the response factors for the oxygen isotopes were not available, they were, due to their similar physical behavior, assumed to be the same for all isotopes. Normalizing the sum of all oxygen isotopes to 100% (SumO2) beginning with 100% $^{16,16}O_2$ at the start and ending with 100% $^{18,18}O_2$.

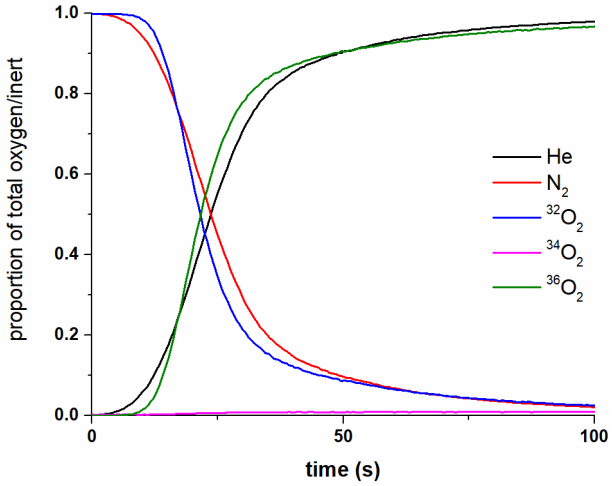

Figure 54: Normalized MS response of switching experiment of oxygen isotope containing gases (from 80% N_2 and 20% $^{16,16}O_2$ to 80% He and 20% $^{18,18}O_2$) applying a flow rate of 20 ml/min at room temperature.

In Figure 54 the normalized responses of the oxygen and the inert switching being presented. At first glance, a discrepancy is clearly visible. Compared to inert switching, the oxygen signals are much steeper and slightly delayed. One plausible reason for this discrepancy can be the much higher diffusion coefficient for helium in nitrogen compared to oxygen in nitrogen. Depending on the gas mixture and the excess phase, the diffusion coefficients of the gases can change drastically. This can be for He as a small gas compared to nitrogen by factors of 4.[192,193] Assuming a much higher diffusion coefficient for He the weaker slope during the exchange as well as the earlier offset can be explained. Due to its higher diffusion rate, helium can travel faster through the reactor compared to oxygen and is detected by the mass spectrometer earlier. But not only the time in which the helium travels through the reactor is slightly decreased by the enhanced diffusion coefficient, but also the back mixing is increased. The higher diffusion coefficient for helium induces an increased back mixing for the gas compared to nitrogen and oxygen, broadening its residence time distribution in comparison to the other gases, resulting in the reduced slope compared to oxygen. Though the faster detection of helium compared to the 18-oxygen can only be explained by a faster transport of the gas towards the detector, the slope can also have other reasons. Since the detector of the mass spectrometer operates in a high vacuum ($<10^{-6}$ mbar), the residence time of the gases inside the detection chamber has to be considered. Due to its higher diffusion rate, helium is much harder to remove in a vacuum chamber and resides much longer compared to other gases. To disregard the helium signal and only analyze the oxygen and nitrogen traces is unfortunately also not an option. Since not only the molecule itself is responsible for its diffusion coefficient, the medium it resides in is a major factor.[192] Due to switching from nitrogen to helium as the main phase in the reactor, the diffusion coefficients for oxygen will be affected during the experiment, which can be hardly corrected.

Until now only a reactor containing solely silicon carbide was considered. During the measurements, catalysts are mixed with the silicon carbide. Comparing the flush out process of nitrogen with the pure silicon carbide bed with the catalyst containing bed (Figure 55) a small deviation can be observed. The smaller catalyst particles (200-300 µm before activation) can fill inter-particle cavities of the larger silicon carbide (300-400 µm) particles and reduce the gas volume of the bed, as well as close off potential dead volumes. The slightly enhanced nitrogen removal observed in this experiment indicates a reduced dead volume, which was to this point not considered in the previously designed model for the reactor (Scheme 9).

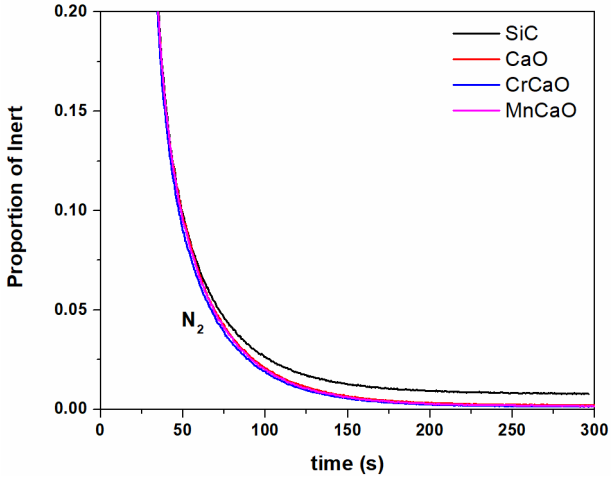

Figure 55: Flush out courses of nitrogen in different catalyst beds (T = 25 °C, $\dot{V}$ = 20ml/min).

Combining all the issues above, a quantitative analysis of the SSITKA experiments will be challenging. Comparing the measurements of the manganese doped calcium oxide and the "pure material (Figure 49 and Figure 50), the differences in the oxygen activation on these materials are at best minor. Results for material parameters obtained by using this model for the reactor will be flawed by a magnitude greater than the actual differences measured in the experiments. The previously introduced model for simulating the reactor behavior has to be altered to consider the dead volumes in the catalyst bed and the influence of the diffusion coefficients, as well as their change during the experiments, have to be considered. Alternatively, the experiments have to be rerun using a different carrier gas than helium. Argon would be a better choice having a similar diffusion coefficient as nitrogen,[193] which could

4.6.3.3. Qualitative SSITKA of the Catalyst-Oxygen Interaction

For the qualitative consideration of the SSITKA experiments, a model for the gas phase/catalyst surface interaction is needed. Various models have been applied to similar experiments conducted in a TAP reactor, but bulk diffusion has been neglected so far, which might due to the lower temperatures of these experiments

(below 600°C).[150] In Scheme 10 a model for the oxygen exchange in the reactor is proposed. The oxygen gas feed passes through an ideal radially mixed plug-flow tubular reactor (PFTR) along the z-axis, filled with catalyst particles. The catalyst is evenly distributed along catalyst bed and consists of simplicity reasons of spherical particles. At the beginning of the experiment, the catalyst and the gas phase is saturated with the ^{16}O isotope. With the start of the simulation, from the inlet (z=0) ^{18}O rich gas feed is fed, passing through the reactor and reacting with the catalyst surface resulting in the release of the mixed ^{16}O-^{18}O (or $^{34}O_2$, the presence of ^{17}O-^{17}O is neglected due to its rarity). The model also considers the bulk diffusion of oxygen. Oxygen atoms on the surface of the catalyst can diffuse along the r-axis into the bulk of the particle, resulting in a 3-dimensional model dependent on the time (t), the position in the reactor (z), and the depth in the catalyst particles (r).

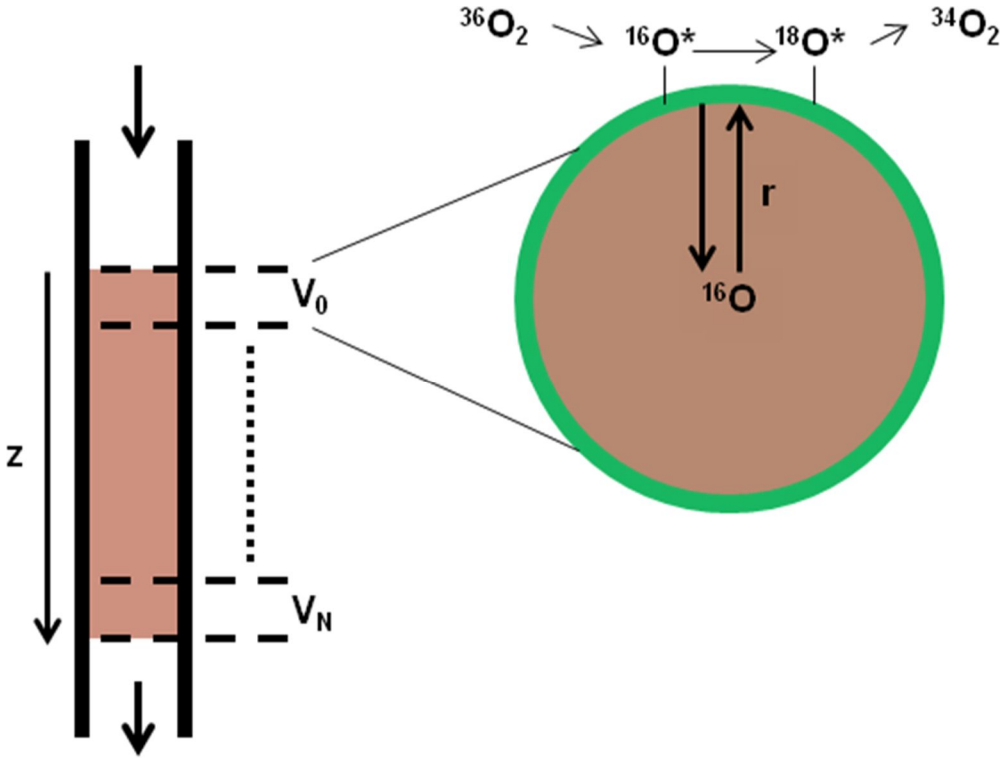

Scheme 10: 3-dimensional model for the oxygen exchange of the gas phase with the catalyst in a PFTR.

,. Two widely accepted microkinetic models used for describing the surface activation of reactants are the Eley-Rideal model and the Langmuir-Hinshelwood model. The Eley-Rideal model describes a mechanism where one of the reactants (B) is adsorbed on the catalyst surface, whereas the other (A) reacts directly from the gas phase with the adsorbent:

$$r = k \cdot p_A \cdot \theta_B \,. \tag{55}$$

In contrast to that, the Langmuir-Hinshelwood model describes a mechanism, where both reactants (A and B) have to be adsorbed on the surface for the reaction:

$$r = k \cdot \theta_A \cdot \theta_B \,. \tag{56}$$

In both cases the coverage (θ) of the surface is usually calculated using the Langmuir adsorption model:

$$\theta_A = \frac{K_A \cdot p_A}{1 + K_A \cdot p_A}, \tag{57}$$

or in case of competitive adsorption with other reactants:

$$\theta_i = \frac{K_i \cdot p_i}{1 + \sum_j K_j \cdot p_j}. \tag{58}$$

Since in this special case, the reactants of the reaction are both oxygen the adsorption constant (K_i) for both reactants can be assumed identical as K. Additionally, since the partial pressure of oxygen is constant during the reaction the surface coverage can be taken as:

$$\theta = \theta_{16O} + \theta_{18O} = const\,, \tag{59}$$

reducing the Langmuir-Hinshelwood model to:

$$r = k \cdot \frac{K \cdot p_A}{1 + K \cdot (p_A + p_B)} \cdot \theta_B\,, \tag{60}$$

with p_A+p_B = const:

$$r = k \cdot \frac{K}{1 + K \cdot (const)} \cdot p_A \cdot \theta_B = k^* \cdot p_A \cdot \theta_B\,, \tag{61}$$

which is basically the Eley-Rideal model. Since in this case, a distinction between these two models is not possible, a decision between both models is needless. One could also further reduce the model and combine all constants regarding the surface coverage of B in constant k and reduce the reaction to a pure gas-phase reaction, but the coverage is needed for the simulation. Not only gas-phase molecules can react to form the mixed isotope molecules but also oxygen from the catalyst surface. Since the experiments are isobaric and isothermal the surface of the catalyst has to be covered with a constant amount of oxygen. Additionally, surface sites might be able to activate oxygen molecules and might be able to exchange oxygen atoms of the catalyst material with the adsorbates. Those two species, since they cannot be easily distinguished by this kind of experiments, are therefore condensed in the

parameter θ_i. Four reactions of the gas phase with the catalyst surface now have to be considered:

$$r_1 = k_1 \cdot p_{36O_2} \cdot \theta_{16O} \,, \tag{62}$$

$$r_2 = k_2 \cdot p_{34O_2} \cdot \theta_{16O} \,, \tag{63}$$

$$r_3 = k_3 \cdot p_{34O_2} \cdot \theta_{18O} \,, \tag{64}$$

$$r_4 = k_4 \cdot p_{32O_2} \cdot \theta_{18O} \,, \tag{65}$$

with k as the reaction rate constant which is temperature dependent according to the Arrhenius equation:

$$k_i = k_{i0} e^{-\frac{E_{Ai}}{RT}} \,. \tag{66}$$

For simplicity reasons, the kinetic isotope effect is neglected in the simulation, reducing the reaction constants k_i to one mutual constant k for all reactions. Whereas the kinetic isotope effect is quite significant in experiments regarding hydrogen, using oxygen isotopes with much higher mass (16 and 18 units compared to 1 and 2 units) the effect is not as strong. Assuming a harmonic oscillator for a diatomic molecule:

$$\nu = \frac{1}{2\,\pi} \sqrt{\frac{k_f}{\mu}} \,, \tag{67}$$

with:

$$\mu = \frac{1}{m_A} + \frac{1}{m_B}, \tag{68}$$

the oscillation frequency in the case of H_2 and D_2 changes significantly by a factor of 1.41, whereas in the case of $^{16,16}O_2$ and $^{18,18}O_2$, the factor changes by just 1.06. Though it will slightly affect the oxygen splitting kinetic. For this qualitative consideration, the effect can be neglected. The differential equations for the partial pressures only regarding the time dependence can now be expressed as:

$$\frac{dp(^{32}O_2)}{dt} = +r_2 - r_4 \,, \tag{69}$$

$$\frac{dp(^{34}O_2)}{dt} = +r_1 - r_2 - r_3 + r_4 \,, \tag{70}$$

and:

$$\frac{dp(^{36}O_2)}{dt} = -r_1 + r_3 \,. \tag{71}$$

Next to the reaction, the gas flux ($\dot{V}$) along the z-axis has to be considered:

$$\frac{dx_i}{dt} = \sum_j \nu_i \frac{r_j}{p_0} + \frac{dx_i \frac{\dot{V}}{V(z)}}{dz}, \tag{72}$$

with:

$$x_i = \frac{p_i}{p_{total}}, \tag{73}$$

$$V(z) = \pi \cdot r^2 \cdot z \cdot \epsilon, \tag{74}$$

and ε the porosity of the catalyst bed (estimated as 1/3). Next to the gas phase in the PFTR, the solid catalyst phase has to be considered. The 18-isotope oxygen can diffuse into the bulk of the material, where the 16-isotope can diffuse out of the lattice by bulk diffusion and is modeled using a modified version of the 1st law of Fick for diffusion:

$$\frac{dx_i}{dt} = D \cdot \frac{dx_i}{dr} \cdot \frac{A(r)}{V(r)}, \tag{75}$$

and temperature dependence for the bulk diffusion estimated by the Arrhenius equation:

$$D = D_0 e^{-\frac{E_A}{RT}}. \tag{76}$$

The modification is necessary due to the area and volume changes to the inner part of the particles. The closer the exchange to the core of the particle, the smaller the total volume (total amount of oxygen atoms in the volume fraction) as well as the exchange area. The volume and area of the particle were calculated by assuming a spherical geometry:

$$V(r) = \frac{4}{3} \cdot \pi \cdot r^3 \tag{77}$$

and:

$$A(r) = 4 \cdot \pi \cdot r^2. \tag{78}$$

To calculate the radius (r) and the total number (N_P) of particles inside the reactor, the specific surface area (S_A) and weighing (m_{cat}) of the catalyst inside the reactor was used:

$$V_{cat} = \frac{m_{cat}}{\rho_{cat}} = N_P \cdot \frac{4}{3} \cdot \pi \cdot r^3 \tag{79}$$

and:

$$S_A = N_P \cdot 4 \cdot \pi \cdot r^2 \,. \tag{80}$$

Having now two equations for the variables, the radius and number of catalysts particles can be estimated. The last missing part for the simulation is the catalyst surface. As stated before, there are probably two distinct surface species that cannot be distinguished on the catalyst surface active surface oxygen directly belonging to the catalyst material and adsorbed oxygen. Considering the high temperatures of the experiments the number of adsorbed oxygen atoms/molecules, compared to the exposed surface oxygen atoms of the catalyst can probably be neglected. The number of oxygen atoms on the surface can be estimated using the surface area (S_A) and the lattice parameter of calcium oxide α (4.808 Å), with two oxygen atoms being present in the square of one lattice parameter, due to its rock salt structure. Assuming only a fraction (n_f) of the surface oxygen atoms are active, θ can now be calculated as followed:

$$\theta = \frac{n_f}{S_A \cdot m_{cat} \cdot \frac{2}{\alpha^2}} \,. \tag{81}$$

Under the assumption, that the active oxygen species on the catalyst surface can exchange oxygen atoms via diffusion with the surrounding, which is the first non-reactive catalyst layer, all parts of the model can now be implemented.

Since the software can only solve 1-dimensional differential equations, the catalyst bed, as well as the catalyst particles are segmented. The catalyst bed is treated as a cascade of Z ideally mixed CSTRs in which the catalyst particles are evenly distributed. In each reactor segment are n particles (Np/Z) which consists of R_R layers. Going from the catalyst surface R_R=0 to the inner part of the particle, the catalyst particles are segmented in multiple layers, where each layer is ideally mixed. In the outer surface layer of the catalyst R_R=0, the gas phase can exchange oxygen atoms with the surface, as well as the bulk. Connecting the diffusion equations with the gas phase reaction. For each of the now R_R times, Z elements a time-dependent differential equation is formulated using the before described model (the Berkeley Madonna code can be found in the Appendix). The now existing model consists of a lot of parameters that are unknown and have to be estimated. For the activation energy for the reaction, 100 kJ/mol and for the diffusion 200 kJ/mol were assumed, which are reasonable values for these constants. For k_0, D_0, and n_f no data is available and therefore have to be guessed for the simulation to result in reasonable reaction courses. With now a physically reasonable model a parameter study can be performed to analyze the measured SSITKA courses. In the Appendix (Figure S 17,

page nn) an exemplary simulation can be found for all gas-phase oxygen species in the individual reactor segments. For clarity and due to the complementarity of the courses of the different oxygen molecules ($^{32}O_2$, $^{34}O_2$, and $^{36}O_2$) only the course for $^{34}O_2$ is discussed in the qualitative simulation, though all are simulated.

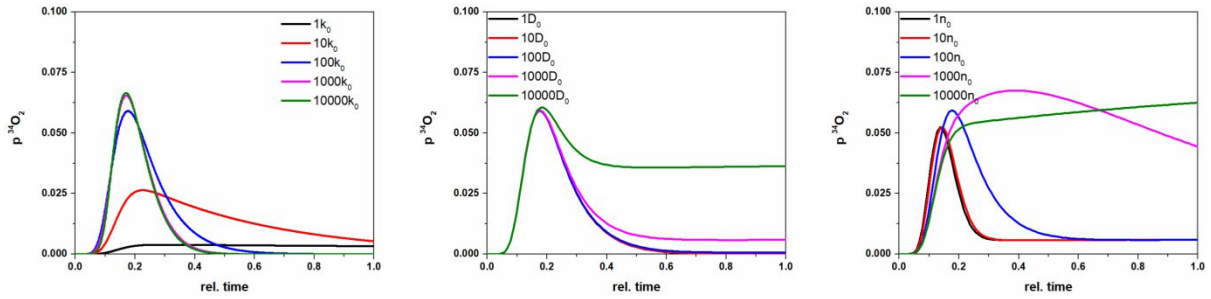

Figure 56: Parameter study of frequency factor k_0 (left), the diffusion coefficient D_0 (middle) and the active surface fraction n_0 (right) on the $^{34}O_2$ response in simulated SSITKA courses.

In Figure 56 simulated isotope exchange courses are depicted varying the reaction rate constant (k_0), the diffusion coefficient (D_0), and the fraction of active surface oxygen atoms (n_f). For the variation of the reaction constant, with increasing value, the $^{34}O_2$ formation is higher at the beginning of the experiment resulting in a narrow peak-like shape. A fast reaction of the gas with the catalyst surface will result in an immediate scrambling of the gas phase oxygen by saturating the catalyst surface with the 18-isotope oxygen, depleting all the reactive 16 oxygen from the surface. When all the 16-oxygen is gone from the gas phase, the formation of $^{34}O_2$ stops, ss the reaction constant too high, an effect cannot be observed. The observed width of the signal is not a result of the low reaction rate but due to the residence time behavior of the reactor. A low reaction rate will cause a significant broadening of the signal. Even though the $^{32}O_2$ isotope is consumed and displaced from the gas phase, the reaction goes on until the 16-oxygen isotope is totally depleted from the catalyst surface. The variation of the rate of diffusion has no impact on the initial formation of the $^{34}O_2$ but induces an "offset" of the $^{34}O_2$ after the gas-phase reaction. Allowing a diffusion of the bulk oxygen to the material surface creates a large reservoir of oxygen (500 µmol in the catalyst compared to 160 µmol/min oxygen flux) allowing a stable formation of $^{34}O_2$ even after the total displacement of the $^{32}O_2$ from the gas phase. The higher the diffusion rate is chosen, the higher the "offset". Varying the fraction of reactive surface oxygen (n_F) has a more complex impact on the shape of the simulation results. In principle, increasing n_F has the same effect as reducing k_0 while increasing the integral of the resulting peak. When the overall number of active oxygen species is low compared to the gas phase oxygen species, the change of n_F has no impact on the simulation (Figure 56, right graph, black and red curve). The scrambled oxygen species is a product from gas-phase oxygen molecules activated on the catalyst surface. With more accessible oxygen, the reservoir of oxygen at the catalyst becomes significant compared to the gas phase. The scrambled oxygen is

now also a product of oxygen exchanged with the catalyst material, therefore the overall integral of the scrambling product increases. With even more accessible oxygen on the surface, the maximum of the peak is retarded. Due to the large reservoir on the catalyst surface, the majority of oxygen in the reactor is 16-oxygen, even after displacing the initial gas phase. When the surface is evenly saturated with 18- and 16-oxygen, the formation of $^{34}O_2$ is maximized. Using these simulation results, the courses in (Figure 49 and Figure 51) can now be qualitatively analyzed.

Due to the temperature dependence of the reaction rate constant as well as the diffusion coefficient and the reaction being performed at three different temperatures, the first obvious assumption would be an increase of those two parameters to explain the change in the shape of the reaction courses. Comparing the results of the SSITKA experiments (Figure 49) with the parameter variation of the reaction and diffusion coefficient (Figure 56, left and middle) proves, that the change of the course with the temperature cannot be explained by an increase of those two parameters. Though an increased offset can be observed switching the gases at higher temperatures, the significant narrowing of the signal caused by the increased reaction rate cannot be observed. The reaction is probably already so fast, that this experiment cannot resolve the reaction rate (compare to Figure 56, left, green and pink plot). Rather than the increase of diffusion and reaction rate, the increase of the abundance of reactive oxygen species (n_F) fits the experimental data rather nicely. An explanation for this behavior can be the formation of new active sites at the surface at higher temperatures, for example by increasing the defect concentration, or removing impurities (e.g. residual hydroxide or carbonate groups) from the material surface. Surface dynamics shown by metal particles in reactive atmospheres[194] are not likely to be the causes of this behavior. A dynamic change of the surface would mean, that all oxygen atoms at the surface would always be available for the oxygen exchange, and the increased temperature would increase the rate of exchange within this surface, but the overall integral of oxygen atoms at the surface would always be the same. With regard to Figure 50, the total integral of exchangeable oxygen atoms appears to increase, contradicting a dynamic surface behavior.

Since the pure calcium oxide and 0.1% manganese sample showed only minor differences in the oxygen exchange behavior, the comparison of low and higher doped samples is more interesting. In Figure 57, the $^{34}O_2$ reaction courses are depicted in comparison to the parameter variation of the diffusion coefficient and the fraction of active oxygen atoms on the surface.

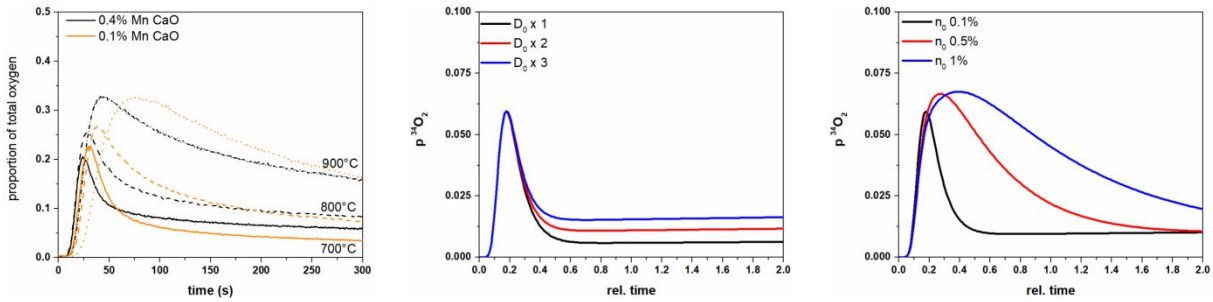

Figure 57: Comparison of experimental data (left) with the diffusion coefficient variation (middle) and the variation of the active surface fraction (right).

Comparing the lower doped sample (left graph, orange) with the simulation results, a good agreement can be found with the n_F variation, as well as a minor increase in the diffusion coefficient. In contrast to that, the shape of the curve of the slightly higher doped sample (left graph, black) shows a different trend. The maximum of the $^{34}O_2$ formation is not as much shifted with the temperature as that of the lower doped sample, the baseline of the scrambled oxygen after switching appears to be significantly higher and the peak like shape is better preserved. These results indicate a significantly altered diffusion coefficient of the higher doped sample compared lower doped one. Rather than cleaning or formation of new active sites with increased temperature, the additional oxygen atoms for exchange become available in this sample by enhanced diffusion. Since the diffusion in solid materials is basically a function of the number of structural defects,[195] the insertion of additional manganese centers in the calcium oxide host lattice might introduce defects, beneficial for the oxygen conductivity.

5. General Discussion

Phase pure metal-doped calcium carbonates as oxide precursors were synthesized by extending the aging time following the precipitation to 24 h, allowing the conversion of the metastable vaterite phase to the thermodynamically favored calcite phase. No indication for phase separation of the dopants can be observed using XRD analysis, neither in the precursors nor in oxide materials. Though the doping metal in the case of Ni appears to have an influence on the crystallization of calcium carbonate during the precipitation process, prolonging the lifetime of the vaterite phase during aging. Whether the metal is directly exchanging a Ca^{2+} in the host lattice also remains unclear. Following the Hume-Rothery rule, none of the dopants are likely to form a stable solid solution, due to the significant difference >15% in atomic dimension. Due to their low concentration in the host lattice, verification is also very challenging and remains to be shown. In the case of Fe^{3+} doped CaO, a clustering of the transition metal is known to occur,[126] probed by EPR. While in the case of e.g. Mn-doped CaO this appears not to be the case.[128]

The first question to be discussed now is whether the catalysts can be considered as doped CaO. A definitive answer can, despite the efforts, unfortunately not be given. However, several indicators can support this claim. Even in the highest doped sample in the case of manganese doped calcium oxide, no phase separation can be observed via XRD (Figure 6, page 39), also a significant lattice contraction was found indicative for the exchange of Ca atoms with smaller atoms. Additional pieces of evidence for the successful exchange of Ca^{2+} center with Mn^{2+} are the results of the EPR measurements, showing especially in the lower doping range very sharp peaks and a splitting constant of 86 G could be measured which is consistent with literature data.[128,160] The narrow linewidth implicates a very weak interaction of Mn with each other, meaning site isolation. In the recorded Raman spectra for 0.1% Mn-doped CaO no signals can be found indicative for surface metal oxides, supporting the claim of lattice incorporation as well. With increasing doping, however, new signals arise, indicating the formation of new manganese species. Comparing those to literature data on manganese oxides or $CaMnO_3$ (Figure S 14: Arrhenius plots for Mn and Ni doping series.Figure S 14, page ii) no matches can be found.[172–175] This can at least confirm the absence of segregated manganese oxide species on the surface. A speculative reason for the emergence of new signals can be the distortion of the isotropic CaO lattice, creating new vibrational modes. This, however, cannot be confirmed in this study. The addition of transition metal dopants to CaO also has a significant influence on the photoluminescence of the sample. Where alkaline dopants have been found to enhance the luminescence intensity of CaO and Ce^{3+} can be used to shift the emission spectrum,[84] here, the doping of CaO with transition metals mainly results in a loss of luminescence. Already with the addition of small amounts (0.04 mol% Mn, 0.1 MnCaO) the overall photoluminescence is strongly reduced and the luminescence derived from edge sites becomes more prominent (feature at 290 nm, Figure 8 left, page 40) due to site isolation.[120] The introduced

transition metals are likely to offer new energy states favoring the non-radiative recombination for surface excitons. The observed behavior appears to be independent of the nature of the dopant (Figure S 2). Nevertheless, the significant reduction of luminescence intensity confirms the alteration of the electronic structure of the material surfaces matching the significantly altered catalytic activity. The TPR measurements can neither prove, nor disprove the successful formation of a solid solution, however, in all measured samples, independent of the doping metal, all metal atoms were reducible, meaning even if incorporated in the host-structure, the dopants are accessible. With increasing doping concentration, the TPR profiles of the Ni- and Mn-doped samples change drastically. The profile of the 1.6% Mn-doped sample is quite similar to that of the reduction expected for MnO_2 but shifted to higher temperatures,[139] proving a stabilizing interaction of the Mn with host material, but also a change of the Mn species, when going to higher doping concentrations. The SSITKA experiments on the 0.1% Mn-doped CaO sample showed no significant differences in the metal-doped sample compared to the pure CaO sample. With the qualitative simulation showing a good sensitivity of those experiments towards the oxygen diffusion coefficient as well as the amount of active surface oxygen species, it can be concluded, that those two parameters are hardly changed with the addition of small amounts of doping. Assuming the Mn to be located at the surface of the catalyst, a significantly increased amount of active surface oxygen should be expected, with manganese oxide being known to be redox active at investigated temperatures. Comparing the lower doped sample 0.1% with the 0.4% sample, the overall shape is still pretty similar, meaning the diffusion and reaction constants are still comparable to those of pure CaO. However, slight differences can be observed. By matching the SSITKA traces with simulated curves (Figure 57, page 99), an increased diffusion coefficient, as well as an increased abundance of active surface species can be reasonably assumed. Assuming a statistic distribution of the dopant in the host lattice, the presence of doping material on the surface has to be expected, thus higher abundance of active oxygen species on the catalyst surface is expected with the increased doping content. With the diffusion coefficient being related to the structural defects in the material, the increase is also reasonable with the increasing amount of dopant.[195] The formation of defects in AEOs by impurities is well known. Substitutional ions with different charge states than the original ions cause the formation of charge compensating defects.[46] Also, due to the different sizes of the cations, a distortion of the lattice is to be expected, which can be seen by the reduced lattice constants calculated from the XRD measurements (Figure 32, page 63). This can significantly alter the diffusion coefficient.

With this, one can also conclude on effects of the dopant on the bulk and surface properties of the catalyst. Up to a concentration of 0.1%, the dopant mainly changes the surface properties of the material, which becomes evident by having a look at the PL measurements. With the PL of CaO being a function of the surface,[196] which was also proven by the oxygen quenching experiments (Figure 10, 11, page 42), the strong reduction and definition of the PL spectrum can prove a surface property change induced by the doping. However, the dopant adds reducibility to the usually

irreducible CaO. Bulk properties, such as the diffusion coefficient are not altered by a measurable degree. At concentrations above 0.4%, also the changes in the diffusion coefficient become evident by the SSTIKA experiments, indicating a strong impact of the dopant on the bulk properties of the material.

With the significantly altered properties, especially in the PL, the materials can also be expected to show significantly altered catalytic performances. The addition of transition metal doping, regardless of its nature, reduces the apparent activation energy of the OCM reaction in steady state experiments (Table 2, page 50) and also alters the selectivity. In general, transition metals with stable oxidations states of 2 caused a slight improvement of the selectivity, whereas Co and Cr doping caused a decrease in selectivity. In the case of MgO, Fe doping could also be found to slightly improve the catalytic performance.[197] In the case of Cr doped CaO, almost no C_2 products at all were formed. Looking at the TPR profile (Figure 17, page 47) a single event reduction peak is observed attributable to an oxidation state change from Cr^{6+} to Cr^{3+}. A single Cr center can thus provide multiple oxygen atoms for adsorbing hydrocarbons, resulting in an overoxidation. Another explanation could be segregated chromium oxide particles at the catalyst surface, but comparing the obtained TPR profile to that of supported chromium oxide particles, a significant shift towards higher temperatures becomes evident, supporting a strong interaction of the Cr ions with the CaO host lattice, though similar trends can be found for single-atom catalysts e.g. Ni atoms on a MgO surface.[140,198] The studies of Freund et al. on doped Cr doped MgO and Mo doped CaO, also revealed significantly different behaviors of the two metals, when gold clusters were deposited on the doped surfaces.[68] Inspecting concentration series of doped CaO an optimum doping concentration can be found at concentration ranges below 0.1% in both, the Mn and Ni doped sample series, where an activation energy minimum can be found, as well as a selectivity maximum.

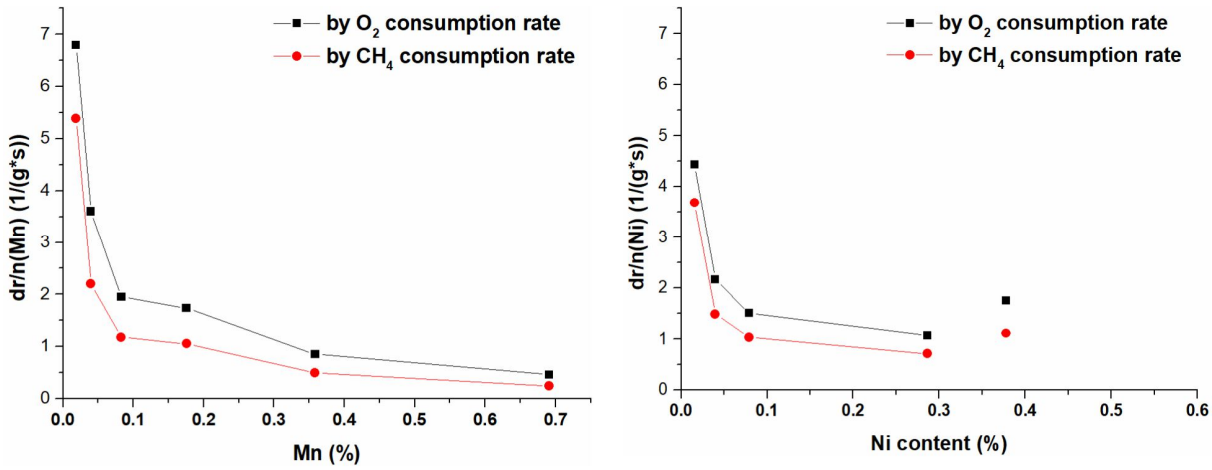

Figure 58: Change of oxygen and methane reaction rates divided by the amount of doping atoms vs total loading (50 mg carbonate precursor, 750 mg SiC, 50 ml/min 3:3:1 of CH_4:N_2:O_2, 705 °C).

In Figure 58 the change of the reaction rate per doping atom is plotted against the doping concentration. Also, in this diagram, it becomes evident, that the contribution of the single doping atom towards the reaction rate becomes less with an increasing amount of dopant. Looking at the EPR data, also a significant broadening of the signal can be observed with the increasing amount of dopant (Figure 15, page 46), indicating Mn-Mn interactions. Exchange interactions between close metal centers in CaO up to a range of 0.59-0.83 nm are a known phenomen.[125–129] Based on the catalytic data and the spectroscopic data obtained from EPR and PL measurements a model is proposed in Scheme 11, showing the interactions of the dopant in the host lattice with oxygen.

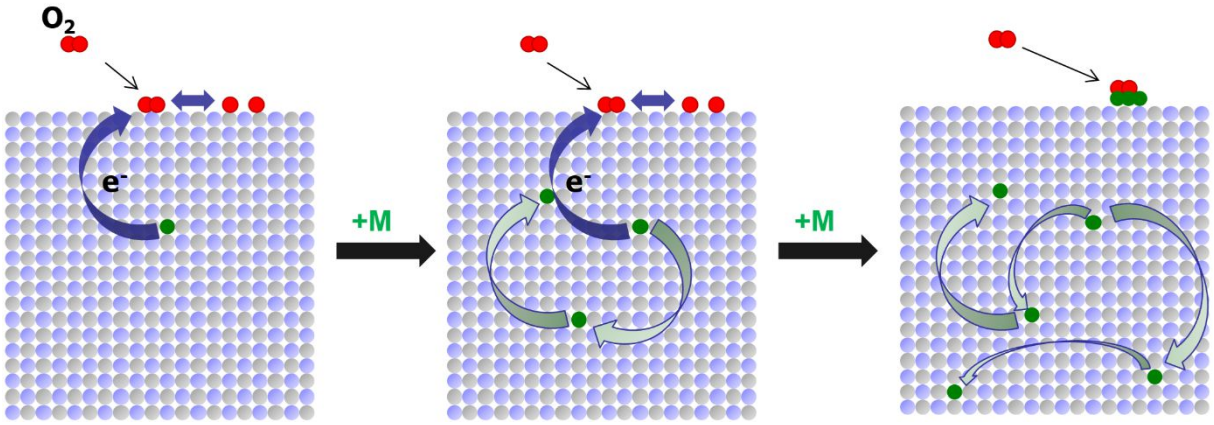

Scheme 11: Proposed mechanism of dopant-adsorbant interaction in transition-metal doped CaO.

The most isolated metal atom being the most efficient for activating oxygen. With additional doping, interactions between the dopants cause a decrease in the effect or even a phase separation in the worst case. Causing a signal broadening in the case of the EPR measurements and pathways for non-radiative relaxation processes in the case of the PL measurements. A different model is proposed by the Nørskov group. They did theoretical calculations for doped AEMOs, with the dopant located in the (110) surface layer, showing potential for increased turnover frequencies. However, their study shows a rather large impact of Sr and Mg impurities on the calculations. Both metals are always present in CaO and cannot be avoided. Also consistent with this work is their finding, that the overall improvements to be achieved by doping CaO are rather limited compared to doping MgO.[70] The study though has to be taken with caution, with the (110) plane most likely not the dominant active site for methane activation (refer to Figure 59).[67]

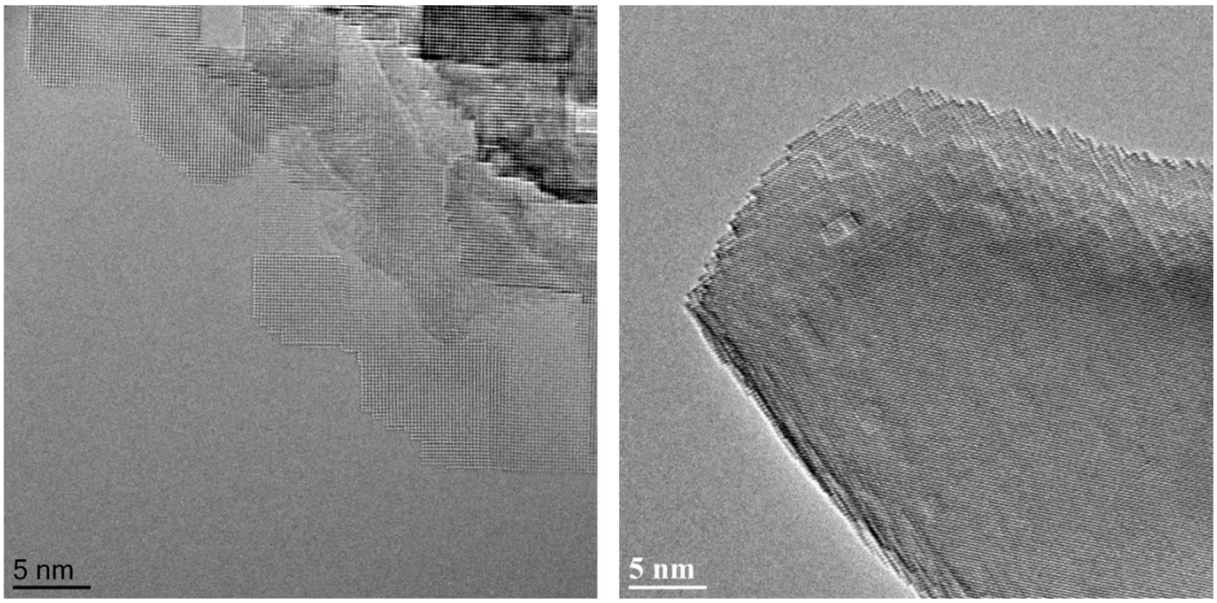

Figure 59: HR-TEM image of MgO (left) and CaO (right) synthesized by decomposing the corresponding hydroxides.[c]

An indication, that the changes in catalytic performances are not due to the generation of a redox catalyst with a Mars-van-Krevelen type kinetics can be seen in the isotope scrambling experiments. Where the doped CaO samples all behave very similarly (Figure 49 and Figure 50 page 84) and an Elay-Rideal model can be used to describe the traces, meaning the gas-phase surface interaction shapes the SSITKA course, completely different behaviors can be observed for the redox-active $NaMnWO_x@SiO_2$ catalyst in the PIOS experiments. The uptake of the isotope is so fast, that at the beginning of the experiment no scrambled oxygen isotopes are formed (Figure 42, page 76). The released and therefore also reactive surface oxygen is, in this case, the bulk oxygen itself and not formed from surface intermediates:

$$O_2(g) \rightleftharpoons O_2(s) \overset{e^-}{\rightleftharpoons} O_2^-(s) \overset{e^-}{\rightleftharpoons} O_2^{2-}(s) \rightleftharpoons 2\,O^-(s) \overset{2e^-}{\rightleftharpoons} 2\,O^{2-}(s). \quad (82)$$

This might also be an indication of why CaO might not be a good OCM catalyst like the $NaMnWO_x@SiO_2$ catalyst. The $NaMnWO_x@SiO_2$ dominantly provides a single species of oxygen, wherein the case of CaO a multitude of species should be present according to the equation (82). Given the possible presence of such intermediates on the surface of CaO under OCM conditions, reaching high selectivity to C_{2+} products is quite challenging, assuming that activated oxygen species and molecular adsorbed oxygen are not selective towards C_2 formation, but directing the reaction towards oxygen insertion.[150,199] The complicated situation occurs because the same site appears to be responsible for the selective as well as the unselective oxidation of

[c] Taken with permission from *Synthesis and characterisation of calcium oxide catalysts for the oxidative coupling of methane (OCM)*[211], a section of the left picture was published,[67] the copyright clearances have been obtained.

methane. This means that the selectivity is dependent on the competitive adsorption of oxygen and methane on the active sites. How far the transition metal doping now affects the oxygen activation in CaO, the isotope experiments, unfortunately, give hardly any insight. It becomes evident, that in all tested catalyst oxygen could be cleaved but the reaction rate of the activation could not be obtained. As stated before, the time scale of the experiment is too large to resolve the rate of reaction. The only statement that can be made is that increasing doping with transition metals increase the oxygen diffusion rate in the bulk catalyst. Also, the in situ TG, IR, and Raman experiments yielded no insight into the oxygen activation on the catalyst surface. As discussed before, the oxygen activation most likely takes place on O^- sites, which can be formed on step sites. The same sites have been proposed to be active for alkane activation[178,200] and CO_2 scrambling.[188] The presence of oxygen in the gas phase is necessary for the reaction to take place,[201] therefore the O^- species alone cannot be active for methyl radical formation. In the case of MgO, methane activation was directly correlated to the abundance of monoatomic step sites, wherein the presence of oxygen the heterolytic splitting of methane forming peroxide species takes place.[67,93] The absence of a Raman signal in the range of 700-1000 cm^{-1} also supports the theory of only a very minor part of the surface, such as step sites, being involved in the reaction, even though the influence of metal impurities in CaO cannot be neglected completely having found the sodium content to be below 50 ppm and the main impurity to be Sr with 150 ppm, which is known to be capable of forming peroxide species.[169]

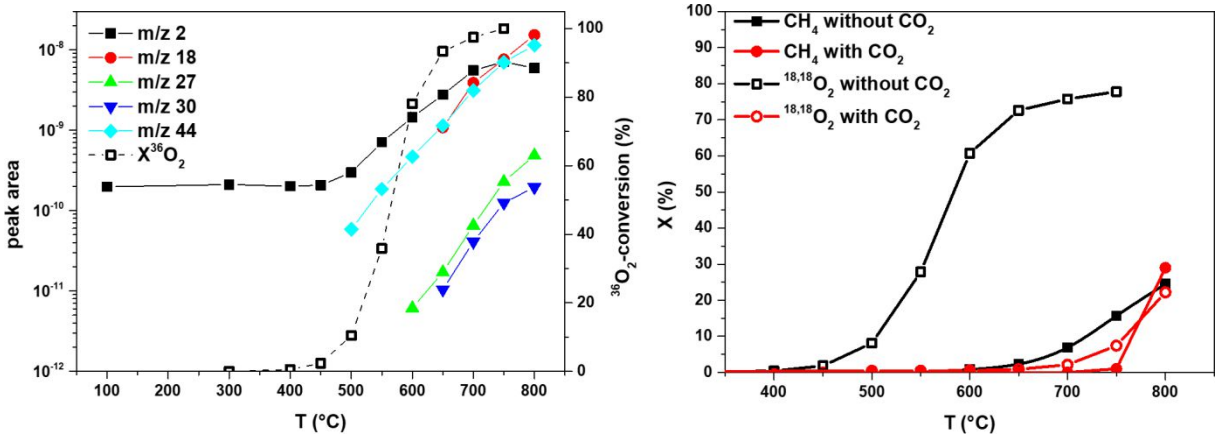

Figure 60: Direct comparison of oxygen exchange in flowing synthetic air (30 ml/min, 80% He and 20% O_2) by dosing 500 µl labeled synthetic air (hollow symbols, dashed line) with product formation during pulsed methane oxidation (flowing 30 ml/min synthetic air and dosing 250 µl CH_4, left); Comparison of conversion of oxygen (black) and CH4 (red) in experiments when 20 % of He is replaced by CO2 over 27 mg of CaO (25763) in 740 mg of SiC (right).

The observed of carbonate formation during in situ experiments (Raman, IR, and TG) and temperature-programmed catalytic tests reveals the biggest drawback regarding designing new catalysts based on AEMOs. Finding (I): accordance in the onset temperature of OCM and oxygen activation (Figure 60, left) as well as (II):

comparable poisoning of the two reactions by CO_2 in the gas phase (Figure 60, right), indicate that similar sites are involved in oxygen activation and OCM over CaO.

The challenge is now to avoid the poisoning effect by side- and by-products of the reaction. Carbon dioxide blocks the active sites, which, depending on the temperature, can have a significant influence on the yield of the reaction.[202–204] At lower temperatures, CO_2 blocks the active sites by carbonate formation, at higher temperatures, it adds to the competitive adsorption on the active sites and can, therefore, influence activity and selectivity of the catalyst. Here, in agreement with findings on MgO,[66] no significant influence was found, despite a significant carbonate accumulation at lower temperatures (Figure 26, left, page 57). This can be attributed to the use of an integral reactor. While in the inlet there is no CO_2, the initial part of the catalyst bed is not affected by carbonate formation, whereas the downstream part of the catalyst bed is converted to carbonate and inactive in the reaction. With increasing temperature more of the catalyst bed is converted to CaO, adding to the overall activity, explaining the steady behavior of conversion and product formation. Another negative influence of carbon dioxide is the enhanced sintering of CaO, reducing the active surface.[205] Hydroxide formation was not observed under reaction conditions, but a partial OH termination of the surface is very likely. As OH can interact with alkanes by H exchange,[123] their influence has to be considered in a microkinetic model for the oxidative coupling of methane on CaO.

Given now the discussed circumstances, the evaluation of the impact of the dopant on the oxygen activation is not feasible. The effect is overshadowed by the blockage of the active sites. Comparing the doped samples in the PIOE experiments, the effects are marginal at best and well in the experimentation error (figure 64, page 81). All of the measurements still show a similar course and are blocked in the same manner, meaning, that the activity is still dominated by the properties of the basic CaO rather than the presence of surface metal particles. This supports the claim, that the dopant mainly modifies the electronic structure of CaO and not creating a supported metal catalyst by phase segregation.

6. Conclusions

The synthesis of transition metal doped calcium carbonate could be optimized, yielding phase pure calcite materials. By decomposing of those precursors, transition metal doped CaO catalysts for the OCM reaction were obtained. EPR and XRD analyses suggest good incorporation of the metals into the host lattice. PL measurements reveal a significant effect of the dopant on the electronic surface structure, the PL spectrum gets more defined as well as less intense, suggesting the creation of pathways for the non-radiative relaxation.

The nature of the dopant has a strong impact on the reactivity, where Ni, Mn, and Zn were found to have a positive effect on activity and selectivity, Cr and Co were found to strongly decrease the selectivity of the reaction towards C_2 products. improvement in the catalytic performance of the doped materials is only minor. An optimum doping concentration was found in the rage of 0.05-0.10 mole%, where the highest selectivity, as well as the lowest apparent activation energies, were found for Mn- and Ni-doped catalysts.

In situ Raman and thermogravimetric experiments confirm the possibility of bulk carbonate formation at lower reaction temperatures (depending on CO_2 partial pressure) and, therefore, CO_2 acting as a catalyst poison under certain reaction conditions. At higher temperatures, competitive adsorption of CH_4, O_2, H_2O, and CO_2 has to be considered to explain the selectivity and activity of the catalyst. The formation of hydroxide species was not found under reaction conditions. No clues were found to the active site or activated oxygen on the catalyst surface.

A simple oxygen scrambling method was developed to qualitatively analyze the oxygen activation capability of calcium oxide. An apparent activation energy towards scrambling was found to be 80 kJ/mol, which is far less than the dissociation barrier of oxygen on pristine CaO surfaces, making defect sites more likely to be the active site for this reaction. Calcium hydroxide and calcium carbonate were found to be inactive (or at least magnitudes less active compared to CaO) towards the oxygen scrambling, and, therefore, the oxygen dissociation. Oxygen scrambling of CO_2 and H_2O with O_2 was observed on CaO even though the activation energy for O_2 scrambling was found to be significantly higher in the presence of those gases, 110 kJ/mol in presence of water and 150 kJ/mol in presence of carbon dioxide. Small amounts of impurities in the gas feed were found to quench the scrambling activity of CaO, explaining why the catalytic activity of CaO is only observed above 500°C. The trends of the scrambling activity did not change with the doping of CaO, suggesting the basic sites are also the active sites on the doped samples.

The onset of OCM reaction and oxygen scrambling were directly correlated suggesting that the same active sites are most likely responsible for both reactions. The ability to dissociatively activate oxygen appears to be imperative for the OCM to take place on CaO. The increased activation energy of O_2 scrambling in presence of

H_2O and CO_2 indicates, that the rate of desorption of surface species formed by the interaction of CaO with water and carbon dioxide, such as OH groups and carbonate species, is most likely the rate-determining step for this reaction.

SSITKA experiments were conducted and a qualitative model was developed to simulate the obtained data. With increasing temperature, the increase of active surface oxygen atoms was found, supporting the findings in the oxygen scrambling experiments of blocked active sites. Doping with low amounts of transition metals did not show major improvements in these experiments, with higher doping amounts, only an enhanced oxygen diffusion rate could be determined.

The results clearly show that neither oxygen nor C-H activation account for the very high reaction temperatures generally applied in OCM over alkaline earth oxides, but the regeneration of the active sites. Based on these findings targets in catalyst development are endorsed that comprise defect engineering to create sites for O_2 and C-H activation and surface modifications to ensure weak interactions of the catalyst with the by-product water and the side product carbon dioxide.

7. Outlook

In the case of MgO, Au deposition on the catalyst surface improved the stability of the transition metal doped catalyst in the OCM reaction, as well as deactivated the pure MgO catalyst. TEM investigations revealed an agglomeration of the gold atoms on kinks, which are known to be active sites for the OCM reaction.[66,67,206] Modifying doped CaO catalysts by gold deposition can also help to stabilize the catalyst. Blocking the kink sites might also result in a weaker interaction with water as well as carbon dioxide, allowing the OCM at reduced temperatures. For this purpose, a new setup has to be designed allowing a physical vapor deposition of gold on the activated CaO surface.

Still, the prospects of a CaO based catalyst being a promising novel catalyst for the OCM reaction is unlikely due to the before discussed restrictions. Also, the insights obtained from basic research on these types of materials are hardly transferable to other systems. Just from the inspection of the PIOE experiments, it becomes evident, that the activation mechanism of irreducible oxides is not comparable to the mechanism on a reducible oxide such as the $NaMnWO_x@SiO_2$ system. Inspecting the vast amount of screened materials so far with limited success (Figure 61), new approaches are needed to find a suitable catalyst.

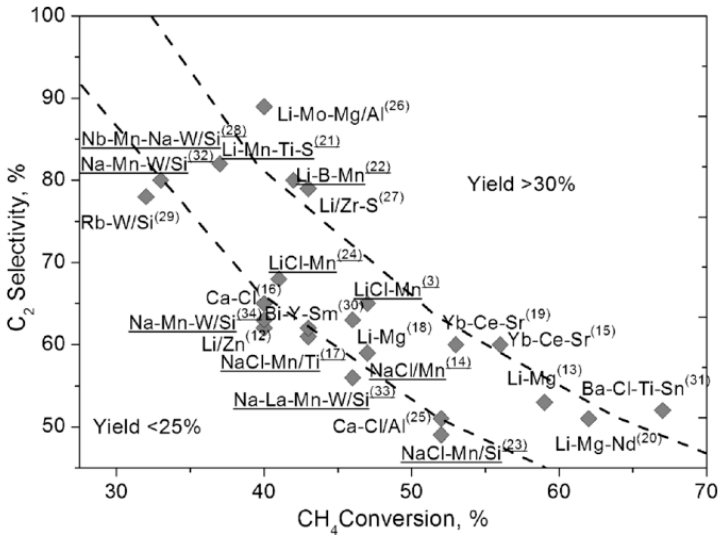

Figure 61: Elemental compositions of OCM catalysts with $Y(C_2)$25% reported in the literature. All the catalysts were tested in a fixed-bed reactor in the co-feed mode under atmospheric pressure at temperatures from 943 to 1223 K, $p(CH_4)/p(O_2)$=1.7–9.0, and contact times from 0.2 to 5.5 s.[d]

[d] Taken from Zavyalova et al., ChemCatChem, **2011**, 3, 1935-1947, with permission from Wiley and Sons.[6]

Theoretical calculations can offer a hint to improved materials, but often only reaction rates can be predicted.[70] Predicting the selectivity of the reaction is still often not feasible. A quite novel approach to finding new catalysts is provided by machine learning algorithms.[207,208] Machine-learning offers a unique opportunity to find the relevant descriptors necessary for a good reaction performance. The downside is the vast amount of reliable and reproducible data needed for the evaluation. Since performances can be influenced by reactor geometries and catalyst history and so on, just taking the data from the literature might not work. Even this work has shown, that already minor impurities can have a significant effect on the catalytic performance. Thus, setting up a machine-learning algorithm to find a new catalyst might require a mass screening of also old and new materials, combined with a detailed analysis of the materials.

An approach to yield a better reaction yield can be the process/reaction engineering. In low conversion ranges, a selectivity of almost 100% can be achieved by feeding an excess of methane, reducing the possibility of a consecutive reaction. To make it economically feasible highly efficient membranes are needed to efficiently recycle the methane.

Also, chemical looping can be an approach to reach a higher yield. By removing oxygen from the gas phase, secondary reactions can be prevented. The $NaMnWO_x@SiO_2$ catalyst has shown a stable, reproducible redox capability allowing in the first step the oxidation of the material with oxygen and after purging the reactor from oxygen a reduction with methane, where C_2 products are being formed.[151] Up to now, the space-time yield is still too low for the economic implementation of chemical looping OCM.[61]

Another approach to make OCM economically feasible can be the coupling of the OCM reaction with other reactions. By for example coupling the OCM reaction with a downstream methanol synthesis a value-adding process can be conceived. By feeding CO_2 to the OCM feed the diluent can be omitted and produced CO and CO_2 can be hydrated to methanol, without previous separation of the OCM products. Since the OCM does not work well at high pressures a low-pressure methanol synthesis would, therefore, be beneficial. First steps have already been taken, showing promising results.[209,210]

Literature Directory

(1) Ruble, I. The U.S. Crude Oil Refining Industry: Recent Developments, Upcoming Challenges and Prospects for Exports. *J. Econ. Asymmetries* **2019**, *20* (August), e00132.

(2) Zimmermann, H.; Walzl, R. Ethylene. In *Ullmann's Encyclopedia of Industrial Chemistry*; Wiley-VCH Verlag GmbH & Co. KGaA: Weinheim, Germany, 2009; pp 405–428.

(3) U.S. Department of Energy. Global Ethanol Production https://afdc.energy.gov/data/10331 (accessed Mar 12, 2020).

(4) Keller, G. E.; Bhasin, M. M. Synthesis of Ethylene via Oxidative Coupling of Methane: I. Determination of Active Catalysts. *J. Catal.* **1982**, *73* (1), 9–19.

(5) Rosenzweig, A. C.; Frederick, C. A.; Lippard, S. J.; Nordlund, P. Crystal Structure of a Bacterial Non-Haem Iron Hydroxylase That Catalyses the Biological Oxidation of Methane. *Nature* **1993**, *366* (6455), 537–543.

(6) Zavyalova, U.; Holena, M.; Schlögl, R.; Baerns, M. Statistical Analysis of Past Catalytic Data on Oxidative Methane Coupling for New Insights into the Composition of High-Performance Catalysts. *ChemCatChem* **2011**, *3* (12), 1935–1947.

(7) Siluria Technologies. Gemini - Natural Gas to Ethylene http://siluria.com/Products/Gemini_-_Natural_Gas_to_Ethylene (accessed Mar 12, 2020).

(8) Siluria Technologies. Oxidative Coupling of Methane http://siluria.com/Technology/Oxidative_Coupling_of_Methane (accessed Mar 12, 2020).

(9) Hammond, C.; Conrad, S.; Hermans, I. Oxidative Methane Upgrading. *ChemSusChem* **2012**, *5* (9), 1668–1686.

(10) Galadima, A.; Muraza, O. Revisiting the Oxidative Coupling of Methane to Ethylene in the Golden Period of Shale Gas: A Review. *J. Ind. Eng. Chem.* **2016**, *37*, 1–13.

(11) iea. Data Table Natural Gas 2017 https://www.iea.org/data-and-statistics/data-tables?country=WORLD&energy=Natural gas&year=2017 (accessed Mar 12, 2020).

(12) Makal, T. A.; Li, J. R.; Lu, W.; Zhou, H. C. Methane Storage in Advanced Porous Materials. *Chem. Soc. Rev.* **2012**, *41* (23), 7761–7779.

(13) He, Y.; Zhou, W.; Qian, G.; Chen, B. Methane Storage in Metal-Organic Frameworks. *Chem. Soc. Rev.* **2014**, *43* (16), 5657–5678.

(14) The World Bank. Increased Shale Oil Production and Political Conflict Contribute to Increase in Global Gas Flaring. https://www.worldbank.org 2019.

(15) GGFR. Improving Energy Efficiency & Mitigating Impact on Climate Change. The World Bank 2011, pp 3–4.

(16) bp. *BP Statistical Review of World Energy 2018*; 2018.

(17) Boucher, O.; Friedlingstein, P.; Collins, B.; Shine, K. P. The Indirect Global Warming Potential and Global Temperature Change Potential Due to Methane Oxidation. *Environ. Res. Lett.* **2009**, *4* (4).

(18) Levalley, T. L.; Richard, A. R.; Fan, M. The Progress in Water Gas Shift and Steam Reforming Hydrogen Production Technologies - A Review. *Int. J. Hydrogen Energy* **2014**, *39* (30), 16983–17000.

(19) York, A. P. E.; Xiao, T.; Green, M. L. H. Brief Overview of the Partial Oxidation of Methane to Synthesis Gas. *Top. Catal.* **2003**, *22* (3–4), 345–358.

(20) Tang, P.; Zhu, Q.; Wu, Z.; Ma, D. Methane Activation: The Past and Future. *Energy Environ. Sci.* **2014**, *7* (8), 2580–2591.

(21) Hansen, J. B.; Højlund Nielsen, P. E. Methanol Synthesis. In *Handbook of Heterogeneous Catalysis*; Wiley-VCH Verlag GmbH & Co. KGaA: Weinheim, Germany, 2008; pp 2920–2949.

(22) Kvisle, S.; Fuglerud, T.; Kolboe, S.; Olsbye, U.; Lillerud, K. P.; Vora, B. V. Methanol-to-Hydrocarbons. In *Handbook of Heterogeneous Catalysis*; Wiley-VCH Verlag GmbH & Co. KGaA: Weinheim, Germany, 2008; pp 2950–2965.

(23) Remans, T. J.; Jenzer, G.; Hoek, A. Gas-to-Liquids. In *Handbook of Heterogeneous Catalysis*; Wiley-VCH Verlag GmbH & Co. KGaA: Weinheim, Germany, 2008; pp 2994–3010.

(24) Dry, M. E. The Fischer-Tropsch (FT) Synthesis Processes. In *Handbook of Heterogeneous Catalysis*; Wiley-VCH Verlag GmbH & Co. KGaA: Weinheim, Germany, 2008; pp 2965–2994.

(25) Aramouni, N. A. K.; Touma, J. G.; Tarboush, B. A.; Zeaiter, J.; Ahmad, M. N. Catalyst Design for Dry Reforming of Methane: Analysis Review. *Renew. Sustain. Energy Rev.* **2018**, *82* (December 2016), 2570–2585.

(26) Akri, M.; Zhao, S.; Li, X.; Zang, K.; Lee, A. F.; Isaacs, M. A.; Xi, W.; Gangarajula, Y.; Luo, J.; Ren, Y.; et al. Atomically Dispersed Nickel as Coke-Resistant Active Sites for Methane Dry Reforming. *Nat. Commun.* **2019**, *10* (1), 1–10.

(27) Palmer, C.; Upham, D. C.; Smart, S.; Gordon, M. J.; Metiu, H.; McFarland, E. W. Dry Reforming of Methane Catalysed by Molten Metal Alloys. *Nat. Catal.* **2020**, *3* (1), 83–89.

(28) Lance, D.; Elworthy, E. G. Process for the Manufacture of Methyl-Alcohol from Methane. FR190607297X, 1905.

(29) Ravi, M.; Ranocchiari, M.; van Bokhoven, J. A. The Direct Catalytic Oxidation of Methane to Methanol—A Critical Assessment. *Angew. Chemie - Int. Ed.* **2017**, *56* (52), 16464–16483.

(30) Otsuka, K.; Wang, Y. Direct Conversion of Methane into Oxygenates. *Appl. Catal. A Gen.* **2001**, *222* (1–2), 145–161.

(31) Polnišer, R.; Štolcová, M.; Hronec, M.; Mikula, M. Structure and Reactivity of Copper Iron Pyrophosphate Catalysts for Selective Oxidation of Methane to Formaldehyde and Methanol. *Appl. Catal. A Gen.* **2011**, *400* (1–2), 122–130.

(32) Ravi, M.; Sushkevich, V. L.; Knorpp, A. J.; Newton, M. A.; Palagin, D.; Pinar, A. B.; Ranocchiari, M.; van Bokhoven, J. A. Misconceptions and Challenges in Methane-to-Methanol over Transition-Metal-Exchanged Zeolites. *Nat. Catal.* **2019**, *2* (6), 485–494.

(33) Periana, R. A.; Taube, D. J.; Evitt, E. R.; Löffler, D. G.; Wentrcek, P. R.; Voss, G.; Masuda, T. A Mercury-Catalyzed, High-Yield System for the Oxidation of Methane to Methanol. *Science (80-.).* **1993**, *259* (5093), 340–343.

(34) Gang, X.; Birch, H.; Zhu, Y.; Hjuler, H. A.; Bjerrum, N. J. Direct Oxidation of Methane to Methanol by Mercuric Sulfate Catalyst. *J. Catal.* **2000**, *196* (2), 287–292.

(35) Ahlquist, M.; Nielsen, R. J.; Periana, R. A.; Goddard, W. A. Product Protection, the Key to Developing High Performance Methane Selective Oxidation Catalysts. *J. Am. Chem. Soc.* **2009**, *131* (47), 17110–17115.

(36) Kao, L. C.; Hutson, A. C.; Sen, A. Low-Temperature, Palladium(II)-Catalyzed, Solution-Phase Oxidation of Methane to Methanol Derivative. *J. Am. Chem. Soc.* **1991**, *113* (2), 700–701.

(37) Zhou, Y.; Zhang, L.; Wang, W. Direct Functionalization of Methane into Ethanol over Copper Modified Polymeric Carbon Nitride via Photocatalysis. *Nat. Commun.* **2019**, *10* (1).

(38) Crabtree, R. H. Aspects of Methane Chemistry. *Chem. Rev.* **1995**, *95* (4), 987–1007.

(39) Schwach, P.; Pan, X.; Bao, X. Direct Conversion of Methane to Value-Added Chemicals over Heterogeneous Catalysts: Challenges and Prospects. *Chem. Rev.* **2017**, *117* (13), 8497–8520.

(40) Wang, L.; Tao, L.; Xie, M.; Xu, G.; Huang, J.; Xu, Y. Dehydrogenation and Aromatization of Methane under Non-Oxidizing Conditions. *Catal. Letters* **1993**, *21* (1–2), 35–41.

(41) Ma, D.; Zhu, Q.; Wu, Z.; Zhou, D.; Shu, Y.; Xin, Q.; Xu, Y.; Bao, X. The Synergic Effect between Mo Species and Acid Sites in Mo/HMCM-22 Catalysts for Methane Aromatization. *Phys. Chem. Chem. Phys.* **2005**, *7* (16), 3102–3109.

(42) Ma, S.; Guo, X.; Zhao, L.; Scott, S.; Bao, X. Recent Progress in Methane Dehydroaromatization: From Laboratory Curiosities to Promising Technology. *J. Energy Chem.* **2013**, *22* (1), 1–20.

(43) Ohnishi, R.; Liu, S.; Dong, Q.; Wang, L.; Ichikawa, M. Catalytic Dehydrocondensation of Methane with CO and CO2 toward Benzene and Naphthalene on Mo/HZSM-5 and Fe/Co-Modified Mo/HZSM-5. *J. Catal.* **1999**, *182* (1), 92–103.

(44) Sakbodin, M.; Wu, Y.; Oh, S. C.; Wachsman, E. D.; Liu, D. Hydrogen-Permeable Tubular Membrane Reactor: Promoting Conversion and Product Selectivity for Non-Oxidative Activation of Methane over an Fe©SiO 2 Catalyst. *Angew. Chemie Int. Ed.* **2016**, *55* (52), 16149–16152.

(45) Ito, T.; Lunsford, J. H. Synthesis of Ethylene and Ethane by Partial Oxidation of Methane over Lithium-Doped Magnesium Oxide. *Nature* **1985**, *314* (6013), 721–722.

(46) Voskresenskaya, E. N.; Roguleva, V. G.; Anshits, A. G. Oxidant Activation Over Structural Defects of Oxide Catalysts in Oxidative Methane Coupling. *Catal. Rev.* **1995**, *37* (1), 101–143.

(47) Arndt, S.; Laugel, G.; Levchenko, S.; Horn, R.; Baerns, M.; Scheffler, M.; Schlögl, R.; Schomäcker, R. A Critical Assessment of Li/MgO-Based Catalysts for the Oxidative Coupling of Methane. *Catal. Rev.* **2011**, *53* (4), 424–514.

(48) Chen, Y.; Mu, X.; Luo, X.; Shi, K.; Yang, G.; Wu, T. Catalytic Conversion of Methane at Low Temperatures: A Critical Review. *Energy Technol.* **2019**.

(49) Grant, J. T.; Venegas, J. M.; McDermott, W. P.; Hermans, I. Aerobic Oxidations of Light Alkanes over Solid Metal Oxide Catalysts. *Chem. Rev.* **2018**, *118* (5), 2769–2815.

(50) Lee, J. S.; Oyama, S. T. Catalysis Reviews : Science and Engineering Oxidative Coupling of Methane to Higher Hydrocarbons. *Catal. Rev. Sci. Eng.* **1988**, *30* (2), 249–280.

(51) Blanksby, S. J.; Ellison, G. B. Bond Dissociation Energies of Organic Molecules. *Acc. Chem. Res.* **2003**, *36* (4), 255–263.

(52) Beck, B.; Fleischer, V.; Arndt, S.; Hevia, M. G.; Urakawa, A.; Hugo, P.; Schomäcker, R. Oxidative Coupling of Methane - A Complex Surface/Gas Phase Mechanism with Strong Impact on the Reaction Engineering. *Catal. Today* **2014**, *228*, 212–218.

(53) Wang, H. Property-Performance Correlations in the Oxidative Coupling of Methane : The Importance of Carbonate Formation and Stability, Technische Universität Berlin, 2018.

(54) Fleischer, V.; Steuer, R.; Parishan, S.; Schomäcker, R. Investigation of the Surface Reaction Network of the Oxidative Coupling of Methane over Na2WO4/Mn/SiO2 Catalyst by Temperature Programmed and Dynamic Experiments. *J. Catal.* **2016**, *341*, 91–103.

(55) Parishan, S.; Nowicka, E.; Fleischer, V.; Schulz, C.; Colmenares, M. G.; Rosowski, F.; Schomäcker, R. Investigation into Consecutive Reactions of Ethane and Ethene Under the OCM Reaction Conditions

over MnxOy–Na2WO4/SiO2 Catalyst. *Catal. Letters* **2018**, *148* (6), 1659–1675.

(56) Campbell, K. D.; Lunsford, J. H. Contribution of Gas-Phase Radical Coupling in the Catalytic Oxidation of Methane. *J. Phys. Chem.* **1988**, *92* (20), 5792–5796.

(57) Sun, J.; Thybaut, J. W.; Marin, G. B. Microkinetics of Methane Oxidative Coupling. *Catal. Today* **2008**, *137* (1), 90–102.

(58) Dooley, S.; Dryer, F. L.; Yang, B.; Wang, J.; Cool, T. A.; Kasper, T.; Hansen, N. An Experimental and Kinetic Modeling Study of Methyl Formate Low-Pressure Flames. *Combust. Flame* **2011**, *158* (4), 732–741.

(59) Schwarz, H.; Geske, M.; Franklin Goldsmith, C.; Schlögl, R.; Horn, R. Fuel-Rich Methane Oxidation in a High-Pressure Flow Reactor Studied by Optical-Fiber Laser-Induced Fluorescence, Multi-Species Sampling Profile Measurements and Detailed Kinetic Simulations. *Combust. Flame* **2014**, *161* (7), 1688–1700.

(60) Pak, S.; Qiu, P.; Lunsford, J. H. Elementary Reactions in the Oxidative Coupling of Methane over Mn/Na2WO4/SiO2 and Mn/Na2WO4/MgO Catalysts. *J. Catal.* **1998**, *179* (1), 222–230.

(61) Fleischer, V.; Simon, U.; Parishan, S.; Colmenares, M. G.; Görke, O.; Gurlo, A.; Riedel, W.; Thum, L.; Schmidt, J.; Risse, T.; et al. Investigation of the Role of the Na2WO4/Mn/SiO2 Catalyst Composition in the Oxidative Coupling of Methane by Chemical Looping Experiments. *J. Catal.* **2018**, *360*, 102–117.

(62) Hermans, I.; Spier, E. S.; Neuenschwander, U.; Turrà, N.; Baiker, A. Selective Oxidation Catalysis: Opportunities and Challenges. *Top. Catal.* **2009**, *52* (9), 1162–1174.

(63) Schlögl, R. Heterogeneous Catalysis. *Angew. Chemie - Int. Ed.* **2015**, *54* (11), 3465–3520.

(64) Sun, M.; Zhang, J.; Putaj, P.; Caps, V.; Lefebvre, F.; Pelletier, J.; Basset, J. M. Catalytic Oxidation of Light Alkanes (C1-C4) by Heteropoly Compounds. *Chem. Rev.* **2014**, *114* (2), 981–1019.

(65) Beck, B.; Harth, M.; Hamilton, N. G.; Carrero, C.; Uhlrich, J. J.; Trunschke, A.; Shaikhutdinov, S.; Schubert, H.; Freund, H.-J.; Schlögl, R.; et al. Partial Oxidation of Ethanol on Vanadia Catalysts on Supporting Oxides with Different Redox Properties Compared to Propane. *J. Catal.* **2012**, *296*, 120–131.

(66) Schwach, P.; Frandsen, W.; Willinger, M.-G.; Schlögl, R.; Trunschke, A. Structure Sensitivity of the Oxidative Activation of Methane over MgO Model Catalysts: I. Kinetic Study. *J. Catal.* **2015**, *329*, 560–573.

(67) Schwach, P.; Hamilton, N.; Eichelbaum, M.; Thum, L.; Lunkenbein, T.; Schlögl, R.; Trunschke, A. Structure Sensitivity of the Oxidative Activation of Methane over MgO Model Catalysts: II. Nature of Active Sites and Reaction Mechanism. *J. Catal.* **2015**, *329*, 574–587.

(68) Nilius, N.; Freund, H.-J. Activating Nonreducible Oxides via Doping. *Acc. Chem. Res.* **2015**, *48*, 1532–1539.

(69) Bajdich, M.; Nørskov, J. K.; Vojvodic, A. Surface Energetics of Alkaline-Earth Metal Oxides: Trends in Stability and Adsorption of Small Molecules. *Phys. Rev. B - Condens. Matter Mater. Phys.* **2015**, *91* (15), 1–10.

(70) Aljama, H.; Nørskov, J. K.; Abild-Pedersen, F. Tuning Methane Activation Chemistry on Alkaline Earth Metal Oxides by Doping. *J. Phys. Chem. C* **2018**, *122* (39), 22544–22548.

(71) Haber, J.; Witko, M. Oxidation Catalysis - Electronic Theory Revisited. *J. Catal.* **2003**, *216* (1–2), 416–424.

(72) Kondratenko, E. V.; Wolf, D.; Baerns, M. Influence of Electronic Properties of Na2O/CaO Catalysts on Their Catalytic Characteristics for the Oxidative Coupling of Methane. *Catal. Letters* **1999**, *58* (4), 217–223.

(73) Sun, X.; Li, B.; Metiu, H. Methane Dissociation on Li-, Na-, K-, and Cu-Doped Flat and Stepped CaO(001). *J. Phys. Chem. C* **2013**, *117* (14), 7114–7122.

(74) Peil, K. P.; Goodwin, J. G. J.; Marcelin, G. Surface Phenomena during the Oxidative Coupling of Methane over Li/MgO. *J. Catal.* **1991**, *131* (1), 143–155.

(75) Karasuda, T.; Aika, K. Isotopic Oxygen Exchange between Dioxygen and MgO Catalysts for Oxidative Coupling of Methane. *J. Catal.* **1997**, *171* (2), 439–448.

(76) Kwapien, K.; Paier, J.; Sauer, J.; Geske, M.; Zavyalova, U.; Horn, R.; Schwach, P.; Trunschke, A.; Schlögl, R. Sites for Methane Activation on Lithium-Doped Magnesium Oxide Surfaces. *Angew. Chem. Int. Ed. Engl.* **2014**, *53* (33), 8774–8778.

(77) Kondratenko, E. V.; Baerns, M. Oxidative Coupling of Methane. In *Handbook of Heterogeneous Catalysis*; Wiley-VCH Verlag GmbH & Co. KGaA: Weinheim, Germany, 2008; pp 3010–3023.

(78) Schwach, P.; Willinger, M. G.; Trunschke, A.; Schlögl, R. Methane Coupling over Magnesium Oxide: How Doping Can Work. *Angew. Chemie Int. Ed.* **2013**, *52* (43), 11381–11384.

(79) McFarland, E. W.; Metiu, H. Catalysis by Doped Oxides. *Chem. Rev.* **2013**, *113* (6), 4391–4427.

(80) Freund, H.-J. Oxygen Activation on Oxide Surfaces: A Perspective at the Atomic Level. *Catal. Today* **2014**, *238*, 2–9.

(81) Cui, Y.; Shao, X.; Baldofski, M.; Sauer, J.; Nilius, N.; Freund, H.-J. Adsorption, Activation, and Dissociation of Oxygen on Doped Oxides. *Angew. Chemie - Int. Ed.* **2013**, *52* (43), 11385–11387.

(82) Lunsford, J. H.; Yang, X.; Haller, K.; Laane, J.; Mestl, G.; Knoezinger, H. In Situ Raman Spectroscopy of Peroxide Ions on Barium/Magnesium Oxide Catalysts. *J. Phys. Chem.* **1993**, *97* (51), 13810–13813.

(83) Kaabar, W.; Bott, S.; Devonshire, R. Raman Spectroscopic Study of Mixed Carbonate Materials. *Spectrochim. Acta - Part A Mol. Biomol. Spectrosc.* **2011**, *78* (1), 136–141.

(84) Hao, Z.; Zhang, X.; Luo, Y.; Zhang, L.; Zhao, H.; Zhang, J. Enhanced Ce3+ Photoluminescence by Li+ Co-Doping in CaO Phosphor and Its Use in Blue-Pumped White LEDs. *J. Lumin.* **2013**, *140*, 78–81.

(85) Stankic, S.; Bernardi, J.; Diwald, O.; Knözinger, E. Optical Surface Properties and Morphology of MgO and CaO Nanocrystals. *J. Phys. Chem. B* **2006**, *110* (28), 13866–13871.

(86) Bengoechea-Encabo, A.; Albert, S.; Sánchez-Garcia, M. A.; Calleja, E. Oxygen-Related Photoluminescence Quenching in Selectively Grown GaN Nanocolumns: Dependence on Diameter. *Mater. Sci. Semicond. Process.* **2016**, *55*, 59–62.

(87) Puust, L.; Kiisk, V.; Eltermann, M.; Mändar, H.; Saar, R.; Lange, S.; Sildos, I.; Dolgov, L.; Matisen, L.; Jaaniso, R. Effect of Ambient Oxygen on the Photoluminescence of Sol–Gel-Derived Nanocrystalline ZrO 2 :Eu,Nb. *J. Phys. D. Appl. Phys.* **2017**, *50* (21), 215303.

(88) Borgwardt, R. H. Calcium Oxide Sintering in Atmospheres Containing Water and Carbon Dioxide. *Ind. Eng. Chem. Res.* **1989**, *28*, 493–500.

(89) Valverde, J. M.; Sanchez-Jimenez, P. E.; Perejon, A.; Perez-Maqueda, L. a. CO2 Multicyclic Capture of Pretreated/Doped CaO in the Ca-Looping Process. Theory and Experiments. *Phys. Chem. Chem. Phys.* **2013**, *15* (28), 11775–11793.

(90) Perreault, P.; Patience, G.-S. Carbonation and Deactivation Kinetics of a Mixed Calcium Oxide–Copper Oxide Sorbent/Oxygen Carrier for Post-Combustion Carbon Dioxide Capture. *Chem. Eng. J.* **2016**, *306*, 726–733.

(91) Matsuda, S.; Kato, A. Titanium Oxide Based Catalysts - a Review. *Appl. Catal.* **1983**, *8* (2), 149–165.

(92) Pan, C. J.; Tsai, M. C.; Su, W. N.; Rick, J.; Akalework, N. G.; Agegnehu, A. K.; Cheng, S. Y.; Hwang, B. J.

Tuning/Exploiting Strong Metal-Support Interaction (SMSI) in Heterogeneous Catalysis. *J. Taiwan Inst. Chem. Eng.* **2017**, *74*, 154–186.

(93) Schwach, P.; Eichelbaum, M.; Schlögl, R.; Risse, T.; Dinse, K.-P. Evidence for Exchange Coupled Electrons and Holes in MgO after Oxidative Activation of CH4: A Multifrequency Transient Nutation EPR Study. *J. Phys. Chem. C* **2016**, *120* (7), 3781–3790.

(94) Stankic, S.; Müller, M.; Diwald, O.; Sterrer, M.; Knözinger, E.; Bernardi, J. Size-Dependent Optical Properties of MgO Nanocubes. *Angew. Chemie Int. Ed.* **2005**, *44* (31), 4917–4920.

(95) Mehrabadi, B. A. T.; Eskandari, S.; Khan, U.; White, R. D.; Regalbuto, J. R. A Review of Preparation Methods for Supported Metal Catalysts. In *Advances in Catalysis*; Elsevier Inc., 2017; Vol. 61, pp 1–35.

(96) Mélinon, P.; Begin-Colin, S.; Duvail, J. L.; Gauffre, F.; Boime, N. H.; Ledoux, G.; Plain, J.; Reiss, P.; Silly, F.; Warot-Fonrose, B. Engineered Inorganic Core/Shell Nanoparticles. *Phys. Rep.* **2014**, *543* (3), 163–197.

(97) Srdic, V.; Mojic, B.; Nikolic, M.; Ognjanovic, S. Recent Progress on Synthesis of Ceramics Core/Shell Nanostructures. *Process. Appl. Ceram.* **2013**, *7* (2), 45–62.

(98) *Handbook of Heterogeneous Catalysis*; Ertl, G., Knözinger, H., Schüth, F., Weitkamp, J., Eds.; Wiley-VCH Verlag GmbH & Co. KGaA: Weinheim, Germany, Germany, 2008.

(99) Pehkonen, S.; Ray, A.; Seger, N.; Ni, X.; Pepe, C.; Prieteo, X.; Nestle, N.; Dehn, F.; Niessner, R.; Schmelz, H.; et al. Solid-State Reactions. **2004**, 1435–1444.

(100) Schüth, F.; Hesse, M.; Unger, K. K. Precipitation and Coprecipitation. In *Handbook of Heterogeneous Catalysis*; Wiley-VCH Verlag GmbH & Co. KGaA: Weinheim, Germany, 2008; pp 100–119.

(101) Nebel, H.; Epple, M. Continuous Preparation of Calcite, Aragonite and Vaterite, and of Magnesium-Substituted Amorphous Calcium Carbonate (Mg-ACC). *Zeitschrift für Anorg. und Allg. Chemie* **2008**, *634* (8), 1439–1443.

(102) Brunauer, S.; Emmett, P. H.; Teller, E. Adsorption of Gases in Multimolecular Layers. *J. Am. Chem. Soc.* **1938**, *60* (2), 309–319.

(103) Bhambhani, M. R.; Cutting, P. A.; Sing, K. S. W.; Turk, D. H. Analysis of Nitrogen Adsorption Isotherms on Porous and Nonporous Silicas by the BET and As Methods. *J. Colloid Interface Sci.* **1972**, *38* (1), 109–117.

(104) Ladavos, A. K.; Katsoulidis, A. P.; Iosifidis, A.; Triantafyllidis, K. S.; Pinnavaia, T. J.; Pomonis, P. J. The BET Equation, the Inflection Points of N 2 Adsorption Isotherms and the Estimation of Specific Surface Area of Porous Solids. *Microporous Mesoporous Mater.* **2012**, *151*, 126–133.

(105) Atkins, P.; Paula, J. de. The Investigation of Structure. In *Atkins' Physical Chemistry*; Oxford University Press: Oxford, New York, 2006; p 702ff.

(106) Vegard, L. Die Konstitution Der Mischkristalle Und Die Raumfüllung Der Atome. *Zeitschrift für Phys.* **1921**, *5* (1), 17–26.

(107) Scherrer, P. Bestimmung Der Inneren Struktur Und Der Größe von Kolloidteilchen Mittels Röntgenstrahlen. In *Kolloidchemie Ein Lehrbuch*; Springer Berlin Heidelberg: Berlin, Heidelberg, 1912; Vol. 277, pp 387–409.

(108) Yildiz, M.; Aksu, Y.; Simon, U.; Otremba, T.; Kailasam, K.; Göbel, C.; Girgsdies, F.; Görke, O.; Rosowski, F.; Thomas, A.; et al. Silica Material Variation for the Mn x O y -Na 2 WO 4 /SiO 2. *Appl. Catal. A Gen.* **2016**, *525*, 168–179.

(109) Hadjiivanov, K. I.; Vayssilov, G. N. Characterization of Oxide Surfaces and Zeolites by Carbon Monoxide as an IR Probe Molecule. *Adv. Catal.* **2002**, *47*, 307–511.

(110) Garrone, E.; Zecchina, A.; Stone, F. S. CO Adsorption on MgO and CaO. *J. Chem. Soc. Farady Trans.* **1988**,

84 (8), 2843–2854.

(111) Coluccia, S.; Garrone, E.; Guglielminotti, E.; Zecchina, A. Infrared Study of Carbon Monoxide Adsorption on Calcium and Strontium Oxides. *J. Chem. Soc. Faraday Trans. 1* **1981**, *77* (5), 1063.

(112) Wang, L. H.; Yi, X. D.; Weng, W. Z.; Wan, H. L. In Situ IR and Pulse Reaction Studies on the Active Oxygen Species over SrF2/Nd2O3 Catalyst for Oxidative Coupling of Methane. *Catal. Today* **2008**, *131* (1–4), 135–139.

(113) Lin, Y.; Xu, Y.-D.; Guo, X. A FT-IR Study on the Interaction of CH4 and O2 with the Surface of SrO-La2O3/CaO Catalysts. *Acta Phys. -Chim. Sin.* **1995**, *11* (10), 902–906.

(114) Wachs, I. E.; Roberts, C. A. Monitoring Surface Metal Oxide Catalytic Active Sites with Raman Spectroscopy. *Chem. Soc. Rev.* **2010**, *39* (12), 5002–5017.

(115) Nakamoto, K. Infrared and Raman Spectra of Inorganic And. *Handb. Vib. Spectrosc.* **2006**, 1872–1892.

(116) Payen, E.; Grimblot, J.; Lavalley, J. C.; Daturi, M.; Maugè, F. Vibrational Spectroscopy in the Study of Oxide (Excluding Zeolites) and Sulfide Catalysts. In *Handbook of Vibrational Spectroscopy*; Chalmers, J. M., Ed.; John Wiley & Sons, Ltd: Chichester, UK, 2006; pp 3005–3041.

(117) Schmid, T.; Dariz, P. Shedding Light onto the Spectra of Lime: Raman and Luminescence Bands of CaO, Ca(OH) 2 and CaCO 3. *J. Raman Spectrosc.* **2015**, *46* (1), 141–146.

(118) Rieder, K. H.; Weinstein, B. A.; Cardona, M.; Bilz, H. Measurement and Comparative Analysis of the Second-Order Raman Spectra of the Alkaline-Earth Oxides with a Nacl Structure. *Phys. Rev. B* **1973**, *8* (10), 4780–4786.

(119) Sternig, A.; Stankic, S.; Müller, M.; Bernardi, J.; Knözinger, E.; Diwald, O. Photoluminescent Nanoparticle Surfaces: The Potential of Alkaline Earth Oxides for Optical Applications. *Adv. Mater.* **2008**, *20* (24), 4840–4844.

(120) Garrone, E.; Zecchina, A.; Stone, F. S. An Experimental and Theoretical Evaluation of Surface States in MgO and Other Alkaline Earth Oxides. *Philos. Mag. Part B* **1980**, *42* (5), 683–703.

(121) MacLean, S. G.; Duley, W. W. Photoluminescence from Surface States in MgO and CaO Powders. *J. Phys. Chem. Solids* **1984**, *45* (2), 227–235.

(122) Zhou, Z.; Shinar, R.; Allison, A. J.; Shinar, J. Enhanced Photoluminescence of Oxygen Sensing Films through Doping with High Dielectric Constant Particles. *Adv. Funct. Mater.* **2007**, *17* (17), 3530–3537.

(123) Paganini, M. C.; Chiesa, M.; Martino, P.; Giamello, E.; Garrone, E. EPR Study of the Surface Basicity of Calcium Oxide. 2: The Interaction with Alkanes. *J. Phys. Chem. B* **2003**, *107* (11), 2575–2580.

(124) Kittel, C.; Abrahams, E. Dipolar Broadening of Magnetic Resonance Lines in Magnetically Diluted Crystals. *Phys. Rev.* **1953**, *90* (2), 238–239.

(125) Biasi, R. S. de; Fernandes, A. A. R. The ESR Linewidth of Dilute Solid Solutions. *J. Phys. C Solid State Phys.* **1983**, *16* (28), 5481–5489.

(126) Biasi, R. S. De; Grillo, M. L. N. Evidence for Clustering in Fe3+ -Doped CaO. *J. Physisc Chem. Solids* **2003**, *64*, 711–713.

(127) Biasi, R. S. De; Grillo, M. L. N. Influence of Copper Concentration on the ESR Spectrum of Cu2+ in CaO. *Solid State Commun.* **2002**, *121*, 697–700.

(128) Biasi, R. S. De; Grillo, M. L. . Influence of Manganese Concentration on the ESR Spectrum of Mn2+ in CaO. *J. Alloys Compd.* **1999**, *282*, 5–7.

(129) Biasi, R. S. De; Grillo, M. L. N. Influence of Gadolinium Concentration on the ESR Spectrum of Gd3+ in CaO. *Solid State Commun.* **2002**, *124*, 131–133.

(130) Tarasov, A.; Schumann, J.; Girgsdies, F.; Thomas, N.; Behrens, M. Thermokinetic Investigation of Binary Cu/Zn Hydroxycarbonates as Precursors for Cu/ZnO Catalysts. *Thermochim. Acta* **2014**, *591*, 1–9.

(131) Choong Kwet Yive, N. S.; Corriu, R. J. P.; Leclercq, D.; Mutin, P. H.; Vioux, A. Thermogravimetric Analysis/Mass Spectrometry Investigation of the Thermal Conversion of Organosilicon Precursors into Ceramics under Argon and Ammonia. 2. Poly(Silazanes). *Chem. Mater.* **1992**, *4* (6), 1263–1271.

(132) Alonso, C.; Morato, A.; Medina, F.; Guirado, F.; Cesteros, Y.; Salagre, P.; Sueiras, J. E.; Terrado, R.; Giralt, A. Preparation and Characterization of Different Phases of Aluminum Trifluoride. *Chem. Mater.* **2000**, *12* (4), 1148–1155.

(133) Düngen, P.; Schlögl, R.; Heumann, S. Non-Linear Thermogravimetric Mass Spectrometry of Carbon Materials Providing Direct Speciation Separation of Oxygen Functional Groups. *Carbon N. Y.* **2018**, *130*, 614–622.

(134) Tarasov, A.; Düdder, H.; Mette, K.; Kühl, S.; Kähler, K.; Schlögl, R.; Muhler, M.; Behrens, M. Investigation of Coking during Dry Reforming of Methane by Means of Thermogravimetry. *Chemie-Ingenieur-Technik* **2014**, *86* (11), 1916–1924.

(135) Studt, F.; Behrens, M.; Kunkes, E. L.; Thomas, N.; Zander, S.; Tarasov, A.; Schumann, J.; Frei, E.; Varley, J. B.; Abild-Pedersen, F.; et al. The Mechanism of CO and CO2 Hydrogenation to Methanol over Cu-Based Catalysts. *ChemCatChem* **2015**, *7* (7), 1105–1111.

(136) Lomonosov, V. I.; Gordienko, Y. A.; Sinev, M. Y.; Rogov, V. A.; Sadykov, V. A. Thermochemical Properties of the Lattice Oxygen in W,Mn-Containing Mixed Oxide Catalysts for the Oxidative Coupling of Methane. *Russ. J. Phys. Chem. A* **2018**, *92* (3), 430–437.

(137) Haneda, M.; Kintaichi, Y.; Bion, N.; Hamada, H. Alkali Metal-Doped Cobalt Oxide Catalysts for NO Decomposition. *Appl. Catal. B Environ.* **2003**, *46* (3), 473–482.

(138) Monti, D. A. M.; Baiker, A. Temperature-Programmed Reduction. Parametric Sensitivity and Estimation of Kinetic Parameters. *J. Catal.* **1983**, *83* (2), 323–335.

(139) Stobbe, E. R.; de Boer, B. A.; Geus, J. W. The Reduction and Oxidation Behaviour of Manganese Oxides. *Catal. Today* **1999**, *47* (1–4), 161–167.

(140) Millet, M.-M.; Algara-Siller, G.; Wrabetz, S.; Mazheika, A.; Girgsdies, F.; Teschner, D.; Seitz, F.; Tarasov, A.; Levchenko, S. V.; Schlögl, R.; et al. Ni Single Atom Catalysts for CO 2 Activation. *J. Am. Chem. Soc.* **2019**, *141* (6), 2451–2461.

(141) Micheli, F.; Sciarra, M.; Courson, C.; Gallucci, K. Catalytic Steam Methane Reforming Enhanced by CO2 Capture on CaO Based Bi-Functional Compounds. *J. Energy Chem.* **2017**, *26* (5), 1014–1025.

(142) Jehng, J. M.; Chen, C. M. Amination of Polyethylene Glycol to Polyetheramine over the Supported Nickel Catalysts. *Catal. Letters* **2001**, *77* (1–3), 147–154.

(143) Borchert, Y.; Sonstrom, P.; Wilhelm, M.; Borchert, H.; Baumer, M. Nanostructured Praseodymium Oxide: Preparation, Structure, and Catalytic Properties. *J. Phys. Chem. C* **2008**, *112* (8), 3054–3063.

(144) Choudhary, V. R.; Mulla, S. A. R.; Uphade, B. S. Oxidative Coupling of Methane over SrO Deposited on Different Commercial Supports Precoated with La2O3. *Ind. Eng. Chem. Res* **1998**, *37* (6), 2142–2147.

(145) Choudhary, V. R.; Rane, V. H.; Chaudhari, S. T. Surface Properties of Rare Earth Promoted MgO Catalysts and Their Catalytic Activity/Selectivity in Oxidative Coupling of Methane. *Appl. Catal. A Gen.* **1997**, *158*, 121–136.

(146) Heracleous, E.; Machli, M.; Lemonidou, A. A.; Vasalos, I. A. Oxidative Dehydrogenation of Ethane and Propane over Vanadia and Molybdena Supported Catalysts. *J. Mol. Catal. A Chem.* **2005**, *232* (1–2), 29–39.

(147) Papa, F.; Gingasu, D.; Patron, L.; Miyazaki, A.; Balint, I. On the Nature of Active Sites and Catalytic

Activity for OCM Reaction of Alkaline-Earth Oxides-Neodymia Catalytic Systems. *Appl. Catal. A Gen.* **2010**, *375* (1), 172–178.

(148) Blasco, T. Oxidative Dehydrogenation of Short Chain Alkanes on Supported Vanadium Oxide Catalysts. *Appl. Catal. A Gen.* **1997**, *157* (1–2), 117–142.

(149) Gleaves, J. T.; Yablonskii, G. S.; Phanawadee, P.; Schuurman, Y. TAP-2: An Interrogative Kinetics Approach. *Appl. Catal. A Gen.* **1997**, *160* (1), 55–88.

(150) Kondratenko, E. V.; Buyevskaya, O. V.; Soick, M.; Baerns, M. Transient Kinetics and Mechanism of Oxygen Adsorption over Oxide Catalysts from the TAP-Reactor System. *Catal. Letters* **1999**, *63* (3–4), 153–159.

(151) Riedel, W.; Thum, L.; Möser, J.; Fleischer, V.; Simon, U.; Siemensmeyer, K.; Schnegg, A.; Schomäcker, R.; Risse, T.; Dinse, K.-P. Magnetic Properties of Reduced and Reoxidized Mn-Na2WO4/SiO2: A Catalyst for Oxidative Coupling of Methane (OCM). *J. Phys. Chem. C* **2018**, *122* (39), 22605–22614.

(152) Rane, V. H.; Chaudhari, S. T.; Choudhary, V. R. Influence of Alkali Metal Doping on Surface Properties and Catalytic Activity/Selectivity of CaO Catalysts in Oxidative Coupling of Methane. *J. Nat. Gas Chem.* **2008**, *17* (4), 313–320.

(153) Elkins, T. W.; Roberts, S. J.; Hagelin-Weaver, H. E. Effects of Alkali and Alkaline-Earth Metal Dopants on Magnesium Oxide Supported Rare-Earth Oxide Catalysts in the Oxidative Coupling of Methane. *Appl. Catal. A Gen.* **2016**, *528*, 175–190.

(154) Holleman, A. F.; Wiberg, N.; Wiberg, E. Kapitel XVII Die Gruppe Der Erdalkalimetalle. In *Lehrbuch der Anorganischen Chemie*; Walter de Gruyter, 2007; pp 1215–1258.

(155) van Geet, A. L. Ammonia Exchange of Nickel-Ammine Complex in Aqueous Ammonia Measured by Proton Magnetic Resonance. *Inorg. Chem.* **1968**, *7* (10), 2026–2029.

(156) Coluccia, S.; Deane, A. M.; Tench, A. J. Photoluminescent Spectra of Surface States in Alkaline Earth Oxides. *Faraday Trans. I* **1978**, *74*, 2913–2922.

(157) Abrams, B. L.; Holloway, P. H. Role of the Surface in Luminescent Processes. *Chem. Rev.* **2004**, *104* (12), 5783–5802.

(158) Stoll, S.; Jeschke, G.; Willer, M.; Schweiger, A. Nutation-Frequency Correlated EPR Spectroscopy: The PEANUT Experiment. *J. Magn. Reson.* **1998**, *130* (1), 86–96.

(159) Schindler, P.; Ghose, S. Electron Paramagnetic Resonance of Mn2+ in Dolomite and Magnesite, and Mn2+ Distribution in Dolomites. *Am. Mineral.* **1970**, *55*, 1889–1896.

(160) Rao, J. L.; Narendra, G. L.; Sreedhar, B.; Lakshman, S. V. J. Electron Spin Resonance and Optical Absorption Spectra of Mn2+ Ions in K2SO4-ZnSO4 Glasses. *Phys. Status Solidi* **1989**, *153* (1), 257–262.

(161) de Biasi, R. S.; Fernandes, A. A. R. The ESR Linewidth of Dilute Solid Solutions. *J. Phys. C Solid State Phys.* **2000**, *16* (28), 5481–5489.

(162) Węgrzyniak, A.; Jarczewski, S.; Węgrzynowicz, A.; Michorczyk, B.; Kuśtrowski, P.; Michorczyk, P. Catalytic Behavior of Chromium Oxide Supported on Nanocasting-Prepared Mesoporous Alumina in Dehydrogenation of Propane. *Nanomaterials* **2017**, *7* (9).

(163) Kanervo, J. M.; Krause, A. O. I. Characterisation of Supported Chromium Oxide Catalysts by Kinetic Analysis of H2-TPR Data. *J. Catal.* **2002**, *207* (1), 57–65.

(164) Neri, G.; Pistone, A.; De Rossi, S.; Rombi, E.; Milone, C.; Galvagno, S. Ca-Doped Chromium Oxide Catalysts Supported on Alumina for the Oxidative Dehydrogenation of Isobutane. *Appl. Catal. A Gen.* **2004**, *260* (1), 75–86.

(165) Müller, M.; Sternig, A.; Stankic, S.; Sto, M.; Bernardi, J.; Kno, E.; Diwald, O. Nanoparticles as a Support :

CaO Deposits on MgO Cubes. *J. Phys. Chem. C* **2008**, *112*, 9120–9123.

(166) Zhu, Y.; Wu, S.; Wang, X. Nano CaO Grain Characteristics and Growth Model under Calcination. *Chem. Eng. J.* **2011**, *175*, 512–518.

(167) Solis, B. H.; Cui, Y.; Weng, X.; Seifert, J.; Schauermann, S.; Sauer, J.; Shaikhutdinov, S.; Freund, H.-J. Initial Stages of CO2 Adsorption on CaO: A Combined Experimental and Computational Study. *Phys. Chem. Chem. Phys.* **2017**, *19* (6), 4231–4242.

(168) Mutch, G. A.; Anderson, J. A.; Vega-Maza, D. Surface and Bulk Carbonate Formation in Calcium Oxide during CO2 Capture. *Appl. Energy* **2017**, *202*, 365–376.

(169) Middleburgh, S. C.; Lagerlof, K. P. D.; Grimes, R. W. Accommodation of Excess Oxygen in Group II Monoxides. *J. Am. Ceram. Soc.* **2013**, *96* (1), 308–311.

(170) Prencipe, M.; Pascale, F.; Zicovich-Wilson, C. M.; Saunders, V. R.; Orlando, R.; Dovesi, R. The Vibrational Spectrum of Calcite (CaCO3): An Ab Initio Quantum-Mechanical Calculation. *Phys. Chem. Miner.* **2004**, *31* (8), 559–564.

(171) Gillet, P.; McMillan, P.; Schott, J.; Badro, J.; Grzechnik, A. Thermodynamic Properties and Isotopic Fractionation of Calcite from Vibrational Spectroscopy of 18O-Substituted Calcite. *Geochim. Cosmochim. Acta* **1996**, *60* (18), 3471–3485.

(172) Abrashev, M.; Bäckström, J.; Börjesson, L.; Popov, V.; Chakalov, R.; Kolev, N.; Meng, R.-L.; Iliev, M. Raman Spectroscopy of CaMnO3: Mode Assignment and Relationship between Raman Line Intensities and Structural Distortions. *Phys. Rev. B* **2002**, *65* (18), 184301.

(173) Li, W.; Gibbs, G. V.; Oyama, S. T. Mechanism of Ozone Decomposition on a Manganese Oxide Catalyst. 1. In Situ Raman Spectroscopy and Ab Initio Molecular Orbital Calculations. *J. Am. Chem. Soc.* **1998**, *120* (35), 9041–9046.

(174) Bernard, M.-C. Electrochromic Reactions in Manganese Oxides. *J. Electrochem. Soc.* **1993**, *140* (11), 3065.

(175) Sopracase, R.; Gruener, G.; Olive, E.; Soret, J. C. Infrared Study of the Phonon Modes in PrMnO3 and CaMnO3. *Phys. B Condens. Matter* **2010**, *405* (1), 45–52.

(176) Granados, M. L.; Poves, M. D. Z.; Alonso, D. M.; Mariscal, R.; Galisteo, F. C.; Moreno-Tost, R.; Santamaría, J.; Fierro, J. L. G. Biodiesel from Sunflower Oil by Using Activated Calcium Oxide. *Appl. Catal. B Environ.* **2007**, *73* (3–4), 317–326.

(177) Andersen, F. A.; Brečević, L.; Beuter, G.; Dell'Amico, D. B.; Calderazzo, F.; Bjerrum, N. J.; Underhill, A. E. Infrared Spectra of Amorphous and Crystalline Calcium Carbonate. *Acta Chem. Scand.* **1991**, *45*, 1018–1024.

(178) Ekstrom, A.; Lapszewicz, J. A. A Study of the Mechanism of the Partial Oxidation of Methane over Rare Earth Oxide Catalysts Using Isotope Transient Techniques. *J. Phys. Chem.* **1989**, *93* (13), 5230–5237.

(179) Ekstrom, A.; Lapszewicz, J. A. The Role of Oxygen in the Partial Oxidation of Methane over a Samarium Oxide Catalyst. *J. Am. Chem. Soc.* **1988**, *110* (15), 5226–5228.

(180) Kalenik, Z.; Wolf, E. E. Temperature Programmed Isotopic Exchange of Lattice Oxygen during Methane Oxidative Coupling. *Catal. Letters* **1991**, *11* (3–6), 309–318.

(181) Acke, F.; Panas, I. Kinetic Study of Heterogeneous Oxygen-Exchange Reactions and Bulk Self-Diffusion of Oxygen. *J. Phys. Chem. B* **1998**, *102* (26), 5158–5164.

(182) Trunschke, A.; Werny, M. J.; Wang, Y.; Girgsdies, F.; Schlögl, R. Fluctuating Storage of the Active Phase in a Mn-Na2WO4/SiO2 Catalyst for the Oxidative Coupling of Methane. *Angew. Chemie Int. Ed.* **2020**, 2–8.

(183) Mellor, I. M.; Burrows, A.; Coluccia, S.; Hargreaves, J. S. J.; Joyner, R. W.; Kiely, C. J.; Martra, G.; Stockenhuber, M.; Tang, W. M. Probing Possible Structure Sensitivity in the Exchange of Isotopic Oxygen with the Surface of MgO. *J. Catal.* **2005**, *234* (1), 14–23.

(184) Kalenik, Z.; Wolf, E. E. Transient and Isotopic Studies of the Oxygen Transport and Exchange during Oxidative Coupling of Methane on Sr Promoted La2O3. *Catal. Letters* **1991**, *9* (5–6), 441–449.

(185) Paganini, M. C.; Chiesa, M.; Martino, P.; Livraghi, S.; Giamello, E. An EPR Study of the Surface Reactivity of CaO and a Comparison with That of MgO. *Stud. Surf. Sci. Catal.* **2005**, *155*, 441–449.

(186) Paganini, M. C.; Chiesa, M.; Dolci, F.; Martino, P.; Giamello, E. EPR Study of the Surface Basicity of Calcium Oxide. 3. Surface Reactivity and Nonstoichiometry. *J. Phys. Chem. B* **2006**, *110* (24), 11918–11923.

(187) Prasanna, K.; Bhattacharya, S. K.; Ghosh, P.; Mahata, S.; Liang, M.-C. Isotopic Homogenization and Scrambling Associated with Oxygen Isotopic Exchange on Hot Platinum: Studies on Gas Pairs (O2, CO2) and (CO, CO2). *RSC Adv.* **2016**, *6* (56), 51296–51303.

(188) Solis, B. H.; Sauer, J.; Cui, Y.; Shaikhutdinov, S.; Freund, H.-J. Oxygen Scrambling of CO2 Adsorbed on CaO(001). *J. Phys. Chem. C* **2017**, *121* (34), 18625–18634.

(189) Lacombe, S.; Zanthoff, H.; Mirodatos, C. Oxidative Coupling of Methane over Lanthana Catalysts II. A Mechanistic Study Using Isotope Transient Kinetics. *J. Catal.* **1995**, *155* (1), 106–116.

(190) Jorgensen, P. J.; Wadsworth, M. E.; Cutler, I. B. Oxidation of Silicon Carbide. *J. Am. Ceram. Soc.* **1959**, *42* (12), 613–616.

(191) Ervin, G. Oxidation Behavior of Silicon Carbide. *J. Am. Ceram. Soc.* **1958**, *41* (9), 347–352.

(192) Ellis, C. S.; Holsen, J. N. Diffusion Coefficients for Helium-Nitrogen and Nitrogen-Carbon Dioxide at Elevated Temperatures. *I EC Fundam.* **1969**, *8* (4), 787–791.

(193) Wasik, S. P.; McCulloh, K. E. Measurements of Gaseous Diffusion Coefficients by a Gas Chromatographic Technique. *J. Res. Nat. Bur. Stand. Sec. A Phys. Ch.* **1969**, *73* (2), 207–211.

(194) Plodinec, M.; Nerl, H. C.; Girgsdies, F.; Schlögl, R.; Lunkenbein, T. Insights into Chemical Dynamics and Their Impact on the Reactivity of Pt Nanoparticles during CO Oxidation by Operando TEM. *ACS Catal.* **2020**, *10* (5), 3183–3193.

(195) Zhu, X.; Yang, W. Defects and Diffusion. In *Mixed Conducting Ceramic Membranes*; Green Chemistry and Sustainable Technology; Springer Berlin Heidelberg: Berlin, Heidelberg, 2017; pp 11–48.

(196) Transactions, E. C. S.; Society, T. E. Photoluminescence Properties of Alkaline-Earth Oxide Nanoparticles P. V. Sushko. *ECS Trans.* **2010**, *28* (3), 67–80.

(197) Niedermaier, M.; Schwab, T.; Kube, P.; Zickler, G. A.; Trunschke, A.; Diwald, O. Catalytic Activity, Water Formation, and Sintering: Methane Activation over Co- and Fe-Doped MgO Nanocrystals. *J. Chem. Phys.* **2020**, *152* (7), 074713.

(198) Millet, M. M.; Frei, E.; Algara-Siller, G.; Schlögl, R.; Tarasov, A. Surface Titration of Supported Ni Catalysts by O2-Pulse Thermal Analysis. *Appl. Catal. A Gen.* **2018**, *566*, 155–163.

(199) Takita, Y.; Lunsford, J. H. Surface Reactions of Oxygen Ions. 3. Oxidation of Alkanes by Ozonide(1-) Ion on Magnesium Oxide. *J. Phys. Chem.* **1979**, *83* (6), 683–688.

(200) Aika, K.; Lunsford, J. H. Surface Reactions of Oxygen Ions. I. Dehydrogenation of Alkanes by Oxygen(1-) Ions on Magnesium Oxide. *J. Phys. Chem.* **1977**, *81* (14), 1393–1398.

(201) Thum, L.; Rudolph, M.; Schomäcker, R.; Wang, Y.; Tarasov, A.; Trunschke, A.; Schlögl, R. Oxygen Activation in Oxidative Coupling of Methane on Calcium Oxide. *J. Phys. Chem. C* **2019**, *123* (13), 8018–8026.

Literature Directory

(202) Xu, Y.; Yu, L.; Cai, C.; Huang, J.; Guo, X. A Study of the Oxidative Coupling of Methane over SrO-La2O3/CaO Catalysts by Using CO2 as a Probe. *Catal. Letters* **1995**, *35* (3–4), 215–231.

(203) Litawa, B.; Michorczyk, P.; Ogonowski, J. Influence of CO2 on the Catalytic Performance Of La2O3/CeO2 and CaO/CeO2 Catalysts in the Oxidative Coupling of Methane. *Polish J. Chem. Technol.* **2013**, *15* (1), 22–26.

(204) Dubois, J.-L.; Cameron, C. J. Synergy between Stable Carbonates and Yttria in Selective Catalytic Oxidation of Methane. *Chem. Lett.* **1991**, *20* (7), 1089–1092.

(205) Maya, J. C.; Chejne, F.; Bhatia, S. K. On the Modeling of the CO2 -Catalyzed Sintering of Calcium Oxide. *AIChE J.* **2017**, *63* (8), 3286–3296.

(206) Schwach, P.; Willinger, M. G.; Trunschke, A.; Schlögl, R. Methane Coupling over Magnesium Oxide: How Doping Can Work. *Angew. Chemie* **2013**, *125* (43), 11591–11594.

(207) Goldsmith, B. R.; Esterhuizen, J.; Liu, J. X.; Bartel, C. J.; Sutton, C. Machine Learning for Heterogeneous Catalyst Design and Discovery. *AIChE J.* **2018**, *64* (7), 2311–2323.

(208) Takahashi, K.; Miyazato, I.; Nishimura, S.; Ohyama, J. Unveiling Hidden Catalysts for the Oxidative Coupling of Methane Based on Combining Machine Learning with Literature Data. *ChemCatChem* **2018**, *10* (15), 3223–3228.

(209) Godini, H. R.; Khadivi, M.; Azadi, M.; Görke, O.; Jazayeri, S. M.; Thum, L.; Schomäcker, R.; Wozny, G.; Repke, J. U. Multi-Scale Analysis of Integrated C1 (Ch4 and Co2) Utilization Catalytic Processes: Impacts of Catalysts Characteristics up to Industrial-Scale Process Flowsheeting, Part i: Experimental Analysis of Catalytic Low-Pressure Co2 to Methanol Conversion. *Catalysts* **2020**, *10* (5), 1–22.

(210) Godini, H. R.; Azadi, M.; Khadivi, M.; Schomäcker, R.; Gallucci, F.; Wozny, G.; Repke, J. U. Multi-Scale Analysis of Integrated C1 (Ch4 and Co2) Utilization Catalytic Processes: Impacts of Catalysts Characteristics up to Industrial-Scale Process Flowsheeting, Part Ii: Techno-Economic Analysis of Integrated C1 Utilization Process Scenarios. *Catalysts* **2020**, *10* (5), 1–17.

(211) Thum, L. Synthesis and Characterisation of Calcium Oxide Catalysts for the Oxidative Coupling of Methane (OCM). 2014.

Abbreviation Directory

Abbreviation	Meaning
a.u.	Arbitrary Units
ads	Adsorption
AEMO	Alkaline Earth Metal Oxide
ALD	Atomic Layer Deposition
AMO	Alkaline Metal Oxide
ATR	Autothermal Reforming
BET	Brunauer Emmett Teller
cas	Cascade
Cat.	Catalyst
CCU	Carbon Capturing Units
des	Desorption
dis	Dissociation
DMT	Dimethyl Terephthalate
DRM	Dry Reforming of Methane
Em/EM	Emission
EPR	Electron Paramagnetic Resonance
Ex/EX	Excitation
FID	Flame Ionization Detector
FT	Fischer-Tropsch
GC	Gas Chromatograph
GHSV	Gas Hourly Space Velocity
HTAx	High Turning Angle
i.D.	Inner Diameter
ICP-OES	Inductive Couple Plasma - Optical Emission Spectroscopy

Abbreviation Directory

IR	Infrared
LEED	Low-Energy Electron Diffraction
MCT	Mercury Cadmium Telluride
MDA	Methane Dehydroaromatization
MFC	Mass Flow Controller
MMA	Methyl Methacrylate
MOF	Metal-Organic Framework
MS	Mass Spectrometer
MTBA	Methyl Tert-Butyl Ether
MTO	Methanol to Olefin
norm.	Normalized
o.D.	Outer Diameter
OCM	Oxidative Coupling of Methane
PFTR	Plug Flow Tubular Reactor
PIOS	Pulsed Isotopic Oxygen Scrambling
PL	Photoluminescence
pura	Puratronic
ref	Reference
REMO	Rare-Earth Metal Oxide
SMSI	Strong-Metal Support Interaction
SR	Steam Reforming
SSITKA	Steady State Isotopic Transient Kinetic Analysis
STM	Scanning Tunneling Microscope
TAP	Temporal Analysis of Products
TCD	Thermal Conductivity Detector
TG	Thermogravimetric

n

Ti	Tubing in
TN	Transient Nutation
To	Tubing out
tot.	total
TPD	Temperature Programmed Desorption
TPIE	Temperature-Programmed Isotope Exchange
TPO	Temperature Programmed Oxidation
TPR	Temperature Programmed Reduction
UV	Ultraviolet
Vis	Visible
XRD	X-ray Diffraction

Symbol Directory

Symbol	Meaning	Special Use
p_i	Pressure / Partial Pressure of Component i)	
A	Absorbance	
α	Lattice Constant	
A(r)	Area of Sphere with Radius r	
A_0	Splitting Parameter	
α_i	Lattice Constant (of Component i)	
B_0	External Magnetic Field	
c	BET Constant	
c_i	Concentration (of Compound i)	
γ	Lattice Constant	
D	Diffusion Coefficient	
ε	Exticntion Coefficient	
E	Energy	
E_A	Activation Energy	
f	Fraction	
F	Number of Substituted Oxygens	3.14
f_i	MS Response Factor	
g	Lattice Constant	4.1
g_e	g-Factor	2.2.6
H_0	Magnetic Field (Ground State)	
H_m	Magnetic Field	
h_P	Planck Constant	
I	Nuclear Spin	2.2.6

i	Component	
I_i	Intensity (of Compound)	
j	Index	
K	Characteristic Number (Monti Baiker Criteria)	3.8
k_i	Kinetic Constant	
K_i	Adsorption Coefficient	
l	Wavelength	
μ	Reduced Mass	
m/z	Mass/Charge	
m_B	Bohr Magneton	2.2.6
m_i	Mass of i	
$m_{i,F}$	Mass/Charge Value (of Compound i, Labeled with F Isotopes)	
m_l	Magnetic Quantum Number	4.2.2
m_S	Spin Quantum Number	2.2.6
ν	Amount of Adsorbed Gas	2.2.1
n	Mole Number	
ν	Frequency of Microwave Radiation	4.2.2
N	Index	
ν	Harmonic Frequency	eq. 67
n_F	Fraction of Active Surface Oxygen	
n_i	Stochiometric Coefficient	
n_m	Cross Section (on Surface)	
N_P	Number of Spherical Particals in Reactor	
π	3.1415266	
Θ	Angle of Incidence	2.2.2
Θ_i	Surface Coverage (of component i)	

Symbol Directory

R	Ideal Gas Constant
r	Particle Radius
r_i	Reaction Rate
S_0	Total Amount of Reducible Species
S_A	Surface Area
S_i	Selectivity (to Compound i)
Std	Standard
t	time
T	Temperature
τ	Mean Residence Time
$\dot{V}$	Volume Flow
$V(r)$	Volume of Sphere with Radius r
V_i	Volume / Partial Volume of i
V_O	Oxygen Vacancy
X_i	Converion (of Compound i)
x_i	Mole Fraction (of Compound i)
z	Axial Reactor Coordinate

Figure Directory

Figure Directory

t

Figure Directory

Scheme Directory

Appendix

Photoluminescence Spectroscopy on doped and undoped

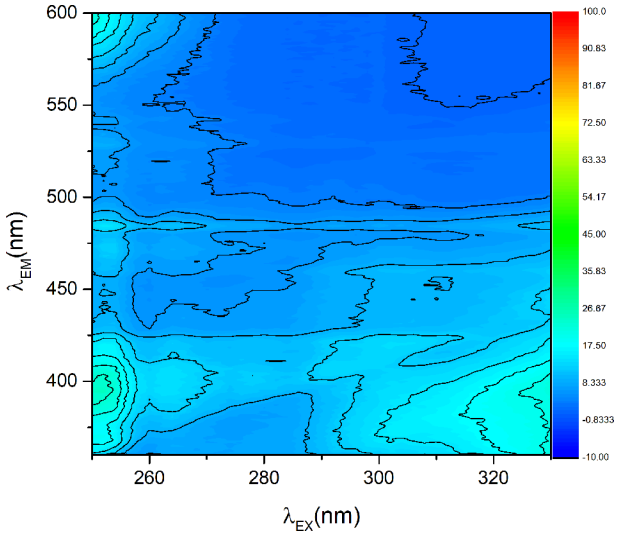

Figure S 1: Photoluminescence spectra at room temperature of 3.2 MnCaO activated at 900°C under dynamic vacuum for 6h.

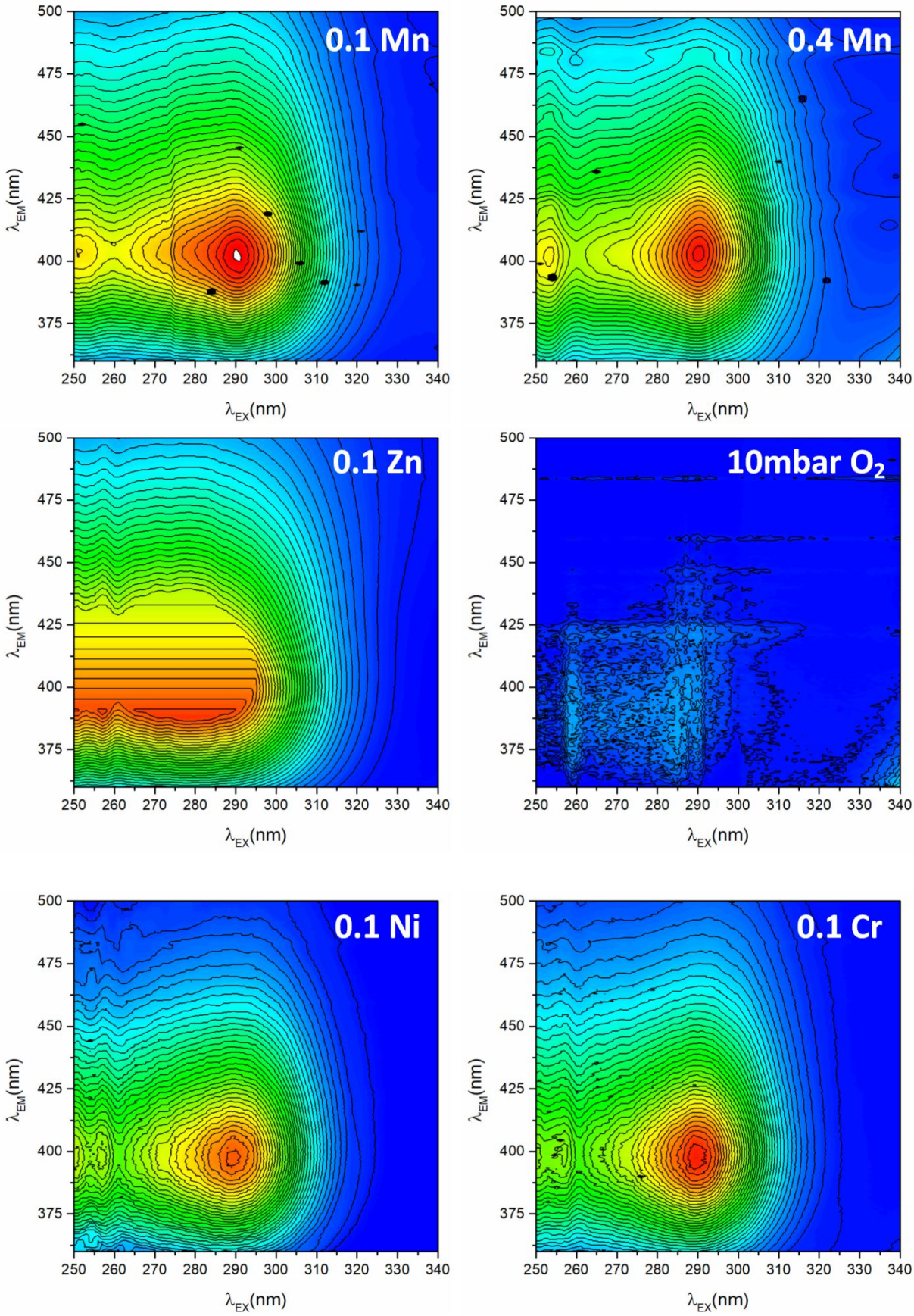

Figure S 2: Doped transition metal-doped CaO samples activated at 900°C under dynamic vacuum for 6h and sealed afterwards in the cuvette.

y

Appendix

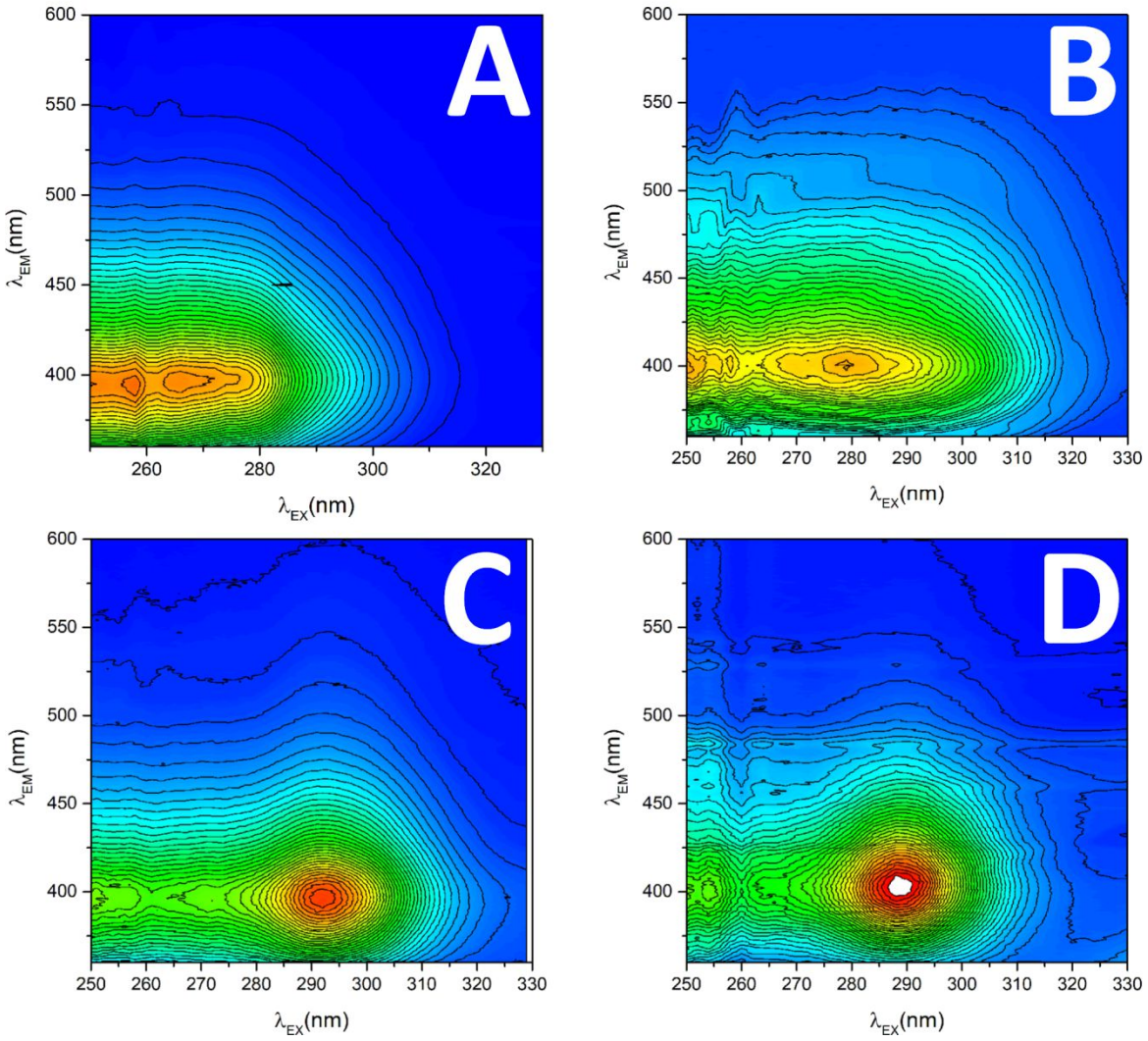

Figure S 3: PL spectra of CaO (A: pure CaO, B: ref CaO) and Mn-doped CaO (C: 0.1 MnCaO, D: 0.4 MnCaO activated at 900°C in a vacuum (It has to be noted the overall intensities follows the trend A>B>>C>D).

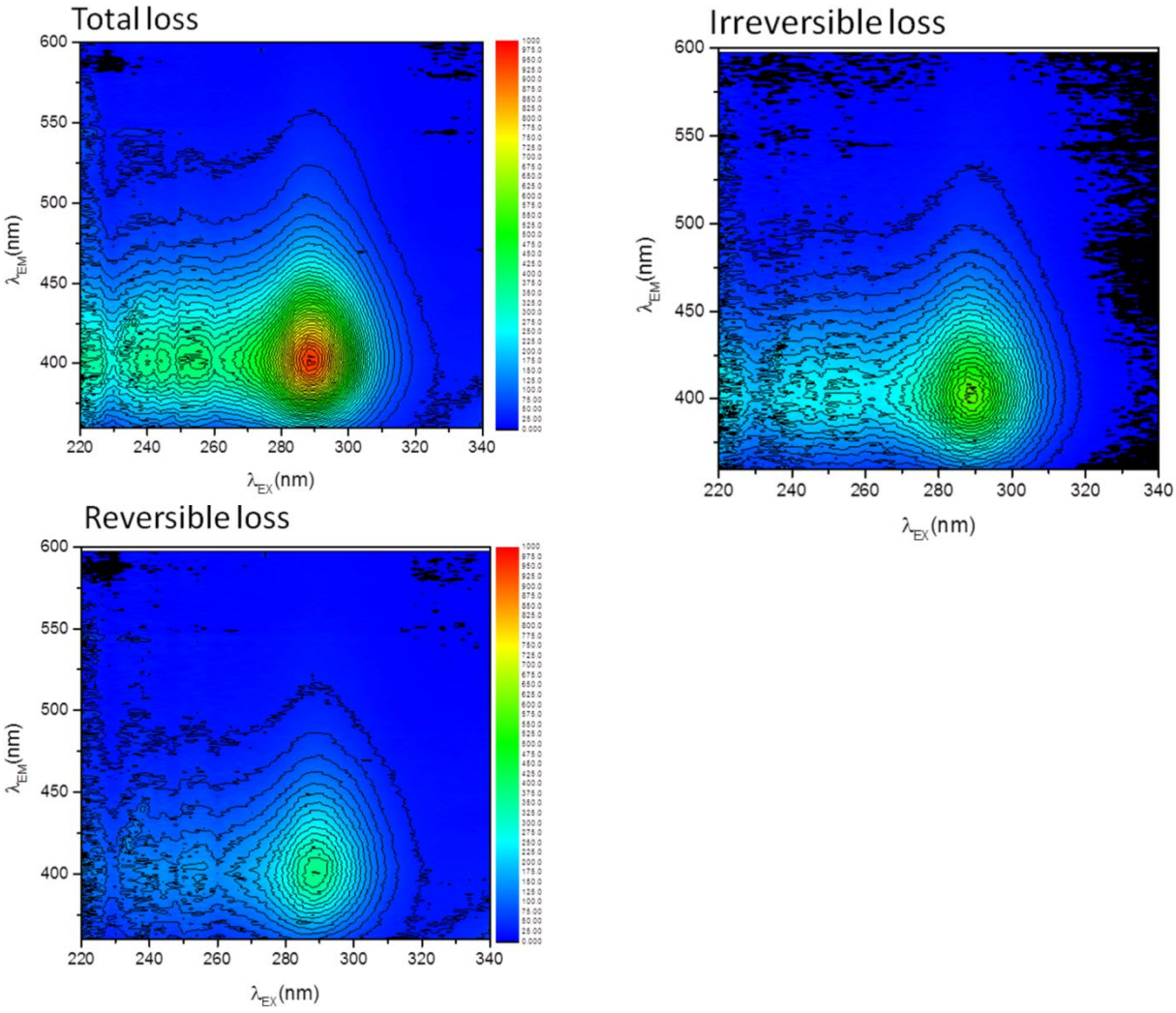

Figure S 4: Total, reversible and irreversible loss of photoluminescence signal (measured PL signal minus PL signal obtained in oxygen atmosphere) upon adding 1 mbar O_2 oxygen to Mn-doped CaO (0.4 mn CaO) activated at 900 °C in vacuum.

Appendix

Electron Paramagnetic Resonance

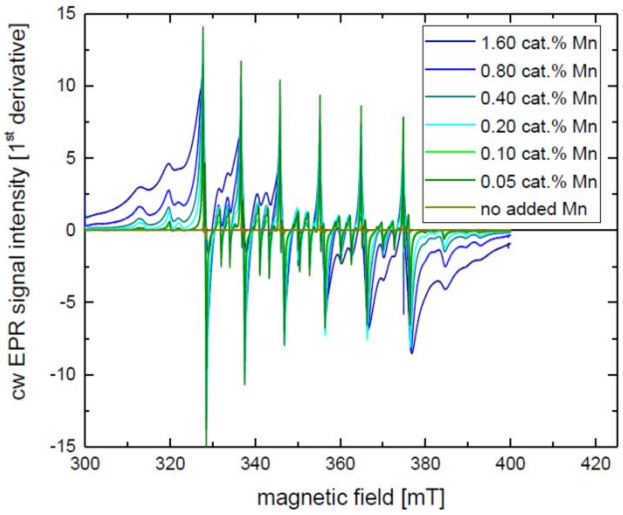

Figure S 5: 9.8 GHZ EPR measurement of Mn-doped $CaCO_3$ samples.

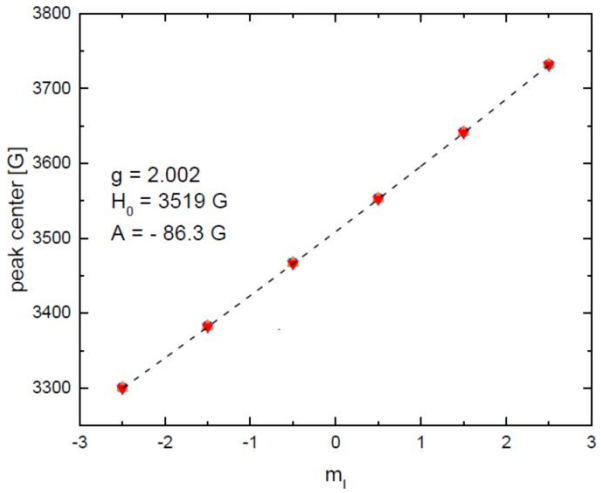

Figure S 6: Fit (dashed line) for EPR peak positions of Mn-doped CaO.

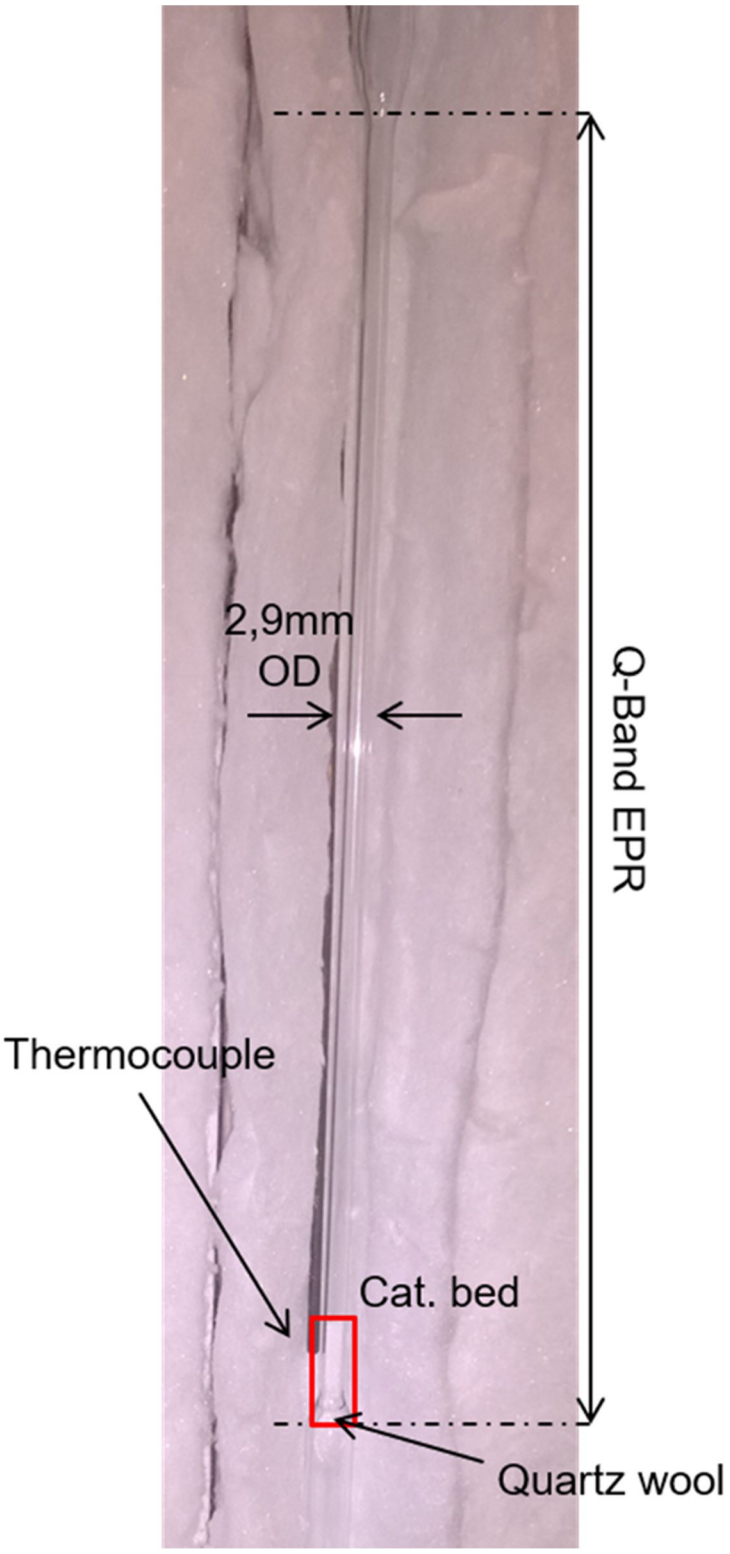

Figure S 7: EPR tube for pre and post reaction sample preparation.

Appendix

Temperature-Programmed Reduction of doped

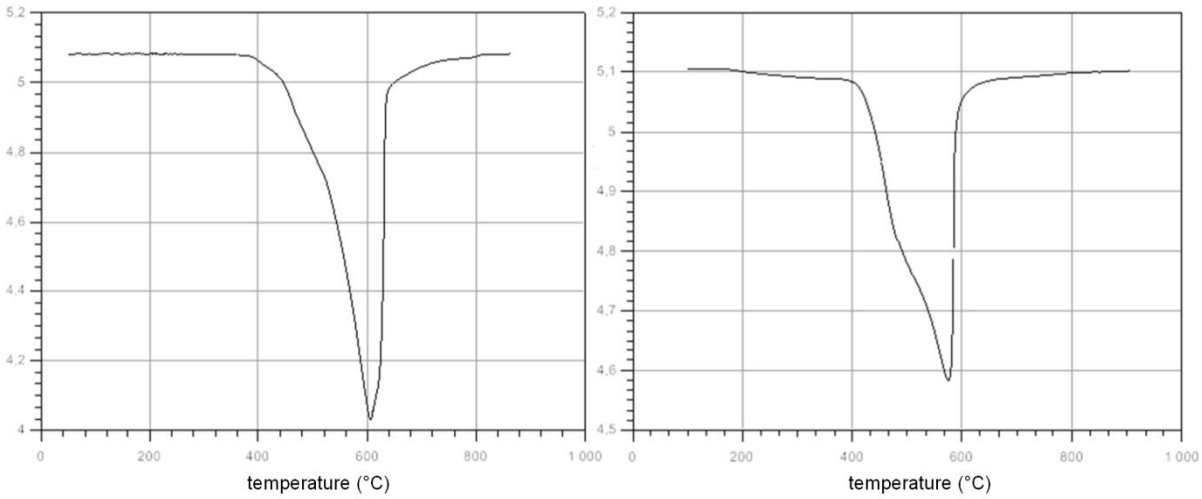

Figure S 8: TPR of Ni doped CaO activated in synthetic air at 900°C for 6 h and afterwards heated in 5% H2 in Ar, 12 °C/min. Left: 0.1%, Ni 0.655 g carbonate precursor, 15 ml/min gas flow, right: 1.6%, Ni 0.437 g carbonate precursor, 20 ml/min gas flow. Integral areas attributable to the total Ni content of the sample.

dd

Steady State Catalytic Tests

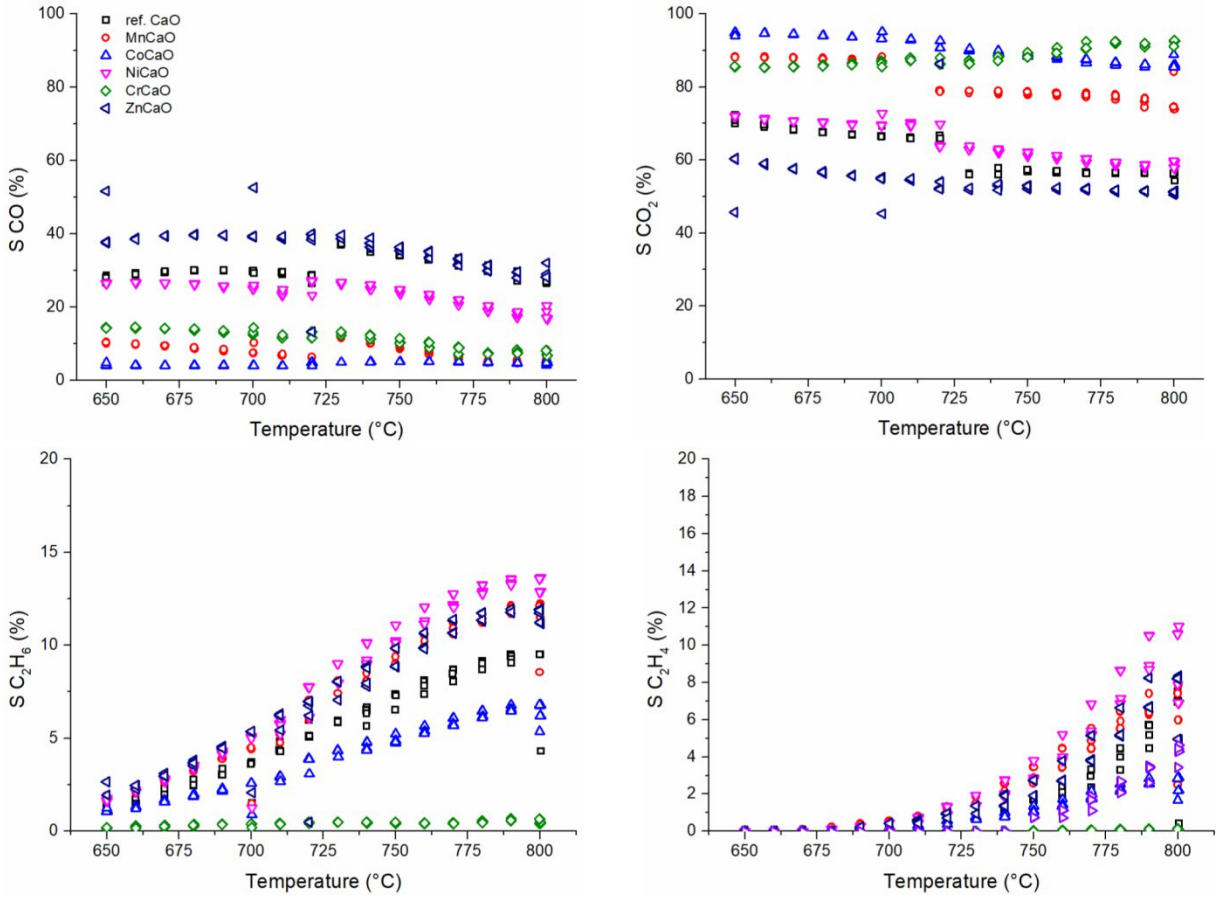

Figure S 9: Temperature dependence of OCM products using doped CaO catalysts (metal content <0.1%, 50 mg carbonate precursor, 750 mg SiC, 50 ml/min 3:3:1 of CH_4:N_2:O_2).

Appendix

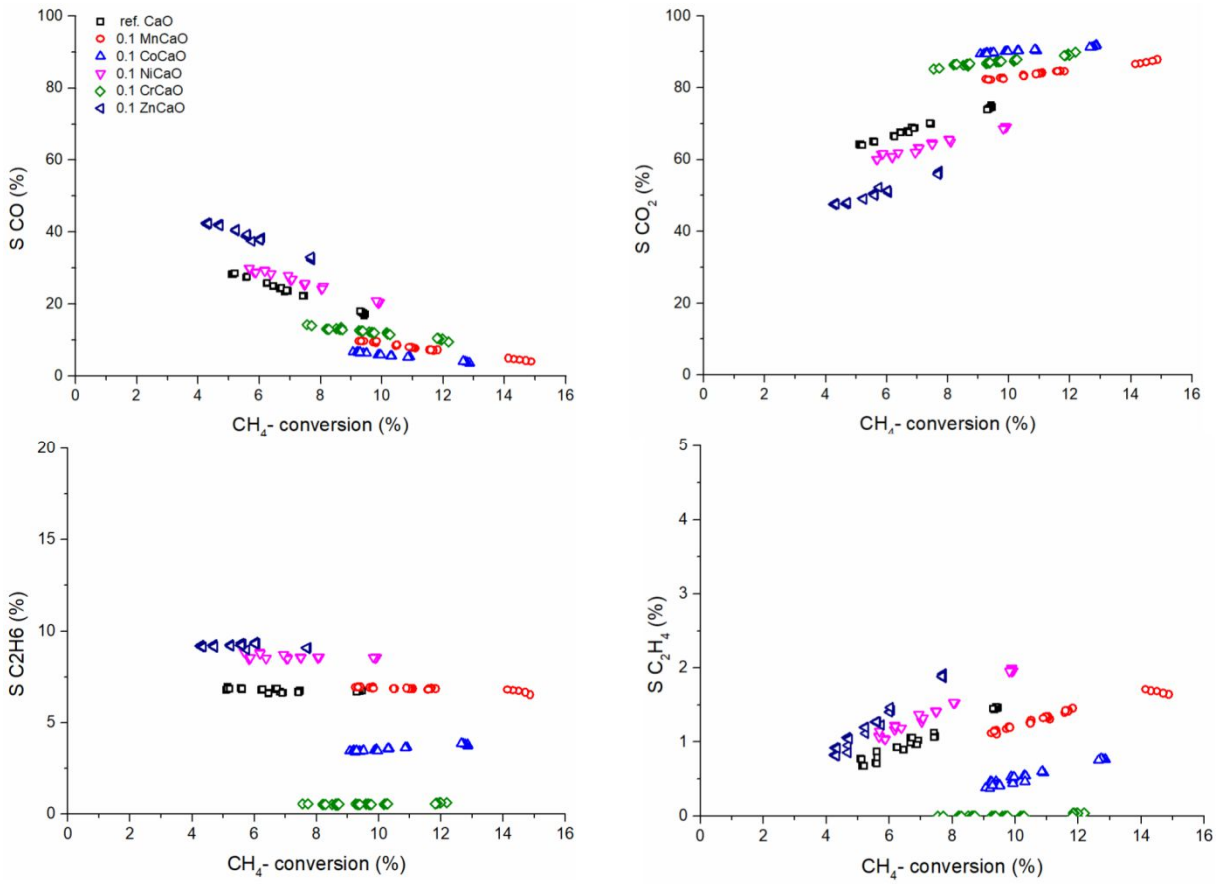

Figure S 10: Dependence of OCM products by GHSV variation using different doped CaO catalysts. GHSV was varied by change of volume flow from 37.5 ml/min up to 200 ml/min.

ff

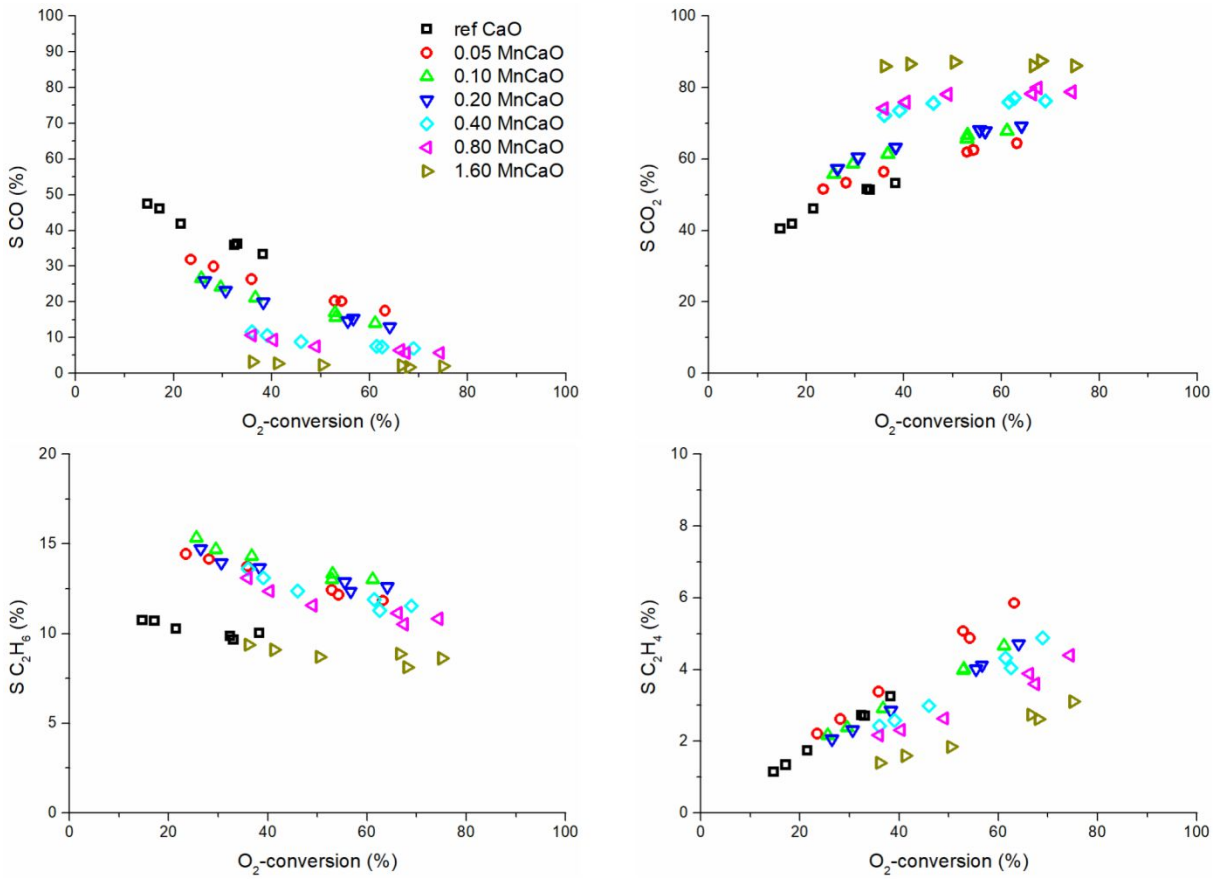

Figure S 11: Dependence of OCM products by GHSV variation using Mn-doped CaO catalysts. GHSV was varied by change of volume flow from 37.5 ml/min up to 200 ml/min.

Appendix

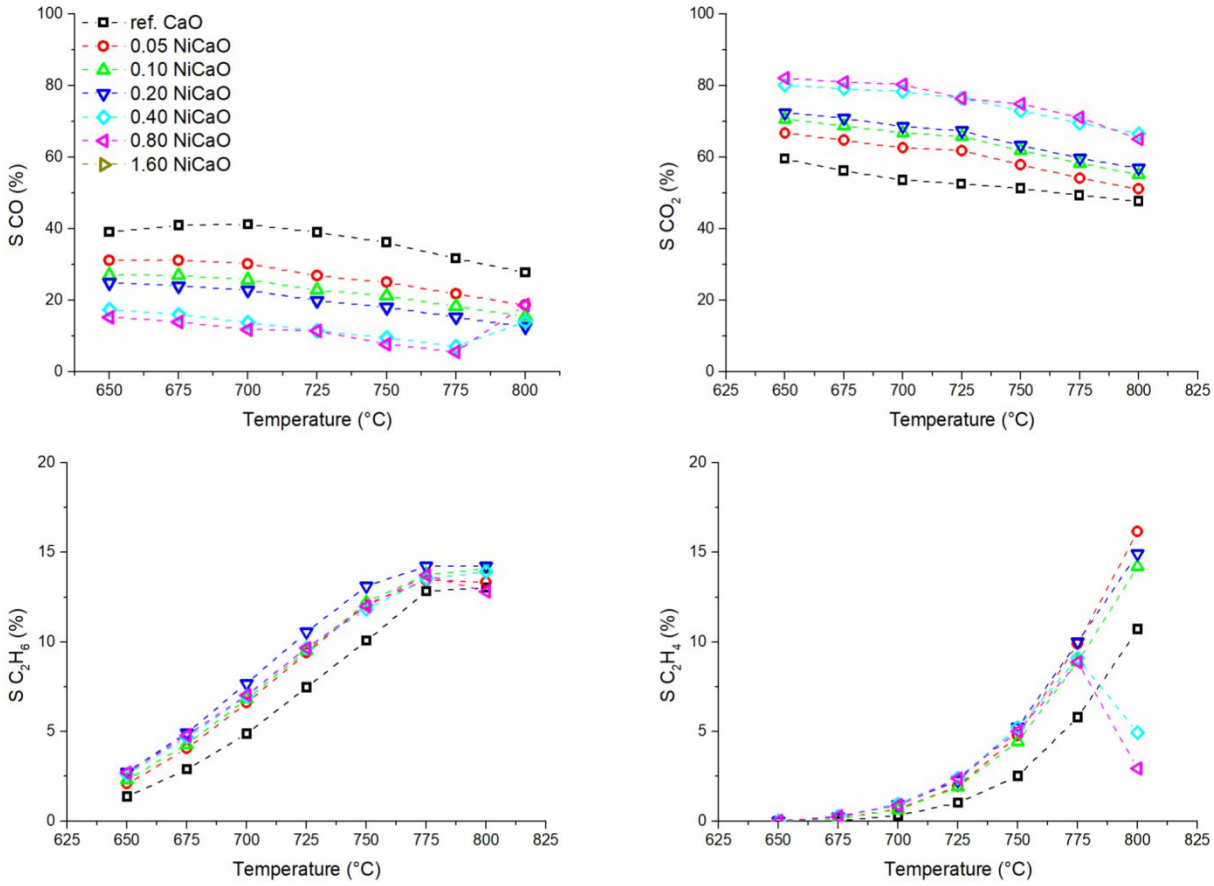

Figure S 12: Temperature dependence of OCM products using Ni-doped CaO catalysts (50 mg carbonate precursor, 750 mg SiC, 50 ml/min 3:3:1 of CH_4:N_2:O_2).

hh

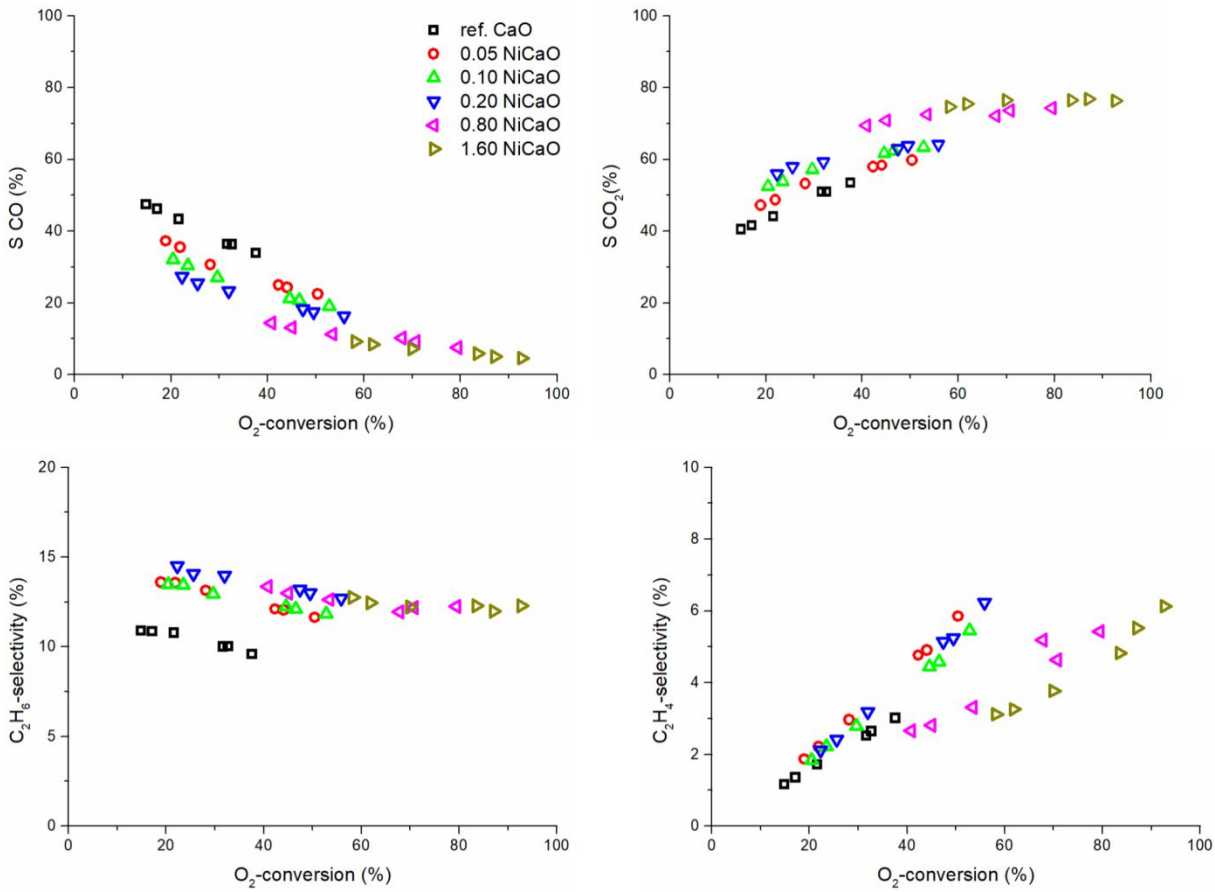

Figure S 13: Dependence of OCM products by GHSV variation using Ni-doped CaO catalysts. GHSV was varied by change of volume flow from 37.5 ml/min up to 200 ml/min.

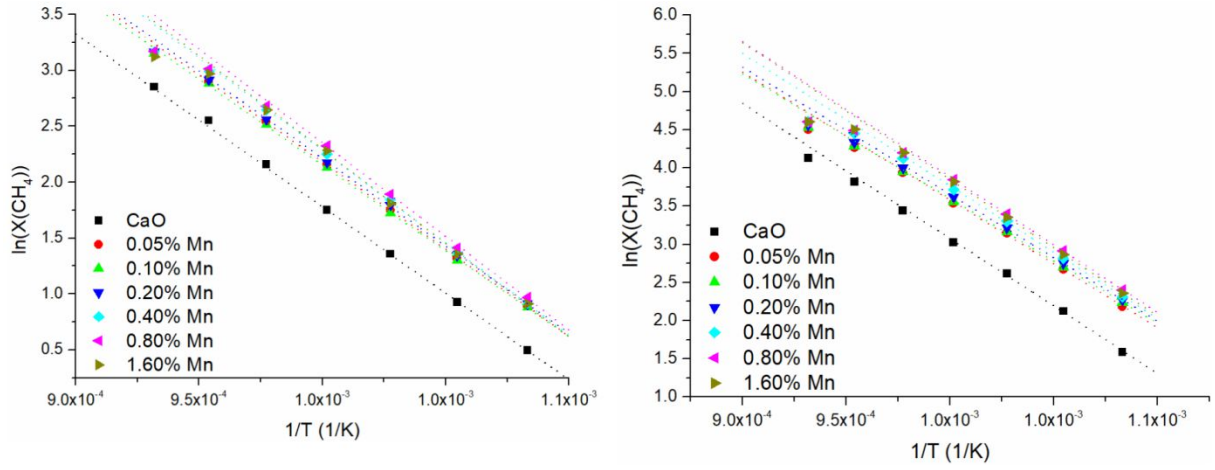

Figure S 14: Arrhenius plots for Mn and Ni doping series.

Appendix

Raman Spectroscopy

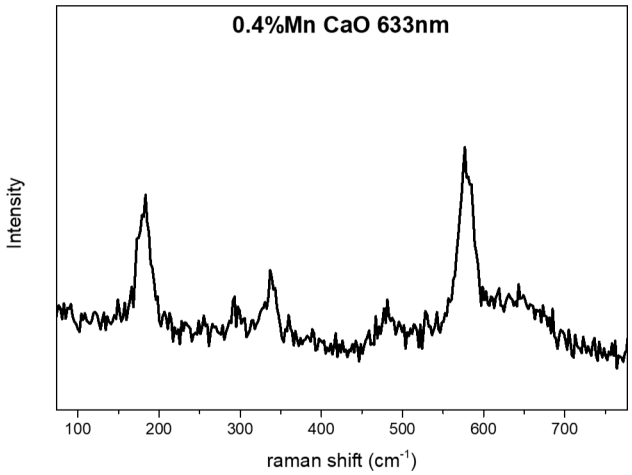

Figure S 15: Room temperature Raman spectra of 0.4Mn CaO activated at 900°C in syn. air.

In Situ Infra-Red Spectroscopy

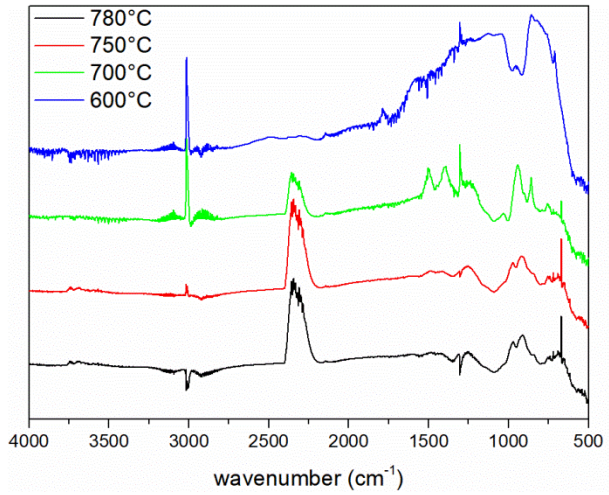

Figure S 16: IR transmission spectra of CaO in OCM feed gas reducing the temperature from 780°C to 600°C corrected by gas phase and "pure" CaO spectrum.

jj

Quantitative SSITKA of the Catalyst-Oxygen Interaction

Berkeley Madonna model for residence time simulation of the empty reactor:

```
{       Parameter       }
dVdt            =       20/60           ;Volume flow (ml/s)


{       Valve           }
Switch1         =       120
Gases           =       2
Gas0[1]         =       1
Gas0[2]         =       0
Gas1[1]         =       0
Gas1[2]         =       1

GasIn[1..Gases]     =       If Time < Switch1 then Gas0[i] else Gas1[i]


{       Tubing IN}
NTi     =       10
VTi     =       0.4
tauI    =       VTi/NTi/dVdt

Init TubeI[1..NTi,1..Gases]     =       Gas0[j]
d/dt (TubeI[1,1..Gases])        =       (GasIn[j]-TubeI[1,j]) /tauI
d/dt (TubeI[2..NTi,1..Gases])   =       (TubeI[i-1,j]-TubeI[i,j])       /tauI


{       Reactor IN      }
NRi     =       10
VRi     =       6*3/7
tauRI   =       VRi/NRi/dVdt

Init RI[1..NRI,1..Gases]        =       Gas0[j]
d/dt (RI[1,1..Gases])           =       (TubeI[NTi,j]-RI[1,j])/tauRI
d/dt (RI[2..NRI,1..Gases])      =       (RI[i-1,j]-RI[i,j])     /tauRI


{       Catalyst Area   }
NC      =       10
VC      =       6*1/7
tauC    =       VC/NC/dVdt

Init Cat[1..NC,1..Gases]        =       Gas0[j]
d/dt (Cat[1,1..Gases])          =       (RI[NRi,j]-Cat[1,j])/tauC
d/dt (Cat[2..NC,1..Gases])      =       (Cat[i-1,j]-Cat[i,j])/tauC

{       Reactor Out     }
NRO     =       10
VRO     =       6*3/7
tauRO   =       VRo/NRo/dVdt

Init RO[1..NRO,1..Gases]        =       Gas0[j]
d/dt (RO[1,1..Gases])           =       (Cat[NC,j]-RO[1,j])/tauRO
d/dt (RO[2..NRi,1..Gases])      =       (RO[i-1,j]-RO[i,j])/tauRO


{       Tubing Out      }
NTO     =       10
VTO     =       0.4
tauO    =       VTO/NTO/dVdt

Init TubeO[1..NTO,1..Gases]             =       Gas0[j]
d/dt (TubeO[1,1..Gases])                =       (Cat[NC,j]-TubeO[1,j])/tauO
d/dt (TubeO[2..NTO,1..Gases])           =       (TubeO[i-1,j]-TubeO[i,j])/tauO


{       MS-Split        }
Split                   =       3.9654
dVdtCascade             =       dVdt/(1+1/Split)
dVdtCSTR                =       dVdt-dVdtCascade


{       MS-Cascade              }
NCascade                =       2
```

Appendix

```
VCascade                        =       0.0383287
tauCascade                      =       VCascade/NCascade/dVdtCascade

Init Cascade[1..NCascade,1..Gases]  =       Gas0[j]
d/dt (Cascade[1,1..Gases])          =       (TubeO[NTO,j]-Cascade[1,j])/tauCascade
d/dt (Cascade[2..NCascade,1..Gases]) =      (Cascade[i-1,j]-Cascade[i,j])/tauCascade


{       MS-CSTR                 }
VCSTR                           =       1.09892
tauCSTR                         =       VCSTR/dVdtCSTR
Init CSTR[1..Gases]             =       Gas0[i]
d/dt (CSTR[1..Gases])           =       (TubeO[NTO,i]-CSTR[i])/tauCSTR


{       MS-Mixing                       }
Init MS[1..Gases]   =       Gas0[i]
d/dt (MS[1..Gases]) =       (CSTR[i]*dVdtCSTR+Cascade[NCascade,i]*dVdtCascade-MS[i]*dVdt)/0.001
TestMS1             =       (CSTR[1]*dVdtCSTR+Cascade[NCascade,1]*dVdtCascade-MS[1]*dVdt)/0.001
TestMS2             =       (CSTR[2]*dVdtCSTR+Cascade[NCascade,2]*dVdtCascade-MS[2]*dVdt)/0.001


{       Fitting         }
HeOut   =       MS[1]*CalHe
CalHe   =       1e-7
N2Out   =       MS[2]*CalN2
CalN2   =       1e-7
```

Qualitative SSITKA of the Catalyst-Oxygen Interaction

Berkeley Madonna model for the qualitative consideration of the oxygen SSITKA experiments:

```
{-------------------------------------------------------------------------------}
{----------------------------Reactor Specifics----------------------------}
{-------------------------------------------------------------------------------}

z               =       10              ;Reactor segments
Vr              =       1               ;Empty Volume Reactor
pC              =       1/3             ;packing parameter
Vfl             =       8.88            ;Volume Flow
Vg              =       Vr*pC           ;Gas Volume
Vgz             =       Vg/z            ;Gas Volume of Segment
T0              =       273.15          ;Standard T
ddtn            =       Vfl/Vgz*T0/T
niz             =       Vgz*0.1*p/(Rg*T)*1e6            ;mol


{-------------------------------------------------------------------}
{----------------------------Parameters----------------------------}
{-------------------------------------------------------------------}

p               =       1               ;bar
T               =       1000            ;K temperature


{-------------------------------------------------------------------}
{----------------------------Constants----------------------------}
{-------------------------------------------------------------------}

Rg              =       8.314           ;Ideal gasconstant


{-------------------------------------------------------------------------------}
{----------------------------Catalysator specifics----------------------------}
{-------------------------------------------------------------------------------}

rr              =       10              ;particle segments
m               =       0.0277          ;g catalyst mass
ny              =       1               ;Stochiometric coefficient oxygen in compound
Mm              =       56.01           ;g/mol molar mass
S               =       40              ;m²/g specific surface area
rho             =       3.37            ;g/cm³ density
```

```
r0                  =       50e-7               ;Particle radius cm


{-------------------------------------------------------------------------}
{----------------------------Geometrics-----------------------------}
{-------------------------------------------------------------------------}

V                   =       m/rho               ;cm³
As                  =       S*100^2*m           ;cm²
nges                =       m/Mm*ny
n0frac              =       0.001               ;fraction of accessible oxygen atoms
n0                  =       n0frac*nges         ;mole Amount of accessible oxygen
n0z                 =       n0/z                ;mole Amount of accessible oxygen per volume fraction
VP                  =       4/3*pi*r0^3         ;Particle Volme
ntot                =       V/(Vp)              ;total amount of particles
ni                  =       ntot/z              ;Number of particles per dz

r0eff               =       r0*(1-n0frac)^(1/3)         ;Diffusion limited raduis
r[1..rr]            =       (rr+1-i)/rr*r0eff           ;Fractual Radius
A[1..rr]            =       ni*r[i]^2*4*pi              ;Radial Diffusion Area
Vi[1..rr-1]         =       ni*(r[i]^3-r[i+1]^3)*4/3*pi ;Radial Volume fraction
Vi[rr]              =       ni*r[rr]^3*4/3*pi           ;Volume Fraction of last Element
n[1..rr]            =       Vi[i]*rho/Mm*ny*1e6         ;µmole Atoms per Volume fraction
n[0]                =       n0z*1e6


{-------------------------------------------------------------------------------}
{--------------------------Particle Simulation--------------------------}
{-------------------------------------------------------------------------------}

D                   =       D0*exp(-Eas/(Rg*T))         ;Solid Diffusion
Eas                 =       200000                      ;J/mol lattice exchange barrier energy
D0                  =       1e3                         ;Diffusion coefficient

Init Os[0..rr,1..z]     =       0

d/dt (Os[0,1..z])       =       (k*(p1[j]*(1-Os[0,j])  +p12[j]*(1-2*Os[0,j])-p2[j]*Os[0,j])D*A[1]*(Os[0,j])-Os[1,j]) /n[0]
d/dt (Os[1..rr-1,1..z]) =       D*((Os[i-1,j]-Os[i,j])*A[i]-(Os[i,j]-Os[i+1,j])*A[i+1]) /n[i]
d/dt (Os[rr,1..z])      =       D*(Os[i-1,j]-Os[i,j])*A[i] /n[i]


{-------------------------------------------------------------------}
{----------------------------Gasphase-----------------------------}
{-------------------------------------------------------------------}

k                   =       k0*exp(-Ea/(Rg*T))          ;Arrhenius equation
Ea                  =       100000                      ;J/mol activation energy
k0                  =       1e6                         ;Frequency factor

d/dt (x1[0])        =       0
d/dt (x12[0])       =       0
d/dt (x2[0])        =       0

Init x1[0]  =       0.2
Init x12[0]=        0
Init x2[0]  =       0

d/dt(x1[1..z])      =       ddtn*(x1[i-1]-x1[i]) +k*(-p1[i]*(1-Os[0,i])+1/2*p12[i]*Os[0,i])    /niz
d/dt(x12[1..z])     =       ddtn*(x12[i-1]-x12[i]) +k*( p1[i]*(1-Os[0,i])-1/2*p12[i]+p2[i]*Os[0,i])       /niz
d/dt(x2[1..z])      =       ddtn*(x2[i-1]-x2[i])    +k*(+1/2* p12[i]*(1-Os[0,i])-p2[i]*Os[0,i]  )         /niz

Init x1[1..z]       =       0
Init x12[1..z]      =       0
Init x2[1..z]       =       0.2

p1[0..z]            =       x1[i]       *p
p12[0..z]           =       x12[i]      *p
p2[0..z]            =       x2[i]       *p

p1z                 =       p1[z]
p12z                =       p12[z]
p2z                 =       p2[z]

{-------------------------------------------------------------------}
{----------------------------Debugging----------------------------}
{-------------------------------------------------------------------}
```

Appendix

debug[1..z]	=	(1-Os[rs,i])*n[rs]
rs	=	0
ntest	=	Arraysum(n[*])*z/1e6
Init n2tot	=	0
d/dt (n2tot)	=	(p2z+0.5*p12z)*Vfl*0.1/(Rg*T0)

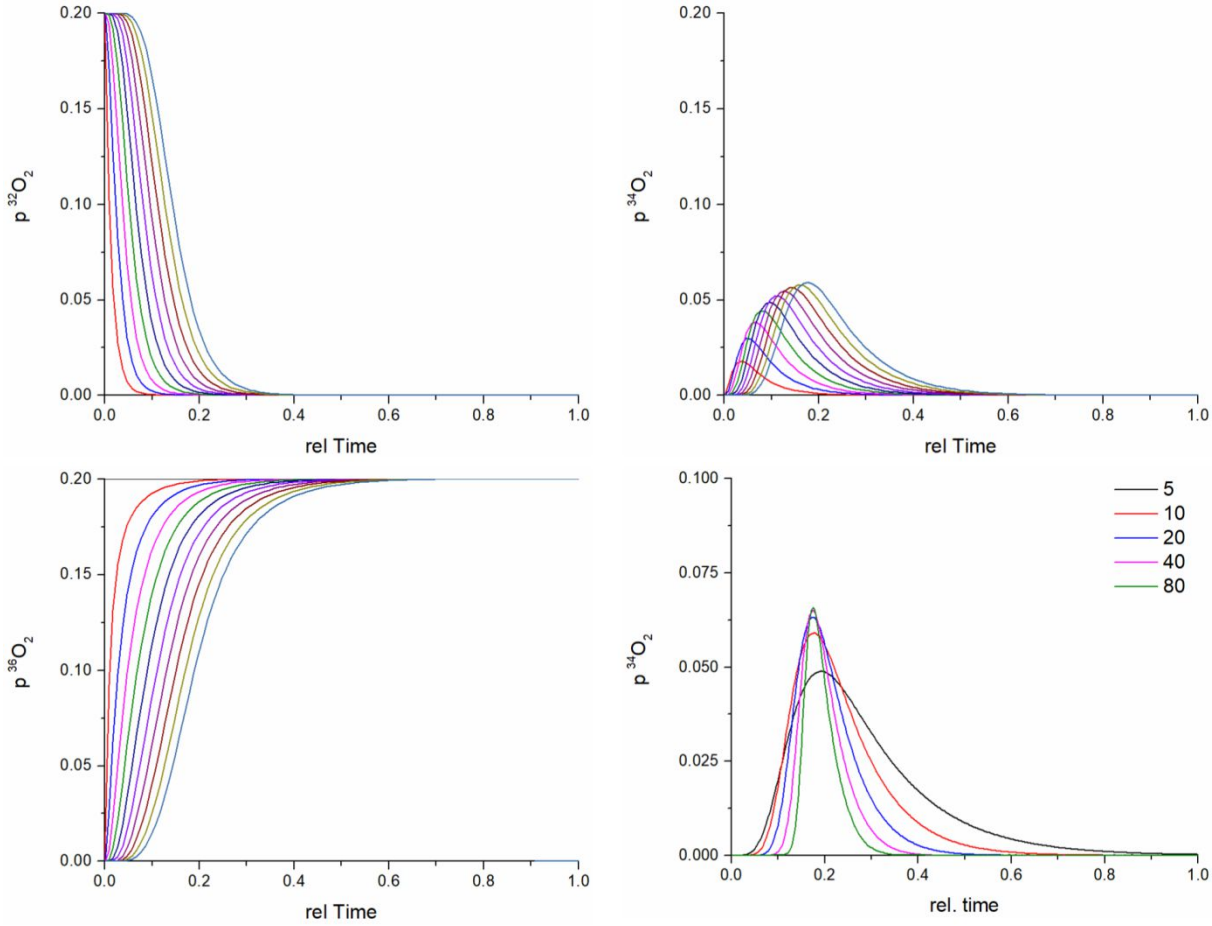

Figure S 17: Simulation of partial pressures of different oxygen isotopes at different reactor sections (N) in the reactor (top left, right and bottom left). Variation of number of segments (N) to divide z.

nn